Climate change impacts on Mediterranean coastal and transitional areas: Assessment, projection, and adaptation

Edited by
Davide Bonaldo, Agustin Sanchez-Arcilla, Achilleas G. Samaras
and Maria Snoussi

Published in
Frontiers in Marine Science

About Frontiers

Frontiers is more than just an open access publisher of scholarly articles: it is a pioneering approach to the world of academia, radically improving the way scholarly research is managed. The grand vision of Frontiers is a world where all people have an equal opportunity to seek, share and generate knowledge. Frontiers provides immediate and permanent online open access to all its publications, but this alone is not enough to realize our grand goals.

Frontiers journal series

The Frontiers journal series is a multi-tier and interdisciplinary set of open-access, online journals, promising a paradigm shift from the current review, selection and dissemination processes in academic publishing. All Frontiers journals are driven by researchers for researchers; therefore, they constitute a service to the scholarly community. At the same time, the *Frontiers journal series* operates on a revolutionary invention, the tiered publishing system, initially addressing specific communities of scholars, and gradually climbing up to broader public understanding, thus serving the interests of the lay society, too.

Dedication to quality

Each Frontiers article is a landmark of the highest quality, thanks to genuinely collaborative interactions between authors and review editors, who include some of the world's best academicians. Research must be certified by peers before entering a stream of knowledge that may eventually reach the public - and shape society; therefore, Frontiers only applies the most rigorous and unbiased reviews. Frontiers revolutionizes research publishing by freely delivering the most outstanding research, evaluated with no bias from both the academic and social point of view. By applying the most advanced information technologies, Frontiers is catapulting scholarly publishing into a new generation.

What are Frontiers Research Topics?

Frontiers Research Topics are very popular trademarks of the *Frontiers journals series*: they are collections of at least ten articles, all centered on a particular subject. With their unique mix of varied contributions from Original Research to Review Articles, Frontiers Research Topics unify the most influential researchers, the latest key findings and historical advances in a hot research area.

Find out more on how to host your own Frontiers Research Topic or contribute to one as an author by contacting the Frontiers editorial office: frontiersin.org/about/contact

Climate change impacts on Mediterranean coastal and transitional areas: Assessment, projection, and adaptation

Topic editors

Davide Bonaldo — National Research Council (CNR), Italy
Agustin Sanchez-Arcilla — Universitat Politecnica de Catalunya, Spain
Achilleas G. Samaras — Democritus University of Thrace, Greece
Maria Snoussi — Mohammed V University, Morocco

Table of
contents

Editorial: Climate change impacts on Mediterranean coastal and transitional areas: assessment, projection, and adaptation

Davide Bonaldo[1]*, Agustin Sanchez-Arcilla[2],
Achilleas G. Samaras[3] and Maria Snoussi[4]

[1]Consiglio Nazionale delle Ricerche, Istituto di Scienze Marine (CNR-ISMAR), Venice, Italy, [2]Laboratori d'Enginyeria Maritima, Universitat Politecnica de Catalunya (UPC-BarcelonaTech), Barcelona, Spain, [3]Department of Civil Engineering, Democritus University of Thrace, Xanthi, Greece, [4]Faculty of Sciences, Mohammed V University in Rabat, Rabat, Morocco

KEYWORDS

coastal oceanography, coastal regions, coastal risk, long-term monitoring, numerical modelling

---

Editorial on the Research Topic
Climate change impacts on Mediterranean coastal and transitional areas: assessment, projection, and adaptation

---

The combination of the regional intensity of climate change trends and a heavy and increasing anthropic pressure makes the Mediterranean coastal and transitional zones a vulnerability hotspot under both present climate and future scenarios. In such systems, in which diverse land-uses and socio-economic patterns are intertwined with the small scale of coastal processes, the formulation of effective response strategies cannot overlook a thorough assessment of recent trends and future evolution of coastal dynamics and climate change impacts. The key knowledge-related challenges on this front are, thus, typically related with the availability of information with the adequate spatial and temporal coverage for capturing the downscaled climate signal, and with the capability to operationalise this information into a decision-making perspective. The studies collected in this Research Topic undertake the twofold challenge of improving the knowledge base and suggesting new paradigms enabling improved and informed adaptation actions.

Ozer et al. discuss the evidences from a long-term monitoring programme along the coasts of Israel (Eastern Med) to characterise the variability of marine dynamics over different time scales. While confirming a tight coupling between coastal and open-sea near-surface processes, they emphasize a higher responsiveness to atmospheric conditions in coastal areas. Long-term observation programmes can be effectively flanked by data from surveys that may not have been specifically designed for this purpose, but still capture relevant processes for the evolution of the state of the ocean. In this direction, Zodiatis et al. integrate data sets from different monitoring initiatives in the South-Eastern Levantine basin (Eastern Med), identifying the evolution of some of the main circulation features in the region and their relationship with neighbouring dynamical structures. Finally, in the

absence of data with the necessary spatial and temporal resolution and coverage, preliminary information can be drawn from easily available data sources and possibly with a modest investment of resources, while prioritising the knowledge gaps to be filled. This can typically be the case in regions undergoing severe climate and socio-economic pressures, where there is an urgent need to support policy and regulatory development in coastal management and planning. Following this logic, Monioudi et al. show how widely available satellite data can be combined with meteo-marine climate and nearshore numerical modelling to achieve an island-scale assessment of the exposure of Cyprus beaches (Eastern Med) to erosion under different climate change scenarios. The need to optimise the investigation effort by benefiting from large existing datasets is particularly pressing in the projection of future risks associated with intense meteo-marine events on coastal systems, in which the computational cost associated with the need for accuracy in describing small-scale processes and the multi-decadal horizon of climate evolution is practically unsustainable for classical model downscaling approaches. Denamiel et al. exemplify a possible response, proposing a methodology for an affordable prediction of meteotsunami hazards based on the combined use of synoptical indexes from available global climate model (GCM) ensembles and targeted downscaling applications.

Malvarez et al. push the analysis of coastal processes towards a source-to-sink dimension by tackling sediment dynamics on the beaches of Marbella (Western Med) in terms of catchment-scale budget, stimulating a reflection on the timeliness of updating sediment management paradigms and its implications in terms of policy and technological advances. Their study also hints at a dynamical concept of coastal resilience, in which the main functions and processes of coastal systems are overall preserved but are allowed to shift in position. Climate challenges may also lead to rethink criteria and techniques for the very definition of coastal vulnerability. This emerges in the contribution by Sánchez-Artús et al., addressing a regional-scale assessment referred to flooding and erosion based on the use of high-resolution hydrodynamic modelling and on the application of the coastal archetype concept. This approach allows capturing the main elements of coastal complexity for a limited number of representative beaches. New paradigms are also needed for the design of coastal infrastructures, particularly as long as their expected life span is comparable with the time scale of climate change effects: referring to the management of port breakwaters, Stagnitti et al. discuss a methodology for assessing the impact of climate change on the performance of upgraded rubble-mound structures based on a set of application-oriented climate parameters. With the contribution by Agharroud et al., the focus is on climate-related risks for a densely anthropized region along the coast of Morocco (South-Western Med). While providing a valuable view on climate risks in the southern Mediterranean basin and an important support for adaptation and policy-making, this work highlights the importance of risk perception and awareness by the population as a prerequisite for suited responses, pointing out that poor socio-economic conditions and high rates of illiteracy can act as a risk magnifier even in areas characterised by relatively low levels of hazard and exposure.

As coastal ecosystems undergo diverse and potentially severe climate threats, they are at the same time a potential provider for crucial ecosystem services, from carbon sequestration and coastal protection (as in the case of coastal wetlands and seagrass meadows) to biodiversity conservation. A versatile and interdisciplinary methodology for the creation of a solid knowledge ground in support of decision-making in this direction is presented by Vitelletti et al., combining data from publicly available repositories with multi-decadal oceanographic climate projections into a habitat suitability application. The work is based on the modelled prediction of possible coralligenous habitat evolution in the Adriatic Sea (North-Eastern Med).

In summary, the works collected in this Research Topic highlight that the response to climate change in coastal areas can be informed not only by long-term monitoring programmes or large international initiatives, but also (and not less importantly) by relatively small and local datasets. The regional and local subjects typically in charge of these datasets should thus be engaged in a closer interaction with academic research entities, aiming at reducing data fragmentation and enhancing a widespread adoption of FAIR (Findability, Accessibility, Interoperability, Reusability) principles in the creation of a knowledge-base for coastal resilience building.

Author contributions

DB: Writing – original draft, Writing – review & editing. AS-A: Writing – original draft, Writing – review & editing. AS: Writing – original draft, Writing – review & editing. MS: Writing – original draft, Writing – review & editing.

Funding

Conflict of interest

The authors declare that the research was conducted in the absence of any commercial or financial relationships that could be construed as a potential conflict of interest.

The author(s) declared that they were an editorial board member of Frontiers, at the time of submission. This had no impact on the peer review process and the final decision

Publisher's note

Check for updates

Thermohaline Temporal Variability of the SE Mediterranean Coastal Waters (Israel) – Long-Term Trends, Seasonality, and Connectivity

Tal Ozer[1,2]*, Isaac Gertman[1], Hezi Gildor[3] and Barak Herut[1,2]*

[1] Israel Oceanographic and Limnological Research, Haifa, Israel, [2] Department of Marine Geosciences, Leon H. Charney School of Marine Sciences, University of Haifa, Haifa, Israel, [3] Institute of Earth Sciences, Hebrew University, Jerusalem, Israel

The high variability of coastal waters together with the growing need for assessing the state of the marine coastal ecosystem, require continuous monitoring at exceptional resolution and quality, especially during the Anthropocene changing seas. We perform a comprehensive analysis of a decadal (March 2011 to June 2021) thermohaline variability of the East Levantine Basin (LB) coastal waters (continuous measurements), its predominating temporal trends and their linkage with atmospheric forcing and advection. We identify statistically significant long-term warming and salinification trends with yearly rates of 0.048°C and 0.006, respectively. Through the use of the X11-ARIMA method temperature and salinity inter-annual trends are examined and associated with previously published open ocean dynamics as well as model reanalysis. We study the linkage between Northern and Southern coastal locations, and identify the along shore northward current as a primary cause of positive temperature anomalies arriving from the south. The coastal salinity long-term trend demonstrates a connection to local precipitation. A less coherent seasonal sequence is found with a bimodal behavior, where, salinity values drop in August on several summers. This drop is attributed to the intensification of the along shore current in the period of June-July, potentially advecting more Atlantic Water. The observations presented here emphasize the relatively strong coupling between coastal water and the open ocean, the influence of the general surface circulation of the LB on the coastal zone and the faster response time and higher sensitivity of the coastal environment to atmospheric forcing.

Keywords: seawater, salinity, climate change, inter-annual, Mediterranean Sea, temperature, variability, mesoscale

INTRODUCTION

The Mediterranean Sea (MS), being a marginal sea, relatively small in size, with a restricted connection to the Atlantic Ocean has a faster response to atmospheric forcing compared to the open ocean. It has therefore been repeatedly acknowledged as a prime location for climate change research (Giorgi, 2006; Giorgi and Lionello, 2008; Schroeder et al., 2012, 2016; Pastor et al., 2018; UNEP/MAP and Plan Bleu, 2020). Atlantic Water (AW) entering the MS at the surface through the Gibraltar Strait undergo continuous transformation due to strong radiation

and intensive evaporation exceeding runoff and precipitation (Robinson et al., 1992; Hamad et al., 2005; Malanotte-Rizzoli et al., 2014; Estournel et al., 2021). In summer, the Levantine Surface Water (LSW) occupies the upper part of the water column with salinity (S) as high as ∼39.7 and temperature (T) of 30°C (Lascaratos et al., 1999; Gertman and Hecht, 2002). The coastal waters of Israel, at the eastern end of the LB, occupy the continental shelf and present some of the highest T and S values of the region. These uniquely high thermohaline values, coupled with extreme oligotrophy (Herut et al., 2000; Kress et al., 2014), make the marine ecosystem of the eastern LB highly sensitive to thermohaline changes, as identified for the global coastal zone (Gissi et al., 2021). Sub-mesoscale dynamics may also have a crucial influence on the physical and biogeochemical characteristics of a confined body of Robinson et al. (1992) coastal water. Such a formation of localized niches separated by transport barriers, was presented by Efrati et al. (2013) and was suggested to have a key role in the dynamics of planktonic communities. In addition to global and local climate induced processes, the coastal marine environment of the MS is affected by a variety of local anthropogenic stresses such as economic development, population increase, and changes in land use patterns (Micheli et al., 2013; Ramírez et al., 2018; UNEP/MAP and Plan Bleu, 2020).

The Sixth Assessment Report of the IPCC (2021) has stated that each of the last four decades has been successively warmer than its previous and accredited a rise of 0.8 to 1.3°C in global surface temperature to human activities. This accumulation of energy has brought about an increase in global sea surface temperature (SST) which is expected to endure in the near future, regardless of reduction of greenhouse gases emissions (Kirtman et al., 2013; Bindoff et al., 2019). Over the next two decades (2031–2050) global SST is predicted to rise with a mean yearly rate of 0.055°C or 0.069°C under low (RCP2.6) or high (RCP8.5) greenhouse gas emissions scenarios, respectively (IPCC, 2019). Furthermore, the rise in SST has also been shown as a contributing factor to the intensification of heavy precipitation events over land worldwide (Collins et al., 2013, 2019), and in the MS (Miglietta et al., 2011; Pastor et al., 2015; Amitai and Gildor, 2016; Desbiolles et al., 2021).

Many authors have identified a SST warming trend of the Mediterranean basin or sub basins, either using in situ measurements (Rixen et al., 2005; Belkin, 2009; Ozer et al., 2017) or longer SST series originating from remote sensing data (Criado-Aldeanueva et al., 2008; Nykjaer, 2009; Skliris et al., 2012; Shaltout and Omstedt, 2014; Pastor et al., 2018, 2020; El-Geziry, 2021; Pastor, 2021). The reported warming rates vary based on the investigated area, period and water mass and are in the range of 0.024 to 0.12°C year^{-1} (**Table 1**). A salinification trend of the MS has also been repeatedly reported with yearly rates ranging from 0.0014 to 0.008 (Krahmann and Schott, 1998; Vargas-Yanez et al., 2010; Ozer et al., 2017; Schroeder et al., 2017; Skliris et al., 2018) (**Table 1**). Skliris et al. (2018) stated that the MS salinification trend is a result of changes in the regional water cycle including a long-term increase in evaporation coupled with a decrease in precipitation (Mariotti et al., 2002; Mariotti, 2010; Romanou et al., 2010; Skliris et al., 2012) and the reduction of

river runoff both through climate change and the damming of major rivers (Rohling and Bryden, 1992; Skliris and Lascaratos, 2004; Skliris et al., 2007; Ludwig et al., 2009). We note that the highest warming and salinification trends (of 0.12°C year^{-1} and 0.008, respectively) were identified in the southeastern MS LSW water (Ozer et al., 2017).

Tanhua et al. (2019) pointed out to the gaps in ocean observing coverage and the ever-growing use of the marine environment for both open ocean and coastal applications and the need to supply these users with operational services. Sustainable, long-term in situ monitoring programs are required for the improvement of coastal forecasts (Brenner et al., 2006), the calibration of remote sensing data and the enhancement of knowledge of the coastal water dynamics and their effects on the coastal ecological system. Pinardi and Coppini (2010) articulated: "The high variability of ocean currents and the need for the assessment of the state of the marine environment require a continuous monitoring of the ocean environment at unprecedented resolution and quality. On the other hand, scientific discoveries require continuous observations of the essential state variables of the system in order to detect new basic mechanisms and processes."

In this study, we perform a comprehensive analysis of the thermohaline variability of regional coastal waters, in order to better characterize the coastal marine environment, its predominating temporal trends and their linkage with atmospheric forcing and advection. Using the time series of the Israeli coastal monitoring stations, unprecedented for this region in terms of temporal resolution, we investigate coastal variability and dynamics in the eastern MS, and elucidate on the issues of: (1) long term and inter annual trends, including a comparison to open ocean findings, (2) the predominance of the seasonal cycle, and (3) the connectivity of coastal waters along the Israeli coast.

MATERIALS AND METHODS

The Israeli Coastal Monitoring Stations

In the framework of the National Monitoring Program of Israel's Mediterranean waters (INMoP), Israel Oceanographic and Limnological Research (IOLR) operates two continuous observation posts with near-real-time data transfer to IOLR server[1]. These stations are located at the westernmost edge of the coal terminals in Hadera (north) and Ashkelon (south), 2.2 kms offshore at water depths of 26 m (**Figure 1**). Hadera station (MedGloss # 80) was established toward the end of 1991, upgraded through the years and currently includes a bottom mounted, up looking, Teledyne RD Instruments 600 KHz Workhorse Monitor Waves ADCP located ∼100 m westward from the terminal end at water depth of 26 m. A Paroscientific Inc. Intelligent Digiquartz 8800 sea level sensor (PAROS) and a SBE16plusV2 Sea-Bird CTD (added to Hadera station in 2011) are installed on the westernmost terminal sporting pole at a depth of 11–12 m. The CTD is equipped with standard T/C duct and pressure sensors together with auxiliary sensors of dissolved oxygen (SBE63 Optode, Sea-Bird electronics) and

---

[1] https://isramar.ocean.org.il

TABLE 1 | Reported temperature and salinity yearly trends from investigations in various areas of the Mediterranean Sea, based on different data sources and time periods.

	References	Period	Data	Scope	Yearly trend
Temperature (°C)	Rixen et al. (2005)	1980–2000	In-Situ	MS	0.024°C
	Criado-Aldeanueva et al. (2008)	1992–2005	Satellite	MS	0.06°C
	Belkin (2009)	1978–2003	In-Situ	MS	0.054°C
	Nykjaer (2009)	1985–2006	Satellite	Western MS	0.03°C
				Eastern MS	0.05°C
	Skliris et al. (2012)	1985–2008	Satellite	MS	0.037°C
				Western MS	0.026°C
				Eastern MS	0.042°C
	Shaltout and Omstedt (2014)	1982–2012	Satellite	MS	0.035°C
	Ozer et al. (2017)	1979–2014	In-Situ	Eastern MS – LSW	0.12°C
				Eastern MS – LIW	0.03°C
	Pastor et al. (2018, 2020)	1982–2016	Satellite	MS	0.035°C
	El-Geziry (2021)	1948–2018	Satellite	Eastern MS	0.04°C
	Pastor (2021)	1982–2021	Satellite	MS	0.03°C
	This study	2011–2021	In-Situ	Eastern MS	0.048°C
Salinity	Krahmann and Schott (1998)	1960–1990	In-Situ	Western MS	0.0043
	Vargas-Yanez et al. (2010)	1950–1999	In-Situ	Western MS	0.0014
	Ozer et al. (2017)	1979–2014	In-Situ	Eastern MS – LSW	0.008
				Eastern MS – LIW	0.005
	Schroeder et al. (2017)	1993–2016	In-Situ	Western MS	0.006
	Skliris et al. (2018)	1950–2015	Objective Analysis (En4)	MS	0.0019
				Western MS	0.002
				Eastern MS	0.0018
	This study	2011–2021	In-Situ	Eastern MS	0.006

Shown trends are limited to shallow and intermediate water only.

fluorescence and turbidity sensors (FLNYU, WetLabs). A twin station at Ashkelon was established in mid-2012. Continuous CTD Raw data of T, S, Pressure, Oxygen, Fluorescence and Turbidity is collected at a high temporal sampling interval of 10 min. In order to ensure the systems durability against fouling it incorporates several antifouling measures including toxin emitting capsules, Bio-Wipers and an in-house developed underwater case minimizing the systems exposure to the surroundings. A routine maintenance procedure is preformed once every 2 months (for each of the stations) which includes the replacement of the CTD to a freshly authenticated instrument and the collection of reference measurements for data validation. Recovered CTDs go through a robust cleaning procedure (following Sea-Bird electronics guidelines) and are examined for biases both pre-cleaning (in comparison to the collected reference data) and post-cleaning in lab-performed comparisons. CTDs are sent to the manufacturer for calibration regularly every 2 years or earlier in the case of an identified drift of one of the sensors (i.e., over three times of the instruments initial accuracy of $\pm 0.001°C$ for T and ± 0.004 for S). The Hadera station CTD dataset encompasses the period of March 2011 to June 2021. Due to various infrastructure difficulties, Ashkelon station experienced large data breaks since its establishment in 2012. For this reason, Ashkelon CTD measurements will only be used here as a basis of comparison to Hadera station data.

Hadera station is located offshore (2.2 km) from the discharge of effluents at the shoreline of the nearby power plant and desalination facility. In order to assess the possible effect of these anthropogenic activities on our measurements, we examined the thermohaline marine monitoring report conducted in the area over the period of 2013 till 2020 (Cohen, 2021). T and S anomalies presented in the report, both for surface and near bottom values, are generally confined to a distance of ∼500 m from the shoreline and have a consistent southward spreading pathway, not effecting the station. Wood et al. (2020) used numerical simulations to study the distribution of desalination brines along the Israeli coast and the spreading of annual mean S anomalies in Hadera limited to under 1 km from the discharge location. To further confirm that Hadera monitoring station can be considered a good representative of northern Israeli coastal waters, a comparison of the daily averaged T time series to Achziv and SST datasets (see below) was performed. This comparison presented a statistically significant fit with a RMSE of 0.46 and Pearson R of 0.99 for the Achziv dataset and a RMSE = 0.66 and Pearson R of 0.98 for the SST dataset (**Supplementary Figure 1**).

Additional Data
Achziv Islands
Over a period of 13 months, from May 2013 to May 2014 Several HOBO T loggers were maintained at two sites in Achziv Islands, located at the northern end of the Israeli Mediterranean coast (**Figure 1**). The averaged data of two loggers deployed at a water depth of 10 m (north and south Islands,
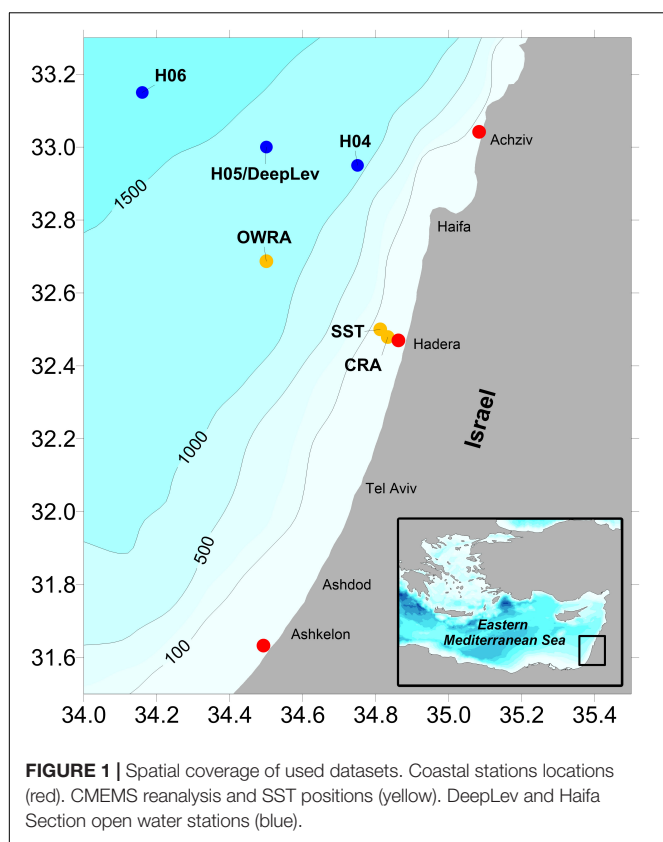
FIGURE 1 | Spatial coverage of used datasets. Coastal stations locations (red). CMEMS reanalysis and SST positions (yellow). DeepLev and Haifa Section open water stations (blue).

1 and 1.3 km offshore) is used in comparison to the Hadera station dataset.

Haifa Section Cruises

Israel Oceanographic and Limnological Research conducts the biannual Haifa section cruise covering stations at water depths of 15–1900 m, extending 90 km off the coast of Israel, as a part of INMoP. A Sea-Bird SBE911plus CTD, interfaced to a SBE Carousel is used to collect continuous profiles of pressure, T, S, dissolved oxygen and fluorescence. Equipment, procedures, and calibrations are detailed in Ozer et al. (2017, 2019). We compare our results to the updated analysis of long-term and inter-annual trends as presented in Ozer et al. (2017) adding the years of 2015 to 2020.

Meteorology

Air T, wind, and precipitation data from four chosen stations in the vicinity of Hadera (Zikhron Ya'akov, Hadera port, Ein HaHoresh, and Ein Carmel) was averaged to attain a daily time series for the studied period of 2011 to 2021. The use of multiple stations covering ∼30 km along the Israeli coastal plain allowed to reduce data breaks, while maintaining the climatic traits of the region. All data originates from the Israel Meteorological Service (IMS) archive available online[2].

---

[2]https://ims.data.gov.il/ims/7

Copernicus Monitoring Environment Marine Service Data

We use two products provided by the E.U. Copernicus Monitoring Environment Marine Service (CMEMS). (1) Daily gap-free remotely sensed L4 SST produced and distributed in near-real time by the Consiglio Nazionale delle Ricerche (Buongiorno Nardelli et al., 2013). We extract the T time series from the high spatial resolution product (HR 0.0625°) in the closest position to Hadera station (32.5°N, 34.81°E). (2) The Mediterranean Sea Physical Reanalysis generated by a numerical system composed of a hydrodynamic model, supplied by the Nucleous for European Modeling of the Ocean and a variational data assimilation scheme (Escudier et al., 2020). Here we extract the daily time series of T and S for a depth of 10.5 m from two grid points of the reanalysis. The first representing coastal water closest to Hadera station (referred hereafter as CRA, 32.48°N, 34.83°E) and the second from an open water location (Z > 1200 m) northwest of Hadera station (referred hereafter as OWRA, 32.69°N, 34.5°E).

DeepLev Mooring Station

In November 2016, the first moored station at the Eastern LB was deployed at 1500m water depth, ∼50km offshore Haifa, Israel (Katz et al., 2020). For this study, we use the T time series from a downward looking Teledyne RD Instruments 300 KHz workhorse ADCP. The ADCP is installed on the upmost buoy of the mooring system, at a depth range of 20–30 m (depending on deployment) and sampling at a 15-min interval. The ADCP integrated T sensor has a reported precision of ±0.4°C and a resolution of 0.01°C. Inter-calibrations with CTD casts taken on deployment and recovery events yielded a mean variance of 0.015°C with a 95% confidence interval of ± 0.056°C ($n = 11$).

Data Analysis

At a preliminary stage the various time series data sets described above were aggregated into a unified database and synchronized based on the time of measurement. Next daily and monthly averages were calculated for all available parameters. T hourly averages grouped by month were attained to infer the range of the diurnal cycle (**Supplementary Figures 2, 3**). In addition, daily standard deviation averages of the complete CTD dataset (over 400,000 measurements in total) were calculated and yielded 0.19°C and 0.032 for T and S, respectively. The seasonal Mann-Kendall test was used to examine the T and S CTD datasets for statistically significant long-term trends (Hirsch et al., 1982; Hussain and Mahmud, 2019).

Ekman Transport Calculation

To ensure that the IMS wind dataset adequately represents off shore conditions, the daily averaged wind was compared with a time series of the ECMWF ERA-5 reanalysis at position 32.5°N, 34.75°E and presented a strong agreement with R^2 of 0.85 and 0.87 for U and V components, respectively (not shown). Next, following Cropper et al. (2014) across and along shore wind stress

(τ) components were derived from averaged daily wind speeds.

$$\tau_{ac} = \rho_a C_d \left(W_{ac}^2 + W_{al}^2\right)^{1/2} W_{ac} \; and$$

$$\tau_{al} = \rho_a C_d \left(W_{ac}^2 + W_{al}^2\right)^{1/2} W_{al}$$

where, W_{ac} and W_{al} are across and along shore winds components achieved by a 25° rotation of the original data, according to the shoreline inclination. ρ_a is the air density of 1.22 kg/m^3 and C_d the typical dimensionless drag coefficient of 1.3×10^{-3}. Next Ekman transport (Q) components were derived from the wind stress field.

$$Q_{ac} = \frac{\tau_{al}}{\rho_w f} \; and \; Q_{al} = \frac{-\tau_{ac}}{\rho_w f}$$

where, ρ_w is the density of sea water of 1025 kg/m^3 and f is the Coriolis parameter defined as $f = 2\Omega \sin(\varphi)$ (where, Ω is the earths angular velocity of 7.292×10^{-5} s^{-1} and φ is the latitude).

Filling Temperature Data Gaps

In order to complete missing CTD T data in the Hadera dataset a multi parameter regression (MPR) was performed. The MPR procedure was based on T records of the ADCP and PAROS, located in the immediate vicinity of the CTD, as well as the close by (~1.3 km) SST dataset (**Supplementary Figure 4**). As a preliminary step the similarity of these datasets was assessed where they overlapped. Daily differences between the CTD T and the additional T datasets were computed and yielded 95% confidence intervals of 0.024, 0.016 and 0.028°C for ADCP, PAROS and SST, respectively. Pearson R correlation ranged from 0.97 to 0.99 (the lowest found between the ADCP and SST), thus all datasets were accepted for the MPR procedure. Depending on the availability of data from these datasets a matrix of coefficients was calculated and used to achieve a complete daily data set of Hadera station over the period of March 01, 2011 to June 08, 2021 (**Supplementary Tables 1, 2**). This method was not implemented for Ashkelon station as the data gaps there were considered too large to overcome. In the analysis of S variations, the monthly averaged data set was used, as no other reference was available in order to complete missing daily data.

Time Series Decomposition

For the determination of seasonal, trend and irregular components we follow Pezzulli et al. (2005) and use the filter based X11-ARIMA method (X11), a variant of the Census Method II Seasonal Adjustment Program, assuming an additive model.

$$X_t = T_t + S_t + I_t$$

where, X_t is the original time series, T_t is the trend component, S_t is the net seasonal component and I_t is the irregular variation. The X11 is a filter based method for seasonal adjustment which follows the 'ratio to moving average' procedure first described by Macaulay (1931) and commonly referred to as "Classical Decomposition." In principle X11 is comprised of three steps which are implemented iteratively: (1) Estimation of the trend by a moving average, (2) Removal of the trend from the time series leaving the seasonal and irregular components, and (3)

Estimation of the seasonal component using moving averages to smooth out the irregulars. After three iterations, the irregular term is finally calculated by removing the final trend and seasonal terms from the original time series. Key features of the X11 decomposition are that the trend is void of the annual cycle and any higher frequencies and that the seasonal term is defined locally in time, thus allowing for inter-annual variations in the seasonal cycle (Pezzulli et al., 2005). For the T decomposition, we use the daily averaged T and apply the moving averages windows of 30 × 365 and 30 × 30 for the trend and seasonal estimations, respectively. Due to the data gaps in the daily S dataset (**Figure 2E**), we implement the X11 decomposition on monthly averaged S and apply the moving averages windows of 2 × 12 and 2 × 2 for the trend and seasonal estimations, respectively. Similarly, the X11 method was also implemented on the daily CMEMS model reanalysis datasets (CRA and OWRA) in order to compare of the trend terms.

Synoptical Anomalies Delineation

The daily T irregular term (acquired by means of the X11 method) was further investigated by applying a threshold filter, parsing through this dataset and marking positive and negative amplitudes and durations. In order to set the thresholds for significant synoptical anomalies, we initially examined the amplitude of the diurnal cycle, which ranged from 0.15°C in winter to 0.3°C in summer for T (**Supplementary Figure 2**) and from 0.001 in winter to 0.003 in summer for S (**Supplementary Figure 3**). Since the S diurnal amplitude was at the level of sensor accuracy, we opted to use the values of ±2 times the average daily standard deviation (0.38°C for T and 0.064 for S) for the anomalies delineation. In every incident that the irregular term crossed the threshold value, the duration of the anomaly was recorded together with the maximal amplitude. Cases of missing data whilst within a given anomaly event were omitted as the anomaly period could not be established. For the S time series, where the X11 method was performed on monthly averages, the following approach was used to calculate daily anomalies. The interpolated sum of trend and seasonal terms (of the monthly X11 analysis) were subtracted from daily averaged CTD data where it was available. The resulting residuals time series was then screened following the same procedure described above for T.

RESULTS AND DISCUSSION

Long-Term Trends and Inter-Annual Fluctuations

A statistically significant warming trend was identified over the observed period (2011–2021) in Hadera station (11–12 m depth) using the seasonal Mann-Kendall test, with a yearly rate of 0.048°C ($p = 0$, $z = 10.92$) (**Figure 3A**). While the coastal dataset has the handicap of covering a relatively short period of time, the achieved trend is in agreement with previous studies (**Table 1**), specifically it is very similar to the trends found in investigations of the eastern MS (Nykjaer, 2009; Skliris et al., 2012; El-Geziry, 2021), all yielding exceptionally high values. When compared to the trends obtained from open water casts offshore the Israeli
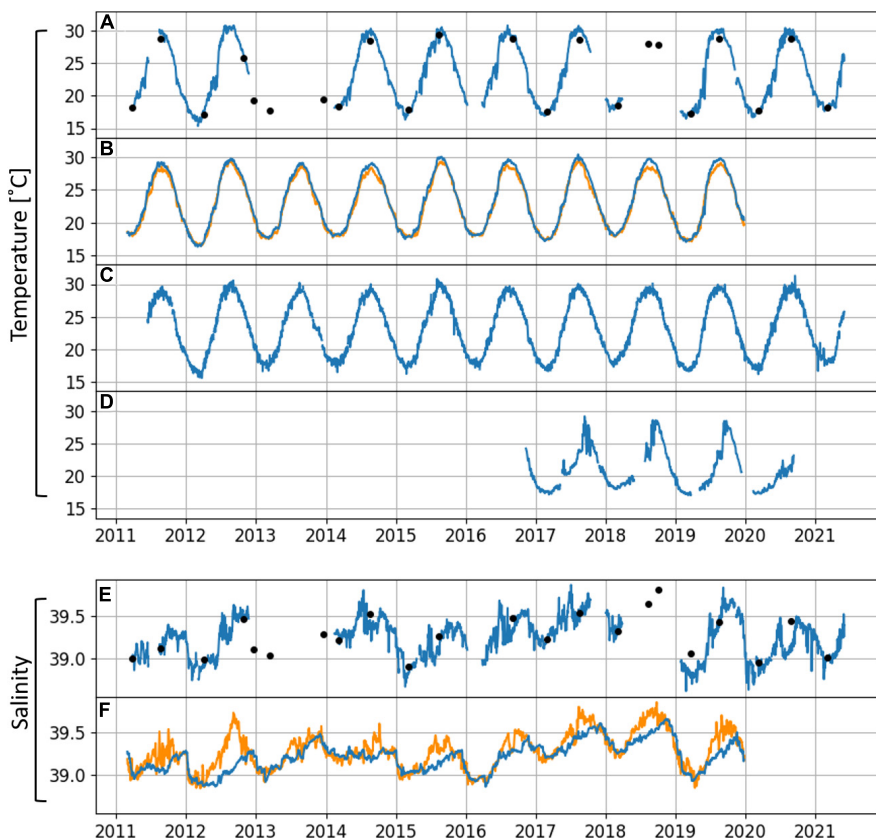
FIGURE 2 | Temperature [**A:** Hadera CTD, **B:** CMEMS reanalysis CRA (blue) and OWRA (orange), **C:** SST, and **D:** DeepLev] and salinity [**E:** Hadera CTD and **F:** CMEMS reanalysis CRA (blue) and OWRA (orange) time series used for lag correlations and additional analysis]. Haifa section open water stations averaged surface values (upper 20 m) in black dots **(A,E)**.
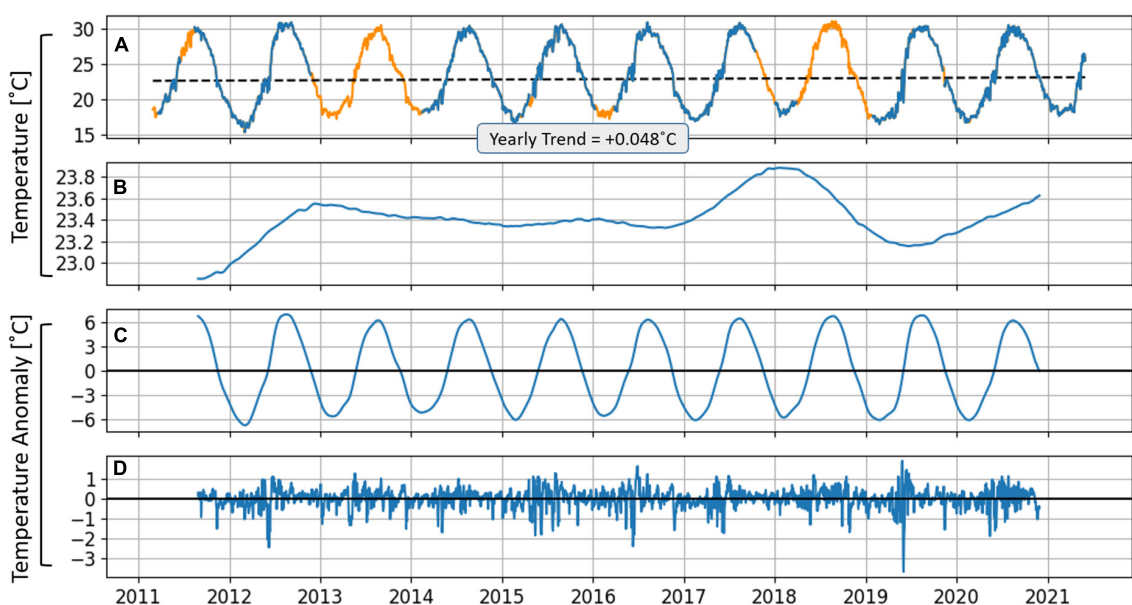
FIGURE 3 | Daily averaged surface water temperature **(A)** – Hadera CTD values (blue) and missing data completed using multi parameter regression (orange). Calculated trend **(B)**, seasonal **(C)**, and irregular **(D)** terms achieved using the X11 decomposition method. Yearly linear trend accepted with the seasonal Mann-Kendall test of 0.048°C ($p = 0$, $z = 10.92$) presented in panel **(A)** (dashed black line and text box).

coast (Ozer et al., 2017, updated analysis covering the years 1979–2020 in **Supplementary Figure 5**), the Hadera trend is similar to that achieved in the analysis of Levantine Intermediate Water (LIW) ($0.03 \pm 0.01°C$ year^{-1}), yet lower than the trend observed in surface water ($0.13 \pm 0.05°C$ year^{-1}). We attribute the disparity between Hadera and LSW trends to the fact that the analysis of LSW was limited to casts performed during the peak of the warming period (end of summer). In contrary, the analysis of LIW was based on bi-annual data (i.e., summer and winter casts). Furthermore, we consider the LIW to be less affected by mesoscale and seasonal processes, thus it is more integrative and reflective of long-term and inter-annual variability.

A significant positive S yearly trend of 0.006 ($p = 4.06 \times 10^{-7}$, $z = 5.06$) was identified in the Hadera CTD dataset (**Figure 4A**). This trend is at the higher end of previously published salinification rates for the MS (**Table 1**), similar to the rates attained in the analysis of LSW and LIW (Ozer et al., 2017 and **Supplementary Figure 5**) and in the western MS (Schroeder et al., 2017). Pastor et al. (2018) reported upper layer salinification trends exceeding 0.004 year^{-1} in the easternmost MS, in agreement with our results. This trend is consistent with the increase in latent heat loss in the eastern MS since the early 1970s (Mariotti, 2010; Skliris et al., 2012) and the large reduction in Nile river runoff since the early1960s (Skliris and Lascaratos, 2004; Suari and Brenner, 2015). The short duration of the dataset analyzed in this study does not support the appraisal of our findings within a broader framework of surface T and S natural variability of longer decadal and multi-decadal scales. These will need

to be addressed in the future, as data accumulates from the coastal stations.

Both T and S trends achieved through the X11 method show inter-annual fluctuation with a clear maximum in the beginning of 2018, which seemingly corresponds with the previously established inter-annual cycle of the Levantine basin in connection with the BiOS mechanism (Civitarese et al., 2010a,b; Gacic et al., 2010; Ozer et al., 2017). Smaller, less prominent extremes are evident at the start of 2013 for T and 1 year later for S (**Figures 3B**, **4B**). A close similarity is found between the T and S X11 trend terms of Hadera and CMEMS reanalysis datasets (**Figure 5**). The T Trends of Hadera and CRA are consistently higher than that of the OWRA, displaying the stronger response and higher sensitivity of coastal waters to the atmospheric forcing and their potential impact on the marine environment (**Figure 5A**). The S extrema of 2014 coincides with low precipitation in the winter of 2013–2014 (**Figure 4B**). Indeed, a correspondence of the coastal S seasonal minimum to the total winter precipitation can be observed throughout the examined period. To demonstrate the influence of precipitation on coastal S, we calculate the regression between S and cumulative precipitation in two winters seasons (covering the months of November to March) where salinity measurements were rarely interrupted. A strong relation is found with R^2 of 0.9324 and 0.885 for the winters of 2014–2015 and 2019–2020, respectively. On several occasions, drops of S values below the regression line are supported by a passing winter storm with several days of continuous high precipitation levels (**Figure 6**). These results point to a strong linkage of the surface S with

FIGURE 4 | Monthly averaged Hadera CTD salinity values **(A)**. Calculated trend **(B)**, seasonal **(C)**, and irregular **(D)** terms achieved using the X11 decomposition method. Yearly linear trend accepted with the seasonal Mann-Kendall test of 0.006 ($p = 4.06 \times 10^{-7}$, $z = 5.06$) presented in Panel A (dashed black line and text box). Total winter precipitation is superimposed on the trend in Panel B (Gray bars).

FIGURE 5 | Temperature **(A)** and Salinity **(B)** trend terms achieved using the X11 decomposition method on daily data for the Hadera CTD dataset (blue, as shown in **Figures 3**, **4**), CMEMS model reanalysis close to Hadera station (i.e., CRA and orange) and CMEMS model reanalysis at open water location (i.e., OWRA and green).
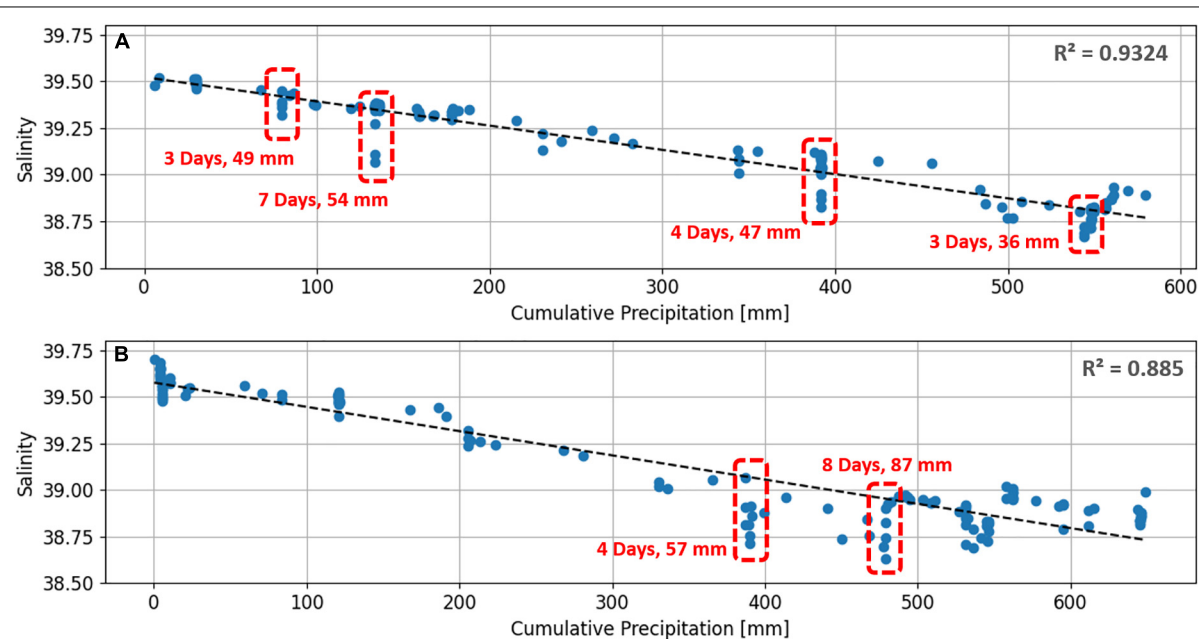
FIGURE 6 | Salinity measurements from Hadera monitoring station projected against winter cumulative precipitation for the winters of 2014–2015 **(A)** and 2019–2020 **(B)**. Calculated regression line are shown in dashed black lines (identical for both winter seasons, y = –0.0013x + 39.55). Red rectangles and adjoining text indicate storms where high precipitation levels were recorded coinciding with a salinity drop below the regression line. Storms duration and total precipitation are indicated in red text.

the local rainfall. As S trends of CRA and OWRA follow the same temporal patterns (**Figure 5B**) we believe this is a close representation of the response to annual changes in the LB regional water budget.

The overall agreement of T and S time series of the OWRA with Hadera station in terms of variance and lags (**Table 2**), as

well as the similarities of the T and S X11 trends discussed above, indicates a relatively strong coupling between coastal water and the open ocean. In contrast, a large difference is found between T time series of Hadera and DeepLev mooring with a time lag of 43 days (**Table 2**). We attribute this inconsistency of DeepLev data to the fact that the T in this dataset is sampled at a deeper

TABLE 2 | Summary values for temperature and salinity contemporaneous datasets compared with Hadera station time series.

	Compared dataset	Min Δ	Max Δ	Mean Δ	Δ STD	Δ CI95%	Pearson r	Offset [Days]
Temperature (°C)	Ashkelon CTD	−3.32	2.10	−0.36	0.63	0.035	0.992	0
	Achziv HOBO	−1.64	1.11	0.00	0.47	0.047	0.995	0
	Reanalysis, coastal (CRA)	−2.03	2.06	0.15	0.62	0.026	0.993	2
	SST	−5.05	2.93	0.15	0.74	0.029	0.988	2
	Reanalysis, open water (OWRA)	−4.50	2.79	0.49	0.92	0.038	0.994	5
	DeepLev 30 m	−2.20	10.02	2.86	3.40	0.224	0.908	43
Salinity	Ashkelon CTD	−0.83	0.78	0.01	0.20	0.087	0.732	0
	Reanalysis, coastal (CRA)	−0.40	0.62	0.08	0.15	0.006	0.788	16
	Reanalysis, open water (OWRA)	−0.51	0.66	0.00	0.15	0.006	0.785	−2

Δ values were calculated by subtraction of the specified dataset from Hadera data. Maximal pearson R correlation value presented, yielded at specified offset from the Hadera station dataset (positive offset values signify that Hadera time series leads the compared dataset).
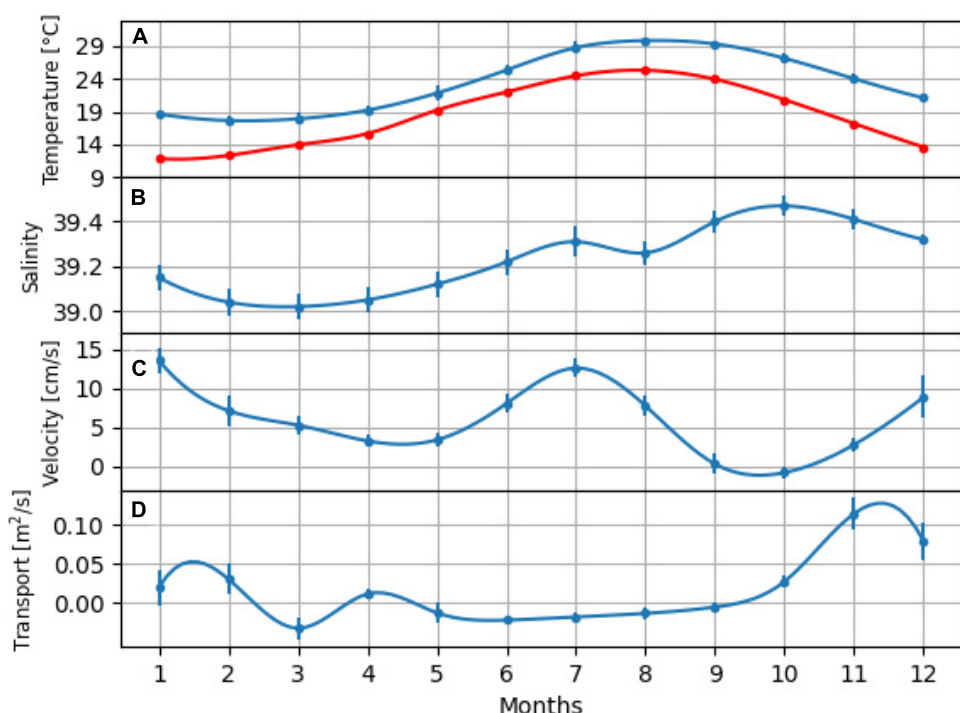
FIGURE 7 | Climatological water temperature (**A**, blue), air temperature (**A**, red), salinity (**B**), along shore current component (**C**), and along shore Ekman transport (**D**). Standard error of averages shown in Vertical bars.

level (∼30 m), below the surface mixed layer in summer, thus the changing level of the vertical mixing has a significant effect on the sampled data.

Climatology and the Seasonal Cycle

A clear seasonal cycle of surface T is evident in our data with average peak values of 29.86°C in August and 17.62°C in February, representing an average offset of +7°C in summer and −5°C in winter from the overlaying long-term trend (**Figures 7A**, **3B,C**). Extreme water T seasonal anomalies are in concordance with large amount of days with air T below 10°C for negative anomalies and above 25°C for positive anomalies (not shown). Lag correlations performed between the average daily air T and CTD thermohaline values confirms

the expected seasonal effect of atmospheric forcing on coastal water characteristics, with the air T time series leading by 15 and 50 days before water T and S, respectively (**Supplementary Figure 6**). The S dataset presents a less coherent seasonal sequence with a bimodal behavior in the summer seasons of 2014, 2016, and 2017, which is apparent also in the climatological S (**Figures 4C**, **7B**). The drop in salinity in August can be attributed to the intensification of the along shore current in the period of June-July (**Figure 7C**), potentially advecting more AW which are lower in their S value. Wind derived along shore Ekman transport is kept close to zero in the summer months (**Figure 7D**), suggesting that the strong current values are mainly of geostrophic origin. Rosentraub and Brenner (2007) reported maximal northward currents in the summer season
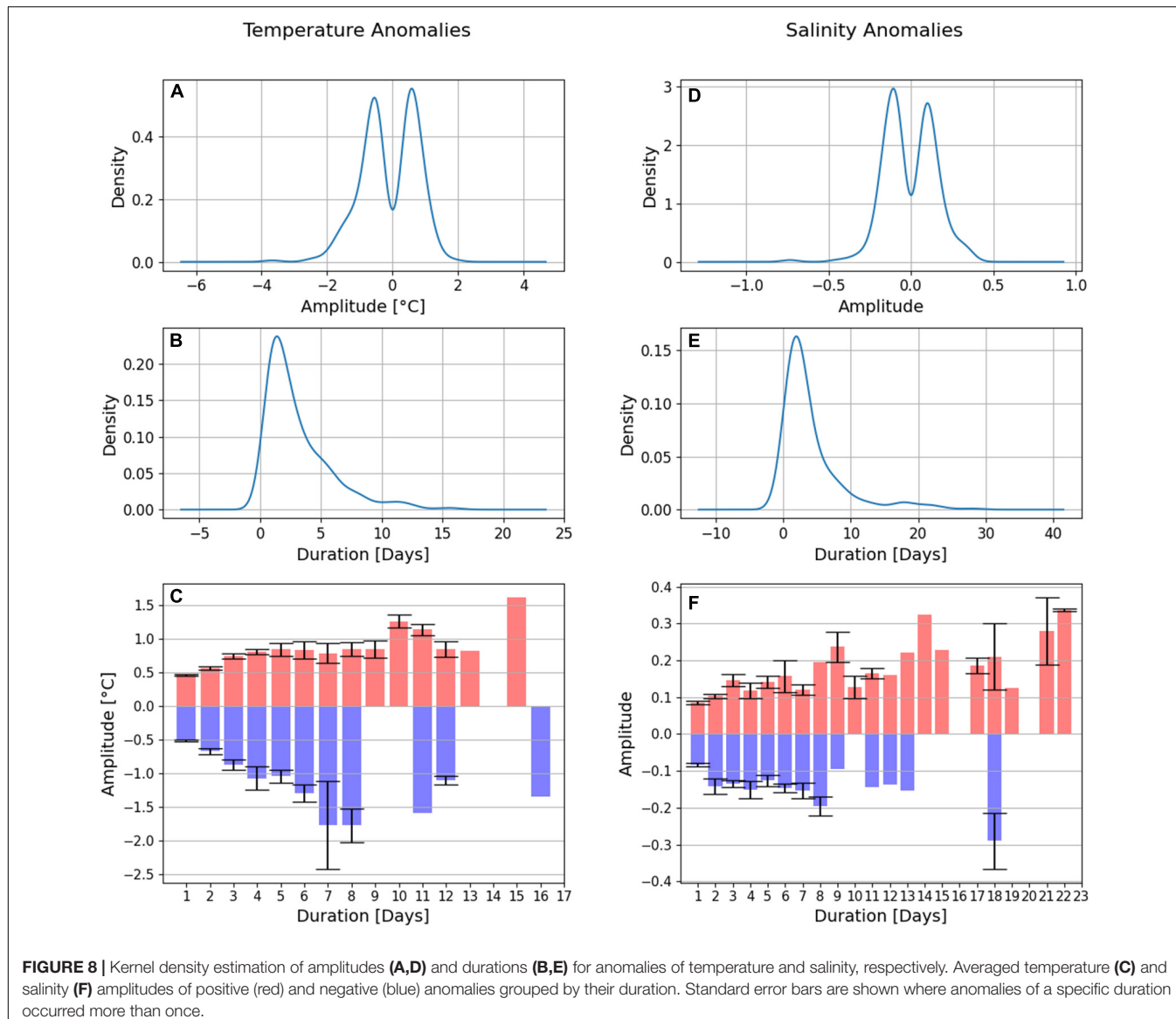
FIGURE 8 | Kernel density estimation of amplitudes **(A,D)** and durations **(B,E)** for anomalies of temperature and salinity, respectively. Averaged temperature **(C)** and salinity **(F)** amplitudes of positive (red) and negative (blue) anomalies grouped by their duration. Standard error bars are shown where anomalies of a specific duration occurred more than once.

over the Israeli continental shelf confined to the upper layer as well as an along-slope baroclinic jet during summer and early winter. The authors related their findings to the general surface circulation of the LB introducing AW into the basin through several established pathways. Mauri et al. (2019) has shown an increase in average dynamic topography during the months of June to August in latitudes of 33–34 N in further support of our hypothesis. Estournel et al. (2021) demonstrated that in summer, the shallower current flows closer to the coastline while in winter it flows above the 1000 m isobath. The climatological extrema S values of 39.47 and 39.01 are reached at the months of October and March, respectively. An extreme seasonal cycle is observed in 2019 with minimal S of 38.8, which we relate to the high precipitation of the preceding winter as discussed earlier. However, this minimum can also be related to an enhanced modified AW flux into the LB, following the reasoning of the BiOS mechanism. An unusual fast recovery brings S as

high as 39.63 by October 2019 and is not supported by the meteorological datasets.

Synoptical Anomalies Analysis

T anomaly amplitudes range from $+2$ to $-2.5°C$ with modal values reached at $-0.67°C$ and $0.69°C$ for negative and positive anomalies, respectively (**Figure 8A**). The range of T anomalies duration is between 0 and 16 days with a maximal Kernel density at 1.5 days (**Figure 8B**). Similar anomaly behavior is observed for S, with a slight preference to negative anomalies and modal Kernel densities at -0.141 and 0.136 for negative and positive anomalies, respectively (**Figures 8D,E**). Averaged T anomaly amplitudes grouped by durations show a relation between the duration of the anomaly and its corresponding amplitude, the longer the anomaly lasts, the higher the amplitude. This apparent dependency is kept for both positive and negative anomalies, but is more coherent in the case of the
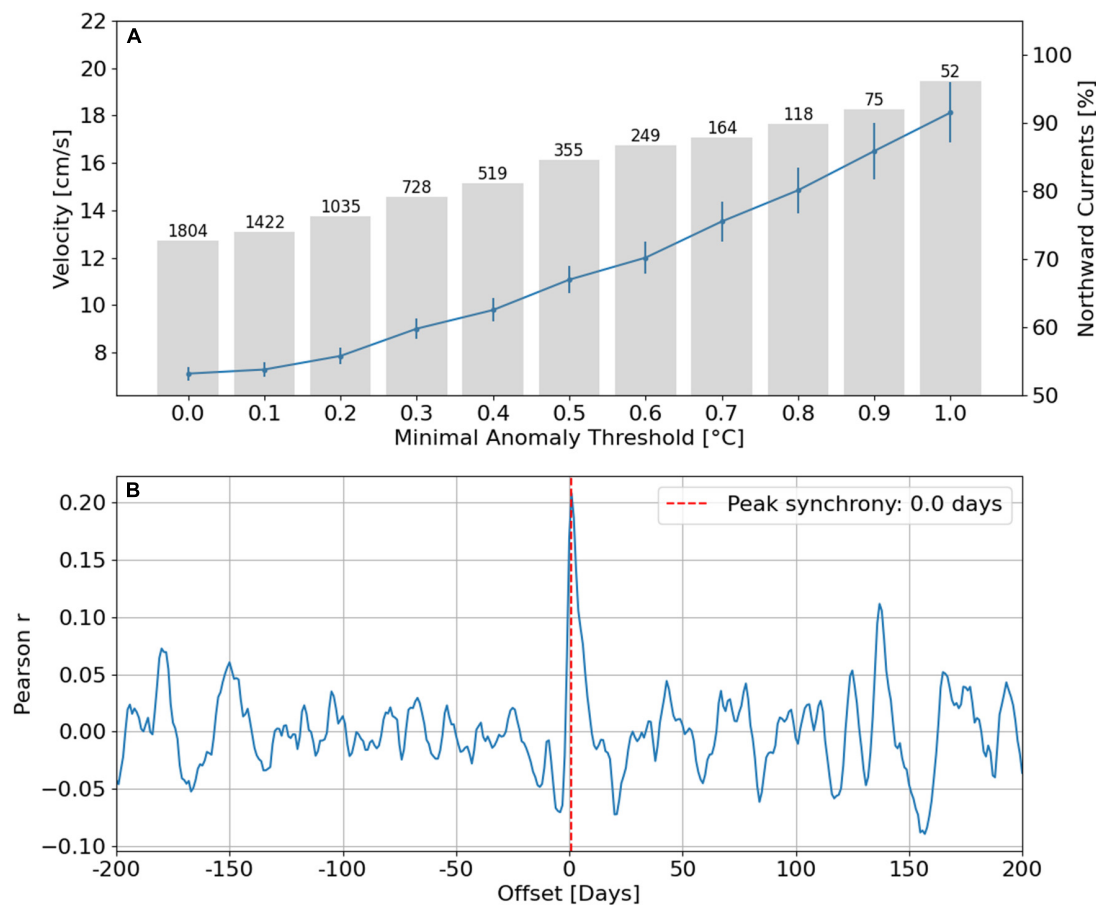
FIGURE 9 | Correspondence between along shore currents and positive temperature anomalies. **(A)** The along shore current time series is filtered for increasing positive temperature anomaly thresholds (shown in the *X* axis). The resulting filtered along shore current dataset is averaged (blue line, vertical bars show standard error) and the percentage of incidents where northward currents coincide with the positive temperature anomaly is calculated (gray bars, total number of data points above the temperature threshold). **(B)** Lag correlation between temperature and along shore current residuals time series. Peak synchrony marked by red dashed line.

latter. A similar, yet less clear relation can be observed for S. For both parameters, the majority of anomaly events last up to 10 days (**Figures 8C,F**). No significant seasonal T and S anomalies were identified (**Supplementary Figure 7**). We additionally perform an analysis of heat waves following the definition of the IPCC, 2019: "marine heatwaves are defined when the daily sea surface temperature exceeds the local 99th percentile over the period 1982 to 2016." The 99th T percentile for the period of measurements in Hadera was calculated, resulting in 30.56°C. Running this filter brings up several heat waves (**Supplementary Table 3**) with somewhat higher maximum T toward 2018, yet our dataset is too short to identify any patterns.

Along-Shore Connectivity

Variance statistics and lag correlations calculated for T and S comparing the Hadera station data to available datasets (**Figure 2**) are presented in **Table 2**. No offsets were found between the 3 stations (Hadera, Ashkelon and Achziv) demonstrating that the 180 km strip of Israeli coastal waters undergo seasonal and

inter-annual changes in synchrony. Ashkelon station was found to be 0.36°C warmer than Hadera station, a fact we relate to its southerly location (100 km south of Hadera station) and to extended continental shelf at the south of Israel (over 20 km in width). A convincing relation was found between the positive T irregular term (from the X11 analysis) and the along shore currents, where the majority of T irregular values are explained by northward currents, the higher the T anomaly, the stronger the current (**Figure 9A**). A zero time offset yielded a maximal correlation between the irregular T and along shore currents (**Figure 9B**). These results suggest that the majority of positive T anomalies are a result of northward transport of water along the Israeli continental shelf, advecting warmer water from the south. No T gradient was found between Hadera and Achziv (distanced ∼70 km, **Table 2**), perhaps signifying that the northern shallow waters of Israel share a stronger connection maintained by coastal dynamics. T comparisons of CRA and Hadera T data yielded similar results with a mean difference of 0.15°C, high correlations and an offset of 2 days. The CRA S was found to be in average 0.08 below Hadera station. As both CRA and SST datasets

are originated from westerly, deeper positions (compared with Hadera station), we infer that atmospheric forcing is enhanced at shallower, more easterly positions and is communicated toward the west over the continental shelf within synoptical timeframe. The large offset of S, where Hadera leads the CRA by 16 days remains unclear. No significant variance in S was found between Hadera and Ashkelon stations (**Table 2**).

CONCLUSION

The continued study of coastal ocean state, variability, health and climate change through environmental monitoring programs plays an important role in broadening our knowledge and understanding of the changing seas, raises the public awareness, informs policy makers and supports the management of the coastal areas. The importance of sustained ocean and coastal observation, aimed at advancing our knowledge of the ocean and its link with climate, promoting the development of early warning systems, and enabling decision-making based on the best available science has become a global consensus (Tanhua et al., 2019). In this study we make use of continuous observations providing exclusive high temporal resolution data in the Eastern coast of the LB and address the issues of (1) long term and inter annual trends, (2) the coastal seasonal cycle, and (3) The connectivity of coastal waters along the Israeli coast. Significant long-term positive trends of T and S are validated by use of the seasonal Mann-Kendall test and compared to previously published findings in other areas of the MS. The T trend of 0.048°C identified in this study supports the exceptionally high warming rates reported in the eastern MS (Nykjaer, 2009; Skliris et al., 2012; El-Geziry, 2021) (**Table 1**). Filter based time series decomposition allows the identification of inter-annual T and S fluctuations associated with previously published open ocean dynamics (Ozer et al., 2017) as well as with CMEMS physical model reanalysis. Our results of higher coastal T trend term (**Figure 5A**), the impact of local winter rainfall on S values (**Figure 6**), and the sensitivity of T anomalies to the prevailing northward alongshore current (**Figure 9**) demonstrate the faster response time and higher sensitivity of the coastal environment to atmospheric forcing. Nonetheless, we infer a relatively strong coupling between coastal water and the open ocean in terms of long-term, inter-annual and seasonal evolution of the surface thermohaline properties. Finally, we stress the importance of the persistence of these monitoring efforts and the introduction of additional sustainable coastal waters stations, which will improve the spatial coverage enabling a better interpretation and understanding of the predominating processes.

DATA AVAILABILITY STATEMENT

The datasets presented in this study can be found in online repositories. The names of the repository/repositories and accession number(s) can be found below: Israel Marine Data Center – https://isramar.ocean.org.il/isramar2009/.

AUTHOR CONTRIBUTIONS

TO led manuscript drafting with the help of BH, IG, and HG. TO and IG contributed to the data acquiring. HG and BH contributed to the interpretation. All authors approved the submitted version.

FUNDING

ACKNOWLEDGMENTS

SUPPLEMENTARY MATERIAL

The Supplementary Material for this article can be found online at: https://www.frontiersin.org/articles/10.3389/fmars.2021.799457/full#supplementary-material

REFERENCES

Amitai, Y., and Gildor, H. (2016). Can precipitation over Israel be predicted from Eastern Mediterranean heat content? *Int. J. Climatol.* 37, 2492–2501.

Belkin, M. (2009). Rapid warming of large marine ecosystems. *Prog. Oceanogr.* 81, 207–213. doi: 10.1016/j.pocean.2009.04.011

Bindoff, N. L., Cheung, W. W. L., Kairo, J. G., Arístegui, J., Guinder, V. A., Hallberg, R., et al. (2019). "Changing ocean, marine ecosystems, and dependent communities," in *IPCC Special Report on the Ocean and Cryosphere in a Changing Climate*, eds H.-O. Pörtner, D. C. Roberts, V. Masson-Delmotte, P. Zhai, M. Tignor, E. Poloczanska, et al. (Geneva: IPCC).

Brenner, S., Murashkovsky, A., and Gertman, I. (2006). Assessment of one year of high-resolution operational forecasts for the Southeastern

Mediterranean shelf region in the MFSTEP project. *Ocean Sci. Discuss.* 3, 2059–2085.

Buongiorno Nardelli, B., Tronconi, C., Pisano, A., and Santoleri, R. (2013). High and ultra-high resolution processing of satellite sea surface temperature data over southern european seas in the framework of myocean project. *Remote Sens. Environ.* 129, 1–16.

Civitarese, G., Gacic, M., Cardin, V., Borzelli, G. L. E., and Spa, T. (2010a). Effects of the adriatic-ionian bimodal oscillating system (Bios) on the biogeochemistry of the Adriatic Sea. *CIESM Org.* 28:2010.

Civitarese, G., Gaèiæ, M., Lipizer, M., and Eusebi Borzelli, G. L. (2010b). On the impact of the bimodal oscillating system (BiOS) on the biogeochemistry and biology of the Adriatic and Ionian Seas (Eastern Mediterranean). *Biogeosciences* 7, 3987–3997. doi: 10.5194/bg-7-3987-2010

Cohen, Y. (2021). *Marine Monitoring by the Israeli Electric Company and H2ID Desalination Plant. RELP- 1 – 2021*. Hadera: Israeli Electric Company.

Collins, M., Knutti, R., Arblaster, J., Dufresne, J. L., Fichefet, T., Friedlingstein, P., et al. (2013). "Long-term climate change: projections, commitments and irreversibility," in *Climate Change 2013: The Physical Science Basis. Contribution of Working Group I to the Fifth Assessment Report of the Intergovernmental Panel on Climate Change*, ed. IPCC (Cambridge: Cambridge University Press).

Collins, M., Sutherland, M., Bouwer, L., Cheong, S. M., Frölicher, T., Jacot Des Combes, H., et al. (2019). "Extremes, abrupt changes and managing risk," in *IPCC Special Report on the Ocean and Cryosphere in a Changing Climate*, eds H.-O. Pörtner, D. C. Roberts, V. Masson-Delmotte, P. Zhai, M. Tignor, E. Poloczanska, et al. (Geneva: IPCC).

Criado-Aldeanueva, F., Del Río Vera, J., and García-Lafuente, J. (2008). Steric and mass-induced Mediterranean sea level trends from 14 Years of altimetry data. *Glob. Planet. Change* 60, 563–575.

Cropper, T. E., Hanna, E., and Bigg, G. R. (2014). Spatial and temporal seasonal trends in coastal upwelling off Northwest Africa, 1981 – 2012. *Deep Sea Res. Part I* 86, 94–111. doi: 10.1016/j.dsr.2014.01.007

Desbiolles, F., Alberti, M., Hamouda, M. E., Meroni, A. N., and Pasquero, C. (2021). Links between sea surface temperature structures, clouds and rainfall: study case of the Mediterranean Sea. *Geophys. Res. Lett.* 48:e2020GL091839.

Efrati, S., Lehahn, Y., Rahav, E., Kress, N., Herut, B., Gertman, I., et al. (2013). Intrusion of coastal waters into the Pelagic Eastern Mediterranean: in situ and satellite-based characterization. *Biogeosciences* 10, 3349–3357.

El-Geziry, T. (2021). Long-term changes in sea surface temperature (SST) within the Southern Levantine Basin. *Acta Oceanol. Sin. Engl. Edn.* 40, 1–7. doi: 10.5402/2013/392632

Escudier, R., Clementi, E., Omar, M., Cipollone, A., Pistoia, J., Aydogdu, A., et al. (2020). *Mediterranean Sea Physical Reanalysis (CMEMS MED-Currents) (Version 1) [Data Set]*. Copernicus Monitoring Environment Marine Service (CMEMS). doi: 10.25423/CMCC/MEDSEA_MULTIYEAR_PHY_006_004_E3R1

Estournel, C., Marsaleix, P., and Ulses, C. (2021). A new assessment of the circulation of Atlantic and intermediate waters in the Eastern Mediterranean. *Prog. Oceanogr.* 198:102673. doi: 10.1016/j.pocean.2021.102673

Gacic, M., Eusebi Borzelli, G. L., Civitarese, G., Cardin, V., and Yari, S. (2010). Can internal processes sustain reversals of the ocean upper circulation? The Ionian Sea example. *Geophys. Res. Lett.* 37, 1–5.

Gertman, I., and Hecht, A. (2002). Annual and long-term changes in the salinity and the temperature of the waters of the South-Eastern Levantine basin. CIESM 2002. Tracking long-term hydrological change in the Mediterranean Sea. Monaco, 22-24-April 2002. *CIESM Workshop Ser.* 16, 75–78.

Giorgi, F. (2006). Climate change hot-spots. *Geophys. Res. Lett.* 33:L08707. doi: 10.1029/2006GL025734

Giorgi, F., and Lionello, P. (2008). Climate change projections for the Mediterranean region. *Glob. Planet. Change* 63, 90–104. doi: 10.1016/j.gloplacha.2007.09.005

Gissi, E., Manea, E., Mazaris, A. D., Fraschetti, S., Almpanidou, V., Bevilacqua, S., et al. (2021). A review of the combined effects of climate change and other local human stressors on the marine environment. *Sci. Total Environ.* 755:142564. doi: 10.1016/j.scitotenv.2020.142564

Hamad, N., Millot, C., and Taupier-Letage, I. (2005). A new hypothesis about the surface circulation in the Eastern Basin of the Mediterranean Sea. *Prog. Oceanogr.* 66, 287–298.

Herut, B., Almogi-Labin, A. B., Jannink, N., and Gertman, I. (2000). The Seasonal dynamics of nutrient and chlorophyll a concentrations on the SE Mediterranean shelf-slope. *Oceanol. Acta* 23(7 SUPPL.), 771–782. doi: 10.1016/s0399-1784(00)01118-x

Hirsch, R. M., Slack, J. R., and Smith, R. A. (1982). Techniques of trend analysis for monthly water quality data. *Water Resour. Res.* 18, 107–121. doi: 10.1029/WR018i001p00107

Hussain, M. M., and Mahmud, I. (2019). pyMannKendall: a python package for non parametric Mann Kendall family of trend tests. *J. Open Source Softw.* 4:1556. doi: 10.21105/joss.01556

IPCC (2019). "Summary for policymakers," in *IPCC Special Report on the Ocean and Cryosphere in a Changing Climate*, eds H.-O. Pörtner, D.C. Roberts, V. Masson-Delmotte, P. Zhai, M. Tignor, E. Poloczanska, et al. (Geneva: IPCC).

IPCC (2021). "Climate change 2021: the physical science basis," in *Contribution of Working Group I to the Sixth Assessment Report of the Intergovernmental Panel on Climate Change*, eds V. Masson-Delmotte, P. Zhai, A. Pirani, S. L. Connors, C. Péan, S. Berger, et al. (Cambridge: Cambridge University Press). doi: 10.1007/s10584-021-03233-7

Katz, T., Weinstein, Y., Alkalay, R., Biton, E., Toledo, Y., Lazar, A., et al. (2020). The first deep-sea mooring station in the eastern levantine basin (DeepLev), outline and insights into regional sedimentological processes. *Deep Sea Res. Part II Top. Stud. Oceanogr.* 171:104663. doi: 10.1016/j.dsr2.2019.104663

Kirtman, B., Power, S. B., Adedoyin, J. A., Boer, G. J., Bojariu, R., Camilloni, I., et al. (2013). "Near-term climate change: projections and predictability," in *Climate Change 2013: The Physical Science Basis. Contribution of Working Group I to the Fifth Assessment Report of the Intergovernmental Panel on Climate Change*, eds T. F. Stocker, D. Qin, G.-K. Plattner, M. Tignor, S. K. Allen, J. Boschung, et al. (Cambridge: Cambridge University Press).

Krahmann, G., and Schott, F. (1998). Longterm increases in western Mediterranean salinities and temperatures: anthropogenic and climatic sources. *Geophys. Res. Lett.* 25, 4209–4212. doi: 10.1029/1998GL900143

Kress, N., Gertman, I., and Herut, B. (2014). Temporal evolution of physical and chemical characteristics of the water column in the Easternmost levantine basin (Eastern Mediterranean Sea) from 2002 to 2010. *J. Mar. Syst.* 135, 6–13. doi: 10.1016/j.jmarsys.2013.11.016

Lascaratos, A., Roether, W., Nittis, K., and Klein, B. (1999). Recent changes in deep water formation and spreading in the Eastern Mediterranean Sea: a review. *Prog. Oceanogr.* 44, 5–36. doi: 10.1016/s0079-6611(99)00019-1

Ludwig, W., Dumont, E., Meybeck, M., and Heussner, S. (2009). River discharges of water and nutrients to the Mediterranean and Black Sea: major drivers for ecosystem changes during past and future decades? *Prog. Oceanogr.* 80, 199–217. doi: 10.1016/j.pocean.2009.02.001

Macaulay, F. R. (1931). The smoothing of time series. By Frederick R. Macaulay. [Pp. 172. New York: national bureau of economic research, incorporated. 1931.]. *J. Inst. Actuar.* 62, 181–182. doi: 10.1017/s0020268100010003

Malanotte-Rizzoli, P., Artale, V., Borzelli-Eusebi, G. L., Brenner, S., Crise, A., Gacic, M., et al. (2014). Physical forcing and physical/biochemical variability of the mediterranean sea: a review of unresolved issues and directions for future research. *Ocean Sci.* 10, 281–322.

Mariotti, A. (2010). Recent changes in the Mediterranean water cycle: a pathway toward long-term regional hydroclimatic change? *J. Clim.* 23, 1513–1525. doi: 10.1175/2009JCLI3251.1

Mariotti, A., Struglia, A., Struglia, M., Zeng, Y., Zeng, N., and Lau, K.-M. (2002). The hydrological cycle in the Mediterranean region and implications for the water budget of the Mediterranean Sea. *J. Clim.* 15, 1674–1690. doi: 10.1175/1520-4422002015<1674:THCITM<2.0.CO;2

Mauri, E., Sitz, L., Gerin, R., Poulain, P. M., Hayes, D., and Gildor, H. (2019). On the variability of the circulation and water mass properties in the Eastern Levantine Sea between. *Water* 11:1741. doi: 10.3390/w11091741

Micheli, F., Halpern, B. S., Walbridge, S., Ciriaco, S., Ferretti, F., Fraschetti, S., et al. (2013). Cumulative human impacts on mediterranean and black sea marine ecosystems: assessing current pressures and opportunities. *PLoS One* 8:e79889. doi: 10.1371/journal.pone.0079889

Miglietta, M., Moscatello, A., Conte, D., Mannarini, G., Lacorata, G., and Rotunno, R. (2011). Numerical analysis of a Mediterranean 'hurricane' over South-Eastern Italy: sensitivity experiments to sea surface temperature. *Atmos. Res.* 101, 412–426. doi: 10.1016/j.atmosres.2011.04.006

Nykjaer, L. (2009). Mediterranean sea surface warming 1985–2006. *Clim. Res.* 39, 11–17.

Ozer, T., Gertman, I., Gildor, H., Goldman, R., and Herut, B. (2019). Evidence for recent thermohaline variability and processes in the deep water of the Southeastern Levantine Basin, Mediterranean Sea. *Deep Sea Res. Part II Top. Stud. Oceanogr.* 171:104651. doi: 10.1016/j.dsr2.2019.104651

Ozer, T., Gertman, I., Kress, N., Silverman, J., and Herut, B. (2017). Interannual thermohaline (1979–2014) and nutrient (2002–2014) dynamics in the levantine surface and intermediate water masses, SE Mediterranean Sea. *Glob. Planet. Change* 151, 60–67. doi: 10.1016/j.gloplacha.2016.04.001

Pastor, F. (2021). *Mediterranean Sea Surface Temperature Report (Spring 2021). Meteorology and Pollutant Dynamics Area*. Valencia: The Mediterranean Center for Environmental Studies (CEAM). doi: 10.13140/RG.2.2.15757.05600

Pastor, F., Valiente, J. A., and Estrela, M. J. (2015). Sea surface temperature and torrential rains in the valencia region: model ling the role of recharge areas. *Nat. Hazards Earth Syst. Sci.* 15, 1677–1693.

Pastor, F., Valiente, J. A., and Khodayar, S. (2020). A Warming Mediterranean: 38 years of increasing sea surface temperature. *Remote Sens.* 12:2687. doi: 10.3390/rs12172687

Pastor, F., Valiente, J. A., and Palau, J. L. (2018). Sea surface temperature in the mediterranean: trends and spatial patterns (1982–2016). *Pure Appl. Geophys.* 175, 4017–4029. doi: 10.1007/s00024-017-1739-z

Pezzulli, S., Stephenson, D. B., and Hannachi, A. (2005). The variability of seasonality. *J. Clim.* 18, 71–88.

Pinardi, N., and Coppini, G. (2010). Preface 'operational oceanography in the mediterranean sea: the second stage of development.'. *Ocean Sci.* 6, 263–267. doi: 10.5194/os-6-263-2010

Ramírez, F., Coll, M., Navarro, J., Bustamante, J., and Green, A. J. (2018). Spatial congruence between multiple stressors in the Mediterranean Sea may reduce its resilience to climate impacts. *Sci. Rep.* 8:14871. doi: 10.1038/s41598-018-33237-w

Rixen, M., Beckers, J. M., Levitus, S., Antonov, J., Boyer, T., Maillard, C., et al. (2005). The Western Mediterranean deep water: a proxy for climate change. *Geophys. Res. Lett.* 32:L12608. doi: 10.1029/2005GL022702

Robinson, A. R., Hecht, A., Michelato, A., Roether, W., Theocharis, A., Unluata, U., et al. (1992). General circulation of the Eastern Mediterranean. *Earth Sci. Rev.* 32, 285–309.

Rohling, E. J., and Bryden, H. L. (1992). Man-induced salinity and temperature increases in Western Mediterranean deep water. *J. Geophys. Res.* 97, 191–111. 11,191-11,198. doi: 10.1029/92JC00767

Romanou, A., Tselioudis, G., Zerefos, C. S., Clayson, C.-A., Curry, J. A., and Andersson, A. (2010). Evaporation–precipitation variability over the Mediterranean and the Black Seas from satellite and reanalysis estimates. *J. Clim.* 23, 5268–5287. doi: 10.1175/2010JCLI3525.1

Rosentraub, Z., and Brenner, S. (2007). Circulation over the Southeastern continental shelf and slope of the Mediterranean Sea: direct current measurements, winds, and numerical model simulations. *J. Geophys. Res. Oceans* 112:C11001. doi: 10.1029/2006JC003775

Schroeder, K., Chiggiato, J., Bryden, H. L., Borghini, M., and Ben Ismail, S. (2016). Abrupt climate shift in the Western Mediterranean Sea. *Sci. Rep.* 6, 1–7. doi: 10.1038/srep23009

Schroeder, K., Chiggiato, J., Josey, S., Borghini, M., Aracri, S., and Sparnocchia, S. (2017). Rapid response to climate change in a marginal sea. *Sci. Rep.* 7:4065. doi: 10.1038/s41598-017-04455-5

Schroeder, K., Garcia-Lafuente, J., Josey, S. A., Artale, V., Nardelli, B. B., Carrillo, A., et al. (2012). "Circulation of the Mediterranean Sea and its variability," in *The Mediterranean Climate: From Past to Future*, ed. P. Lionello (Amsterdam: Elsevier).

Shaltout, M., and Omstedt, A. (2014). Recent sea surface temperature trends and future scenarios for the Mediterranean Sea. *Oceanologia* 56, 411–443. doi: 10.5697/oc.56-3.411

Skliris, N., and Lascaratos, A. (2004). Impacts of the Nile river damming on the thermohaline circulation and water mass characteristics of the Mediterranean Sea. *J. Mar. Syst.* 52, 121–143. doi: 10.1016/j.jmarsys.2004.02.005

Skliris, N., Sofianos, S., and Lascaratos, A. (2007). Hydrological changes in the Mediterranean Sea in relation to changes in the freshwater budget: a numerical modelling study. *J. Mar. Syst.* 65, 400–416. doi: 10.1016/j.jmarsys.2006.01.015

Skliris, N., Sofianos, S., Gkanasos, A., Mantziafou, A., Vervatis, V., Axaopoulos, P., et al. (2012). Decadal scale variability of sea surface temperature in the Mediterranean Sea in relation to atmospheric variability. *Ocean Dyn.* 62, 13–30. doi: 10.1007/s10236-011-0493-5

Skliris, N., Zika, J. D., Herold, L., Josey, S. A., and Marsh, R. (2018). Mediterranean sea water budget long-term trend inferred from salinity observations. *Clim. Dyn.* 51, 2857–2876. doi: 10.1007/s00382-017-4053-7

Suari, Y., and Brenner, S. (2015). Decadal biogeochemical history of the south east Levantine basin: simulations of the river Nile regimes. *J. Mar. Syst.* 148, 112–121. doi: 10.1016/j.jmarsys.2015.02.004

Tanhua, T., McCurdy, A., Fischer, A., Appeltans, W., Bax, N., Currie, K., et al. (2019). What we have learned from the framework for ocean observing: evolution of the global ocean observing system. *Front. Mar. Sci.* 6:471. doi: 10.3389/fmars.2019.00471

UNEP/MAP, and Plan Bleu. (2020). *State of the Environment and Development in the Mediterranean*. United Nations Environment Programme: Nairobi.

Vargas-Yanez, M., Zunino, P., Benali, A., Delpy, M., Pastre, F., Moya, F., et al. (2010). How much is the western Mediterranean really warming and salting? *J. Geophys. Res. Oceans* 115:C04001. doi: 10.1029/2009JC005816

Wood, J. E., Silverman, J., Galanti, B., and Biton, E. (2020). Modelling the distributions of desalination brines from multiple sources along the mediterranean coast of Israel. *Water Research* 173:115555. doi: 10.1016/j.watres.2020.115555

Assessment of the variation of failure probability of upgraded rubble-mound breakwaters due to climate change

Martina Stagnitti[1]*, Javier L. Lara[2], Rosaria E. Musumeci[1] and Enrico Foti[1]

[1]Department of Civil Engineering and Architecture, University of Catania, Catania, Italy, [2]Instituto de Hidráulica Ambiental de Cantabria, Universidad de Cantabria, Santander, Spain

The effects of climate change on coastal areas are expected to significantly influence the risk for port operations. In the present work, a novel methodology for the quantitative assessment of the performances of upgraded rubble-mound breakwaters under a changing climate is proposed. For each considered upgrading option, the failure probability related to a certain limit state is calculated through the implementation of Monte Carlo (MC) simulations, using the factor of change (*FoC*) method to include the projected future climate. Three indexes are defined for the immediate and intuitive interpretation of the results: i) the ratio between the calculated and the maximum acceptable failure probability during lifetime (*r*); ii) the rate of the growth of the failure probability during lifetime (*s*); iii) the coefficient of variation of the failure probability due to both the intrinsic uncertainty of the MC simulation and the variability of future climate (*v*). The methodology was applied to the case study of the Catania harbor breakwater, considering the failure of different upgrading solutions due to the collapse of the outer armor layer and to excessive mean overtopping discharge. The results revealed the acceptability of the structural and hydraulic performances of all the tested configurations, under both present and future climate. Moreover, a high climate-related variability of the future failure probability was found. The usefulness of the proposed indexes for designer and decision-makers was also demonstrated. In particular, *r* gives direct information about the acceptability of the structure performances, enabling the immediate comparison between different configurations and climate scenarios. The index *s* is fundamental to calculate the appropriate times to implement repair interventions during the structure lifetime. Finally, *v* allows the identification of those situations which requires the design of highly flexible maintenance plans, able to adapt to a very variable climate avoiding excessive costs.

KEYWORDS

upgrading options, maintenance plan, climate variability, monte carlo technique, harbor defense structures

1 Introduction

Climate change is affecting worldwide coastal areas, generally enhancing erosion and flooding phenomena, which threat the existence of marine ecosystems as well as the development of economic activities linked to seaside tourism or port trade (Foti et al., 2020). The hydraulic performances of coastal and harbor defense structures are directly influenced by the effects of global warming, and in particular by mean sea level rise (Church et al., 2013; Galassi and Spada, 2014), increase of extreme storm surge height and frequency of occurrence (Lowe and Gregory, 2005; Vousdoukas et al., 2016), inter-annual variability of wave characteristics (Hemer et al., 2013; Camus et al., 2017; Morim et al., 2019), and reduction of extreme sea levels return period (Vousdoukas et al., 2018). Future increased wave run-up heights and overtopping rates are expected (Chini and Stansby, 2012; Isobe, 2013; Arns et al., 2017), with consequent alteration of port operability (Sanchez-Arcilla et al., 2016; Camus et al., 2019; Izaguirre et al., 2021). The risk of climate change in port operations and breakwater integrity is even more high when harbor breakwaters are aging and deteriorated. Indeed, structural degradation may reduce the safety and serviceability of structures (Li et al., 2015). Therefore, the design of upgrading solutions for existing harbor breakwaters in the face of climate change represents a challenge (Burcharth et al., 2014; Hughes, 2014), because of the intrinsic uncertainty of climate projections (Morim et al., 2018), and the impossibility to apply the assumption of stationary forcing (Chini and Stansby, 2012; Davies et al., 2017) typical of the traditional deterministic or semi-probabilistic design (i.e. level 0 and level I) methodologies.

Reliability-based design methods, which use the failure probability as a measure of the performance of the structure, should be employed for the assessment of the response of existing and upgraded breakwaters under a changing climate. Indeed, probabilistic approaches enable the inclusion of the uncertainty of the design variables, namely external forcing, coefficients of empirical design formulas, parameters describing geometry and material of the structure, in a more or less sophisticated way (Burcharth, 1987; Burcharth, 1993). Moreover, the concept of return period typical of traditional level 0 and I design methods, e.g. the ones proposed by Tomasicchio et al. (1996) and Burcharth and Sørensen (1999), is overcome. Even if the theoretical basis of the probabilistic design of harbor breakwaters date back to second half of the twentieth century (CIAD project group, 1985; van der Meer, 1988b; Burcharth, 1993), only recently it has been included in national codes and guidelines (US Army Corps of Engineers, 2002; Ports and Harbours Bureau et al., 2009; ROM 1.0-09, 2010). Several studies have been conducted for the definition of methodologies for the assessment of the failure probability of vertical or rubble-mound breakwaters, usually based on level III calculation methods, such as the Monte Carlo (MC) simulation

technique (Castillo et al., 2004; Kim and Suh, 2010; Maciñeira et al., 2017; Lara et al., 2019).

However, there are few investigations which consider the influence of the effects of global warming on the structure response. Takagi et al. (2011) presented a methodology to evaluate the potential failure risk due to the sliding of vertical breakwaters in a future storm event using a MC simulation. Future wave climate was generated by imposing a 10% increase of the future wind speed of tropical cyclones in the Asia-Pacific Region, to be used as input of the spectral wave model SWAN. Also Suh et al. (2012) and Kim and Suh (2014) investigated the influence of future mean sea level and wave climate on the time-dependent risk of caisson sliding during the service life of the breakwater, using existing projection data-set as input of the MC simulations. Uncertainties in design variables (i.e. design wave height, horizontal and vertical wave force, friction coefficient) were modeled by the calculation of the corresponding mean and standard deviation as a function of their characteristic value, bias and coefficient of variation, which have been deduced from existing literature. Moreover, severe storm waves comparable with the design waves were assumed to occur approximately once a year, and to be composed by 1000 waves. Galiatsatou et al. (2018) proposed a reliability-based approach coupled with economic optimization techniques for the assessment of the performances and of the costs of differently upgraded rubble-mound breakwaters. Future climate conditions were defined based on state of art estimations of the 100-year extreme significant wave height and mean sea level rise increase, neglecting variations of storm surge height. The probability of port downtime was calculated using both level II and level III methods, with reference to the ultimate limit state (ULS) due to armor layer instability, excessive overtopping or toe scouring, and the serviceability limit state (SLS) due to wave transmission or wave diffraction.

The actual state of art of the probabilistic assessment of the performances of rubble-mound structures under the effects of climate change presents two main gaps. First, the expected future sea level and wave climate are included in a rough way. Indeed, projected mean sea level rise and variations of the significant wave height are used to adjust the present wave climate conditions, ignoring possible modifications of storm surge height, and with a simplified estimation of the frequency of occurrence and duration of extreme wave storms. The second research gap refers to the lack of indexes to quantitatively compare present and future performances of different configurations of the structure. In this context, the present work proposes a probabilistic methodology for the quantitative assessment of the influence of the effects of climate change on the response of upgraded rubble-mound harbor breakwaters, with reference to ULS or SLS due to independent failure modes. The factor of change method (Kilsby et al., 2007; Fatichi et al., 2011; Peres and Cancelliere, 2018) is employed to include the effects of climate change on wave climate, and the MC technique

is used to estimate the failure probability of the structure. Easy-to-calculate indexes are defined to allow the comparison between the present and future responses of the tested configurations. In this way, the results of the application of the proposed methodology can guide both the design of upgrading solutions and maintenance plans for existing breakwaters and the related decision-making processes, minimizing the risk of over or under-design and providing useful inputs for the cost-benefit analysis.

The paper is organized as follows. Section 2 describes the proposed probabilistic methodology and presents the data used for its application to the emblematic case study of the Catania harbor breakwater (Italy) under present, RCP4.5 and RCP8.5 climate scenarios. The obtained results on marine climate and failure probability are compared and discussed in section 3. Finally, section 4 summarizes the main conclusions of the work and suggests possible future developments.

2 Methods and materials

2.1 Characterization of local extreme wave climate

The probabilistic assessment of the performances of upgraded rubble-mound breakwaters requires the statistical characterization of local extreme wave climate, considering both present and future scenarios. To this aim, time series of wave climate descriptors are needed, which can be derived from buoy measurements or reanalysis models for the present climate, and from climate projection models for the future scenarios. In particular, the following wave climate variables are here considered: i) significant wave height; ii) mean wave period; iii) sea storm duration. Moreover, the storm surge phenomenon is studied, focusing on its correlation with extreme significant wave height.

For the present climate, the directional extreme value analysis of the offshore significant wave height (H_{s0}) is performed, by applying the peak over threshold (POT) method to detect the extreme events and evaluate the mean number of storms per year (λ). In the present work, peaks with H_{s0} higher than 1.50 m are considered, assuming a minimum temporal distance equal to 12 hours between independent events (Boccotti, 2004). The adaptation of extreme value distributions (e.g. Generalized Extreme Value, Weibull, Generalized Pareto) to the obtained samples of extreme events is performed through the method of moments estimation (MME). Such a method allows the calculation of the scale, shape and location parameters of the selected probability distribution functions by replacing the theoretical mean, standard deviation, skewness and kurtosis for the specified distribution by the corresponding sample moments. The scale parameter (α_{sc}) provides indications about the scale on the horizontal axis of the probability density

function (PDF) plot. The shape parameter (κ_{sh}) affects the general shape of the PDF. Finally, the location parameter (ζ_{lc}) gives information about where the probability distribution is centered in the horizontal axis of the PDF plot. The best fitting distribution is identified through the visual comparison between the sample data and the PDF, as well as through the Kolmogorov-Smirnov goodness-of-fit test, which determines whether a sample comes from a specific distribution.

The effects of climate change on extreme wave climate are introduced by modifying the scale, shape and location parameters of the distribution fitted to the present directional extreme H_{s0}, based on factors of change (FoC) derived from the comparison of the projected future scenarios and the baseline climate provided by the same projection model (Kilsby et al., 2007; Fatichi et al., 2011; Peres and Cancelliere, 2018). The FoC method consists in the evaluation of the difference between statistics (e.g. mean, standard deviation, skewness, kurtosis) of a climate variable computed for the future scenario and for the present control period provided by the projection model, by applying the following formula:

$$FoC = \frac{M_{m,f}}{M_{m,c}} \qquad (1)$$

where $M_{m,f}$ and $M_{m,c}$ are the generic statistical moments evaluated for the modeled future and control periods, respectively. Once the FoC is calculated, the future value of the considered statistical moment (M_f) is evaluated by multiplication to the observed moment in the control period ($M_{obs,c}$):

$$M_f = FoC \times M_{obs,c} \qquad (2)$$

The FoC method is here applied considering the samples of extreme H_{s0} derived from the application of the POT method, with threshold equal to 1.50 m and minimum distance between independent events equal to 12 hours, to the time series of the observed control period, the modeled control period and the future period. The future period is divided into sub-periods, using a yearly moving time window covering the same number of years of the control period. For each future sub-period, the MME method is employed to estimate α_{sc}, κ_{sh} and ζ_{lc} of the extreme value distributions of H_{s0} which take into account the effects of climate change, using as input data mean, standard deviation, skewness and kurtosis of extreme H_{s0} calculated through equations 1 and 2.

The statistical characterization of mean wave period, sea storm duration and storm surge height is performed by modeling their correlation to H_{s0}. When dealing with coastal structure design, both copula functions (Muhaisen et al., 2010; Mercelis et al., 2014; Salvadori et al., 2015; Malliouri et al., 2021; Radfar et al., 2022) and site-specific empirical relationships (Takagi et al., 2011; Suh et al., 2013; Mercelis et al., 2014; Maciñeira et al., 2017; Tabarestani et al., 2020) are widely employed to model the correlation between dependent climate variables. In the present work, the definition of empirical

relationships between H_{s0} and the offshore mean wave period (T_{m0}), the sea storm duration (d_s) and the storm surge height (h_{ss}) is proposed, because of their greater ease of use. The site-specific coefficients of such empirical relationships, whose mathematical form is considered not to change in time, are calculated through the application of the least squares method to both the measured (or reanalysis) and projected data-sets, thus obtaining different values for present and future climate scenarios. The latter are analyzed using the same yearly moving time window defined for the application of the *FoC* method.

Once the offshore wave climate has been characterized, the wave propagation towards the breakwater needs to be performed. Wave propagation is usually simulated by means of numerical models, which take into account shoaling, refraction and breaking processes.

2.2 Calculation of the failure probability during lifetime

Once the most suitable upgrading concepts for the considered rubble-mound breakwater have been identified (Burcharth et al., 2014) and designed applying traditional (i.e. level 0 or II) methods, their performances during lifetime can be assessed in terms of failure probability, and then compared to the design requirements. The useful life of harbor breakwaters is long enough to experience the effects of climate change (Hallegatte, 2009), because its minimum length ranges between 25 and 50 years, depending on the economic repercussions due to partial or total loss of functionality (Tomasicchio et al., 1996; ROM 1.0-09 (2010)). Therefore, future scenarios accounting for the effects of climate change must be considered for the probabilistic calculations.

Here, a methodology for the assessment of the failure probability of upgraded harbor rubble-mound breakwaters during lifetime under the effects of climate change is proposed. First, a failure tree is defined. Then, the main failure modes referred to ULS or SLS are selected, assuming that they are related according to a series system. The series system, which implies that the failure of the structure occurs if at least one of the considered failure modes takes place, is typically employed for coastal structures (US Army Corps of Engineers, 2002). The governing equation of the selected failure mode (e.g. stability of the armor layer, mean overtopping discharge, toe berm stability, etc) is derived from state of art or site-specific experimental or numerical equations, and re-written as a reliability function (US Army Corps of Engineers, 2002; Jonkman et al., 2015):

$$Z = R - S \tag{3}$$

where R is the resistance of the structure to the external solicitations S, being both R and S stochastic variables. R is usually linked to the geometry of the structure and to the characteristics of the component materials, whereas S sually

contains the water density and the hydrodynamic parameters. If $Z<0$ (i.e. $R<S$), the selected limit state is overcome by the structure and the failure occurs. When the failure probability (i.e. $P_f = P(Z<0)$) is greater or smaller than the acceptance limit, the structure is under-designed or over-designed, and needs to be modified to improve its performances or reduce the construction costs, respectively. The modified structure is the new object of the probabilistic calculations, and the optimization process goes on in an iterative way until the design requirements are reached (Kim and Suh, 2006; Malliouri et al., 2021).

Figure 1 summarizes the proposed procedure to be applied for the calculation of the probability that the structure reaches a certain limit state, described by a reliability function Z. A level III method is employed, which is based on the implementation of probabilistic simulations through the MC technique. Such a method overcomes the concept of design return period, which is typical of level 0 or level I design approaches, and uses the whole probability distributions of the variables involved in the design process, also modeling their reciprocal correlations. According to the indications of ROM 1.0-09 (2010), each realization of the MC simulation is a life cycle of the structure, which consists of a known number of meteorological years. For a certain climate scenario, during each meteorological year, a certain number of sea storms is randomly generated from the probability distribution functions of the wave climate parameters for the considered site, which have been previously defined following the procedure described in section 2.1. Such sea storms may cause or not the achievement of the considered limit state. Therefore, the failure probability during lifetime is defined as the probability that the structure reaches at least once the considered limit state during its life cycle. The failure probability during a t-years life cycle and its standard deviation are calculated as follows (Lara et al., 2019):

$$P_{f,t} = P_f(0,t) = \frac{N_f(0,t)}{N_r} \tag{4}$$

$$\sigma_{P_{f,t}} = \sigma_{P_f}(o,t) = \sqrt{\frac{P_f(0,t) \times \left(1 - P_f(0,t)\right)}{N_r}} \tag{5}$$

Where $N_f(0,t)$ is the number of t-years life cycles with at least one failure (i.e. $Z<0$) and N_r is the total number of simulated life cycles (i.e. realizations of the MC simulation). The given definition of $P_{f,t}$ implies that the following relationship is valid:

$$P_{f,t} = P_f(0,t) = \sum_{i=1}^{t} P_f(i-1,t) \tag{6}$$

The length of the structure life cycle t is set equal to the structure lifetime (L) suggested by codes and guidelines which include the use of level III design methods, e.g. ROM 1.0-09 (2010). Therefore, in the following the failure probability $P_{f,L}$ is considered. The maximum acceptable failure probability during lifetime ($P_{f,Lmax}$), whose value
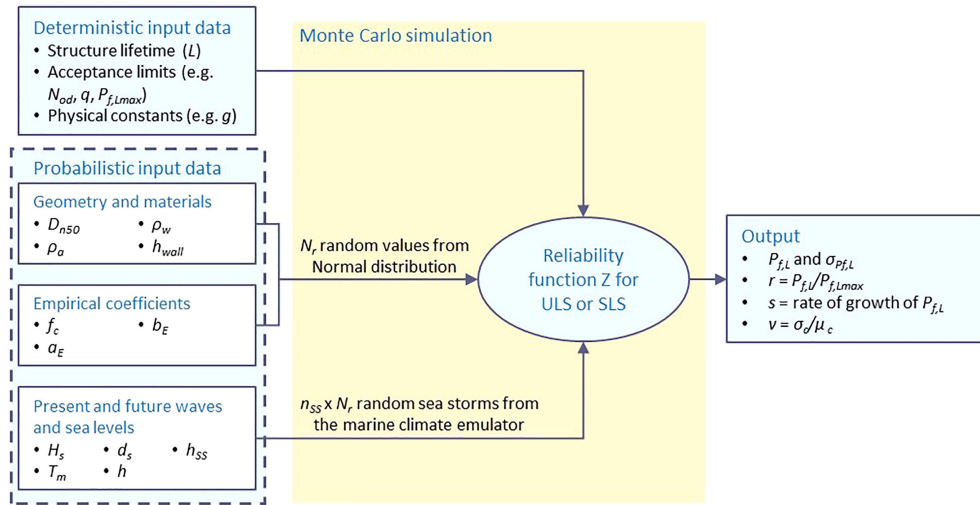
FIGURE 1
Block diagram of the proposed methodology for assessment of the failure probability of upgraded harbor rubble-mound breakwaters.

depends on the design requirements, is also fixed according to the above mentioned codes and guidelines. The most appropriate number of realizations of the MC simulation is selected through a preliminary analysis of the stabilization process of $P_{f,L}$ and of its coefficient of variation ($CV = \sigma_{P_f,L}/P_{f,L}$) by varying N_r. The aim of such an analysis is the identification of the value of N_r able to provide a compromise between accuracy of the simulation results and calculation times. In the present work, a maximum acceptable CV equal to 0.35 is considered. It should be noted that the required number of realizations to obtain a certain CV increases for lower $P_{f,L}$.

The N_r life cycles are randomly simulated using as input data the probability distributions of the involved stochastic variables, which are: i) descriptors of the structure geometry and materials (e.g. density of water and of blocks, slope of the armor layer, height of the wave wall); ii) empirical coefficients of the reliability function; iii) descriptors of sea level and wave climate. The first two groups of variables are described using normal distributions, whose mean and standard deviation are deduced from existing literature or available data-sets (van der Meer, 1988b; Burcharth, 1992; Lara et al., 2019). The corresponding random values are generated for each simulated life cycle, under the hypothesis of no changes of the structure composition, geometry and behavior during lifetime, and imposing truncation limits to the normal distributions to avoid unrealistic values. Instead, the random generation of sea levels and sea storms occurring during the structure useful life is performed by a marine climate emulator, whose detailed description is presented in section 2.3. The number of sea storms (n_{ss}) to generate for each life cycle is evaluated as follows:

$$n_{ss} = L \times \lambda \qquad (7)$$

where λ is the mean annual frequency of sea storms derived from the POT analysis of the H_{s0} time series corresponding to the selected climate scenario (see section 2.1). Therefore, for each simulation a total of $n_{ss} \times N_r$ different sea storms are simulated. Finally, physical constants (e.g. g) and limits values of parameters used to quantify the structure performances (e.g. limit damage conditions or mean overtopping discharges) are considered as deterministic variables.

In order to enable the immediate and quantitative comparison between the failure probabilities during lifetime calculated for different structure configurations under both present and future climate, easy-to-calculate indexes are here proposed. The first index (r), which is defined to quantify the safety level ensured by the structure, is calculated according to the following formula:

$$r = \frac{P_{f,L}}{P_{f,Lmax}} \qquad (8)$$

If r is greater than one, the failure probability is not acceptable, otherwise the performances of the structure are sufficient to satisfy the design requirements. Besides the value of $P_{f,L}$, also the rate of the growth of the failure probability during lifetime provides useful information about the performances of the structure and indications to plan possible structural interventions. Such a rate can be calculated as the slope s of the linear regression model which describes the variation of $P_{f,t}$ from the null value of the year zero to the final value corresponding to the year L (see equation 6). If the effects of possible maintenance interventions are not included, s is always greater than or equal to zero, meaning that $P_{f,t}$ can only increase or remain constant during the period between the years

zero and L. Finally, since the time series of climate data under a certain scenario are elaborated using a yearly-moving time window of fixed length (see section 2.1), the enhancement of the MC outputs uncertainty due to the variability of the input climate among the defined sub-periods can be quantified using the following coefficient of variation:

$$v = \frac{\sigma_c}{\mu_c} \tag{9}$$

where σ_c and μ_c are the standard deviation and the mean of $P_{f,L}$ calculated with reference to the above-mentioned sub-periods of the considered future scenario. If the coefficient of variation is greater than or equal to one, $P_{f,L}$ shows high variability as the future time window changes.

2.3 Marine climate emulator

A marine climate emulator has been designed to generate random sea storms and sea levels, also considering the effects of climate change, to be used for the performance of the MC simulations described in section 2.2. The required input data are the extreme value distributions of H_{s0} and the site-specific empirical relationships between H_{s0} and T_{m0}, d_s and h_{ss}, which are defined for the present and future scenarios following the procedure described in section 2.1. The mean water depth at the breakwater site (h) is assumed independent from the other climate descriptors and normally distributed, with standard deviation calculated according to the following formula (Castillo et al., 2006):

$$\sigma = \frac{(h + h_{at}) - (h - h_{at})}{4} \tag{10}$$

where h_{at} is the astronomical tide characteristic of the studied site.

For each climate scenario, and for each defined sub-period, a random offshore sea storm is generated according to the following procedure:

1. an initial random H_{s0} is drawn from the central fit of the extreme value distribution of offshore significant wave height;
2. a final random H_{s0} is drawn from the normal distribution having mean equal to H_{s0} previously generated from the central fit, and standard deviation corresponding to the width of the 95% confidence bounds (*CB*) of the extreme value distribution of the offshore significant wave height;
3. an initial random value of each H_{s0}-dependent variable (i.e. T_{m0}, d_s and h_{ss}) is generated form the central fit of the corresponding site-specific empirical relationships, using as input the last drawn H_{s0};

4. a final random value of each H_{s0}-dependent variable is generated form the normal distribution having mean equal to the value previously generated from the central fit of the site-specific empirical law and standard deviation corresponding to the width of its 95% *CB*.

The above described procedure is repeated $n_{ss} \times N_r$ times, in order to obtain the required number of offshore sea storms for the performance of the MC simulation (see section 2.2).

The offshore wave conditions need to be propagated towards the coast. As stated in section 2.1, wave propagation is usually simulated by means of numerical models. However, the numerical propagation of each randomly generated wave condition towards the breakwater site would significantly increase the calculation time required for the performance of MC simulations. Therefore, the possibility to define more or less complex site-specific formulations calibrated on a data-set made up of measured or reanalysis extreme offshore wave conditions and corresponding numerically propagated ones should be considered, in order to avoid the performance of a numerical simulation for each sea storm to generate. Such site-specific formulations include the propagation processes simulated with the numerical model in a simplified manner, thus taking into account both shoaling and refraction, as well as wave breaking. Wave breaking is further checked at the breakwater site using the breaking criteria for the identification of depth limited or steepness limited waves. The application of such criteria requires the knowledge of the water depth at the breakwater site for each simulated sea storm, which is calculated as the sum between the corresponding h_{ss} and a random value of h drawn from its normal distribution.

2.4 Case study

2.4.1 The Catania harbor breakwater

The Catania harbor breakwater was selected for the application of the proposed methodology for the quantitative assessment of the performances of upgraded rubble-mound breakwaters under a changing climate. The Port of Catania, which is located on the Eastcoast of Sicily, is one of the Italian commercial ports of national interest, thanks to its barycentric position with respect to the Suez Channel, the Strait of Gibraltar, the European ports and the North-African ports (see Figure 2A). The "Levante" breakwater represents the main protection of the harbor basin from the offshore waves (see Figure 2B). The wave rose and the plot of extreme H_{s0} against mean wave direction showed in Figure 2C indicate that the most energetic sea states come from the angular sector centered in the 90°N direction. The Catania harbor breakwater was born in the XVIII century as a composite structure, and then

converted into the present 2.25 km long rubble-mound breakwater (Franco, 1994; Oumeraci, 1994; Takahashi, 2002). The actual armor layer appears severely damaged, and its mean sea side slope significantly reduced, because of the off-shore slip of the 62 t cubic concrete blocks. The deteriorated structure, which lost the original geometrical and structural homogeneity, may not be able to withstand the increasingly frequent extreme marine events and properly limit the consequent overtopping discharges. Such a condition would correspond to limitations to the harbor activities, which must be overcome to ensure the satisfaction of the actual and projected future demand of port services. Therefore, the local Port Authority decided to perform a restoration and upgrading intervention.

Following the suggestions of Burcharth et al. (2014), upgrading solutions which consist in the heightening of the existing wave wall and/or the addition of extra armor blocks were considered. The extra armor units can be placed according to a regular design slope or following the irregularities of the existing structure through the construction of a single or double layer, with a toe berm to ensure their stability. In particular, the following six configurations have been verified through the performance of physical and numerical tests (Stagnitti et al., 2020; Stagnitti et al., 2022):

1. configuration E, which is the existing structure whose wave wall height is +8.50 m above mean sea level (see Figure 3A);
2. configuration EM, which consists in the simple heightening of the wave wall up to +9.50 m above mean sea level (see Figure 3B);
3. configuration AS, which consists in the armor layer restoration with 30 t Antifer according to the design slope of 1:2 (see Figure 3C);
4. configuration AD, which consists in the addition of a double layer of 30 t Antifer smaller than the existing ones, following the irregularities of the present armor layer (see Figure 3D);
5. configuration CM, which involves the addition of a single layer of 62 t cubes equal to the existing ones, following the irregularities of the present armor layer (see Figure 3E);
6. configuration CS, which consists in the raising of the wave wall up to +9.50 m above mean sea level and the addition
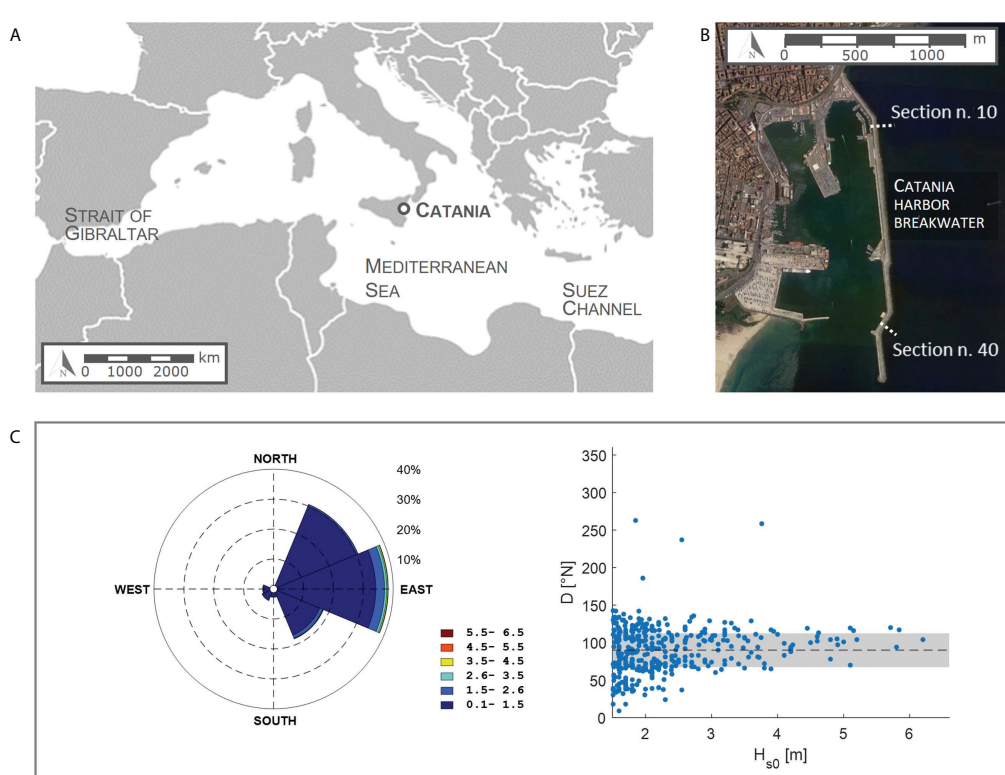
FIGURE 2
(A) Location of Catania. (B) Layout of the port of Catania, and indication of the outer breakwater representative cross-sections (satellite view from Google Earth 2020). (C) Wave rose and plot of the offshore significant wave heights greater than 1.50 m against mean wave direction (the shaded area represents the 45°-wide sector centered in the 90°N direction).

of a single layer of 62 t cubes equal to the existing ones according to the design slope of 1:2, after the regularization of the present armor layer (see Figure 3F).

It should be noted that the non-homogeneity of the existing armor layer has strong consequences on the design of the quarry stone berm to be constructed at the toe of the additional blocks. Indeed, if the toe berm is designed with a constant shape for the whole breakwater, without including the reshaping of the existing armor layer, at some cross-section the additional blocks may not be directly in contact with the internal slope of the berm.

2.4.2 Composite modelling

The definition of the reliability functions to be used for the assessment of the failure probability of existing and upgraded breakwaters requires the identification of formulas for the description of damage dynamics and overtopping phenomenon valid for the considered structures. Because of the non-conventional nature of the existing and upgraded Catania harbor breakwater, the response of the existing and upgraded structure to increasing wave load was assessed through the combination of experimental and numerical results on damage dynamics and overtopping phenomena, i.e. by performing the composite or hybrid modeling (Oumeraci, 1999; Guanche et al., 2015; Di Lauro et al., 2019;

Kamphuis, 2020). In this way, the performances of existing design formulas in representing damage progression and overtopping phenomenon were assessed, and new site-specific relationships were defined. In particular, the experimental results were employed to investigate damage dynamics of the outer armor layer and acquire data for the calibration of the numerical model, whose outputs were used for the analysis of the overtopping phenomenon.

The experimental campaign was carried out at the Hydraulic Laboratory of the University of Catania (Stagnitti et al., 2020; Stagnitti et al., 2022). A total of 192 two-dimensional physical model tests were performed at 1:70 scale inside a flume 18.00 m long, 1.20 m high and 2.40 m wide, built within a tank equipped with a flap-type wavemaker for the generation of random waves using JONSWAP spectra. The six configurations described in section 2.4.1 were studied considering two representative cross-sections of the breakwater, namely sections no. 10 and no. 40 (see Figure 2B), in order to assess how the lack of uniformity along the existing armor layer may influence the design of upgrading solutions. Configurations AS, AD and CM at section no. 10 are characterized by the lack of direct contact between the additional armor blocks and the toe berm (e.g. Figures 3C–E), contrary to configuration CS at section no. 10 and AS, AD, CM and CS at section no. 40 (e.g. Figure 3F). For each tested configuration, five different sea states of 4500 waves, divided into three equal intervals, were generated. The
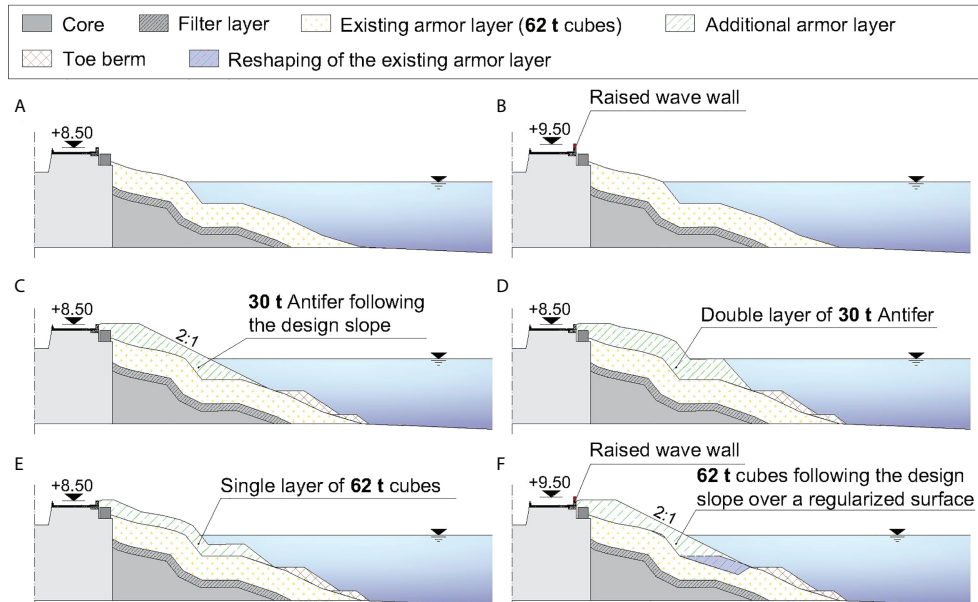
FIGURE 3
Configurations of the Catania harbor breakwater: **(A)** existing structure; **(B)** existing structure with heightened wave wall; **(C)** upgraded structure with additional 30 t Antifer units placed according to a 2:1 slope; **(D)** upgraded structure with additional double layer of 30 t Antifer units; **(E)** upgraded structure with one additional layer of 62 t cubes; **(F)** upgraded structure with additional 62 t cubes placed according to a 2:1 slope over the reshaped existing armor layer, and with heightened wave wall.

reproduced waves were perpendicular to the structure, since the most energetic sea storms reaching the Catania harbor breakwater come from 90°N (see Figure 2C). The first four sea states correspond to wave conditions having return period equal to 5, 10, 50 and 100 years, respectively. Instead, the fifth sea state is characterized by significant wave height equal to 120% of the 100-years return period one. Experimental data regarding wave characteristics, reflection phenomenon, damage dynamics and mean overtopping discharge were acquired. In particular, the incident and reflected wave motion was measured through the four-gauge method of Faraci et al. (2015). Damage progression of the outer armor layer was investigated through the analysis of the traditional damage parameter N_{od} and of novel descriptors of the armor surface roughness. Finally, a specially designed measuring system was employed for the acquisition of the overtopping volumes. o mean sea level) in the range 0.88÷2.13 and Iribarren number in the range 2.15÷2.76.

The stability of the upgrading solutions with additional armor layer (i.e. configurations AS, AD, CM and CS) was examined in depth. To the authors' knowledge, no damage progression formulas exist for rubble-mound structures with more than two layers of cube-shaped units placed according a slope of 1:2. Therefore, the experimental N_{od} measured at the end of each sea state were compared to the traditional formula of van der Meer (1988a), hereinafter vdM formula, which is valid for double layers of cubes laid on a slope of 1:1.5 with a notional permeability equal to 0.4:

$$\frac{H_s}{\Delta D_{n50}} = f_c \times \left(6.7 \frac{N_{od}^{0.4}}{N_w^{0.3}} + 1 \right) \times \left(\frac{2\pi H_s}{gT_m^2} \right)^{-0.1} \qquad (11)$$

where N_w is the number of incident waves, $\Delta = \rho a / \rho w - 1$ and D_{n50} are respectively the relative density and the median nominal diameter of the armor blocks, H_s is the incident significant wave height, T_m is the mean wave period, g is the gravity acceleration and f_c is an empirical coefficient equal to 1.00 with a standard deviation (σ) equal to 0.10. As expected, the vdM formula does not provide a good approximation of the experimental damage, since the tested structures differ from the traditional structure type for which the vdM formula was calibrated, in terms of geometry, layering and porosity. In particular, the vdM formula overestimates the measured N_{od}, which is accordance with the fact that the tested sections are characterized by a slope flatter than 1:1.5. The adaptation of the vdM formula to the experimental data was performed through the calibration of the empirical coefficient f_c, using the least squares method. The physical model results reveal the existence of two different responses of the structure in the case of direct or not direct contact between the additional armor units and the toe berm, hereinafter indicated as SS and NSS configurations. For this reason, two different f_c were calculated, distinguishing between SS and NSS configurations. Figures 4A, B shows the experimental N_{od} as a function of the stability parameter $H_s/\Delta D_{n50}$, together with the fitted equation 11 and its

95% *CB*. As reported in Table 1, the experimental f_c is equal to 1.72 ($\sigma = 0.29$) and 1.35 ($\sigma = 0.20$) for SS and NSS configurations, respectively.

The experimental results on overtopping and reflection phenomena were employed for the calibration of the numerical model of the Catania harbor breakwater, which allowed the construction of larger data-set for the investigation of the overtopping phenomenon. The extensively validated IH2VOF numerical model (Lara et al., 2008; Guanche et al., 2009; Di Lauro et al., 2019), was employed, which is able to solve the 2D Volume-Averaged Reynolds averaged Navier–Stokes (VARANS) equations (Lara et al., 2011). Section n. 40 of the Catania harbor breakwater was studied (see Figure 2B), considering configurations E and CS, which according to the experimental results are the less and most performing solutions, respectively. The 2D simulations were performed inside a numerical flume 4.50 m wide and 0.65 m high, meshed using a uniform grid with Δx equal to 0.020 m and Δy equal to 0.010 m. The porosity parameters characteristic of each layer of the structure, namely α, β, c_A and n Lara et al., 2011), were calibrated on the basis of the state of art suggestions and the experimental reflection coefficient and mean overtopping discharge. In particular, according to Lara et al. (2008), for all the porous media α and c_A were set equal to 200 and 0.34, respectively. Instead, n and β have been calibrated against experimental results, thus obtaining: i) $n=0.32$ and $\beta=1.20$ for the core; ii) $n=0.35$ and $\beta=2.00$ for the filter layer; iii) $n=0.30$ and $\beta=1.50$ for the existing armor layer; iv) $n=0.25$ and $\beta=5.00$ for the additional armor layer; v) $n=0.35$ and $\beta=3.00$ for berm at the toe of the additional armor layer. The hydraulic response of the two considered configurations was investigated by simulating five sea states of 1500 waves, each of which was repeated six times in order to take into account the effect of wave sequence on overtopping phenomena. Therefore, a total of 60 numerical simulations were performed. The good correspondence between the experimental and numerical results is showed in Figures 4C, D, where the non-dimensional mean overtopping discharge q^* is expressed as a function of the non-dimensional structure free-board R_c/H_s, being R_c the maximum value between the crest level and the wave wall height referred to mean sea level.

The numerical q^* was compared to the prediction of the traditional formula proposed by (EurOtop, 2018), hereinafter EurOtop formula:

$$q^* = \frac{q}{\sqrt{gH_s^3}} = a_E \times exp\left[-\left(b_E \times \frac{R_c}{H_s \gamma_f} \right)^{1.3} \right] \qquad (12)$$

where γ_f is the roughness factor (equal to 0.47 for double layer of artificial cubes), and a_E and b_E are empirical parameters equal to 0.09 ($\sigma = 0.0135$) and 1.50 ($\sigma = 0.1500$), respectively. Despite the predictions of the EurOtop formula are quite good, two site-specific
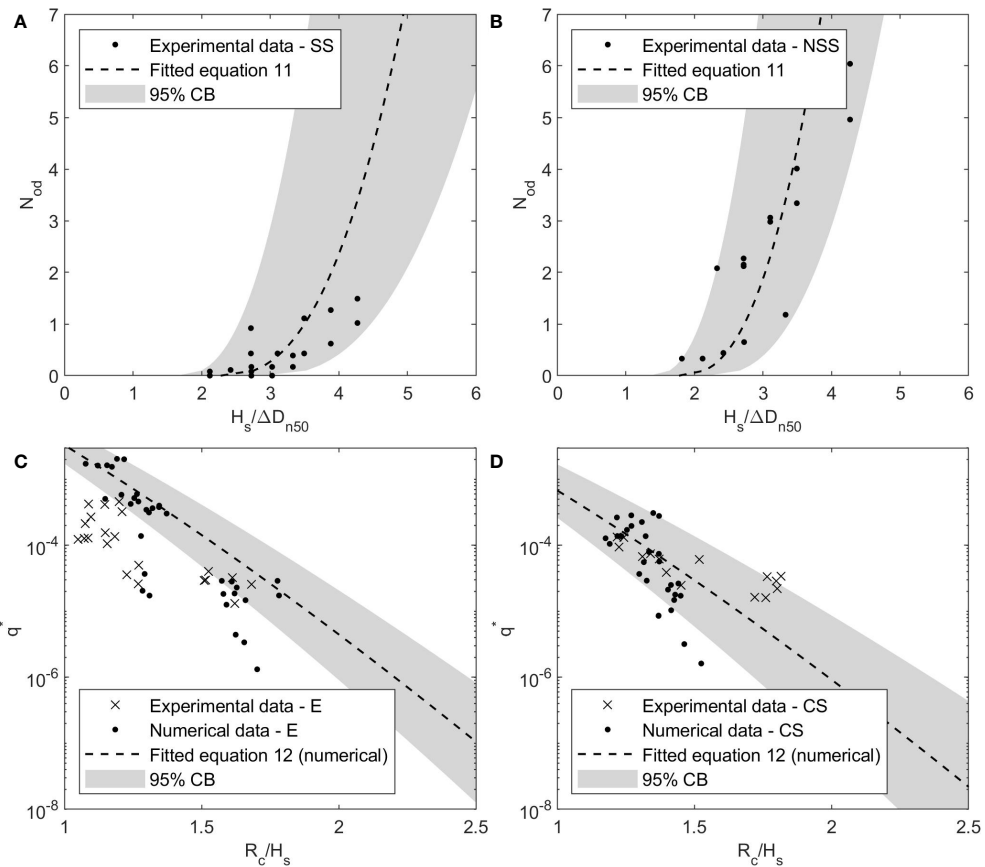
FIGURE 4

Site-specific experimental formulas for the variation of the damage parameter N_{od} as a function of the stability number for: **(A)** SS configurations; **(B)** NSS configurations. Comparison between experimental and numerical data and site-specific numerical formulas for the variation of the non-dimensional mean overtopping discharge as a function of the non-dimensional structure free-board: **(C)** configuration E; **(D)** configuration CS "q*" is the name of the plotted variable.

formulas were fitted to the numerical data acquired for configurations E and CS at section no. 40, using the least squares method. Figures 4C, D shows equation 12 adapted to the numerical data and the 95% *CB* of the fitting. As reported in Table 1, the experimental a_E and b_E are equal to 0.30 (σ = 0.14) and 1.50 (σ = 0.01) for configuration E, and to 0.06 (σ = 0.05) and 1.50 (σ = 0.15) for configuration CS. It should be noted that the site-specific a_E and b_E are quite similar to the EurOtop ones. However, the fitted empirical coefficients improve the performances of equation 12 in reproducing q^* higher than 10^{-3} for configuration E, and q^* lower than 5×10^{-5} for configuration CS.

2.4.3 Climate data

The evaluation of the performances of the upgraded Catania harbor breakwater requires wave climate and sea level data for the studied site, to be used as input for the MC simulations. As regards the present climate, the freely available measured wave data of the Italian National Sea Wave Measurement Network

(RON) were employed (Piscopia et al., 2004), which consists of time series of offshore significant wave height (H_{s0}), peak wave period (T_{p0}), mean wave period (T_{m0}) and mean wave direction (D) for the period 1989-2014. From 1989 to 2001 the wave measurements were taken every three hours, whereas from 2002 to 2014 the acquisition interval was thirty minutes. The present mean sea level was deduced from the design data provided by the local Port Authority, and it is equal to 16.50 m and 19.00 m for sections n. 10 and 40, respectively. The second value was selected as the mean of the normal distribution of h, whose standard deviation was calculated through equation 10, assuming that h_{at} is equal to 0.20 m (see Table 1). The storm surge was introduced using the ERA5 reanalysis data (Hersbach et al., 2019), which are available for the period 1989-2017, with a time step of 10 minutes.

For the future climate, the ocean surface wave projections and the water level change time series for the European coast provided by the Copernicus Climate Change Service were employed (Caires and Yan, 2020; Yan et al., 2020). Such data

TABLE 1   Mean (m) and standard deviation (σ) of the normally distributed variables used to perform the Monte Carlo simulations, and parameter k for the calculation of the lower (l) and upper (u) limits of the truncated distributions (f_c coefficient of the ULS reliability function, a_E and b_E coefficients of the SLS reliability function, h mean water depth, D_{n50} mean nominal diameter, Δ relative density, h_{wall} height of the wave wall measured with respect to the toe of the structure).

Variable	Formulation	m	σ	k	l	u
f_c [-]	vand der Meer (1988)	1.00	0.10	–	–	–
	Experimental SS	1.72	0.29	–	–	–
	Experimental NSS	1.35	0.20	–	–	–
a_E [-]	EurOtop Manual (2018)	0.09	0.01	–	–	–
	Numerical E	0.30	0.14	–	–	–
	Numerical CS	0.06	0.05	–	–	–
b_E [-]	EurOtop Manual (2018)	1.50	0.15	–	–	–
	Numerical E	1.50	0.10	–	–	–
	Numerical CS	1.50	0.15	–	–	–
h [m]	present	19.00	0.10	–	–	–
	RCP4.5	19.36 ÷ 19.42	0.10	–	–	–
	RCP8.5	19.24 ÷ 19.33	0.10	–	–	–
$Dn50$ [m]	30 t Antifer	2.35	0.03	3.00	2.25	2.45
	62 t Cubes	3.00	0.03	3.00	2.90	3.10
Δ [-]	–	1.23	0.05	4.00	1.04	1.42
h_{wall} [m]	Configuration E	27.5	0.03	4.00	27.38	27.62
	Configuration CS	28.5	0.03	4.00	28.38	28.62

were generated by the ECMWF's Wave Model (SAW) and the Deltares Global Tide and Surge Model (GTSM) version 3.0, respectively, forced by surface wind from a member of the EURO-CORDEX climate model ensemble (i.e. the HIRHAM5 regional climate model downscaled from the global climate model EC-EARTH). The wave data-set is made of hourly time series of H_{s0}, T_{p0}, T_{m0} D and wave spectral directional width for the European coastline along the 20 m bathymetric contour with 30 km spatial resolution. The sea level data-set consists of time series of mean sea level, storm surge residual, tidal elevation and total water level, with a time step of 10 minutes. The wave and sea level time series are available for the following climate scenarios: i) the baseline climate (HIST), which refers to the period 1976-2005; ii) the future climate RCP4.5, which corresponds to an optimistic emission scenario where emissions start declining beyond 2040; iii) the future climate RCP8.5, where emissions continue to rise throughout the century (i.e. business-as-usual scenario). It should be noted that the future wave data refers to the period 2041-2100 for both RCP4.5 and RCP8.5. On the contrary, the future water level time series covers the years 2071-2100 for RCP4.5, and the years 2041-2070 for RCP8.5. For this reason, in the present work only the periods 2071-2100 under RCP4.5 scenario and 2041-2070 under RCP8.5 scenario were considered. For the future scenarios, the mean of the normal distribution of present h was corrected by adding the projected mean sea level rise (SLR), which according to the employed data-set ranges between 0.36 ÷ 0.42 m and 0.24 ÷ 0.33 m for RCP4.5 and RCP8.5, respectively (see Table 1).

The statistical characterization of the extreme local wave climate was performed according to the procedure described in section 2.1. As discussed in section 2.4.1, under the present climate the most energetic sea storms come from the 90°N direction (see Figure 2C). Therefore, extreme events, whose rounded frequency of occurrence (λ) is equal to 13 events/year, were considered to come from such direction. Moreover, only the years 1989-2005 of the measured time series of H_{s0} were used for the analysis of present extreme wave climate, in order to ensure a statistically significant comparison with the baseline HIST scenario. The visual comparison between different extreme value PDF and the sample of extreme H_{s0}, and the results of the Kolmogorov-Smirnov test with statistical significance level equal to 5% revealed that the best fitting distribution for present extreme H_{s0} is the Weibull distribution with $a_{sc}=1.14$, $\kappa_{sh}=1.30$ and $\zeta_{lc}=1.56$. According to the climate projection model, no significant variations of extreme wave direction are expected for the future scenarios. Therefore, the effects of climate change on the present Weibull distribution have been introduced by modifying its a_{sc}, κ_{sh} and ζ_{lc}, using the *FoC* method. The *FoC* method has been applied using a 17-years moving window for the analysis of the future time series, in order to analyze sub-periods having the same length of the considered present period. In this way, 14 sub-periods have been obtained for each future scenario. The ranges of the calculated a_{sc}, κ_{sh} and ζ_{lc} are summarized in Figure 5A. Depending on the considered sub-period, λ ranges between 12÷13 events/year and 13÷14 events/year under RCP4.5 and RCP8.5, respectively (see Figure 5B). Figure 6 shows the plots of some of the fitted Weibull

distributions in terms of H_{s0} expressed as a function of the return period (T_r), which refer to the present climate and the sub-periods 2084-2100 under RCP4.5 scenario and 2053-2069 under RCP8.5 scenario.

The correlations between extreme H_{s0} and T_{m0}, d_s and h_{ss} were modeled through the definition of site-specific empirical formulas, whose coefficients were calculated considering the present and the future scenarios (see section 2.1). The offshore mean wave period was calculated by adapting the formula proposed by Boccotti (2004):

$$T_{m0} = b_{Tm}\pi\sqrt{\frac{H_{s0}}{4g}} \qquad (13)$$

where b_{Tm} is the empirical non-dimensional coefficient evaluated through the least squares method, and H_{s0} and T_{m0} are measured in m and s, respectively. The estimate of the wave storms duration (measured in hours) was performed using the following linear relationship, which is similar to the one proposed by Laface and Arena (2016) for the equivalent exponential storm model:

$$d_s = b_{ds}H_{s0} \qquad (14)$$

where b_{ds} (hours/m) is an empirical coefficient dependent on the site characteristics, evaluated through the least squares method. Finally, the storm surge height (h_{ss}, measured in meters) was using the following linear relationship, which is similar to the one proposed by Salmun et al. (2011):

$$h_{SS} = b_{SS}H_{s0} \qquad (15)$$

where b_{ss} is an empirical non-dimensional coefficient depending on the site characteristics, evaluated through the least squares method. Figures 5C–E shows the ranges of the fitted site-specific empirical coefficients.

According to the procedure for the generation of random sea storms described in section 2.3, the definition of a site-specific formulation for wave propagation towards the breakwater site is required. A previously generated data-set of deep-water and corresponding shallow water wave conditions was available for the studied site. In particular, the offshore significant wave height and mean wave period time series for the years 2006-2019 provided by Korres et al. (2019) were propagated towards the the breakwater site using the spectral wave model SWAN (Booij et al., 1999). The analysis of the correlation between extreme H_{s0} and corresponding propagated H_s revealed that the following linear relationship provides a quite reliable description of the propagation process for the site of interest:

$$H_s = c_{Hs}H_{s0} \qquad (16)$$

where c_{Hs} is the empirical coefficient estimated through the application of the least squares method, which is equal to 0.70, with lower and upper 95% CB equal to 0.69 and 0.72, respectively. The coefficient of determination of the fitted formula is $R^2 = 0.87$. As regards the mean wave period, it was found that T_m at the
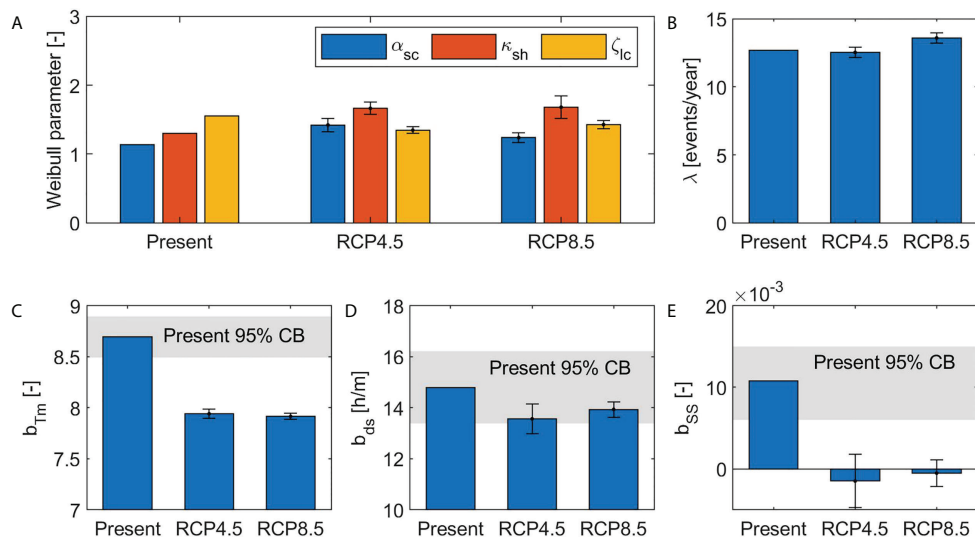
FIGURE 5
Characterization of the local extreme wave climate under present and future scenarios: **(A)** scale (a_{sc}), shape (κ_{sh}) and location (ζ_{lc}) parameters of the Weibull distribution of extreme H_{s0}; **(B)** mean number of sea storms per year; **(C)** coefficient of the site-specific empirical relationship between significant wave height and mean wave period; **(D)** coefficient of the site-specific empirical relationship between significant wave height and sea storm duration; **(E)** coefficient of the site-specific empirical parameter of the relationship between significant wave height and storm surge height. The mean (bar value) and standard deviation (vertical error bars) were calculated with reference to the 14 future sub-periods of each future scenario.
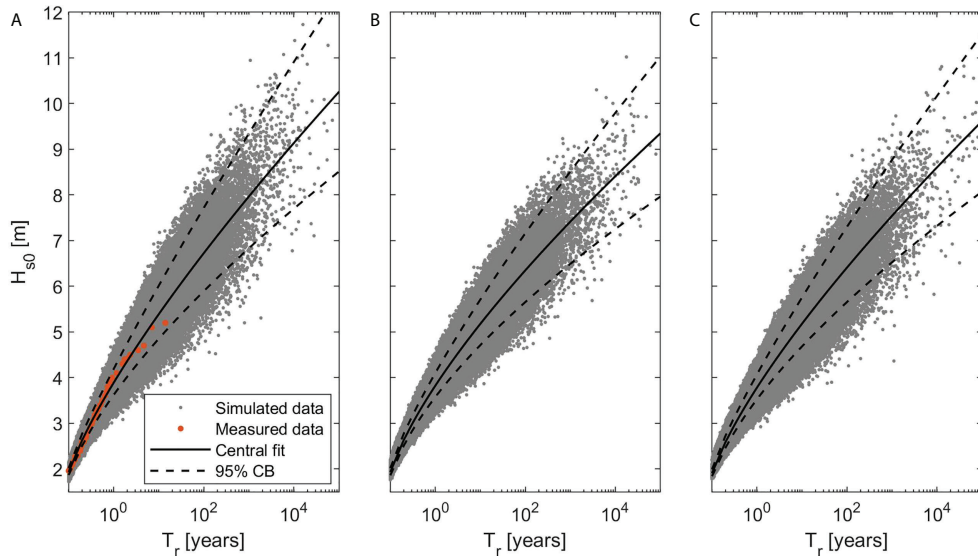
FIGURE 6

Central fit and 95% confidence bounds of the Weibull distribution of extreme offshore significant wave height for the site of Catania: **(A)** present (1989-2005); **(B)** sub-period 2084-2100 under RCP4.5 scenario; **(C)** sub-period 2053-2069 under RCP8.5 scenario.

breakwater site can be assumed equal to T_{m0}, with R^2 of the fitted regression model equal to 0.98. The above-described simplified formulation for wave propagation is justified by the very mild slope of the bathymetry of the site of interest, and also by the quite high depth at the toe of the structure (i.e. between 16.50 and 19.00 m under MSL, with 100-year return period dispersion parameter $k_d h$ between 0.50 and 0.60). Under the hypothesis of no modification of the local bathymetry, the site-specific wave propagation relationships were employed for both present and future scenarios. The breaking conditions were checked at the breakwater site through the application of criteria proposed by Kamphuis (1991) and Goda (2009).

More details about the extreme value distributions of H_{s0} and the fitted site-specific empirical relationships between climate variables are provided in the Supplementary Material.

2.4.4 Monte Carlo simulations

The simplified fault tree represented in Figure 7 was considered. For ULS, the collapse of the armor layer was analyzed, considering the case of addition of an extra armor layer over the existing one (i.e. configurations AS, AD, CM and CS). Instead, for SLS, the excessive mean overtopping discharge was studied for the existing structure (i.e. configuration E) and the solution with both raise of the wave wall and addition of extra armor unit (i.e. configuration CS). The proposed methodology for the calculation of the failure probability (see section 2.2) was applied to section n. 40 of the Catania harbor breakwater, which is the most exposed one to the wave motion (see Figure 2B).

For each considered limit state, MC simulations were performed to assess the failure probability during lifetime, considering the present climate (1989-2005) and the future scenarios RCP4.5 (2071-2100) and RCP8.5 (2041-2070). Both the state of art formulas and the ones adapted to the experimental and numerical data were considered (see section 2.4.2), in order to compare the results and assess the effect of using specific design formulations. For the ULS, the following reliability function was derived by writing equation 11 in accordance with the format of equation 3:

$$Z_1 = f_c \times \left(6.7 \frac{N_{od}^{0.4}}{N_w^{0.3}} + 1 \right) \times \Delta D_{n50} - H_s \times \left(\frac{2\pi H_s}{gT_m^2} \right)^{0.1} \quad (17)$$

where the number of incident waves N_w is calculated as the ratio between the sea storm duration expressed in seconds and the mean wave period, i.e. $(3600\ d_s)/T_m$. The coefficient f_c, D_{n50} and Δ are assumed to follow a normal distribution (van der Meer, 1988b; Burcharth, 1992), whose mean (m) and standard deviation (σ) are reported in Table 1. The normal distributions of D_{n50} and Δ ere truncated, in order to avoid the unrealistic values during the random generation process. Therefore, such distributions were characterized also through the parameter k which allows the calculation of the lower (l) and upper (u) truncation limits:

$$l = m - k\sigma$$
$$u = m + k\sigma \quad (18)$$

The damage parameter N_{od} as set equal to 2.00, which is the damage limit correspondent to the collapse of the outer armor
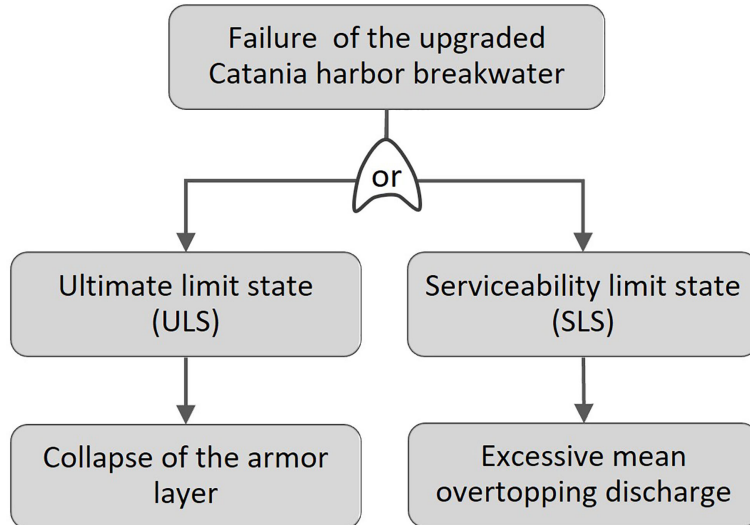
FIGURE 7
Fault tree for the upgraded Catania harbor breakwater.

layer (CIRIA et al., 2007). For the SLS, the following reliability function was derived by writing equation 12 in accordance with the format of equation 3:

$$Z_2 = q - \sqrt{gH_s^3} \times a_E \times exp\left[-\left(b_E \times \frac{R_c}{H_s \gamma_f}\right)^{1.3}\right] \quad (19)$$

where $R_c = h_{wall} - (h+h_{ss})$. The parameter h_{wall} which is the height of the wave wall measured with respect to the toe of the structure, follows a normal distribution (Lara et al., 2019) that was truncated to avoid the random generation of unrealistic values. The coefficients a_E and b_E are assumed normally distributed. Table 1 reports the characteristics of the above mentioned normal distributions. The limit q was set equal to 5×10^3 m³/s m, which is the the acceptable mean overtopping discharge to ensure safety for larger yachts (EurOtop, 2018).

According the indications of ROM 1.0-09 (2010), the structure useful life was set equal to 50 years, and $P_{f,Lmax}$ for both ULS and SLS was assumed equal to 10^{-1}. The number of generated life cycles (N_r) for each MC simulation, which was defined through the analysis of the convergence of $P_{f,L}$ was 2.25×10^4, and the obtained CV were in the range 0.02÷0.35 (see Supplementary Material for more details). Since the rounded λ is equal to 13 events/year for the present climate (see section 2.4.3), according to equation 7, 650 random sea storms were generated for each of the 50 simulated life cycles under present climate, thus obtaining a total of 1.46×10^7 sea storms. As regards the future sub-periods, λ ranges between 12÷14 events/year (see section 2.4.3), and hence 600÷700 random H_{s0} were generated for each of the 50 simulated life cycles. Therefore, for each future

sub-period a total of $1.35 \div 1.58 \times 10^7$ sea storms were generated. For instance, Figure 6 shows the point clouds of the simulated H_{s0} as a function of the return period, considering the present climate and two representative future sub-periods under RCP4.5 and RCP8.5 scenarios, together with the corresponding Weibull distributions used for the random generation.

3 Results and discussion

3.1 Marine climate

The extreme wave climate and sea levels characteristic of the site of Catania under present and future climate (see section 2.4.3) were analyzed and compared, in order to acquire preliminary information useful for the interpretation of the final outcomes obtained through the application of the proposed methodology for the quantitative assessment of the performances of upgraded rubble-mound breakwaters under a changing climate.

As regards the extreme significant wave height, Figure 5A shows that the Weibull distributions of extreme H_{s0} calculated for the future sub-periods are characterized by higher a_{sc} and κ_{sh} than the present ones, but lower ζ_{lc}. As a consequence, future extreme H_{s0} lower than the present ones are expected for the site of interest, in agreement with the findings of both global (Hemer et al., 2013; Camus et al., 2017; IPCC, 2019; Morim et al., 2019) and regional (Lionello et al., 2008) existing studies. Instead, the frequency of occurrence of extreme events is not expected to suffer significant modifications in the future. Indeed, the data reported in Figure 5B shows that the maximum variations of λ are equal to ± 1 event/year.

The expected future decrease of extreme H_{s0} involves that also T_{m0}, d_s and h_{ss} are likely to decrease under the RCP4.5 and RCP8.5 scenarios. Indeed, according to equations 13-15, such variables are directly correlated to H_{s0}. Moreover, as showed in Figure 5C, the empirical coefficient of the site-specific relationship between H_{s0} and T_{m0}, namely b_{Tm}, assumes values slightly lower than the present one, by 0.09 times on average, thus increasing the reduction of the future T_{m0} due to the expected lower H_{s0}. Figure 5E reveals also that the future values of coefficient of the site-specific relationship between H_{s0} and h_{ss}, namely b_{ss}, are lower then the present one, by 1.09 times on average. Therefore, future h_{ss} is expected to be lower than the present one not only because of the decrease of H_{s0}, but also because of the lower projected $b_{ss.}$ As regards the coefficient of the site-specific relationship between H_{s0} and d_s, namely b_{ds}, no significant differences between present and future were found. Indeed, the future values vary within the 95% CB if the present estimate of b_{ds} (see Figure 5D).

Besides the variations of extreme wave climate, also mean sea level rise, which for the site of Catania is expected to reach values up to 0.42 m (see section 2.4.3), significantly affects the hydraulic performances of rubble-mound breakwaters, especially in the presence of depth-limited wave conditions. For the present case study, the failure probability due to the collapse of the outer armor layer (ULS) is influenced only by the projected reduction of extreme sea storm energy (see equation 17), whereas the failure probability due to excessive mean overtopping discharge depends on the combined effect of the expected less energetic wave climate and increased mean sea level (see equation 19).

3.2 Collapase of the outer armor layer (ULS)

The acceptability of the stability performances of the additional armor layer of the upgraded Catania harbor breakwater during lifetime is evaluated using the index r (see equation 8). Figure 8A shows the calculated r for each upgrading solution, considering both the traditional and site-specific reliability functions (i.e. vdM, SS and NSS). The displayed results refer to the present climate and to the sub-period with the highest $P_{f,L}$ of each future scenario, namely 2084-2100 under RCP4.5 and 2053-2069 under RCP8.5. The standard deviation of r, calculated by dividing $\sigma_{Pf,L}$ by $P_{f,Lmax}$, is represented by the vertical error bars and ranges between 0.001÷0.025, being directly proportional to $P_{f,L}$(see equation 5) and r.

The index r calculated with the traditional and site-specific reliability functions is always smaller than one, which means that despite of the weight of the additional armor units (i.e. 62 t cubes or 30 t Antifer), all the upgraded configurations satisfy the design requirements, under both present and future climate. The results reveal that the future r is in general lower than the

present one, for both the considered scenarios. In particular, the lowest values of r were found for the end of century under RCP4.5 scenario. Figure 9A shows that the percentage difference between future and present r (i.e. 100 $(r_{fut}$-$r_{pres})$/r_{pres}) ranges between -72% and -6%. The quantitative comparison between present and future r demonstrates that all the considered upgrading options, which ensure acceptable performances under the present climate, are adequate also in the presence of the effects of climate change. Therefore, the cost-benefit analysis for the choice of the optimal solution will not be affected by the expected impacts of global warming on the considered structure. Such findings are consistent with the outcomes presented in section 3.1, and in particular with the fact that for the future lower. H_s are expected for the site of Catania. Indeed, the analysis of Z_1, expressed as a function of the only H_s by using equations 13-14, revealed that its first-order derivative with respect to H_s is always negative, thus implying that to lower values of H_s correspond higher Z_1. Anyway, the differences between present and future r are quite contained, and the order of magnitude of r does not change.

Figure 8A also shows that the values of evaluated for the upgrading solutions which consist in the addition of 30 t Antifer blocks, are higher than the ones calculated for the upgrading options which consist in the addition of 62 t cubic units, by 16 ÷ 24 times on average times when using the vdM formula, and by 3 ÷ 11 and 14 ÷ 22 for the SS and NSS formulas, respectively. Therefore, as expected, the doubling of the weight of the extra armor blocks involves a significant reduction of the probability of collapse of the outer armor layer. The use of the traditional or site-specific reliability functions produces substantial differences between the resulting r. Indeed, the vdM formula is far more conservative, giving r greater than the ones calculated with the SS and NSS formulations, by 34 and 8 times on average, respectively. Such a result indicates that the use of the traditional vdM formula would lead to a solution with a larger safety margin. Reasonably, r calculated for the case of additional armor blocks in direct contact with the toe berm (i.e. SS) is always smaller than the one evaluated in the case of absence of such direct contact (i.e. NSS), by a factor of 62% on average.

The rate of the growth of the failure probability during lifetime is displayed in Figure 8B, with reference to the present climate and the future sub-periods 2084-2100 under RCP4.5 and 2053-2069 under RCP8.5. The index s behaves similarly to r. Indeed, as showed in Figure 9B, the future s values are always lower than the corresponding present ones, and the percentage difference between future and present s (i.e.100 $(s_{fut}$-$r_{pres})$/r_{pres}) ranges between -63% and -8%. Figure 8B also shows that the upgrading solutions with additional 30 t Antifer units are characterized by higher s than the ones calculated for the solutions with extra 62 t cubes, by a factor of 19÷32, 4÷8 and 16÷17 when using the vdM, SS and NSS formulas, respectively. Moreover, the application of the vdM formula gives s greater by 49 and 9 times on average than the SS and NSS formulations,
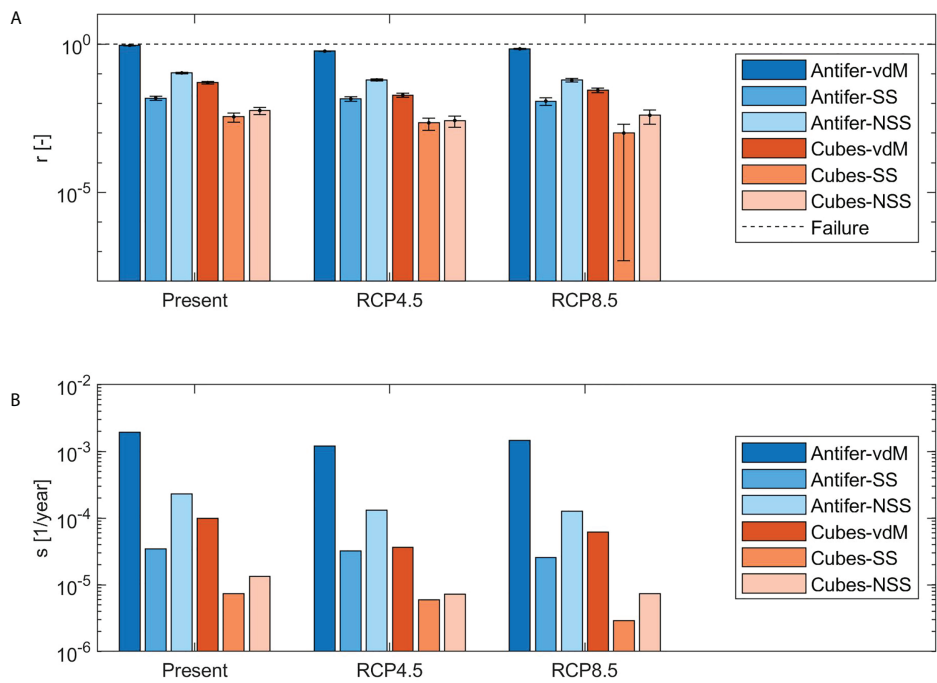
FIGURE 8
Indexes of the failure probability during lifetime due to the collapse of the outer armor layer, calculated for the present period (1989-2005) and the future sub-periods characterized by the highest $P_{f,L}$, i.e. 2084-2100 under RCP4.5 and 2053-2069 under RCP8.5: **(A)** ratio between $P_{f,L}$ and the acceptance limit (the vertical error bars represent the MC standard deviation); **(B)** rate of the growth of the failure probability during lifetime.

respectively. The best performances of the the additional armor layer in direct contact with the toe berm are confirmed. Indeed, s calculated with the SS formulation is on average 61% lower than s calculated with the NSS equation. The assessment of s of various upgrading options under different climate scenarios is fundamental for the design of maintenance plan able to ensure sufficient stability of the structure during lifetime. Indeed, if limit values of $P_{f,L}$ are fixed and s is known, the appropriate times to implement repair interventions can be calculated.

The variability of $P_{f,L}$ due to the use of a moving time window for the analysis of the future periods (i.e. 2071-2100 under RCP4.5 scenario and 2041-2070 under RCP8.5 scenario) is quantified by the coefficient of variation v (see equation 9). Figure 10 reveals that for both future scenarios, the highest values of v correspond to configurations characterized by the lowest r, namely the upgrading solutions with additional armor layer made up by 62 t cubes. Such a result is in accordance with the fact that in such cases v is most affected by the uncertainty of the MC simulations, which corresponds to higher $\sigma_{Pf,L}$, and hence greater CV. When considering the end of the century under RCP4.5 scenario, v assumes values between 0.38 and 0.88, thus indicating a low variability condition. Instead, the values of v calculated for the mid of the century under RCP8.5 range between 0.84 and 2.27, being always greater than the corresponding values for the end of the century under RCP4.5

scenario. When v is higher than one, which indicates the high variability of $P_{f,L}$, special attention should be paid to the flexibility of maintenance interventions during the planning processes. Indeed, design strategies that are reversible and flexible must be selected to keep the cost of being wrong about future climate change as low as possible (Hallegatte, 2009).

3.3 Excessive mean overtopping discharge (SLS)

The acceptability of the hydraulic performances of the existing and upgraded Catania harbor breakwater was also assessed, considering the SLS due to excessive mean overtopping discharge. Figure 11A shows the index r (see equation 8), which was calculated for the existing structure (i.e. configuration E) and for the upgrading solution with additional 62 t cubes over the regularized armor layer and further raised wave wall (i.e. configuration CS), considering both the traditional and site-specific formulas (i.e. EurOtop and empirical-numerical formulas). As for the failure probability due to the collapse of the outer armor layer (see section 5.2), the displayed values of r refer to the present climate and to the sub-period with the highest $P_{f,L}$ of each future scenario, namely 2084-2100 under RCP4.5 and 2053-2069
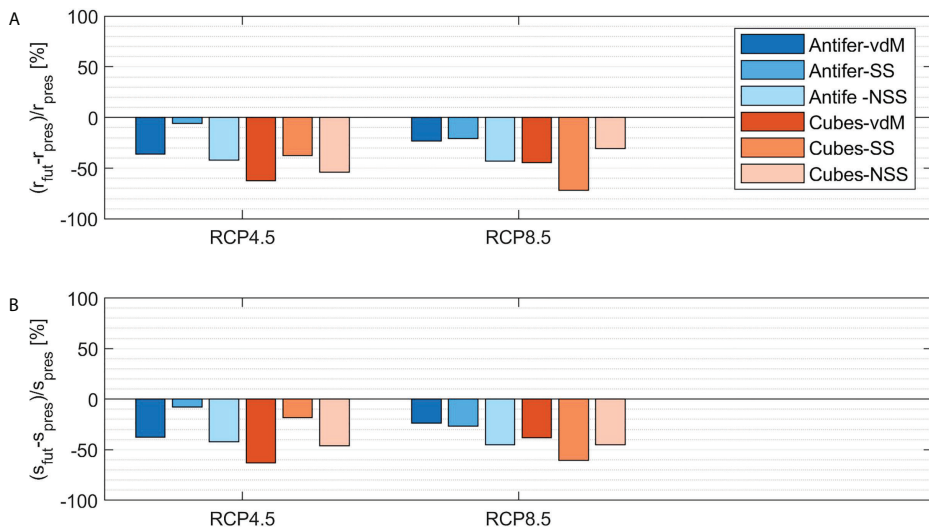
FIGURE 9
Comparison between the indexes of the failure probability due to the collapse of the outer armor layer, calculated for the present period (1989-2005) and the future sub-periods characterized by the highest $P_{f,L}$, i.e. 2084-2100 under RCP4.5 and 2053-2069 under RCP8.5: **(A)** ratio between $P_{f,L}$ and the acceptance limit; **(B)** rate of the growth of the failure probability during lifetime.

under RCP8.5. The standard deviation of r derived from $\sigma_{Pf,L}$ (see equation 5), which is indicated by the vertical error bars, varies in the range 0.004÷0.019.

The calculated r is always smaller than one, despite of the considered structure configuration (i.e. E or CS) and reliability function, under both present and future climate. Therefore, since the SLS is never reached and the design requirements are always satisfied, the upgrade could be not necessary when considering only the response of the breakwater in terms of mean overtopping discharge. However, configuration E ensures r very close to failure threshold, being r in the range 0.20÷0.94 depending on the employed formulation. The upgrading solution CS produces the reduction of r by about 0.77 and 0.94 times, employing the traditional and site-specific reliability function, respectively. As expected, the addition of extra units over the existing armor layer and the heightening of the wave wall involve a significant reduction of the probability of occurrence of excessive mean overtopping rates. The comparison between the obtained results for the present, RCP4.5 and RCP8.5 scenarios displayed in Figure 11A reveals that the future r is in general lower than the present one. As showed in Figure 12A, the percentage difference between future and present r ranges between -50% and -14%, with the highest reduction of r corresponding to the end of the century under RCP4.5 scenario. Therefore, both the existing and upgraded structure provide sufficient performances in the presence of the effects of climate change.

Such an outcome is consistent with the fact that lower H_s and h_{ss} are expected for the site of Catania (see section 3.1), but it may appear in contrast with the projected SLR without a

thorough analysis of the influence of each climate variable of equation 19. Figure 13 shows the comparison between $\partial Z_2/\partial H_s$ and $\partial Z_2/\partial H_c$, evaluated for a set of possible H_s and R_c. $\partial Z_2/\partial H_s$ is negative, and its absolute value is higher than the positive $\partial Z_2/\partial H_c$, for each considered couple H_s-R_c. Therefore, the increase of Z_2 due to decreasing H_s occurs at a greater rate than the decrease of Z_2 due to decreasing R_c, and vice versa. In order to make clear such a finding, in Figure 13 the case of H_s equal to 6.00 m and R_c equal to 8.50 m above mean sea level is highlighted. Following the above explanation, the fact that future r is lower than the present one is reasonable. Indeed, the reliability function Z_2 suffers most the effect of slightly lower H_s than the influence of higher R_c caused by SLR. Anyway, the differences between present and future probability of failure are modest. Indeed, the order of magnitude of r does not change.

The use of the EurOtop formula or of its adaptation to the numerical data produces differences between the resulting r. Indeed, the empirical-numerical formula is more conservative for configuration E, giving r greater by about 0.66 times than the traditional one. On the contrary, the empirical-numerical formula is less conservative for configuration CS, giving smaller r by about 0.36 times than the traditional one. Hence, in the latter case the lack of specific formulation does not imply the design of a not sufficiently performing structure. However, the differences between r evaluated through the traditional and adapted formula for mean overtopping discharge are modest with respect to the discrepancies observed for the armor layer stability, by two orders of magnitude (see section 3.2).

Figure 11B shows the growth of the failure probability during the structure lifetime, calculated for the present climate
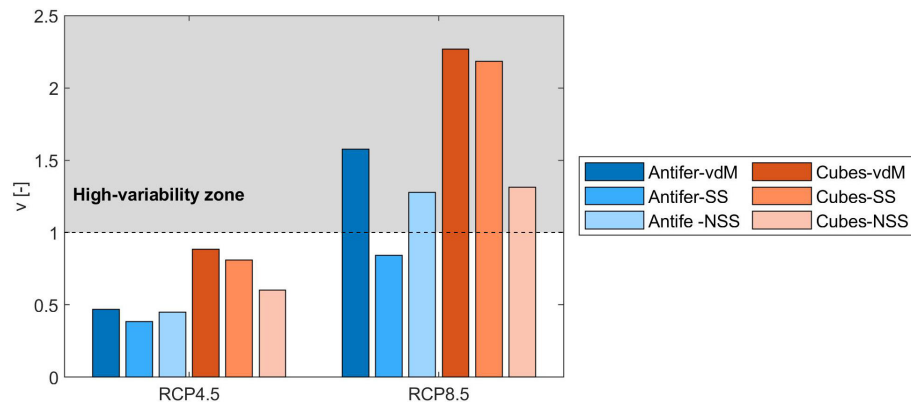
FIGURE 10
Coefficient of variation of the failure probability during lifetime due to the collapse of the outer armor layer, calculated with reference to the fourteen sub-periods of RCP4.5 and RCP8.5 future scenarios.

and the future sub-periods 2084-2100 under RCP4.5 and 2053-2069 under RCP8.5. As already observed for the ULS related to the collapse of the outer armor layer, the index s behaves similarly to r. Indeed, as showed in Figure 12B, the percentage difference between future and present s ranges between -49% and -11%. Configuration CS is characterized by lower s than the ones calculated for configuration E, on average by a factor of 0.77 and 0.94 when using the traditional and site-specific reliability function, respectively. Furthermore, for configuration E the empirical-numerical formula provides s higher than the EurOtop one, by about 0.66 times. On the contrary, for configuration CS the site-specific formula gives s lower than the traditional one, by about 0.39 times. The knowledge of s corresponding to the considered upgrading options under different climate scenarios allows the definition of maintenance plan able to ensure adequate hydraulic performances during the whole structure lifetime.

As for the ULS due to the collapse of the outer armor layer, the variability of future $P_{f,L}$ during the periods 2071-2100 under RCP4.5 scenario and 2041-2070 under RCP8.5 scenario is quantified using the coefficient of variation v (see equation 9). In accordance with the findings discussed in section 3.2, Figure 14 shows that for both future scenarios the highest values of v correspond to the upgraded configuration CS, which is characterized by the lowest r. The values of coefficient of variation calculated for the mid of the century under RCP8.5 scenario are greater than the corresponding values for the end of the century under RCP4.5 scenario. In particular, v of RCP4.5 scenario assumes values in the range 0.57÷1.00. Therefore, $P_{f,L}$ is characterized by low variability for all the tested cases under RCP4.5 scenario. On the contrary, v of RCP8.5 scenario ranges between 2.03 and 2.36, thus indicating the high variability of $P_{f,L}$, and hence the necessity to design reversible and flexible

maintenance plan to ensure the best compromise between performances and costs.

4 Conclusion

The effects of climate change on coastal areas produce the increase of risk for port integrity, thus implying the need for upgrade exiting harbor breakwater. In this context, the present work proposes a methodology for the assessment of the impact of climate change on the performances of upgraded rubble-mound structures, based on the calculation of the failure probability during lifetime due to independent failure modes. The limits of existing design methodologies are overcome, which are mainly linked to the rough inclusion of expected future climate variations and to the lack of quantitative indexes for the comparison between the results.

The probability that the structure reaches a certain ULS or SLS during the lifetime is calculated through the MC simulation technique. After simulating a certain number of structure random life cycles, the failure probability during lifetime is defined as the ratio between the number of life cycles with at least one failure and the total number of realizations of the MC simulation. The failure occurs when the reliability function describing the failure mode assumes negative values. Such a function is derived from traditional or site-specific empirical relationships between hydrodynamic, geometry and material variables, which are all described by probability density functions derived from state of art or from adaptation to the available data. The probability distribution of extreme significant wave height identified through the POT method is calculated using the MME adaptation method, whose combination with the *FoC* method allows the inclusion of the effects of projected
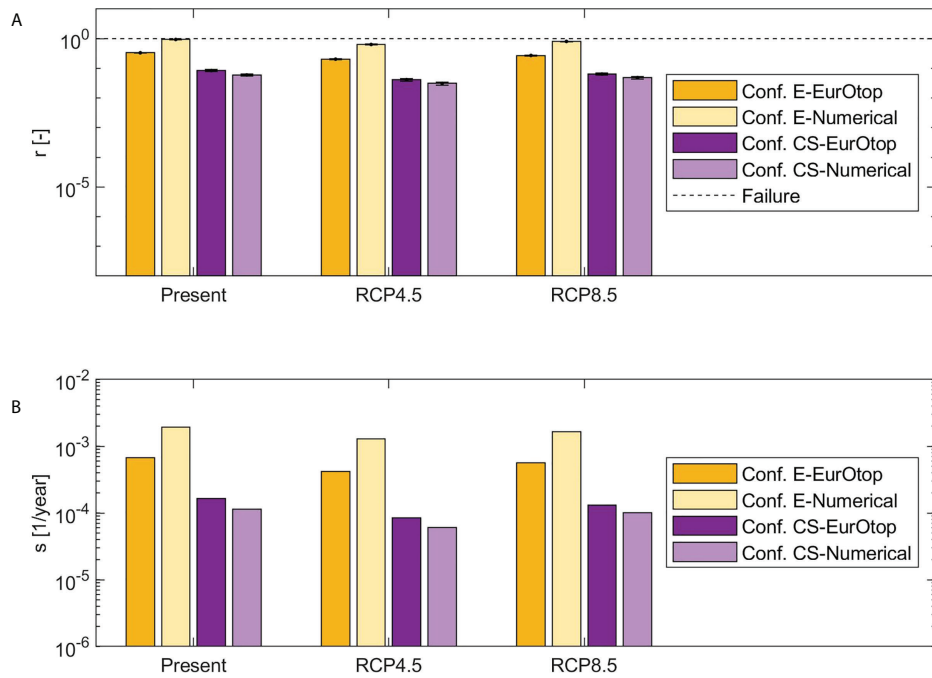
FIGURE 11
Indexes of the failure probability during lifetime due to excessive wave overtopping, calculated for the present period (1989-2005) and the future sub-periods characterized by the highest $P_{f,L}$ i.e. 2084-2100 under RCP4.5 and 2053-2069 under RCP8.5: **(A)** ratio between $P_{f,L}$ and the acceptance limit (the vertical error bars represent the MC standard deviation); **(B)** rate of the growth of the failure probability during lifetime.
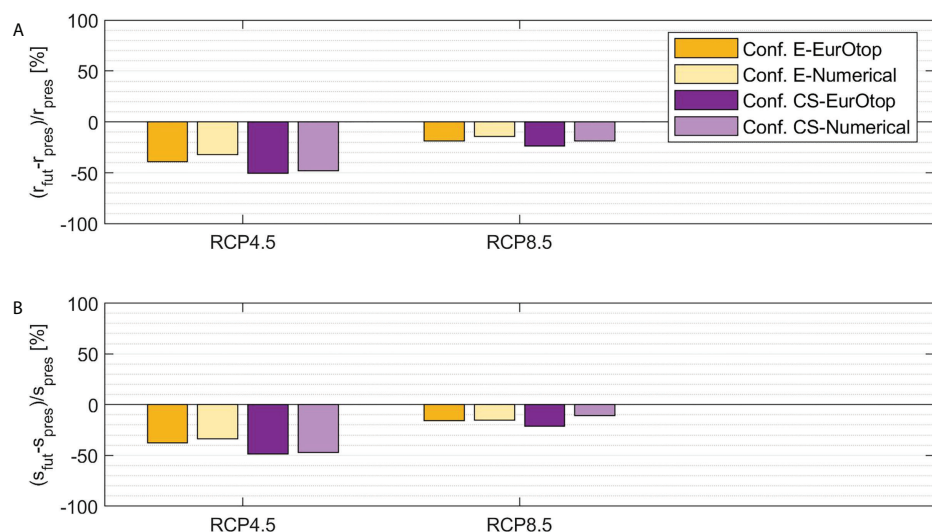
FIGURE 12
Comparison between the indexes of the failure probability due to excessive wave overtopping, calculated for the present period (1989-2005) and the future sub-periods characterized by the highest $P_{f,L}$, i.e. 2084-2100 under RCP4.5 and 2053-2069 under RCP8.5: **(A)** ratio between $P_{f,L}$ and the acceptance limit; **(B)** rate of the growth of the failure probability during lifetime.
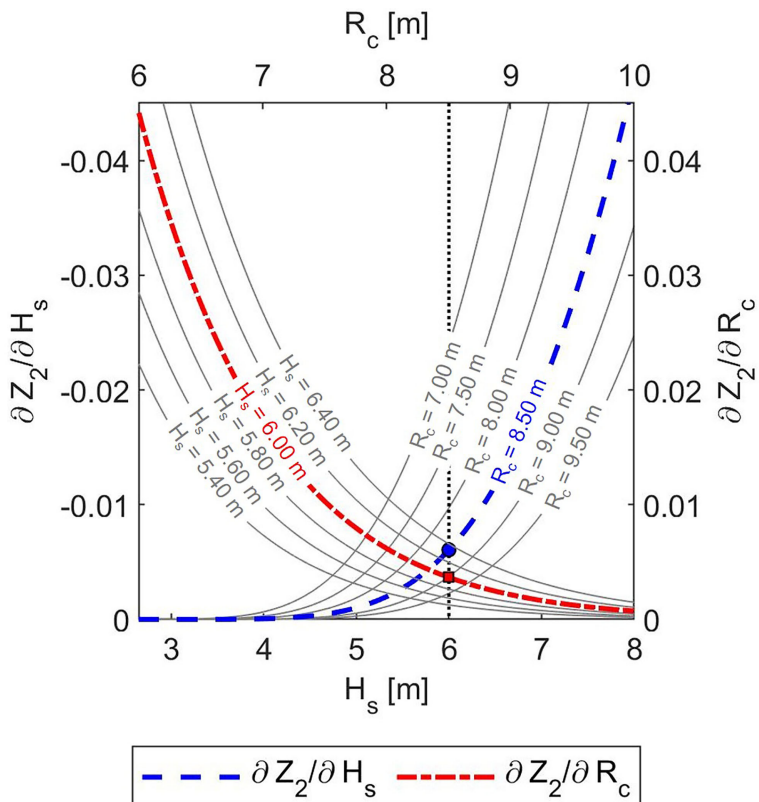
FIGURE 13

Comparison between the first-order partial derivatives of the reliability function Z_2 for excessive wave overtopping discharge, evaluated considering a_E and b_E suggested by (EurOtop, 2018) and a set of H_s and R_c. The circle and the square indicate the first-order partial derivatives of Z_2 in the case of $H_s = 6.00$ m and $R_c = 8.50$ m.

climate change (Kilsby et al., 2007; Fatichi et al., 2011; Peres and Cancelliere, 2018). Moreover, the correlations between wave climate descriptors are modeled by site-specific empirical relationships, calibrated for both the present and future scenarios. Once the failure probabilities have been assessed, the following three index are calculated to enable the quantitative comparison between present and future climate scenarios, and also between different configurations of the structure: i) r is the ratio between the calculated and the maximum acceptable failure probability during lifetime, which assumes values greater (smaller) than one if the failure occurs (does not occur); ii) s, whose unit of measure is 1/year, represents the rate of the growth of the failure probability along the lifetime; iii) v is a measure of the dispersion of the obtained failure probabilities due to the combination of the uncertainty due to MC convergence and the variability of future climate.

The proposed methodology was applied considering the failure probability due to the collapse of the outer armor layer (ULS) or to excessive mean overtopping discharge (SLS) during lifetime of different upgraded configurations of the Catania

harbor breakwater (Italy). The index r calculated with the traditional and site-specific reliability functions under present climate is always smaller than one, thus indicating acceptable structural and hydraulic performances for all the tested configurations. In accordance with the climate projections for the site of interest (Caires and Yan, 2020; Yan et al., 2020), lower r and s were calculated for both ULS and SLS under RCP4.5 and RCP8.5 scenarios, although their order of magnitude does not change. The variation of $P_{f,L}$ due to future climate variability was quantitatively assessed through the index v, which assumes values equal or greater than one for highly dispersed data. The maximum values of v were found under RCP8.5 scenarios, for those configurations characterized by the lowest failure probabilities.

The obtained results demonstrate that the proposed methodology is able to give useful quantitative information to optimize both design and decision-making processes of upgrading solutions for harbor breakwater under the effects of climate change. Indeed, the index r is measure of the adequacy of upgrading options to withstand future external forcing. Moreover, the knowledge of s for different climate scenarios gives useful information for the
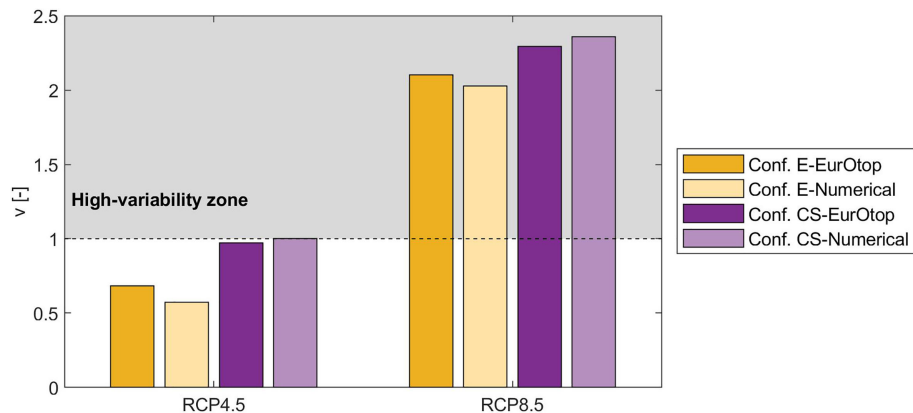
FIGURE 14
Coefficient of variation of the failure probability during lifetime due to excessive wave overtopping, calculated with reference to the fourteen sub-periods of RCP4.5 and RCP8.5 future scenarios.

design of maintenance plan based on the calculation of the appropriate times to implement repair interventions during the structure lifetime. Finally, the outcomes of the analysis of the index ν allow the identification of the upgrading options whose $P_{f,L}$ presents high variability under the considered future scenarios. In such cases, highly flexible maintenance plan should be designed, in order to reach an optimal compromise between structure performances and costs. Future research should focus on the inclusion of the structural modifications of the breakwater due to deterioration processes and/or maintenance interventions, which clearly influence the growth of the failure probability during lifetime.

Data availability statement

The raw data supporting the conclusions of this article will be made available by the authors, without undue reservation.

Author contributions

JL, RM and EF contributed to conception and design of the study. MS organized the database, performed the probabilistic analysis and wrote the first draft of the manuscript. All authors contributed to manuscript revision, read, and approved the submitted version.

Funding

Acknowledgments

Conflict of interest

The authors declare that the research was conducted in the absence of any commercial or financial relationships that could be construed as a potential conflict of interest.

Publisher's note

All claims expressed in this article are solely those of the authors and do not necessarily represent those of their affiliated organizations, or those of the publisher, the editors and the reviewers. Any product that may be evaluated in this article, or claim that may be made by its manufacturer, is not guaranteed or endorsed by the publisher.

Supplementary material

The Supplementary Material for this article can be found online at: https://www.frontiersin.org/articles/10.3389/fmars.2022.986993/full#supplementary-material

References

Arns, A., Dangendorf, S., Jensen, J., Talke, S., Bender, J., and Pattiaratchi, C. (2017). Sea-Level rise induced amplification of coastal protection design heights. *Sci. Rep.* 7, 40171. doi: 10.1038/srep40171

Boccotti, P. (2004). *Idraulica marittima* (Turin, Italy: UTET Università).

Booij, N. R. R. C., Ris, R. C., and Holthuijsen, L. H. (1999). A third-generation wave model for coastal regions: 1. model description and validation. *J. geophysical research: Oceans* 104, 7649–7666.

Burcharth, H. F. (1987). *The lessons from recent breakwater failures. in developments in breakwater design* (Vancouver: World Federation of Engineering Organizations Technical Congress). doi: 10.1029/98JC02622

Burcharth, H. F. (1992). "Introduction of partial coefficients in the design of rubble mound breakwaters," in *Coastal structures and breakwaters* (London, England: Thomas Telford), 543–566.

Burcharth, H. F. (1993). "Reliability evaluation and probabilistic design of coastal structures," in *International seminar on hydro-technical engineering for future development of ports and harbors* (Un'yushō Kōwan Gijutsu Kenkyūjo).

Burcharth, H. F., Andersen, T. L., and Lara, J. L. (2014). Upgrade of coastal defence structures against increased loadings caused by climate change: A first methodological approach. *Coast. Eng.* 87, 112–121. doi: 10.1016/j.coastaleng.2013.12.006

Burcharth, H. F., and Sørensen, J. D. (1999). "Design of vertical wall caisson breakwaters using partial safety factors," in *Coastal Engineering: Proceedings of the 26th Conference on Coastal Engineering*, (Reston, VA, US: American Society of Civil Engineers). 2138–2151.

Caires, S., and Yan, K. (2020). Ocean surface wave time series for the European coast from 1976 to 2100 derived from climate projections, (for [extracted period], [experiment], etc). *Copernicus Climate Change Service (C3S) Climate Data Store (CDS)*. doi: 10.24381/cds.572bf382

Camus, P., Losada, I., Izaguirre, C., Espejo, A., Menéndez, M., and Pérez, J. (2017). Statistical wave climate projections for coastal impact assessments. *Earth's Future* 5, 918–933. doi: 10.1002/2017EF000609

Camus, P., Tomás, A., Díaz-Hernández, G., Rodríguez, B., Izaguirre, C., and Losada, I. (2019). Probabilistic assessment of port operation downtimes under climate change. *Coast. Eng.* 147, 12–24. doi: 10.1016/j.coastaleng.2019.01.007

Castillo, E., Losada, M. A., Mínguez, R., Castillo, C., and Baquerizo, A. (2004). Optimal engineering design method that combines safety factors and failure probabilities: Application to rubble-mound breakwaters. *J. waterway port coastal ocean Eng.* 130, 77–88. doi: 10.1061/(ASCE)0733-950X(2004)130:2(77)

Castillo, C., Mínguez, R., Castillo, E., and Losada, M. A. (2006). An optimal engineering design method with failure rate constraints and sensitivity analysis. Application to composite breakwaters. *Coast. Eng.* 53, 1–25. doi: 10.1016/j.coastaleng.2005.09.016

Chini, N., and Stansby, P. (2012). Extreme values of coastal wave overtopping accounting for climate change and sea level rise. *Coast. Eng.* 65, 27–37. doi: 10.1016/j.coastaleng.2012.02.009

Church, J. A., Clark, P. U., Cazenave, A., Gregory, J. M., Jevrejeva, S., Levermann, A., et al. (2013). "Sea Level change," in *Tech. rep* (Cambridge, England: PM Cambridge University Press).

CIAD project group (1985). "Final report CIAD project group. breakwaters. computer aided evaluation of the reliability of a breakwater design," in *Tech. rep* (Zoetermeer, the Netherlands: CIAD Association).

CIRIA, CUR and CETMEF (2007). *The rock manual: the use of rock in hydraulic engineering. 2nd edition* Vol. c683 (London, England:C683, CIRIA).

Davies, G., Callaghan, D. P., Gravois, U., Jiang, W., Hanslow, D., Nichol, S., et al. (2017). Improved treatment of non-stationary conditions and uncertainties in probabilistic models of storm wave climate. *Coast. Eng.* 127, 1–19. doi: 10.1016/j.coastaleng.2017.06.005

Di Lauro, E., Lara, J. L., Maza, M., Losada, I. J., Contestabile, P., and Vicinanza, D. (2019). Stability analysis of a non-conventional breakwater for wave energy conversion. *Coast. Eng.* 145, 36–52. doi: 10.1016/j.coastaleng.2018.12.008

EurOtop. (2018). *Manual on wave overtopping of sea defences and related structures. An overtopping manual largely based on European research, but for worldwide application*. J. W. Van der Meer, N. W. H. Allsop, T. Bruce, J. De Rouck, A. Kortenhaus, T. Pullen, et al. www.overtopping-manual.com.

Faraci, C., Scandura, P., and Foti, E. (2015). Reflection of sea waves by combined caissons. *J. Waterway Port Coastal Ocean Eng.* 141, 04014036. doi: 10.1061/(ASCE) WW.1943-5460.0000275

Fatichi, S., Ivanov, V. Y., and Caporali, E. (2011). Simulation of future climate scenarios with a weather generator. *Adv. Water Resour.* 34, 448–467. doi: 10.1016/j.advwatres.2010.12.013

Foti, E., Musumeci, R. E., and Stagnitti, M. (2020). Coastal defence techniques and climate change: A review. *Rendiconti Lincei. Sci. Fisiche e Naturali* 31, 123–138. doi: 10.1007/s12210-020-00877-y

Franco, L. (1994). Vertical breakwaters: the italian experience. *Coast. Eng.* 22, 31–55. doi: 10.1016/0378-3839(94)90047-7

Galassi, G., and Spada, G. (2014). Sea-Level rise in the mediterranean sea by 2050: Roles of terrestrial ice melt, steric effects and glacial isostatic adjustment. *Global Planetary Change* 123, 55–66. doi: 10.1016/j.gloplacha.2014.10.007

Galiatsatou, P., Makris, C., and Prinos, P. (2018). Optimized reliability based upgrading of rubble mound breakwaters in a changing climate. *J. Mar. Sci. Eng.* 6, 92. doi: 10.3390/jmse6030092

Goda, Y. (2009). A performance test of nearshore wave height prediction with clash datasets. *Coast. Eng.* 56, 220–229. doi: 10.1016/j.coastaleng.2008.07.003

Guanche, R., Iturrioz, A., and Losada, I. J. (2015). Hybrid modeling of pore pressure damping in rubble mound breakwaters. *Coast. Eng.* 99, 82–95. doi: 10.1016/j.coastaleng.2015.02.001

Guanche, R., Losada, I. J., and Lara, J. L. (2009). Numerical analysis of wave loads for coastal structure stability. *Coast. Eng.* 56, 543–558. doi: 10.1016/j.coastaleng.2008.11.003

Hallegatte, S. (2009). Strategies to adapt to an uncertain climate change. *Global Environ. Change* 19, 240–247. doi: 10.1016/j.gloenvcha.2008.12.003

Hemer, M. A., Fan, Y., Mori, N., Semedo, A., and Wang, X. L. (2013). Projected changes in wave climate from a multi-model ensemble. *Nat. Climate Change* 3, 471–476. doi: 10.1038/nclimate1791

Hersbach, H., Bell, B., Berrisford, P., Horányi, A., Sabater, J. M., Nicolas, J., et al. (2019). Global reanalysis: goodbye era-interim, hello era5. *ECMWF Newsl* 159, 17–24. doi: 10.21957/vf291hehd7

Hughes, S. A. (2014). Coastal engineering challenges in a changing world. *J. Appl. Water Eng. Res.* 2, 72–80. doi: 10.1080/23249676.2014.977360

IPCC (2019). *IPCC Special Report on the Ocean and Cryosphere in a Changing Climate*. H.-O. Pörtner, D.C. Roberts, V. Masson-Delmotte, P. Zhai, M. Tignor, E. Poloczanska, et al. (eds.)

Isobe, M. (2013). Impact of global warming on coastal structures in shallow water. *Ocean Eng.* 71, 51–57. doi: 10.1016/j.oceaneng.2012.12.032

Izaguirre, C., Losada, I., Camus, P., Vigh, J., and Stenek, V. (2021). Climate change risk to global port operations. *Nat. Climate Change* 11, 14–20. doi: 10.1038/s41558-020-00937-z

Jonkman, S. N., Steenbergen, R. D. J. M., Morales-Nápoles, O., Vrouwenvelder, A. C. W. M., and Vrijling, J. K. (2015). *Probabilistic design: risk and reliability analysis in civil engineering*. (Netherlands: TU Delft, Department Hydraulic Engineering).

Kamphuis, J. (1991). Incipient wave breaking. *Coast. Eng.* 15, 185–203. doi: 10.1016/0378-3839(91)90002-X

Kamphuis, J. W. (2020). *Introduction to coastal engineering and management* Vol. 48 (Singapore: World Scientific).

Kilsby, C. G., Jones, P. D., Burton, A., Ford, A. C., Fowler, H. J., Harpham, C., et al. (2007). A daily weather generator for use in climate change studies. *Environ. Model. Software* 22, 1705–1719. doi: 10.1016/j.envsoft.2007.02.005

Kim, S.-W., and Suh, K.-D. (2006). Application of reliability design methods to donghae harbor breakwater. *Coast. Eng. J.* 48, 31–57. doi: 10.1142/S0578563406001325

Kim, S.-W., and Suh, K.-D. (2010). Reliability analysis of breakwater armor blocks: Case study in korea. *Coast. Eng. J.* 52, 331–350. doi: 10.1142/S0578563410002208

Kim, S.-W., and Suh, K.-D. (2014). Determining the stability of vertical breakwaters against sliding based on individual sliding distances during a storm. *Coast. Eng.* 94, 90–101. doi: 10.1016/j.coastaleng.2014.09.001

Korres, G., Ravdas, M., and Zacharioudaki, A. (2019). *Mediterranean Sea waves hindcast (cmems med-waves) set* (Lecce, Italy: Copernicus Monitoring Environment Marine Service (CMEMS). doi: 10.25423/CMCC/MEDSEA_HINDCAST_WAV_006_012

Laface, V., and Arena, F. (2016). A new equivalent exponential storm model for long-term statistics of ocean waves. *Coast. Eng.* 116, 133–151. doi: 10.1016/j.coastaleng.2016.06.011

Lara, J. L., Losada, I. J., and Guanche, R. (2008). Wave interaction with low-mound breakwaters using a rans model. *Ocean Eng.* 35, 1388–1400. doi: 10.1016/j.oceaneng.2008.05.006

Lara, J. L., Losada, I. J., Maza, M., and Guanche, R. (2011). Breaking solitary wave evolution over a porous underwater step. *Coast. Eng.* 58, 837–850. doi: 10.1016/j.coastaleng.2011.05.008

Lara, J. L., Lucio, D., Tomas, A., Di Paolo, B., and Losada, I. J. (2019). High-resolution time-dependent probabilistic assessment of the hydraulic performance for historic coastal structures: Application to luarca breakwater. *Philos. Trans. R. Soc. A* 377, 20190016. doi: 10.1098/rsta.2019.0016

Lionello, P., Cogo, S., Galati, M. B., and Sanna, A. (2008). The mediterranean surface wave climate inferred from future scenario simulations. *Global Planetary Change* 63, 152–162. doi: 10.1016/j.gloplacha.2008.03.004

Li, Q., Wang, C., and Ellingwood, B. R. (2015). Time-dependent reliability of aging structures in the presence of non-stationary loads and degradation. *Struct. Saf.* 52, 132–141. doi: 10.1016/j.strusafe.2014.10.003

Lowe, J., and Gregory, J. (2005). The effects of climate change on storm surges around the united kingdom. *Philos. Trans. R. Soc. A: Mathematical Phys. Eng. Sci.* 363, 1313–1328. doi: 10.1098/rsta.2005.1570

Maciñeira, E., Peña, E., Bajo, V., Sande, J., and Noya, F. (2017). "Probabilistic design of a secondary breakwater in the new harbour basin of the port of la coruña," in *Coastal structures and solutions to coastal disasters 2015: Resilient coastal communities* (Reston, VA, US: American Society of Civil Engineers), 482–490.

Malliouri, D. I., Memos, C. D., Soukissian, T. H., and Tsoukala, V. K. (2021). Assessing failure probability of coastal structures based on probabilistic representation of sea conditions at the structures' location. *Appl. Math. Model.* 89, 710–730. doi: 10.1016/j.apm.2020.08.001

Mercelis, P., Dufour, M., Alvarez Gebelin, A., Gruwez, V., Doorme, S., Sas, M., et al. (2014). "Generation of multivariate wave conditions as input for a probabilistic level iii breakwater design," in *International Conference on Offshore Mechanics and Arctic Engineering*, (New York, US: American Society of Mechanical Engineers) Vol. 45431. V04BT02A022.

Morim, J., Hemer, M., Cartwright, N., Strauss, D., and Andutta, F. (2018). On the concordance of 21st century wind-wave climate projections. *Global planetary Change* 167, 160–171. doi: 10.1016/j.gloplacha.2018.05.005

Morim, J., Hemer, M., Wang, X. L., Cartwright, N., Trenham, C., Semedo, A., et al. (2019). Robustness and uncertainties in global multivariate wind-wave climate projections. *Nat. Climate Change* 9, 711–718. doi: 10.1038/s41558-019-0542-5

Muhaisen, O. S., Elramlawee, N. J., and García, P. A. (2010). Copula-evt-based simulation for optimal rubble-mound breakwater design. *Civil Eng. Environ. Syst.* 27, 315–328. doi: 10.1080/10286600903134246

Oumeraci, H. (1994). Review and analysis of vertical breakwater failures - lessons learned. *Coast. Eng.* 22, 3–29. doi: 10.1016/0378-3839(94)90046-9

Oumeraci, H. (1999). "Strengths and limitations of physical modelling in coastal engineering–synergy effect with numerical modelling and field measurement," in *Proceedings of HYDRALAB-workshop*(Hannover, Germany), 7–38.

Peres, D. J., and Cancelliere, A. (2018). Modeling impacts of climate change on return period of landslide triggering. *J. Hydrology* 567, 420–434. doi: 10.1016/j.jhydrol.2018.10.036

Piscopia, R., Inghilesi, R., Corsini, S., and Franco, L. (2004). *Italian Wave Atlas* (Italy, US Lib: University of Roma TRE). Congr.G1989.21.C7, pp. 134.

Ports and Harbours Bureau, Ministry of Land, Infrastructure, Transport and Tourism and Port and Airport Research Institute, N (2009). *Technical standards and commentaries on port and harbour facilities in Japan* (Tokyo, Japan: The Overseas Coastal Area and Development Institute of Japan).

ROM 1.0-09 (2010). *Recommendations for the project design and construction of breakwaters (Part 1: Calculation and Project Factors. Climate Agents)*. Spain: Puertos del Estado.

Radfar, S., Shafieefar, M., and Akbari, H. (2022). Impact of copula model selection on reliability-based design optimization of a rubble mound breakwater. *Ocean Eng.* 260, 112023. doi: 10.1016/j.oceaneng.2022.112023

Salmun, H., Molod, A., Wisniewska, K., and Buonaiuto, F. S. (2011). Statistical prediction of the storm surge associated with cool-weather storms at the battery, new york. *J. Appl. meteorology climatology* 50, 273–282. doi: 10.1175/2010JAMC2459.1

Salvadori, G., Durante, F., Tomasicchio, G., and D'Alessandro, F. (2015). Practical guidelines for the multivariate assessment of the structural risk in coastal and off-shore engineering. *Coast. Eng.* 95, 77–83. doi: 10.1016/j.coastaleng.2014.09.007

Sanchez-Arcilla, A., Sierra, J. P., Brown, S., Casas-Prat, M., Nicholls, R. J., Lionello, P., et al. (2016). A review of potential physical impacts on harbours in the mediterranean sea under climate change. *Regional Environ. Change* 16, 2471–2484. doi: 10.1007/s10113-016-0972-9

Stagnitti, M., Iuppa, C., Musumeci, R. E., and Foti, E. (2020). Catania harbor breakwater: Physical modelling of the upgraded structure. *Coast. Eng. Proc.* 36, 2–2. doi: 10.9753/icce.v36v.papers.2

Stagnitti, M., Musumeci, R. E., and Foti, E. (2022). Surface roughness measurement for the assessment of damage dynamics of existing and upgraded cube-armored breakwaters. *Coast. Eng.*

Suh, K.-D., Kim, S.-W., Kim, S., and Cheon, S. (2013). Effects of climate change on stability of caisson breakwaters in different water depths. *Ocean Eng.* 71, 103–112. doi: 10.1016/j.oceaneng.2013.02.017

Suh, K.-D., Kim, S.-W., Mori, N., and Mase, H. (2012). Effect of climate change on performance-based design of caisson breakwaters. *J. Waterway Port Coastal Ocean Eng.* 138, 215–225. doi: 10.1061/(ASCE)WW.1943-5460.0000126

Tabarestani, M. K., Feizi, A., and Bali, M. (2020). Reliability-based design and sensitivity analysis of rock armors for rubble-mound breakwater. *J. Braz. Soc. Mechanical Sci. Eng.* 42, 1–13. doi: 10.1007/s40430-020-2207-8

Takagi, H., Kashihara, H., Esteban, M., and Shibayama, T. (2011). Assessment of future stability of breakwaters under climate change. *Coast. Eng. J.* 53, 21–39. doi: 10.1142/S0578563411002264

Takahashi, S. (2002). *Design of vertical breakwaters. PHRI reference document no. 34.* (Japan: Port and Airport Research Institute).

Tomasicchio, U., Adamo, F., Benassai, E., Boccotti, P., Colombo, P., Lamberti, A., et al. (1996). *Istruzioni tecniche per la progettazione delle dighe marittime* (Italy: Ministero dei Lavori Pubblici).

US Army Corps of Engineers (2002). *Coastal engineering manual* (Vicksburg, Mississippi, US: US Army Engineering Research and Development Center).

van der Meer, J. W. (1988a). "Stability of cubes, tetrapods and accropode," in *Breakwaters '88* (London, England: Thomas Telford American Society of Civil Engineers), 59–68.

van der Meer, J. W. (1988b). Deterministic and probabilistic design of breakwater armor layers. *J. waterway port coastal ocean Eng.* 114, 66–80. doi: 10.1061/(ASCE)0733-950X(1988)114:1(66)

Vousdoukas, M. I., Mentaschi, L., Voukouvalas, E., Verlaan, M., Jevrejeva, S., Jackson, L. P., et al. (2018). Global probabilistic projections of extreme sea levels show intensification of coastal flood hazard. *Nat. Commun.* 9, 1–12. doi: 10.1038/s41467-018-04692-w

Vousdoukas, M. I., Voukouvalas, E., Annunziato, A., Giardino, A., and Feyen, L. (2016). Projections of extreme storm surge levels along europe. *Climate Dynamics* 47, 3171–3190. doi: 10.1007/s00382-016-3019-5

Yan, K., Muis, S., Irazoqui Apecechea, M., and Verlaan, M. (2020). Water level change time series for the European coast from 1977 to 2100 derived from climate projections, (for [extracted period], [experiment], etc). *Copernicus Climate Change Service (C3S) Climate Data Store (CDS)*. doi: 10.24381/cds.8c59054f

Assessment and projections of sediment budget resilience in Marbella, Spain

Gonzalo Malvarez[1,2*†], Fatima Navas[1,2†] and José Luis del Rio[1,3†]

[1]Coastal Environments Research Group, Plan Andaluz de Investigación, Desarrollo e Innovación Recursos Naturales y Medioambiente 911 (PAIDI RNM911), Seville, Spain, [2]Area of Physical Geography, Universidad Pablo de Olavide, Sevilla, Spain, [3]Department of Research and Innovation, Ministry of Agriculture, Livestock, Fishery and Sustainable Development, Andalusia, Spain

This paper discusses how the beaches of Marbella, on the southwestern Mediterranean coast of Spain, may no longer stay in their natural resilience envelope due to a critically delicate natural sediment transport balance and a degree of artificialization that has entered the whole sedimentary system into a new resilience state. The combination of vigorous terrain and millenary human action and disruptions across and alongshore on the coastline have increased stress on sediment availability. Although sediment circulation in the coastal cell has often been studied, the investigation of the connection between soil loss and river sediment transport and retention at a major dam remains a challenge. In this article, a first-order sediment yield prediction was established by using a GIS-based model applied to the area's main river basin, and validation of model results is provided by empirical measurements of sedimentation in the main reservoir lake of La Concepción using Differential Global Positioning System (D_GPS)/Echo-sounder combination and measurements from remotely piloted aircraft compared with preconstruction blueprint topography documenting spot heights where sediments accumulated or eroded over 50 years. The marine circulation is interpreted from previous research by the authors that established a source-sink pattern similar to the Atlantic platform-fed marine system that originated the significant Cabopino dunes. The significant erodibility that we have estimated seems matched by potentially high sediment accumulation rates along selected profiles and spot heights across the bottom of the reservoir lake, and, in combination with the marine circulation model, our results identify that sediment budget key elements in Mediterranean settings, such as soil loss, sediment entrapment in reservoirs, and the coastal marine circulation, are in a state of deficit that suggests that the resilience envelope is surpassed and the system as a whole is entering a new resilience state in which the engineering factor is key. Some ecosystem services, such as the protection offered by the natural resilience of the beach and dune system of Cabopino, are no longer recoverable in the current artificialization state of the system as a whole.

1 Introduction

In the Bay of Marbella, in the southwestern reaches of Mediterranean Spain, we investigate the complex issue of sediment circulation from terrigenous sources and its influence on chronic beach erosion that appears to be occurring in the littoral cell in the last decades. In natural conditions, the setting, at the confluence of the Atlantic and Mediterranean ecosystem transitional environments, provides the basis for vegetation patterns that cover with great efficiency the river basin's slopes, affecting significantly the sediment production as the river basins' soils appear to be fully sealed from rainfall with high vegetation interception rates. Thus, beach systems are adjusted to sporadic sediment input to which morphodynamic marine processes respond with narrow beach faces and surf zone where low-energy waves initiate littoral drift and, consequently, redistribute sediments on narrow steep beaches. This is the natural circulation model on most Mediterranean coasts, where beaches develop due to the connection between terrigenous and marine sedimentary systems (Malvárez et al., 2021). A peculiarity of the environment in the Bay of Marbella (Figure 1), as in other Mar de Alboran coastal stretches, is that the continental shelf stores large deposits in some places that serve as a source when connected to the beach-dune system, generating large strand-like settings. Most Mediterranean

coastal dunes fronted by steep continental shelves are not associated with glacial deposits but rather with those of river mouths and/or coastal lagoons (Pye, 1983). Sometimes, when conditions are favorable and sediment budgets are sufficient, Mediterranean dunes can grow to extents and volumes comparable to European Atlantic dunes, even under low-energy settings from both wave and wind forcings, as well as intermittent and limited sediment supply. This is the case of the Cabopino dunes, at the eastern end of the Bay of Marbella (Figure 2), with a vegetation that is more complex and diffuse than that of Atlantic or other open-ocean-type dunes (Sanjaume and Gracia, 2011). This vegetation assembly is also more sensitive to Mediterranean/Atlantic exchange and sediment feeding (Malvarez et al., 2019); thus, sediment transport stability from source to sink is key to the natural resilience of the beach–dune system. However, interruption of sediment supply from marine sources to the coastal system, as well as sediment cell nearshore circulation patterns, can disconnect, if not eliminate completely, the nearshore–beach–dune feeding pathway (Willis and Griggs, 2003). The continental shelf fronting Marbella is steep, and the input area of the coastal system is reduced to fluvial yields to the west. The circulation to the east provided sufficient sourcing to beaches in Marbella and even to the Cabopino dune complex, but sequential elimination of input has led the transport to bypass the system and now head
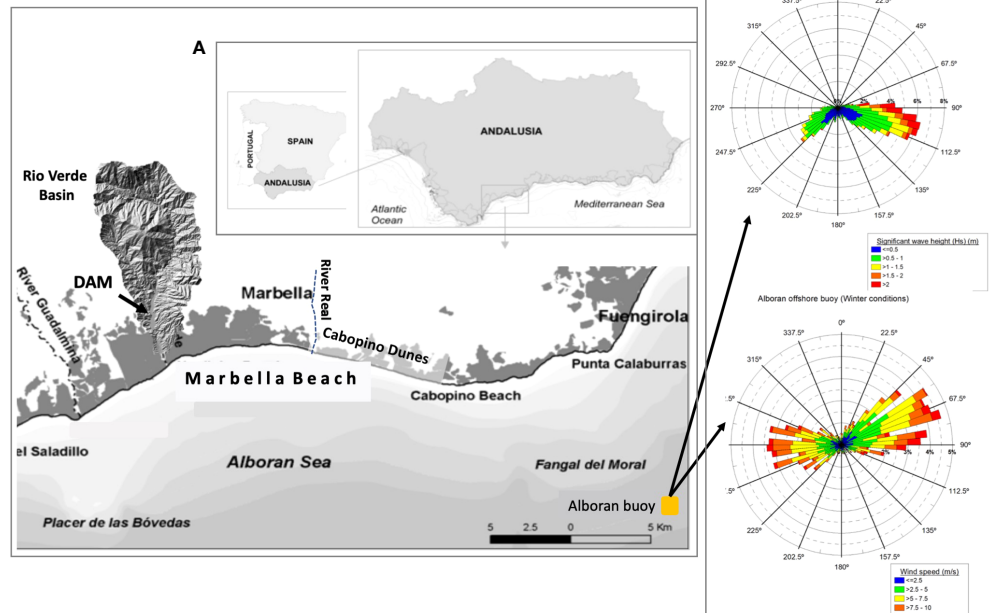
FIGURE 1
(A) Map of the study area shows the location of the embayment. The river basin of Rio Verde is drawn to indicate the scale of the basin, which has been modeled for sediment production and is interrupted by the La Concepción dam. (B) Wave rises in winter from Alboran Sea wave buoys illustrate the intense bi-directionality of wind waves.
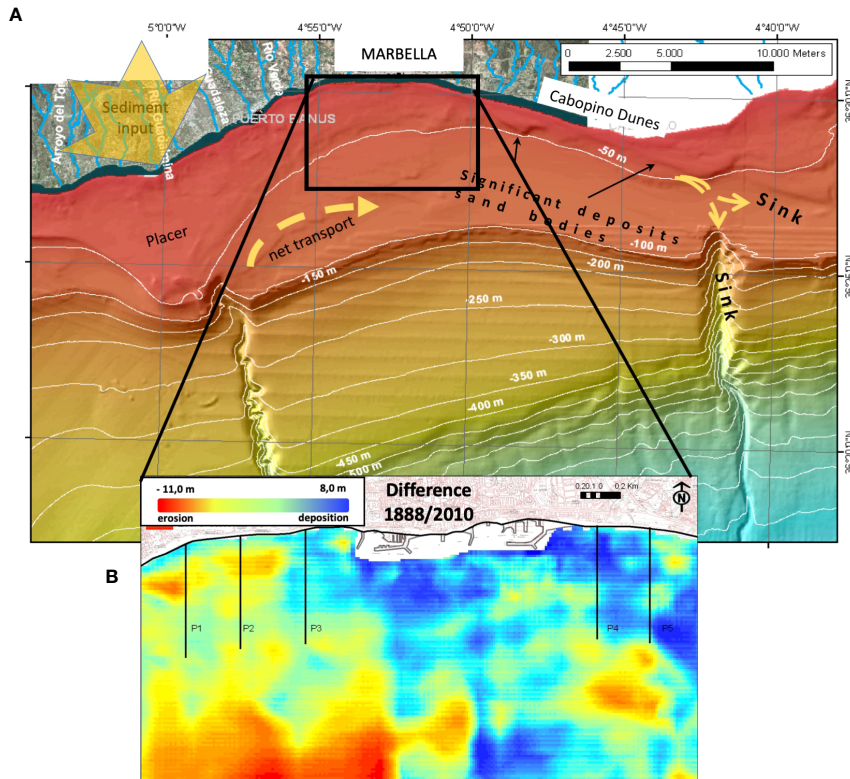
FIGURE 2

(A) Continental shelf of Marbella Bay. **(B)** Bathymetric changes from the 1888 seabed map and 2010 bathymetry (from Guisado-Pintado et al., 2015).

directly to deep sinks like canyons and sand bodies beyond closure depth for beach interaction (see Figure 2).

Human-induced changes to the natural sediment transport balance have pushed most of the natural coastal systems into a situation of fragile equilibrium. Severe modifications of natural processes are not solely constrained to direct destruction from urbanization or infrastructure on the coastal strip but, more importantly, affect the sediment feeding system by introducing changes in the original settings that generated coastal features such as beaches and dunes (Anthony et al., 2014). Additionally, human action has influenced vegetation cover in river basins and, thus, soil loss has been a long-term issue that has even provided, during most of the Holocene, substantial filling to the lower reaches of the drainage network that, although were estuaries during the Late Pleistocene, form deltas nowadays (Senciales and Malvárez, 2003). However, valley infilling and prograding shorelines have stopped as a result of the intensification of human action, and erosional processes are not only evident along the coastal strip itself but also in the terrestrial hinterland and nearshore environments that control the natural sediment nourishment of beaches (Del Río et al., 2020).

An extraordinary positive balance in sediment yield is caused when the degradation of the upper and mid-reaches of

the river basins, brought about by land use change, induces increased yields and sedimentary surplus in the coastal cell (Anthony et al., 2014). Abundant material for the marine environment generates significant deposits on the upper shelf. Volume growth of coastal deposits and littoral drift dominated these phases, generating wide beaches and, then, dune systems. Often, the existence of a long well-fed beach system facilitated economic activity associated with tourism in its many aspects (Navas, 1996; Giordano et al., 2015). However, infrastructure and activities that are deployed and maintained for the recreational industry are at risk from (and pose a risk to) coastal morphological changes (Cooper and McKenna, 2008; Navas et al., 2017) and, consequently, management initiatives are implemented systematically to maintain the position of the shoreline and tourism-related facilities. These facilities are traditionally viewed as human interventions in a natural system, but they have evolved to such an extent that some authors maintain that they now form an integral part of a coupled human-natural coastal system (CHANS), that is characteristic of (and response to) conditions prevailing in the Anthropocene (Polhill and Gotts, 2009; Lazarus, 2017; Quinn and Wood, 2017). In natural beaches, changes in morphology are driven by dynamic forces (waves, currents), operating on a

particular volume of sediment, within the boundaries of the surrounding geological framework and position of sea level (e.g., Cooper et al., 2004; Pilkey and Cooper, 2004). How coastal systems operate in the coupled human- and natural-driven conditions is becoming of great interest, with the increased urbanization (Navas et al., 2012) and the intensification of economic activities in coastal areas that involve built infrastructure and often associated sea defenses, whether hard or soft.

In Marbella, during the late nineteenth century and mostly through the twentieth century, the increasing concern in the management of water and beaches led to the construction of dams in the hinterland and groins and many other infrastructures along the shorelines (Malvarez, 2012). Dams were first constructed to generate water flows for iron production and irrigation and then, mostly during the late twentieth century, to satisfy the increasing demand for water as a result of the massive urban development along the coast of Marbella (Figure 1) (Del Río et al., 2020). This has promoted the rapid reversal of the morphodynamic processes that affect the sedimentary units (e.g., beaches, dunes, and submerged sand bars) of the coastal system, resulting in severe erosion of beaches and the interruption of dune building trends.

Socioeconomic activities and related land use had a severe impact on soil erodibility during the last four centuries. In the eighteenth century, the economy revolved around the primary sector, mainly sugar cane cultivation. Later, at the beginning of the nineteenth century, the most powerful iron smelting industry of Spain settled in the largest river basin of the Marbella's hinterland, the river Verde. Two minerals melting infrastructures, that used wood as fuel and water for cooling the smelting furnaces, were constructed along the river bank and led to the vast deforestation of the surrounding forests in barely 17 years (Madoz, 1848; García-Montoro, 1983). The high-water demand associated with sugar cane cultivation led to the construction, between 1882 and 1903, of 7 dams and reservoirs of some 10^6 m^3 in the lower reaches of the Guadalmina and Guadaiza rivers. During the first decade of the twentieth century, the iron melting and sugar cane manufacturing industries disappeared, and the tourism industry began to progressively increase in importance, reaching its peak during the second half of the twentieth century. Within this period, the number of households increased from 2,000 to 35,000, and the population increased from 10,000 to 100,000 inhabitants. According to the Institute of Statistics and Cartography of Andalusia, the number of inhabitants living in Marbella in 2021 was 147,958, which represents an acute growth of a steady 200% per decade during the last four decades. In response to population increase, the La Concepción Dam was built in 1971 in the lower course of the river Verde, which has the greatest water

course in terms of drainage area and length (Figure 1). Besides ensuring a fresh water supply, the La Concepción Dam is also used for flood control, given the seasonality of the precipitation regime in the area. To keep constant water storage during the dry season, a complex water transport system connecting the Guadalmansa, Guadalmina, and Guadaiza rivers, generating a one-way freshwater flux towards La Concepción, was built in 1995. This reservoir lake also receives water from a desalination plant constructed in 1992. Artificial lakes created by the dams tend to silt up due to unresolved land degradation on the steep and bare slopes.

Since shoreline retreat and beach dynamics have been documented in previous research and reports (e.g., Malvarez et al., 2019), in this paper we focus on the linked processes that have generated stress on the natural resilience of the coast of Marbella. This is carried out by documenting calculations of soil loss from the river basin and reservoir lake siltation caused by the construction of the dam at La Concepción. Then, a qualitative assessment addresses natural resilience in the current scenario, where sediment input is restricted to the coastal cell. The nature and efficiency of beach management arrangements are coupled with natural processes as a vital component of coastal resilience. However, as many natural systems are massively distorted by human action, natural and built environments coexist in a blurred and complicated definition of resilience (Masselink and Lazarus, 2019). The concept of a sediment budget then implies an accounting view on the feeding and circulating mechanisms of the coastal cell, whose longevity and potential adaptability are subjected to alternating fluctuations in input and output within the system feeding and sinking sediments (Del Río et al., 2020). Thus, in this study, we take this view and incorporate inherent complex interactions of coastal environments in their natural state as natural resilience. The concept of the resilience of a given natural (eco)system can be regarded as the ability of a system to persist by maintaining the key structures and processes that characterize that domain (Francis, 2013). This implies an adaptive capacity of the system to reorganize in the face of disturbance while maintaining key structures and processes. In a coastal setting, features can shift in position (e.g., by roll-over, retreat/advance) and retain all the key structures and functioning. This contrasts with the definition of engineering resilience, sometimes also called recovery, where the system and functions need to be restored in the same position (Adger et al., 2005; Francis, 2013; Flood and Schechtman, 2014).

Given the multiple components present when a complex natural and human-intervened coastal site is to be studied, in this paper, we present (i) an approach to quantify sediment production and yield from the main river basin in the coastal system, then (ii) an estimation of reservoir lake infilling over the years of the dam's operation.

2 Materials and methods

2.1 Study site environmental settings

The climate regime of the study area is semi-arid, with mild air temperatures in winter that range from 15°C to 24°C. The precipitation regime is seasonal, sharply concentrated in autumn and winter. Heaviest rainfall events, reaching thresholds that occasionally range from 160 to 300 millimeters (mm) in 24 h, are consistent with the arrival of cold fronts coming from the east, originated by the warming of the Mediterranean Sea, causing serious flooding.

The arid climate, the occurrence of episodic, heavy rainfall events discharging large volumes of water with high-energy on steep, impervious soils sparsely vegetated in some cases, would contribute to producing overland flows triggering severe soil erosion and, consequently, potentially high sediment yield rates at the basin scale. The majority of the river basins reveal the presence of alluvial fans, though the largest formation in terms of volume of lithogenous sediments is located on the foothills of the mountain range surrounding the municipality of Marbella to the north, whose origin dates from the Late Pleistocene according to Lario et al. (1993).

The river basins in the western section of the Marbella's hinterland, the Guadalmina and Guadaiza rivers, have a narrow and elongated morphology, while central watersheds (Verde and Real rivers) show a wider typical leaf shape, as shown in Figure 3 (Rio Verde). According to CMA (1999); CMA (2005), and following the soil classification system of the World Reference Base for Soil Resources (IUSS-FAO, 2014), the prevailing soil types of the river basins are lithosols, cambisols, luvisols, regosols, and fluvisols, whose textures range from sandy-loam (calcareous fluvisols) to silty-loam (chromic luvisols, Rendsina soils, and cambisols rich in calcium) and clay-loam (eutric regosols and eutric cambisols). Following the Hydrologic Soil Group defined by NRCS (1986), such textures are associated with soils having low permeability (Figure 4A).

In the marine environment, beach profiles are usually steep and far from dissipative, modally adjusted to short-period waves generated by the local winds of the Alboran Sea, generating a steep and narrow surf zone (Malvárez, 1999). In terms of wave climate, sea waves are common and only rarely does swell occur given the limited effective fetch with an average distance of 500 km (Figure 1B). The wave climate in the region is characterized by long intervals of calms of over 77%/year, in which the wave heights are less than 1 m. Mean heights are around 0.8 m in summer and 1.3 m in winter with wave periods of 4–5 s corresponding to short-crested waves forced by local winds. Wave and wind approaches are characterized by the alternation of almost 50% of westerly and easterly winds, both in summer and winter seasons (see Figure 1B). The tidal range is microtidal (<0.2 m average astronomical tidal range) and semidiurnal and, thus, the main forcing on the coast is wave action.

In terms of high-energy events, decadal records show that storms are characterized by a low variability of wave approach; the majority are easterly events (80° to 135°) with deep water wave heights greater than 5 m, although closure depths are estimated in the Bay to be extraordinarily shallow at some 3.5 m at some 200 m from the shoreline (MTERD, 2022).
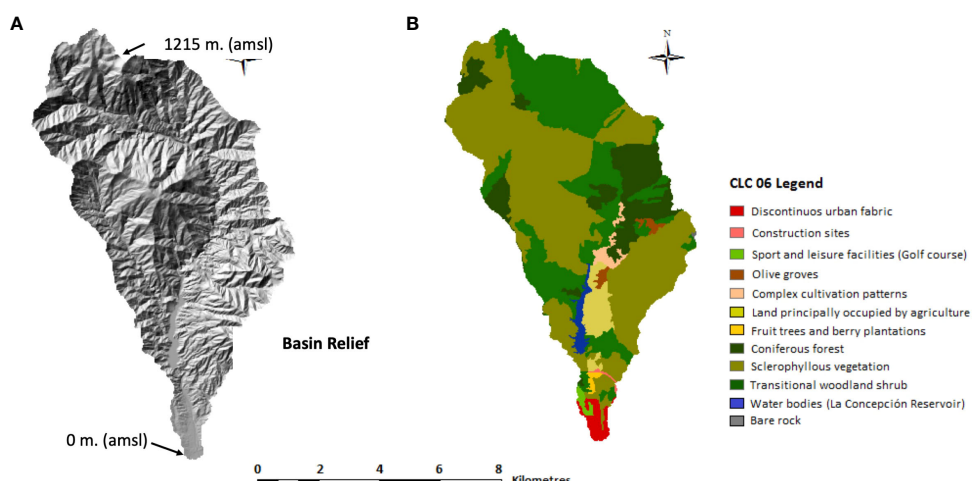
FIGURE 3
Topography and land cover classes of the river Verde basin. **(A)** Topography has been calculated by using the digital elevation model (DEM) at a 25-m spatial resolution taken from the National Geographic Survey of Spain; **(B)** land cover classes have been represented according to the official Corine Land Cover dataset collected in 2006.

FIGURE 4
Soil categories and midslope of the river Verde basin. **(A)** Soil types shown following the nomenclature stated by the Food and Agriculture Organization (FAO). **(B)** Midslope has been calculated in degrees by using the digital elevation model (DEM) at a 25-m spatial resolution provided by the National Geographic Survey of Spain.
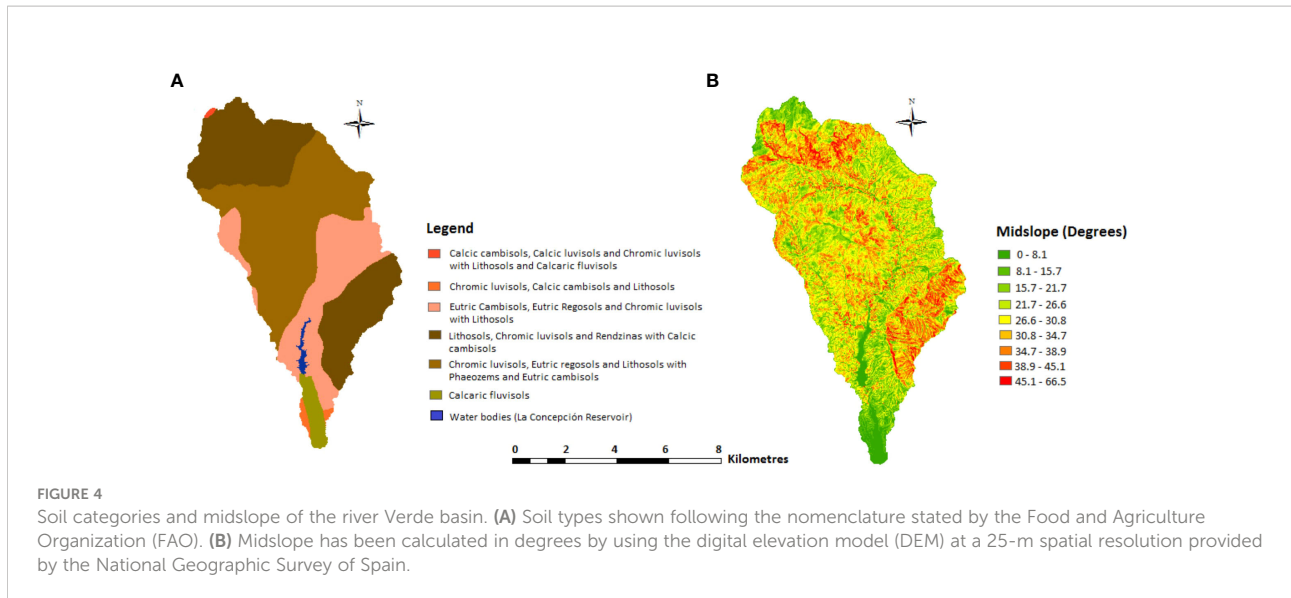
2.2 Methods

The approach provided in this paper is based on the combination of modeled predictions of potential sediment yield at basin scale using a GIS-based model, associated with measurements obtained with D_GPS and Echo-sounder surveys conducted to establish the bottom topography of the reservoir lake formed by the dam of La Concepción. The measured bathymetry was then overlaid over a topographic surface reconstructed from blueprint documentation obtained prior to dam construction. The relationship between sediment yield and retention by the dam is estimated by a number of spot elevations comparing the results of a 2019 survey and 1966 digitized data at La Concepción. This comparison is aimed at quantifying and qualifying the overall accumulation and its implications in sediment starvation in the coastal area. Finally, a resilience conceptual model is described in order to consider sediment budget resilience.

2.2.1 Sediment yield modeling in the river Verde basin
2.2.1.1 Justification and overview of the sediment yield model used

In general, soil erosion and sediment yield models fall into three categories: (i) empirically, (ii) conceptually, and (iii) physically based models. The latter, such as the Water Erosion Prediction Project (WEPP) or Areal Nonpoint Source Watershed Environment Response Simulation (ANSWERS) models, among others, offer the most accurate predictions. They do, however, involve a large number of physical parameters integrated by equations that have been developed to work at small scale (small basins) and under very specific

physical conditions (Merrit et al., 2003). This implies that a huge amount of onsite input data are required to run these models with sufficient accuracy. It is important to state at this stage that some data that are needed to run these models (e.g., grain size distribution in the hinterland, land management practices, or hydrological data with temporal and spatial variability) were not available in the literature nor were they collected by the Public Administration. The predictions provided in this work constitute the first attempt to estimate the sediment yield potential in the study area. In such cases, where input data required by more complex modeling tools are either lacking or too limited, the use of empirical models becomes the single feasible solution (Merrit et al., 2003; Rajabi et al., 2022) to predict the sediment behavior at medium-sized river basins. Several empirical models have been developed since the mid-twentieth century (e.g., AGricultural NonPoint Source (AGNPS) or SEdiment Delivery Distributed models (SEDD)), but the Modified Universal Soil Loss Equation (M-USLE; Wischmeier and Smith, 1960; Williams, 1975; Eq. 1) was used to obtain a first-order prediction of sediment yield of the river Verde basin during a single rainfall event.

$$Y = 11.8 * (Q * q_p)^{0.56} * K * LS * C * P \qquad (1)$$

Where Y is the sediment yield prediction in metric tons, Q is the runoff volume in cubic meters, q_p is the peak flow rate in cubic meters per second, K is the USLE soil erodibility factor, LS is the USLE slope length and gradient factor, C is the USLE cover management factor, and P is the USLE erosion control practice factor.

Leaving aside the above, the choice of using the M-USLE against other sediment yield models is sustained by three additional criteria:

1. Data requirements: The input data required by the M-USLE model are described in greater depth within **Section 2.2.1.2**. Nevertheless, reliable data on topography, soil types, precipitation, and land cover have been made available in the literature and by the Regional Government of Andalusia and were consulted accordingly.

2. Validity of the model: The USLE family of models has been globally used to predict soil erosion and sediment yield at the basin scale since the mid-twentieth century and has been the subject of recurrent validations over time. In fact, the USLE was used by the Regional Government of Andalusia to estimate those soil erodibility and cover management factors that were used for the calculations provided in this work, and the M-USLE is being used recently to predict potential sediment yield in other Mediterranean watersheds (Gwapedza et al., 2020; Berteni et al., 2021; Yousuf et al., 2022; among others).

Software requirements: The use of a Geographic Information System (GIS) for water erosion and sediment yield modeling provides valuable advantages, such as the facilitation of multiple-source data processing in a timely and cost-effective manner (Pandey et al., 2016). Following this premise, a raster-based spatial analysis model called Arc-MUSLE, developed as a redistributable ArcGIS® extension integrating the M-USLE empirical equation by Zhang et al. (2009), was used for sediment yield predictions. The application of the Soil and Water Assessment Tool (SWAT) model was also explored but, as a physically based model, it required (i) hydrological data, such as flow direction, length, and accumulation through the hydrographic network, (ii) spatial variability of the rainfall stations distribution, and (iii) single classification and spatial variability of soils along the watershed that were not available nor were they inviable to be collected in the study area. Due to these reasons, the use of SWAT was ruled out, and the M-USLE was selected as the most appropriate model that matched the scope of this work.

2.2.1.2 Modelling assumptions and input data

Assumption 1: Sediment yield against soil erosion.

The M-USLE was developed by Williams (1975) as a watershed-based model to estimate the sediment yield, defined by the United States Geological Survey as the amount of terrigenous sediment per unit area removed from a watershed by flowing water during a single storm event. Conversely, the original USLE and RUSLE models were developed to predict the long-term average annual rate of soil erosion from agricultural fields under specific cropping and management practices. Considering the above, the use of the M-USLE is more in line with (i) the nature of the process studied in this work, the prediction of sediment yield rather than soil erosion, (ii) the

spatial scale, at the watershed level instead of at experimental field plot scale, and (iii) the temporal framework, at an event-based scale against long-term annual predictions.

Assumption 2: The runoff energy factor as the main driver of sediment yield.

The original USLE and RUSLE models consider the rainfall erosivity factor (R), a multi-annual average index that measures the rainfall kinetic energy and intensity to assess the effect of rainfall on sheet and rill erosion. Instead, the M-USLE considers the runoff energy factor, defined within Eq. 1 as $11.8*(Q*q_p)^{0.56}$, as the main driver of sediment yield. In fact, the runoff was demonstrated to be better correlated to sediment yield than the R factor, and it was deemed as the best single indicator for sediment yield estimations (Williams, 1975). ArcMUSLE calculates the runoff volume (Q in Eq. 1) following the Curve Number method, developed by the Natural Resources Conservation Service of the United States in 1964 and subjected to subsequent revisions so far. In those areas where no runoff data are available, as it occurs in the study area, this method may estimate the depth of direct runoff from the rainfall depth. The q_p is obtained by applying the graphical peak discharge method, developed by the same United States Organization in 1986 as a function of the drainage area, the runoff depth, the time of travel for sheet and shallow flows, and Manning's roughness coefficient. This last is a methodology commonly used in civil engineering studies in the United States to calculate the resistance of flood flows in channels and flood plains.

Assumption 3: Input data.

Data used to run the model followed Zhang et al. (2009), and thus, layers for topography, land cover classes, soil types, and a 2-year, 24-h rainfall event required were developed from various data sources as input data for the sediment yield assessment at the basin scale.

1. Topography: Watershed topography of the river Verde basin was integrated in ArcMUSLE as a raster layer on the basis of the 25-m resolution DEM, developed by the Spanish National Geographic Institute following the European Terrestrial Reference System 1989 (ETRS89).

2. Land cover data: Land use categories of the river Verde basin (Figure 3B) were extracted from the 2006 CORINE Land Cover (CLC) database, developed by the EU Copernicus. Three attributes were bound to each land cover class; (i) land cover codes, according to the classification system stated by the United States Geological Survey (USGS), (ii) the cover management factor (USLE C factor), and (iii) the Manning's roughness coefficients. Land cover codes used by the CLC 2006 were converted into the USGS Land Cover classification according to Anderson et al. (1976). Given the lack of recent USLE C factor repositories in Andalusia, the cover management factor was defined

according to those empirical values published by the Spanish Institute for Nature Conservation (ICONA) and following Moreira (1991) and Panagos et al. (2015a). Manning's roughness coefficients were determined according to Engman (1986) and Vieux (2004).

Soil types: Soil types of the river Verde basin were extracted from the Soil Map of Andalusia (Figure 4A; CMA (2005), where soils are spatially classified as categories rather than as single soil types. Three attributes were linked to each soil category; the midslope (Figure 4B), the soil erodibility factor (USLE K factor), and the Hydrologic Soil Groups (HSGs). These HSGs consist of four qualitative groups (A–D) through which soils are categorized according to their runoff potential, which is logically a function of their texture and soil layer depth (A group means loamy sand, sandy loam, and silt loam soils having low runoff potential and D means soils having high runoff potential and having greater than 40% clay). The midslope was calculated on the basis of the DEM. Considering that soil categories comprised more than one soil type and, consequently, a wide range of soil textures interbedded, the definition of representative USLE K Factors and HSG required the prior establishment of the prevailing texture of each soil category on the basis of the World Reference Base for Soil Resources (IUSS-FAO, 2014). The USLE K factor was then determined following the empirical values published by Stewart et al. (1975); Schwab et al. (1981); Parveen and Kumar (2012), and Panagos et al. (2014), and the HSGs were fixed according to the Natural Resources Conservation Services of the United States Department of Agriculture (NRCS, 1986).

Precipitation data: According to Zhang et al. (2009), ArcMUSLE considers the most intense 24-h rainfall event registered in two consecutive years to define the storm event triggering sediment yield. The 2 years assessed were selected according to the same period as both the Soil Map of Andalusia and the CORINE Land Cover database were developed (2005 and 2006, respectively). The daily rainfall volume recorded from the 1 January 2005 until the 31 December 2006 by the weather station installed by the State Meteorological Agency of the Spanish Government in the Marbella harbor was then analyzed. The heaviest rainfall event occurred on 7 November 2006 and registered 91.8 mm in 24 h. Thus, it is reasonable that the two-year rainfall event considered represents conveniently the nature of the storm events that activate the sediment yield processes in the river Verde watershed.

Other input data: Sediment yield assessment is completed by providing (i) the Antecedent Moisture Condition (AMC), (ii) the volume of precipitation (in inches), and (iii) the Conservation Practice Factor (USLE P Factor). First, and following Singh (1982), the AMC of the watershed was determined by analyzing the volume of precipitation registered during the five days prior to the rainfall event considered for the

analysis. Therefore, 14.5 mm was registered in Marbella from 2 to 6 November 2006, consistent with average moisture conditions' according to the Curve Number Method (NRCS, 1986). Secondly, the volume of precipitation was introduced in the modeling interface. Finally, given that the USLE P Factor is not estimated by the Regional Government of Andalusia for soil erosion risk modeling, a value of $p = 1$, equivalent to "no conservation practices conducted," was assumed for the sediment yield prediction according to Panagos et al. (2015b), which likewise matches with the default value proposed by Zhang et al. (2009) in those areas where the USLE P Factor value is unknown.

2.2.2 Topography comparison of before and after dam construction

To calculate the approximate position of the bottom topography in the reservoir lake of La Concepción before and after the construction of the dam, we had to determine the initial topography of the valley before the start of sediment retention (1966) and the current topography of the valley after 50 years of sedimentation. First, to obtain the topography of the valley prior to dam construction, secondary sources were searched. Large format plans of the original blueprint documents from the engineering works of 1966 (Water Management Authority; from Demarcación Hidrográfica de las Cuencas Mediterráneas Andaluzas) were first scanned to obtain the topography of the valley prior to dam construction. This surface is called here the 1966 topography (Figures 5, 6). A field visit was carried out to occupy with a Differential GPS the original 1960s bench marks and other topographic triangulation posts. These, and numerous other landmark coordinates obtained from the Orthophoto PNOA 2018 published by the Instituto Cartográfico de Andalucía, were used to carefully georeference the scanned plans using QuantumGIS (QGIS) in order to digitize contour lines from the original scanned plan. After georeferencing the scanned image, vector layers of points were generated. Vector point layers marked the 121.5, 96.5, 71.5, 61.5, 56.5, 51.5, and 46.5 m.

To obtain the current elevation values for the same surface, now under some 50 m of water in some sections of the La Concepción lake, a vessel was used equipped with a chirp (Garmin Striker Plus 9SV CHIRP Sounder) and integrated GPS for navigation and the 800-kHz transducer for depths with a vertical resolution of 0.1 m in measuring the vertical distance between the water level and the bottom surface. In addition, measurements were made with a GPS Leica Zeno 20 in differential mode using corrections and increased precision by 3G on the shore of the reservoir, thus obtaining the coordinates and height around the water body as a baseline for later calculations. For correct elevation data of the water mark at the time of the survey in 2019, topographic data was generated using a DJI Inspire 1 Remotely Piloted Aircraft (RPA) equipped with a 4K ZENMUSE X3 camera for photogrammetry. Up to

120 images were combined using Pix4D software to develop a Digital Elevation Model with a theoretical precision of 4 cm in three dimensions. Overlap was established at 70%–80% side and front, respectively. Comparison with known bench marks allowed precise estimation of shoreline elevation. Data from the drone survey were used to support shoreline position elevation detection, as well as to document sedimentation bodies that were emerging at the time of the survey at the higher end of the reservoir lake.

In terms of uncertainty levels, the individual methods (i.e., Echo-sounder, GPS, and RPA) may be in the centimeter range of error, but the accumulated error is hard to estimate given the pitch and roll and other effects of the boat in motion. The network of control points occupied by the GPS was used to minimize through global corrections, the potential deviations of the Echo-sounder and RPA. Data acquired with various techniques introduce an overall uncertainty level that could only be tested in the combined files introduced in the GIS for spatial analysis. Thus, once these measurements were obtained, points were exported to QGIS software, and a vector layer of points was created as 2019 elevation points (Figure 5). After corrections, depth values were transformed to a height above mean sea level using lake shoreline elevation from the drone survey, corrected by benchmarks reoccupied at 1966 points with the D_GPS taken to tie elevations. Likewise, numerous features visible in the 1966 plans were visited to use them as ground control points.

2.2.3 Assessment of sediment budget resilience

In order to assess resilience in this paper, the principle of resilience is defined as "the capacity of a system to absorb disturbance and reorganize while undergoing change so as to still retain essentially the same functions, structure, identity, and feedbacks" (Scheffer and Carpenter, 2003; Folke, 2006; Flood and Schechtman, 2014; Kombiadou et al., 2020). Specifically, the concept used here for assessing resilience follows Kombiadou et al. (2020). A fundamental principle is that the state of resilience can be represented in a Basin of Attraction (BoA) model where three dimensions are used: a, b and c. These are related to the position of the system within the shape of the BoA (Gunderson et al., 2012; Kombiadou et al., 2020). Figure 7A illustrates resilience concepts used in this article expressed in relation to the usual description for wave geometry, (a) Latitude is the wave length of the BoA and indicates how much the system is able to change irreversibly; (b) Resistance is the wave height of BoA and depicts the amplitude of changing range prior to stepping to another trough; (c) Precariousness is the position of the system state in relation to a threshold, a point of no return as the system enters a new BoA. The measure of restoration of the system by natural or assisted "engineering" depicts its ability

to recover and stay in the same state and/or position. It is understood that the natural state and position of the system should be the long-term state and position and that any significant change in beach profile and, more specifically, a shift in position landwards of the entire system implies natural resilience "moving" into a new BoA.

3 Results

3.1 Sediment yield prediction in the river Verde basin

The potential sediment yield predicted in the river Verde basin during the 2-year, 24-h rainfall event considered was 294,000 t (Figure 8A). Potential sediment production of the rest of the river basins feeding the Bay of Marbella during the same precipitation event was also estimated, and results are shown in Table 1.

Estimated values presented in Table 1 suggest that potential sediment yield and the drainage area of the river basins seem to be fairly well correlated, except in the case of river Real, where the occurrence of a forest fire in 2005, which was also assumed within the calculations according to the original data source, is probably underestimating the potential sediment yield modeled by ArcMUSLE. The spatial distribution of potential sediment yield and surface runoff rate estimated in the river basin is shown in Figure 8B, where darker areas mark the maximum rate of surface runoff. Steep-slope agricultural lands (midslope ranging from 26.6° to 34.7°; Figure 4B) located on the eastern hillside of the reservoir would also register a high runoff rate and sediment yield. Such results would be consistent (i) with their low Manning's roughness coefficient ($n = 0.035$) when compared to the coniferous forest or sport and leisure facilities' roughness values ($n = 0.6$ and 0.45, respectively) and (ii) with their moderately high cover management factor (USLE C factor = 0.1457) in comparison with the C factor registered by dense and scattered forested areas ($C = 0.0015$ and 0.0296, respectively).

The erosive trend obtained in the Discontinuous Urban Fabric (CLC-06) might be interpreted as urban soil erosion rather than sediment yield, so it has been kept out of the calculations of our study.

The minimum sediment yield registered in the limestone rock formations of Sierra Blanca and Sierra de las Nieves, in the lower and upper reaches of the river basin to the east and north, respectively (highlighted in Figure 8A), seems to be consistent considering the soil types of mountain chains. Lithosols, calcic cambisols, and chromic luvisols, mainly composed of limestones with slates, greywackes, marbles, and quartzites interbedded with moderately low runoff potential (Hydrologic Soil Group B), would result in a prevailing water infiltration over the formation of surface runoff and soil erosion.
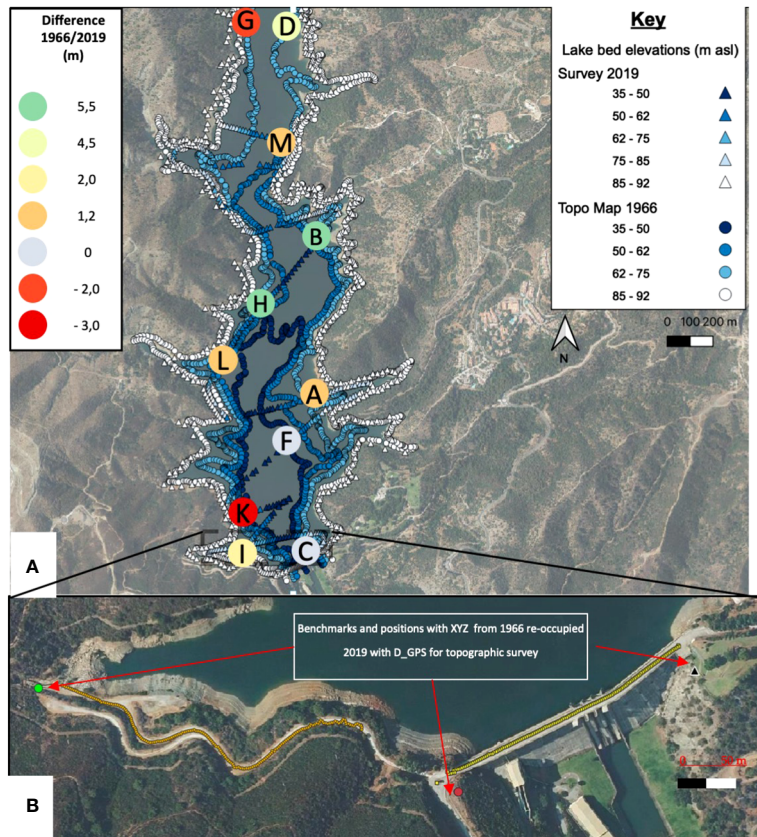
FIGURE 5

(A) Location of original digitized and surveyed elevations from 1966 to 2019 and spot heights used for comparison. Color in labels indicates the sedimentation/erosion observed in the comparison between 1966 and 2019 in meters. The letter inside the circle symbol refers to the letter mentioned in the text. **(B)** Benchmarks and positions with XYZ coordinate provided by the blueprint documents of dam construction from 1966. Points and marked ways were reoccupied in 2019 with D_GPS to establish the link between topographic surveys.

3.2 Sediment accumulation in reservoir lake after dam construction

The elevation was digitized using the original topography of the valley prior to dam construction in 1966. Elevations are related to the mean sea level (MSL of Spanish altimetric datum). Depths, obtained by Echo-sounder and GPS boat survey in 2019, were calculated relative to known locations corrected from local bench marks established in 1966 when the dam was constructed,

thus tying the datum to the original 1966 data digitized. The data obtained from the boat survey are shown in Figure 5.

Although volume comparison would have been easier by overlapping two modeled raster surfaces, the comparison of the interpreted surfaces was complex due to the many issues in overlapping the 1966 and 2019 topographies. Data were concentrated in the case of the 1966 digitized lines and also along Echo-sounder lines. Gaps between lines forced interpolation, resulting in inaccurate raster models, and

TABLE 1 Potential sediment yield predicted in the main hydrographic network in 2005–2006.

River basin	Watershed area	Potential sediment yield
River Guadalmina	6,666 Ha–66.66 km^2	170,000 tons
River Guadaiza	4,868 Ha–48.68 km^2	65,000 tons
River Verde	**15,506 Ha–155.06 km^2**	**294,000 tons**
River Real	2,651 Ha–26.51 km^2	109,000 tons

Commas were used in the second and third columns as a thousand separator and dots in the second column as a decimal separator. Result obtained in the river Verde watershed is highlighted in bold.
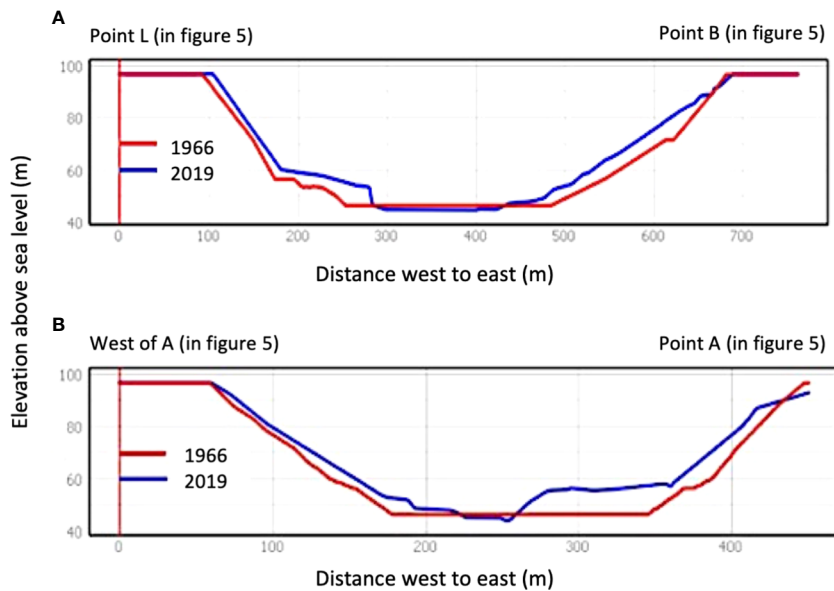
FIGURE 6
Cross sections of the reservoir lake of La Concepción. Labels are referred to Figure 5 locations. **(A)** Cross section from the east shore of spot elevation B to the west of spot elevation L. **(B)** From east of point A to directly east.
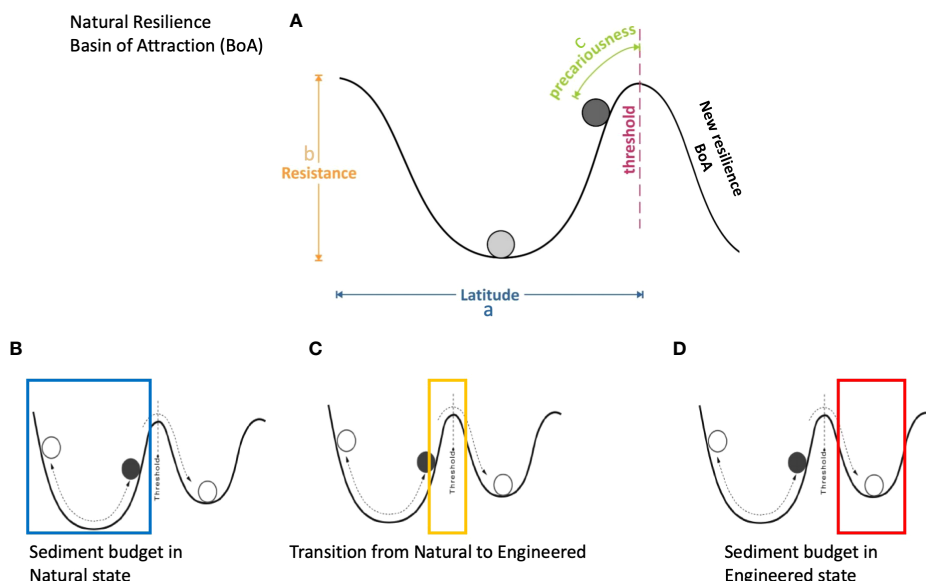
FIGURE 7
(A) Key concepts in the Basin of Attraction model. Once the sediment budget is artificialized, resistance and latitude are greatly diminished, thus compromising sustainability and/or adaptability. **(B)** The system in its natural state moves well within the threshold for centuries. **(C)** As the threshold is surpassed frequently due to stress from the input, the system enters a different BoA. **(D)** Once the system feeding is eliminated, there is no return to the broad natural BoA, and the engineered state remains in a low-resistance BoA.

although surfaces were generated by overlapping the data digitized from 1966 and the depths surveyed in 2019, the results were deemed inaccurate. Instead, comparing directly overlapping point data from the two vector layers yielded much more accurate results. The comparison of selected spot elevations is used to help clarify the outcomes of the analysis. It was decided to establish 11 spot elevations in the lake to be representative of bottom topography change at areas where

FIGURE 8
Spatial distribution of sediment yield and runoff rate in the river Verde basin. **(A)** Most erosive areas were predicted in the river Verde basin using the M-USLE. Deforested areas during the nineteenth century were outlined through a dashed line in black according to [18]. **(B)** Areas of the river Verde basin where the highest runoff rates (darker areas) would be registered according to the predictions obtained by using the M-USLE.

sedimentation or erosion was expected. The average sedimentation at the spot elevations is 2.95 m and is distributed following the center-left-hand side of the lake in what appears to be delta formations of successive sediment transport events. Points D, B, H, and E differ by an average of 5.6 m. There are, however, some erosion spots cut into the bottom sediment pack. Points G and K registered a deepening of 1.9 and 2.9 m, respectively, over the years, and both are located at the right margin of the lake. Thus, the overall increase in the elevation of the bottom surface indicates sedimentation. As an example of the evolution of lake bed bathymetry, two cross-section profiles were drawn, and the bottom topography was represented for the two dates under consideration. Corresponding to the cross sections (Figure 6A, B) that extend from shores east of spot elevation B to the west of L in Figure 6A, two localized accumulations at the banks indicate possible deltas from the right and left banks due to the contribution of small streams in the proximity. However, their sediment supply seems to be substantial as the morphology interpreted along the x-axis of the figure between 200 and 300 m averages an accumulation of 5 to 6 m. The wedge observed from 500 m to the actual shoreline appears to describe a different morphology of gradual accumulation rather than deltaic deposition due to the calcareous nature of the slopes on the left bank of the river and, thus, the lake. Taking an average value over the entire lake of 2.0 m, considering cut and fill, and given the approximate area of 2×10^6 m^2, accumulation of 4×10^6 m^3 can be calculated which yields a rate of 75.5×103 m^3 year^{-1}.

4 Discussion

The circulation of sediments in the input/output approach offered by the traditional sediment budget model requires free flow from source to sinks and sustainability of fresh input when sinks are permanent, as they appear to be in the deep canyons offshore of Marbella. However, the main management action since the 1970s has been to rebuild the occupation at the frontline, reconstructing roads, parks, and bars/restaurants. This artificially induced engineering resilience, where the system position is preserved, does not intend to maintain the link between source and sink and eliminates the ecosystem services naturally offered as the protection function of the beach. The total volume in front of rigid occupied areas will be reduced and the system will be less and less effective in its inland protection, thus tending to a smaller degree of resilience with time. Higher storm impacts, or even the loss of protection functions such as total erosion of the berm and dune, could be expected in the current climate change trends, with rising sea levels and more frequent and intense storminess in the Mediterranean.

Figure 7 shows, as a conceptual characterization, the beach system of Marbella and its sediment budget resilience (Figure 7A). The natural resilience depicts a narrow, shallow BoA where the conditions of resistance are easily exceeded given that (i) wave direction is highly bimodal and (ii) storm waves can activate a very active surf zone, inducing powerful littoral drift in both eastern and western directions. The sediment input in the system could be translated in the latitude of the BoA, which is critically reduced given the significant decrease in sediment yield due to dam

retention. The conceptual assessment would induce the system to move from a scenario of natural resilience (Figure 7C) to one of engineered resilience (Figure 7D). As sediment volumes from the beach system are in circulation and away, the natural resilience moves beyond the threshold of the BoA into a new natural/ ecological scenario. Since no new sediment is input in the quantities registered in the original BoA, it moves to an engineering resilience BoA (Figure 7D), typically constrained into a set of boundary conditions. The current situation is hardly a sustainable competition against the system's attempt to move away from a natural BoA. The new BoA, where the system would develop, would typically be of less resistance and latitude given the limited availability of resources (economic, technological, and beach fill material). The results suggest that an adaptation is not achievable in the long term if sediment yields are not activated by local drainage systems.

The Bay of Marbella is limited to the east by the Cabopino dune system, where some formations of very significant infralittoral prisms suggest the classic geometry of spits but lie submerged (Malvarez et al., 2019). These formations document a previous tendency for sediment accumulation with the structure of a drift-aligned coastline. The morphology corresponds with those in which the feeding system must have been generated by large deposits or injections at a recent time. Likewise, the "source" zone is likely updrift within the Bay of Marbella and fed directly by fluvial input as the coastal cell does not seem connected to other sources (fluvial or marine) further afield to the west from the Guadalmina River (see Figure 1 for reference).

The recent evolution of the shoreline in the Bay of Marbella has shown a consistent retreat since 1956. Though the shoreline has been overall transgressive, its position has been heavily influenced by engineering structures, such as the groin fields of 1973, which produced a net advance of the shoreline but introduced localized hotspots of erosion, causing a sequence of narrow/steep sections at intervals (McDowell et al., 1993). The deterioration of back beach resources for storm protection caused various initiatives to be put in place since the 1970s to date, resulting in significant beach fills over the years (Malvarez, 2012). The sediment volume, which is estimated for the most recent replenishment to allow the creation of a 40-m average width beach over some 6-km stretch (20 m narrower than the beach resulting after the beach nourishment intervention of 1990) is $4.5 \times 10^5 \, \text{m}^3$ (MTERD, 2022). This amount would generate a profile that aims at remaining for the tourist season rather than increasing the system's resilience. Given that the estimated sediment transport in the cell is of some $1.45 \times 10^6 \, \text{m}^3 \, \text{year}^{-1}$ as calculated using the CERC formula, the beach nourishment project only sustains resilience at a mere emergency level, following trends of engineering resilience dependency (Malvarez et al., 2021).

As a direct discussion of the results obtained from the calculation of the model for sediment production and yield, we find that the M-USLE version, made extensive to the river

basin, was necessary and satisfactory for the scale and scope of this research. Working scale makes it inviable to collect soil erosion data from the watershed by adding plot size experiments or calibrations. The GIS-based model taking M-USLE inputs and calculations is, actually, the only viable source of information that may be assumed for the study area. Moreover, the intended goal of characterizing a first-order approach to sediment production without intentions to precisely quantify a total load into the marine environment follows the literature for similar studies that, almost inevitably, result in uncalibrated outcomes for real sediment yield, an almost impossible task given the complexity of the processes involved (Zhang et al., 2009; Parveen and Kumar, 2012). The present study focused on illustrating cause and effect rather than a precise quantification of the process. The accumulations found in the reservoir lake respond to the complete interruption of the sediment yield of the main river course. Although predictable, such a direct link had not been established in any of the local basins and represents a significant contribution in demonstrating empirically what many authors are arguing from a theoretical standpoint when attempting to link beach erosion to river basin sediment yield restrictions brought about by human action (Podolak and Doyle, 2015). This topic, of fundamental importance and not yet studied with the necessary detail, highlights the retention of sediments by dams, which has been the subject of studies, but not with satisfactory rigor and application of innovative methods. Access to secondary information sources that require extensive search and time-consuming networking, such as original civil engineering blueprints for works of some 60 years in the past, shows the importance of the intended rigor of data acquisition.

The relationship between land use and sociodemographic changes provides a necessary context to understand the motivations for the events. Many beach nourishment projects include as the main cause for the need to replenish the cut-off of riverine input, failing to document or even attempting to quantify this cause-effect issue (Malvárez et al., 2003; MTERD, 2022). The high complexity brought about when coastal areas become coupled with human interventions and natural processes, where both elements interact in equal measure at times (Masselink and Lazarus, 2019), has led much research to date to focus on addressing whether socioeconomic development affects shoreline stability. Most researchers agree that the impact of infrastructure development has to be negative on the overall resilience of the natural system to maintain its dynamic equilibrium if the sediment balance is altered artificially. However, the assessment of coastal resilience continues to be the future objective of new research, as proxies such as sediment starvation cannot be categorically assumed to have a quantifiable effect on beach erosion. The main sediment source to Mediterranean littoral systems comes from the hydrographic network (McDowell et al., 1993; Liquete et al., 2004; Syvitski et al., 2005; among others), and considering the behavior of reservoir lakes and dams as

lithogenous sediment traps (Willis and Griggs, 2003; Randle et al., 2006; among others), their impact on the terrestrial sediment dynamics would be as expected. Damming the main water course of a river produces a huge reduction in the sediment volume transported downstream and, ultimately, leads to severe coastal erosion. The results obtained in this study demonstrate that over the 2.14 km^2 of the reservoir La Concepción, a large volume of sediment has been trapped with positive sedimentation at the various spot heights above 5.6 m. The potential sediment accumulation scenario in the reservoir presented in Figure 5 seems like encouraging results that allow the interpretation that a bypass of sediments could be a management option. Taking the average value to be representative of a distributed sedimentation, a total volume of 11.98×10^6 m^3 is estimated to be accumulated over the 53 years that elapsed between 1966 and 2019. This represents a rate of 2.26×10^6 m^3 year^{-1}, which is directly missing from the coastal cell. However, given that some sediments would have fed the lower reaches of the river basin, the volume estimated is to be taken as less than that missing in the related coastal cell. The calculated sediment transport, as stated above, is 1.45×10^6 m^3 year^{-1} (MTERD, 2022). The embayment of Marbella, like other similar cells of Costa del Sol, is a unidirectional cell that sources from the west and sinks in the east (Senciales and Malvárez, 2003), which implies that the circulation, when interrupted, induces beach erosion in a constant rate that the natural system cannot replenish unassisted.

The excellence of beaches in terms of width, sea water quality, and available services are the main criteria used by decision-makers for tourist appeal, which became the central activity in the economy of Costa del Sol since the 1950s. However, water management, as well as beach conservation, has been one of the main focuses for managers as key resources for the tourism industry. Although many shoreline stabilization projects have been implemented over the years, decision-makers never succeeded in containing the erosive processes from the 1970s of the twentieth century thus far (Anthony et al., 2014). Attempts toward shoreline stabilization have followed the usual sequence of technology and financial-based investment under pressure from local citizens and the tourism industry (Malvárez, 2012). However, the apparent connection highlighted in research and technical reports has not yielded any attempts to even envisage a sediment management strategy of any sort taking into account river basin dynamics in their artificialized functioning, including reservoir lakes (e.g., full pumped sediment bypass, dredging, flushing, sluicing, or venting).

The exploitation of terrigenous sedimentary deposits retained in reservoir lakes in water management could have been of interest, but, although the Costa del Sol was the object of intense beach nourishment for the stabilization of the coast during the 1990s, the use of river dredging or any sediment redirecting from reservoirs has not been considered. The European Sediment Network (SedNet) has been stating, for nearly two decades since its creation by the European Commission in 2002, the extreme importance of introducing

the sediment management paradigm within the river basin management plans of Member States (Brils, 2020). To achieve such a goal, at first instance, it is required that decision-makers perceive the dredged sediments from reservoir lakes as a natural resource susceptible to being reused rather than as waste. However, this approach does not seem to have received the necessary support at the government level thus far. The cause is unknown, although it could be based on economic and environmental issues. SedNet has documented a wide range of successful experiences in Belgium (River Scheldt; Creation of a controlled flood area), the United Kingdom (Wallasea; A wetland creation project), and Sweden (Port of Gavle; Creation of a new port area) concerning the extraction of dredged fluvial and marine sediments for their subsequent reuse as raw materials for construction purposes (Brils, 2020). Other experiences documented in Puerto Rico and China have revealed that these types of actions are commonly very expensive and largely dependent on the lithology and composition of terrigenous sediments (Morris and Fan, 1998). This is especially sensitive in this case study, given the presence of a significant outcrop of peridotites within the studied river basin of the Verde River, partially located on an erosive section of the basin (Figure 7), with high slopes and poor vegetation coverage. Peridotites are very abundant in olivines and pyroxenes, and though not heavy pollutants if naturally transported to the sea, they might eventually host heavy metals that can determine higher natural backgrounds that can be taken as contamination when these materials have to be dredged. This particularity might have inferred the sediments retained in La Concepción had a problematic chemical composition for the subsequent reuse. On the other hand, some research initiatives financed by the European Commission, such as the AGRIPORT Project, succeeded in demonstrating the economic and environmental viability of reusing polluted sediments previously dredged from ports in agriculture (Iannelli et al., 2010; Renella, 2021). SedNet has also demonstrated the successful reuse of polluted sediments in some port engineering operations in the Baltic Sea Region. Spain already has experience in this type of procedure; such is the case of the decontamination of the Flix reservoir in Tarragona in Cataluña, northern Spain, carried out by the AcuaMed company, in cooperation with the Administration General of the State (AcuaMed, 2007).

The Flix reservoir case could be used as a conceptual model but also as a quantitative one since the investment of 190 million euros in decontamination enabled the recovery of a total volume of 1×10^6 m^3 of toxic sludge. If we consider that the approximate volume intended for nourishing the beaches of Marbella for 10 years (2006:2016) is 8.4×10^4 m^3, it may seem like the plausible solution of bypassing the sediments trapped in La Concepción placing the sediments directly onto the beach or nearshore environments as an economically viable scenario.

Despite the high public investment and environmental limitations, it would be interesting to pursue viability studies that provide greater insight into this approach. It may also be of high interest to assess how the reutilization of terrigenous sediments would fit within the Green Deal and Blue Bioeconomy strategies of the European Commission for conducting shoreline stabilization projects. This is now the reference framework for medium-term environmental policies in Europe (Del Río et al., 2022). Despite this, the instruments for managing the water resources at national and regional scales generally overlook this conceptual paradigm, opting instead for the application of simpler and more direct measures, such as the abandonment of hydraulic infrastructures once they undergo filling (e.g., the Robledo de Chavela reservoir, Madrid in 2014, among others).

The adaptation that is expected from a coastal system in natural conditions under current climate change will not be achieved as sea level rise and increasing erosion due to marine-induced flooding are expected along the coastal strip (Malvárez et al., 2003). There seems to be a critical need to fix the system's position. However, the protection function of the beach is not preserved and, even if the percentage of recovery is high due to frequent beach restoration projects in the area, the total volume in front of rigid occupied areas will experience a consistent reduction.

A comprehensive framework in which natural conditions, managerial decisions, and resilience assessment can be combined should be the main focus of sediment transport approaches following an integrated method. Coastal water resources of both marine and land-based segments of coastal areas could continue to be utilized in a sustainable way by integrating these concepts.

5 Conclusion

This study explores the natural and managed settings of Mediterranean coastal systems that may no longer stay in the resilience envelope without engineered support in the form of direct sediment feeding to the marine system. Modeled sediment production and measured sediment deposits in a reservoir lake affecting the main basin in Marbella Bay are used in an attempt to establish the link between sediment starvation and chronic erosion of the Bay's beaches. The behavior of coastal systems to be expected during the Anthropocene requires that hinterland and marine sediment bodies be studied in conjunction and that strategies to manage and monitor their reduced resilience include a broad and deep analysis of sediment production on slopes, sediment flow within basins, as well as its marine distribution due to coastal currents once the materials have reached the beach environments. None of these seem to have been considered in the scenario analyzed in this study, where *ad*

hoc management structures have dealt with reactive measures to control and distribute water for socioeconomic short-term development and to fix shoreline positions to safeguard coastal structures and promote economic growth. The resilience of the natural system is not fully understood by authorities and, thus, short-term solutions will not accommodate the long-term adaptation required. Even though this study has been conducted at a local scale, it may be assumed that the impact of the outcomes obtained may be representative of a general condition or situation at national or even international scales. This argument is underpinned on the basis that the main drivers of coastal erosion which have been tackled here, namely (i) major land-use changes in the middle and lower reaches of river basins, (ii) dam constructions, and (iii) the widespread development of sea defense infrastructures, are recurrent responses faced by decision-makers to deal with the socioeconomic development of the majority of coastal regions in Spain and many countries worldwide.

Data availability statement

The datasets presented in this article are not readily available because Data formats and size not easy to share except if requested. Requests to access the datasets should be directed to gcmalgar@upo.es.

Author contributions

Sediment circulation in the coastal cell has often been studied, but investigations linking soil loss and river sediment transport and retention at a dam remains a challenge. In this article, sediment yield predictions and quantitative validation of model results is provided for the main reservoir lake of the highly developed Marbella. Sediments accumulated or eroded over 50 years are then linked to the issue of marine circulation as a source-sink pattern from the fluvial to the marine environment. The resilience of the sedimentary continuum river-beach-dune system in the Mediterranean is affected by urban sprawl and water management leading the coastal environment into this situation of artificial resilience. The significant erodibility that we have estimated seems matched by potentially high sediment accumulation rates along selected profiles and spot heights across the bottom of the reservoir lake and, in combination to the marine circulation model, our results identifies that sediment budget key elements in Mediterranean settings such as soil loss, sediment entrapment in reservoirs and the coastal marine circulation is in a state of deficit that suggest the natural resilience envelope is surpassed and the system as a whole is entering a new resilience state in which engineering assistance is key. All authors contributed to the article and approved the submitted version.

Funding

Acknowledgments

Conflict of interest

The authors declare that the research was conducted in the absence of any commercial or financial relationships that could be construed as a potential conflict of interest.

Publisher's note

All claims expressed in this article are solely those of the authors and do not necessarily represent those of their affiliated organizations, or those of the publisher, the editors and the reviewers. Any product that may be evaluated in this article, or claim that may be made by its manufacturer, is not guaranteed or endorsed by the publisher.

References

AcuaMed (2007). "Informe de viabilidad de la actuación 4.d," in *Eliminación de la contaminación química del embalse del flix* (Tarragona, Spain: Aguas de las Cuencas Mediterráneas S.A)

Adger, W. N., Hughes, T. P., Folke, C., Carpenter, S. R., and Rockstrom, J. (2005). Social-ecological resilience to coastal disasters. *Science* 309 (5737), 1036–1039. doi: 10.1126/science.1112122

Anderson, J. R., Hardy, E. E., Roach, J. T., and Witmer, R. E. (1976). *A land use and land cover classification system for use with remote sensor data. 2nd ed* (Washington D.C: Department of the Interior, Geological Survey). doi: 10.3133/pp964

Anthony, E. J., Marriner, N., and Morhange, C. (2014). Human influence and the changing geomorphology of Mediterranean deltas and coasts over the last 6000 years: From progradation to destruction phase? *Earth-Sci. Rev.* 139, 336–361. doi: 10.1016/j.earscirev.2014.10.003

Berteni, F., Dada, A., and Grossi, G. (2021). Application of the MUSLE model and potential effects of climate change in a small alpine catchment in northern Italy. *Water* 13, 2679. doi: 10.3390/w13192679

Brils, J. (2020). Including sediment in European river basin management plans: Twenty years of work by SedNet. *J. Soils Sediments* 20 (12), 4229–4237. doi: 10.1007/s11368-020-02782-1

CMA (1999). *Los Criterios y estándares para declarar un suelo contaminado en andalucía y la metodología y técnicas de toma de muestras y análisis para su investigación* (Andalusia, Spain: Junta de Andalucía).

CMA (2005). *Mapa de suelos de andalucía a escala 1:400.000* (Andalusia, Spain: Red de Información Ambiental de Andalucía (REDIAM).

Cooper, J. A. G., and McKenna, J. (2008). Working with natural processes: The challenge for coastal protection strategies. *Geogr. J.* 174 (4), 315–331. doi: 10.1111/j.1475-4959.2008.00302.x

Cooper, J.A.G., Jackson, D.W.T., Navas, F., McKenna, J., and Malvárez, G. (2004). Identifying storm impacts on an embayed, high-energy coastline: examples from western Ireland. *Marine Geology* 210 (1-4), 261–280. doi: 10.1016/j.margeo.2004.05.012

Del Río, J. L., Malvárez, G., and Navas, F. (2020). Reservoir lake effects on eroded littoral systems: The case of the bay of marbella, southern Spain. *J. Coast. Res.* 95 (SI), 443–447. doi: 10.2112/SI95-086.1

Del Río, J. L., Malvárez, G., and Navas, F. (2022). "Impact of legal framework and scientific research in reservoir lake sediment management on coastal erosion and shoreline management in spain's south Mediterranean basins," in *Actas de las XI jornadas de geomorfología litoral Galicia 2022*. Eds. R. Blanco, M. Costa, A. Gómez, D. Cajade, A. Fontán, R. González, A. Bernabéu and L. López (Galicia, Spain: Servicio de Publicaciones e Intercambio Científico de la Universidad de Santiago de Compostela), 383–387.

Engman, E. (1986). Roughness coefficients for routing surface runoff. *J. Irrigation Drainage Eng.* 112 (1), 39–53. doi: 10.1061/(ASCE)0733-9437(1986)112:1(39

Flood, S., and Schechtman, J. (2014). The rise of resilience: Evolution of a new concept in coastal planning in Ireland and the US. *Ocean Coast. Manage.* 102, 19–31. doi: 10.1016/j.ocecoaman.2014.08.015

Folke, C. (2006). Resilience: The emergence of a perspective for social–ecological systems analyses. *Global Environ. Change* 16 (3), 253–267. doi: 10.1016/j.gloenvcha.2006.04.002

Francis, R. (2013) *Analysis of resilience in manmade and natural systems (Report D.1.1 of the Resilience2050.eu FP7 EU project)*. Available at: https://s3.eu-central-1.amazonaws.com/innaxis-comm/RESILIENCE2050/D1.1+Resilience2050.pdf.

García-Montoro, C. (1983). La siderurgia de río Verde y la deforestación de los montes de marbella. *Cilniana* 5, 10–17.

Giordano, A., Navas, F., and Malvárez, G. (2015). Herramienta para medir el cambio en el medio físico aplicado a la ensenada de marbella. *Geotemas* 15, 181–184.

Guisado-Pintado, E., Malvarez, G., and Ojeda, J. (2015). Procesos y dinámica costera en ensenada de marbella: evolución morfosedimentaria reciente. *Geotemas* 15, 29–32.

Gunderson, L. H., Allen, C. R., and Holling, C. S (2012). *Foundations of ecological resilience*. Island Press.

Gwapedza, D., Nyamela, N., Hughes, D. A., Slaughter, A. R., Mantel, S. K., and van der Waal, B. (2020). Prediction of sediment yield of the inxu river catchment (South Africa) using the MUSLE. *Int. Soil Water Conserv. Res.* 9, 37–48. doi: 10.1016/j.iswcr.2020.10.003

Iannelli, R., Bianchi, V., Masciandaro, G., Ceccanti, B., and Pretner, A. (2010). "Agricultural reuse of polluted dredged sediments: the AGRIPORT European project," in *12th IWA international conference on wetland systems for water pollution control* (Venice: International Water Association).

IUSS-FAO (2014). *International soil classification system for naming soils and creating legends for soil maps* Vol. 106 (Rome: World Soil Resources Report no).

Kombiadou, K., Matias, A., Costas, S., Carrasco, A. R., Plomaritis, T. A., and Ferreira, O. (2020). Barrier island resilience assessment: Applying the ecological principles to geomorphological data. *Catena* 194, 104755. doi: 10.1016/j.catena.2020.104755

Lario, J., Zazo, C., Somoza, L., Goy, J. L., Hoyos, M., Silva, P. G., et al. (1993). Los Episodios marinos cuaternarios de la costa de málaga (España). *Rev. la Sociedad Geol. Española* 6 (3-4), 41–46.

Lazarus, E. (2017). Toward a global classification of coastal anthromes. *Land* 6 (1), 1–27. doi: 10.3390/land6010013

Liquete, C., Canals, M., Arnau, P., Urgeles, R., and Durrieu de Madron, X. (2004). The impact of humans on strata formation along Mediterranean margins. *Oceanography* 17 (4), 70–79. doi: 10.5670/oceanog.2004.05

Madoz, P. (1848). *Diccionario geográfico-estadístico-histórico de españa y sus posesiones de ultramar* (Madrid, Spain: Tomo XI).

Malvárez, G. (2012). "The history of shoreline stabilization on the Spanish Costa del sol," in *Pitfalls of shoreline stabilisation: Selected case studies*. Eds. A. Cooper and O. H. Pilkey (Netherlands: Springer), 235–249. doi: 10.1007/978-94-007-4123-2_14

Malvárez, G., Ferreira, O., Navas, F., Cooper, J. A. G., Gracia-Prieto, F. J., and Talavera, L. (2021). Storm impacts on a coupled human-natural coastal system: Resilience of developed coasts. *Sci. Total Environ.* 768, 144987. doi: 10.1016/j.scitotenv.2021.144987

Malvárez, G., Navas, F., Guisado-Pintado, E., and Jackson, D. W. (2019). Morphodynamic interactions of continental shelf, beach and dunes: The cabopino dune system in southern Mediterranean Spain. *Earth Surface Processes Landforms* 44 (8), 1647–1658. doi: 10.1002/esp.4600

Malvárez, G., Pollard, H. J., and Dominguez, R. (2003). The planning and practice of coastal zone management in southern Spain. *J. Sustain. Tourism* 11 (2-3), 204–223. doi: 10.1080/09669580308667203

Malvárez, G. (1999). Procesos morfodinámicos litorales en la Costa del Sol. In: *Elementos de los paisajes de la provincia de Málaga*. Eds E. Ferre and J. M. Senciales (Servicio de Publicaciones de la Universidad de Málaga), 171–230.

Masselink, G., and Lazarus, E. D. (2019). Defining coastal resilience. *Water* 11 (12), 2587. doi: 10.3390/w11122587

McDowell, A. J., Carter, R. W. G., and Pollard, H. J. (1993). "The impact of man on the shoreline environment of the Costa del sol, southern Spain," in *Tourism vs. environment: The case for coastal areas*. Ed. P. P. Wong (Netherlands: Kluwer Academic Publishers), 189–209. doi: 10.1007/978-94-011-2068-5_13

Merrit, W. S., Letcher, R. A., and Jakeman, A. J. (2003). A review of erosion and sediment transport models. *Environ. Model. Software* 18, 761–799. doi: 10.1016/S1364-8152(03)00078-1

Moreira, J. M. (1991). "Capacidad de uso y erosión de suelos," in *Una aproximación a la evaluación de tierras en andalucía* (Andalusia, Spain: Agencia de Medio Ambiente).

Morris, G. L., and Fan, J. (1998). "Reservoir sedimentation handbook," in *Design and management of dams, reservoirs and watersheds for sustainable use* (New York: McGraw-Hill Book Company).

MTERD (2022). "Proyecto constructivo para la regeneración de playa entre la playa de Venus y punta El ancón, en el término municipal de marbella (Málaga)," in *Estudio de impacto ambiental* (Andalusia, Spain: Referencia), 29–0404.

Navas, F. (1996). "La ocupación urbana de la franja litoral de Newcastle (Irlanda del norte) y sus efectos medioambientales," in *II jornadas de geografía Urbana*. Eds. A. Ramos, G. Ponce and J. M. Dávila(Alicante: Instituto Universitario de Geografía UA), 449–456.

Navas, F., Carrero, R., and Cáceres, F. (2012). "A new approach to future scenarios for the EU COASTANCE project," in *A coastal governance experience in Andalusia* (Andalusia, Spain: Consejería de Medio Ambiente).

Navas, F., Malvarez, G. C., and Moré, G. (2017). *Coastal hazard prevention: A methodology for cost-benefit analysis* (Seville, Spain: The EcosHAZ project. Universidad Pablo de Olavide, Sevilla).

NRCS (1986). "Urban hydrology for small watersheds," in *Technical report release no. 55* (Washington D.C: United States Department of Agriculture).

Panagos, P., Borrelli, P., Meusburger, K., Alewell, C., Lugato, E., and Montanarella, L. (2015a). Estimating the soil erosion cover-management factor at the European scale. *Land Use Policy* 48, 38–50. doi: 10.1016/j.landusepol.2015.05.021

Panagos, P., Borrelli, P., Meusburger, K., van der Zanden, E. H., Poesen, J., and Alewell, C. (2015b). Modelling the effect of support practices (P-factor) on the reduction of soil erosion by water at European scale. *Environ. Sci. Policy* 51, 23–34. doi: 10.1016/j.envsci.2015.03.012

Panagos, P., Meusburger, K., Ballabio, C., Borrelli, P., and Alewell, C. (2014). Soil erodibility in Europe: A high-resolution dataset based on LUCAS. *Sci. Total Environ.* 479-480, 189–200. doi: 10.1016/j.scitotenv.2014.02.010

Pandey, A., Himanshu, S. K., Mishra, S. K., and Singh, V. P. (2016). Physically based soil erosion and sediment yield models revisited. *Catena* 147, 595–620. doi: 10.1016/j.catena.2016.08.002

Parveen, R., and Kumar, U. (2012). Integrated approach of universal soil loss equation (USLE) and geographical information system (SIG) for soil loss risk assessment in upper south koel basin, jharkhand. *J. Geogr. Inf. System* 4 (6), 588–596. doi: 10.4236/jgis.2012.46061

Pilkey, O. H., and Cooper, J. A. G. (2004). Society and Sea Level Rise. *Science* 303 (5665), 1781–82. doi: 10.1126/science.1093515

Podolak, C. J., and Doyle, M. W. (2015). Reservoir sedimentation and storage capacity in the united states: Management needs for the 21st century. *J. Hydraulic Eng.* 141 (4), 02515001. doi: 10.1061/(ASCE)HY.1943-7900.0000999

Polhill, J. G., and Gotts, N. M. (2009). Ontologies for transparent integrated human-natural system modelling. *Landscape Ecol.* 24 (9), 1255–1267. doi: 10.1007/s10980-009-9381-5

Pye, K. (1983). Coastal dunes. *Prog. Phys. Geogr.* 7 (4), 531–557. doi: 10.1177/030913338300700403

Quinn, J. E., and Wood, J. M. (2017). Application of a coupled human natural system framework to organize and frame challenges and opportunities for biodiversity conservation on private lands. *Ecol. Soc.* 22 (1), 39. doi: 10.5751/ES-09132-220139

Rajabi, A. M., Yavari, A., and Cheshomi, A. (2022). Sediment yield and soil erosion assessment by using empirical models for shazand watershed, a semi-arid area in center of Iran. *Natural Hazards* 112, 1685–1704. doi: 10.1007/s11069-022-05244-8

Randle, T. J., Yang, C. T., and Daraio, J. (2006). "Erosion and reservoir sedimentation," in *Managing water in the west. erosion and sedimentation manual* (Washington DC: Technical Service Center), 2.1–2.94.

Renella, G. (2021). Recycling and reuse of sediments in agriculture: Where is the problem? *Sustainability* 13 (4), 1648. doi: 10.3390/su13041648

Sanjaume, E., and Gracia, F. J. (2011). *Las dunas de españa* (Madrid: Sociedad Española de Geomorfología).

Scheffer, M., and Carpenter, S. R. (2003). Catastrophic regime shifts in ecosystems: Linking theory to observation. *Trends Ecol. Evol.* 18 (12), 648–656. doi: 10.1016/j.tree.2003.09.002

Schwab, G. O., Frevert, R. K., Edminster, T. W., and Barnes, K. K. (1981). *Soil water conservation engineering* (New York: John Wiley & Sons).

Senciales, J. M., and Malvárez, G. (2003). La desembocadura del río vélez (provincia de málaga, españa). evolución reciente de un delta de comportamiento mediterráneo. *Rev. C. G* 17 (1-2), 47–61.

Singh, K. P. (1982). "Runoff conditions for converting storm rainfall to runoff with S.C.S curve numbers," in *State water survey contract report no. 288. Illinois* (Illinois, USA: Department of Energy and Natural Resources).

Stewart, B. A., Woolhiser, D. A., Wischmeier, W. H., Caro, J. H., and Frere, M. H. (1975). "Control of water pollution from cropland. volume I," in *A manual for guideline development* (Washington D.C: Agricultural Research Centre, United States Department of Agriculture).

Syvitski, J. P. M., Vorosmarty, C. J., Kettner, A. J., and Green, P. (2005). Impact of humans on the flux of terrestrial sediment to the global coastal ocean. *Science* 308 (5720), 376–380. doi: 10.1126/science.1109454

Vieux, B. E. (2004). *Distributed hydrologic modeling using GIS* (Netherlands: Springer Netherlands). doi: 10.1007/978-94-024-0930-7

Williams, J. R. (1975). "Sediment-yield predictions with universal equation using runoff energy factor," in *Present and prospective technology for predicting sediment yields and sources* (New Orleans: Agricultural Research Service), 244–252.

Willis, C. M., and Griggs, G. B. (2003). Reductions in fluvial sediment discharge by coastal dams in California and implications for beach sustainability. *J. Geol.* 111 (2), 167–182. doi: 10.1086/345922

Wischmeier, W. H., and Smith, D. D. (1960). "A universal soil-loss equation to guide conservation farm planning," in *Transactions of the 7th international congress of soil science* (Wisconsin, USA: Elsevier Publishing for International Society of Soil Science), 418–425.

Yousuf, A., Bhardwaj, A., and Yousuf, F. (2022). Development and evaluation of GIS-based runoff and sediment yield watershed scale model. *Arabian J. Geosci.* 15, 1570. doi: 10.1007/s12517-022-10863-3

Zhang, Y., Degroote, J., Wolter, C., and Sugumaran, R. (2009). Integration of modified universal soil loss equation (MUSLE) into a GIS framework. *Land Degradation Dev.* 20 (1), 84–91. doi: 10.1002/ldr.893

Check for updates

Twenty years of in-situ monitoring in the south-eastern Mediterranean Levantine basin: Basic elements of the thermohaline structure and of the mesoscale circulation during 1995-2015

George Zodiatis[1,2]*, Steve Brenner[3], Isaac Gertman[4], Tal Ozer[4], Simona Simoncelli[5], Marinos Ioannou[6] and Sotiris Savva[6]

[1]Coastal & Marine Research Lab, Institute of Applied and Computational Mathematics, Foundation for Research and Technology, Heraklion, Crete, Greece, [2]ORION Research, Nicosia, Cyprus, [3]Department of Geography and Environment, Bar Ilan University, Ramat Gan, Israel, [4]Israel Oceanographic and Limnological Research, Haifa, Israel, [5]Istituto Nazionale di Geofisica e Vulcanologia, Bologna, Italy, [6]Department of Fisheries and Marine Research, Nicosia, Cyprus

The in-situ data gathered over two decades since mid-1990s in the South-Eastern Levantine Basin from 34 hydrographic campaigns and from 35 bi-weekly and monthly Voluntary Observing Ships (VOS) transects, after the pioneering POEM cruises, have provided insight on the dominant meso-scale coherent circulation features of this sub-basin. The most pronounced feature, the anticyclonic Cyprus Eddy, migrates over the broad region of the Eratosthenes seamount and exhibits significant seasonal and inter-annual spatial-temporal variability. Another prominent structure of the sub-basin is the anticyclonic Shikmona Eddy generated by instabilities of the strong northward flowing jet along the south-easternmost shelf and slope of the Levantine basin. Its evolution and co-existence with the Cyprus Eddy, cause the periodic re-establishment of the Shikmona Gyre, which was first observed during the POEM cruises in mid-1980s. The offshore, cross basin, eastward flowing Mid-Mediterranean Jet (MMJ) defines the northern and southern flanks of these sub-basin scale anticyclonic eddies and transports the lower salinity Modified Atlantic Water (MAW) in the subsurface layer, through the warmest and most saline waters of the Mediterranean. Periodically, the MMJ bifurcates and/or is diverted northward, along the western coast of Cyprus due to westward and northward spatial fluctuations of the Cyprus Eddy's western boundaries. The current long term in-situ monitoring of the sub-basin provides an overview of the extent of the main water masses and characterizes their variability throughout the period considered. The analysis of the data indicates an increase of the temperature and salinity of the Levantine Surface Water (LSW) and of the

subsurface MAW. The Eastern Mediterranean Transient Water (EMTW) is shown to occupy the deep cavities in the vicinity of the Eratosthenes seamount while its upper boundary was found to be lifted to shallower depths over a period of two decades.

1 Introduction

The Physical Oceanography of the Eastern Mediterranean (POEM) collaborative cruises carried out during mid to end of 1980s are considered as a major breakthrough in the modern investigation of the physical oceanography in the Eastern Mediterranean. For the first time new in-situ, reliable instruments, such as the CTDs were used to gather high vertical resolution (1 m) quasi-synoptic mesoscale data on board several research vessels from Cyprus, Greece, Israel, Italy, and Turkey (Robinson et al., 1992). During the multi-national POEM cruises, a detailed pattern of the mesoscale circulation in the Eastern Mediterranean Levantine Basin was defined, consisting of several alternating cyclonic and anticyclonic eddies and gyres, and an offshore, cross basin jet, named as the Mid Mediterranean Jet (MMJ) which transports Modified Atlantic Water (MAW) eastward. The Rhodes Gyre was found to be flanked to the south by the eastward flowing MMJ, and to the west by the warm, anticyclonic Ierapetra eddy, which is located southeast of Crete (Ozsoy et al., 1991; Robinson et al., 1992). The dominant circulation features in the south-eastern Levantine were two anticyclonic gyres, the Mersa-Matruh gyre located offshore between Libya and Egypt, and a non-permanent, multi-pole Shikmona Gyre, consisting of three anticyclone eddies (Hecht et al., 1988; Robinson et al., 1992) - one eddy offshore Egypt, a secondary eddy offshore Israel-Lebanon and a third eddy closer to the Eratosthenes sea mount (SM). The latter was the most pronounced and named as the Cyprus Eddy by Brenner (1989); Brenner (1993). It was described as a transient or recurrent feature (Robinson et al., 1992; Robinson and Golnaraghi, 1993; Malanotte-Rizzoli et al., 1999), although the generation mechanisms of the Cyprus and Shikmona eddies and the Shikmona Gyre remained unresolved. Later Millot and Taupier-Letage (2005), based only on satellite images of sea surface temperature (SST), claimed that the MMJ was absent and that MAW flowed eastward along the North African shelf and slope as first proposed by Nielsen (1912).

Prior to POEM, Ovchinnikov et al. (1976) provided an extensive description of the basin wide circulation which emphasized the dominant cyclonic Rhodes Gyre in the Eastern Mediterranean Levantine (EML) basin and corroborated the anticlockwise EML circulation described by Nielsen (1912), but no evidence of other prominent circulation features was provided. Following POEM, Pinardi et al. (2015) presented a synthesis of the Mediterranean Sea circulation structure and dynamics from a 23-year long ocean reanalysis from 1987-2007 (Adani et al., 2011) which allowed, for the

first time, a comprehensive description of the time-mean surface and intermediate depth circulation including its low frequency components and the main water mass formation processes. They noted that the Eastern Mediterranean circulation depicted by the reanalysis dataset was very close to that described by the early basin-scale circulation studies (Robinson et al., 1992; Malanotte-Rizzoli et al., 2003) except for the subdivision of the Ionian Sea into northern and southern regions by the variable jet referred to as the Atlantic Ionian Stream (AIS). An analysis of the circulation during 1987-2014 was also presented in Section 3.1 of von Schuckmann et al. (2016) based on an expanded reanalysis dataset (Simoncelli et al., 2014), with a main focus on the Ionian circulation and its impact on the salinity distribution. The AIS was shown to influence thermohaline characteristics and water mass formation in the Levantine basin (Simoncelli et al., 2018) depending on the direction of transport of the relatively fresh surface waters of Atlantic origin. Menna et al. (2021) confirmed the influence of the quasi-decadal reversal of the Northern Ionian circulation on the thermohaline properties of the Levantine Surface Water (LSW) and Levantine Intermediate Water (LIW) as well as on the presence of MAW in the Cyprus Eddy during periods of anticyclonic circulation in the Northern Ionian.

The Eastern Mediterranean Levantine thermohaline structure is characterized by high salinity in the upper, near surface and in the intermediate water layers, known respectively as LSW and the LIW, and lower salinity layers just below the surface (MAW) and in the deepest layers comprising Eastern Mediterranean Deep Water (EMDW). The most variable water mass of the Levantine basin is the relatively low salinity MAW, which originates from the Atlantic inflow through the Strait of Gibraltar. While flowing eastward, the salinity of this water increases from 36.3 due to net evaporation. It reaches as far as the Levantine basin where the MAW appears as a well-pronounced subsurface salinity minimum between 40 and 80 m, with salinity ranging from 38.60 to 38.95 (Ovchinnikov et al, 1976; Hecht et al., 1988; Ozsoy et al., 1991).

The main source of LIW is the Rhodes gyre where it is formed during winter by convective mixing processes (Hecht and Gertman, 2001). It spreads in the intermediate layers across the Levantine basin, then westward through the Sicily Channel (Pinardi et al., 2015; Schroeder et al., 2017; Simoncelli et al., 2018), and finally contributes to the Mediterranean Outflow Water (MOW) flowing through the Strait of Gibraltar spreading in the deeper layers of the North Atlantic Ocean (McDowell and Rossby, 1978; Armi and Zenk, 1984; Armi et al., 1988; Karlin et al., 1988; García-Lafuente et al., 2021).

Below the EMDW, at depths deeper than 1500 m, the Eastern Mediterranean Transient Waters (EMTW), later referred to as Cretan Deep Water by Pinardi et al. (2015) and Simoncelli et al. (2018), are found with salinity and temperature values slightly higher (Klein et al., 1999) than the layer above. In contrast to EMDW, which is usually formed in the Adriatic Sea (Lascaratos et al., 1999), the EMTW formation was only observed once during the Eastern Mediterranean Transient (EMT) period (Roether et al., 1996). It started to spill into the Ionian Sea and the Levantine basin from the Cretan Sea through the Cretan Arc straits in 1989 and stopped around 1993 (Theocharis et al., 1999). In order to sink to the sea floor and spread in the bottom layer, the new water mass had to have a potential density anomaly higher than 29.2 kg/m^3. Such dense water near the bottom of the Cretan Sea was first observed in October 1987, but this isopycnal surface was raised high enough to spill over the sill of Cretan Arc straits only in 1989, and thus explaining the weak initial signal of EMTW during 1987-1992. This first phase of the EMT was related to the redistribution of salinity in the Eastern Mediterranean due to an anticyclonic basin-wide circulation in Ionian Sea during 1986-1987 (Malanotte-Rizzoli et al., 1999; Section 3.1 of von Schuckmann et al., 2016). The interannual switching between periods of salinification and freshening of the upper layers in the Levantine basin, as well as intensification of dense water formation in the Adriatic Sea or in the Aegean Sea were connected with reversals in the direction of the upper layer circulation in the North Ionian referred to as the Adriatic-Ionian Bimodal Oscillation System (BIOS) by Gačić et al. (2010); Gačić et al. (2011) or as the Northern Ionian Reversal (NIR) by Pinardi et al. (2015). Typical winter cooling in the Aegean after the first stage of the EMT was enough to cause the massive formation of very dense water on the Lesvos–Lemnos Plateau and Cyclades followed by cascading in to the Cretan Sea (Gertman et al., 2006). In the next stage the dense water formation and spilling into the Ionian and Levantine were further intensified by an extraordinary decrease of water temperature (by about 0.35°C) which was forced by a prolonged cold air-temperature anomaly throughout the Middle East during the winters 1992, 1993, and 1994, which is attributed to the massive injection of volcanic aerosols into atmosphere by the eruption of Mount Pinatubo in June 1991 (Genin et al., 1995). The EMTW formation rate in the period from mid-1992 to late 1994 was about 3 Sv, which is 10 times larger than normal rate of EMDW formation in the Adriatic Sea. Simoncelli et al. (2018) demonstrated the capability of the reanalysis dataset to successfully reproduce the main water masses formation events in the Mediterranean Sea, including the formation of the Cretan Deep Water and its density increase from the first to the second phase of the EMT.

Various physical and biogeochemical processes in the Cyprus Eddy were also studied by Hecht et al. (1988); Brenner (1989); Brenner et al. (1991); Krom et al. (1992); Brenner (1993); Zodiatis et al. (1998); Zohary et al. (1998); ; Krom et al. (2005); Groom et al. (2005); Zodiatis et al., 2004; Zodiatis et al. (2005a); Zodiatis et al. (2005b); Zodiatis et al., 2007; Hayes et al. (2011); Christiansen et al. (2012); Menna et al. (2012); Schroeder et al. (2012); Zodiatis et al. (2013); Hayes et al. (2014); Zodiatis et al. (2016); Hayes et al. (2019); Barboni et al. (2021); Menna et al. (2021); Menna et al. (2022) using in-situ data gathered from different observing platforms, such as Surface Velocity Program (SVP) Lagrangian drifters, Argos

floats, gliders, research vessels and remote sensing data. Most recently Schroeder and Chiggiato (2022) presented a concise summary of the circulation and water mass properties of the Mediterranean in general, and specifically the Eastern Mediterranean, within the context of the general oceanography of the Mediterranean, past, present, and future.

The present work aims to provide an overview of the dominant mesoscale hydrodynamical features of the Eastern Mediterranean Levantine Basin, addressing among other issues the previous uncertainties regarding the Cyprus Eddy, the Shikmona gyre, the Shikmona Eddy; the path of the offshore cross basin MMJ and the associated transport of MAW; and temporal changes in the characteristics of the water masses, especially MAW and deep-water transients. To address these issues two large datasets gathered in the SE Levantine basin in the post POEM period from 1995-2015 were analyzed: a) more than 2000 high vertical resolution in-situ CTD profiles gathered during the Cyprus Basin Oceanography (CYBO), CYCLOPS, MSM14-1 and Haifa Section (HaiSec) research cruises (Tables 1A, B) more than 500 XBTs profiles gathered during the Mediterranean Forecasting System Pilot Project (MFSPP; Manzella et al., 2003; Pinardi et al., 2003;) and the Mediterranean Forecasting System Towards Environmental Predictions project (MFSTEP; Manzella et al., 2007; Pinardi and Coppini, 2010) (Table 1B).

The paper is organized as follow: a) in the Methods section the research cruises, the VOS transects, the datasets and their processing are described; b) the Results and Discussions section is sub-divided into two main subsections describing the thermohaline structure and the mesoscale flow features obtained from: 1) the CYBO, HaiSec, CYCLOPS and MSM14-1 cruises, and 2) the MFSPP and MFSTEP Volunteer Observing Ship (VOS) transects; and c) in the Conclusions the overall results addressing the above mentioned hydrodynamic and hydrographic uncertainties in the SE Levantine basin are summarized.

2 Methods

A total of more than 2000 deep CTD casts suitable for hydrographical analyses were gathered in the post POEM period, from 1995-2015 during 31 CYBO and HaiSec cruises (Table 1A). Profiles were obtained using SBE 911plus CTDs on board multi-purposed vessels, such as "Argonaut" and "Flying Enterprise" of the EDT Towage and Salvage/EDT Offshore company, on board the R/V "Aegaeo" of the *HCMR-Hellenic Center for Marine Research*, and on board of the R/V "Shikmona" of the *IOLR-Israel Oceanographic and Limnological Research*. Locations of the CTD stations are shown by the red dots in Figure 1. The profilers measured pressure, temperature, conductivity, and oxygen. The sensors were factory calibrated annually, mainly at the facilities of the SBE. The raw CTD data were pre-processed following the recommended procedure for the SBE 911plus, using the SBE Data Processing software. The pre-processing steps include conversion from raw binary data to engineering units in ASCII format, separation of the downcast from the up-cast profiles, low pass filtering of pressure channel to reduce high frequency noise, correction for pressure inversions caused by ship motion, derivation of the corrected salinity (psu) and bin averaging of the downcast profile into 1 dbar pressure intervals.

TABLE 1 The chronology of (a) the CYBO, HaiSec, CYCLOPS, and MSM14-1 cruises, and (b) the XBT transects Limassol (Cyprus) − Port Said (Egypt) and Limassol − Alexandria (Egypt).

	Table 1a					Table 1b			
No.	Cruise	Start	End	# CTD Profiles	No.	Transect	Start	End	# XBT Profiles
1	CYBO-01	20/09/1995	17/10/1995	73	1	CY-01- MFSPP	27/09/1999	28/09/1999	23
2	CYBO-02	06/05/1996	13/05/1996	77	2	CY-02 MFSPP	25/10/1999	26/10/1999	19
3	CYBO-03	21/10/1996	30/10/1996	85	3	CY-03-MFSPP	22/11/1999	23/11/1999	24
4	CYBO-04	06/05/1997	12/05/1997	89	4	CY-04-MFSPP	13/12/1999	14/12/1999	23
5	CYBO-05	18/10/1997	04/11/1997	88	5	CY-05-MFSPP	27/12/1999	28/12/1999	24
6	CYBO-06	24/07/1998	02/08/1998	91	6	CY-06- MFSPP	10/01/2000	11/01/2000	22
7	CYBO-07	12/01/1999	19/01/1999	85	7	CY07-MFSPP	24/01/2000	25/01/2000	17
8	CYBO-08	14/04/1999	22/04/1999	89	8	CY-08-MFSPP	07/02/2000	08/02/2000	20
9	CYBO-09	05/05/2000	12/05/2000	87	9	CY-09-MFSPP	21/02/2000	22/02/2000	19
10	CYBO-10	26/08/2000	02/09/2000	87	10	CY-10-MFSPP	06/03/2000	07/03/2000	20
11	CYBO-11	06/04/2001	11/04/2001	81	11	CY-11-MFSPP	20/03/2000	21/03/2000	19
12	CYCLOPS-1	06/05/2001	15/05/2001	54	12	CY-12 MFSPP	03/04/2000	03/04/2000	20
13	CYBO-12	23/08/2001	29/08/2001	89	13	CY-13-MFSPP	17/04/2000	18/04/2000	20
14	CYBO-13	24/03/2002	31/03/2002	77	14	CY-14-MFSPP	01/05/2000	02/05/2000	19
15	CYCLOPS-2	11/05/2002	26/05/2002	67	15	CY-15-MFSPP	19/05/2000	20/05/2000	19
16	CYBO-14	25/08/2002	31/08/2002	87	16	CY-16-MFSPP	09/06/2000	10/06/2000	19
17	CYBO-15	17/05/2003	25/05/2003	92	17	CY-17-MFSPP	26/06/2000	27/06/2000	21
18	HaiSec	27/08/2003	27/08/2003	6	18	CY-01-MFSTEP	26/05/2004	27/05/2004	19
19	CYBO-16	23/08/2003	31/08/2003	86	19	CY-02-MFSTEP	22/09/2004	23/09/2004	18
20	CYBO-17	25/04/2004	03/05/2004	88	20	CY-03-MFSTEP	20/10/2004	21/10/2004	18
21	CYBO-18	16/08/2004	25/08/2004	90	21	CY-04-MFSTEP	06/12/2004	07/12/2004	17
22	CYBO-19	05/09/2005	13/09/2005	88	22	CY-05-MFSTEP	13/01/2005	14/01/2005	16
23	CYBO-20	16/05/2006	24/05/2006	76	23	CY-06-MFSTEP	26/02/2005	27/02/2005	19
24	CYBO-21	21/07/2007	27/07/2007	70	24	CY-07-MFSTEP	22/03/2005	23/05/2005	18
25	CYBO-22	18/08/2009	27/08/2009	79	25	CY-08-MFSTEP	18/04/2005	19/04/2005	19
26	CYBO-23	23/08/2010	31/08/2010	78	26	CY-09-MFSTEP	18/05/2005	19/05/2005	16
27	MSM14-1	17/12/2009	12/01/2010	50	27	CY-10-MFSTEP	13/06/2005	14/06/2005	16
28	CYBO-24-HaiSec	28/10/2012	31/10/2012	20	28	CY-11-MFSTEP	18/07/2005	19/07/2005	8
29	CYBO-25-HaiSec	23/12/2012	27/12/2012	30	29	CY-12-MFSTEP	22/08/2005	23/08/2005	9
30	CYBO-26-HaiSec	22/12/2013	25/12/2013	20	30	CY-01-CYBO-09	07/05/2000	11/05/2000	6
31	HaiSec-31	11/03/2014	11/03/2014	7	31	CY-02-CYBO-15	20/05/2003	25/05/2003	36
32	Haisec-32	20/08/2014	20/08/2014	9	32	CY-03-CYBO	10/03/2005	10/03/2005	7
33	HaiSec-33	09/03/2015	09/03/2015	8	33	CYC04-CYBO	02/10/2006	03/10/2006	22
34	Haisec-34	19/08/2015	19/08/2015	8	34	CY-05-CYBO	18/08/2008	19/08/2008	19
					35	CY-06-CYBO	19/07/2010	21/07/2010	17

The number of profiles per cruise are listed.
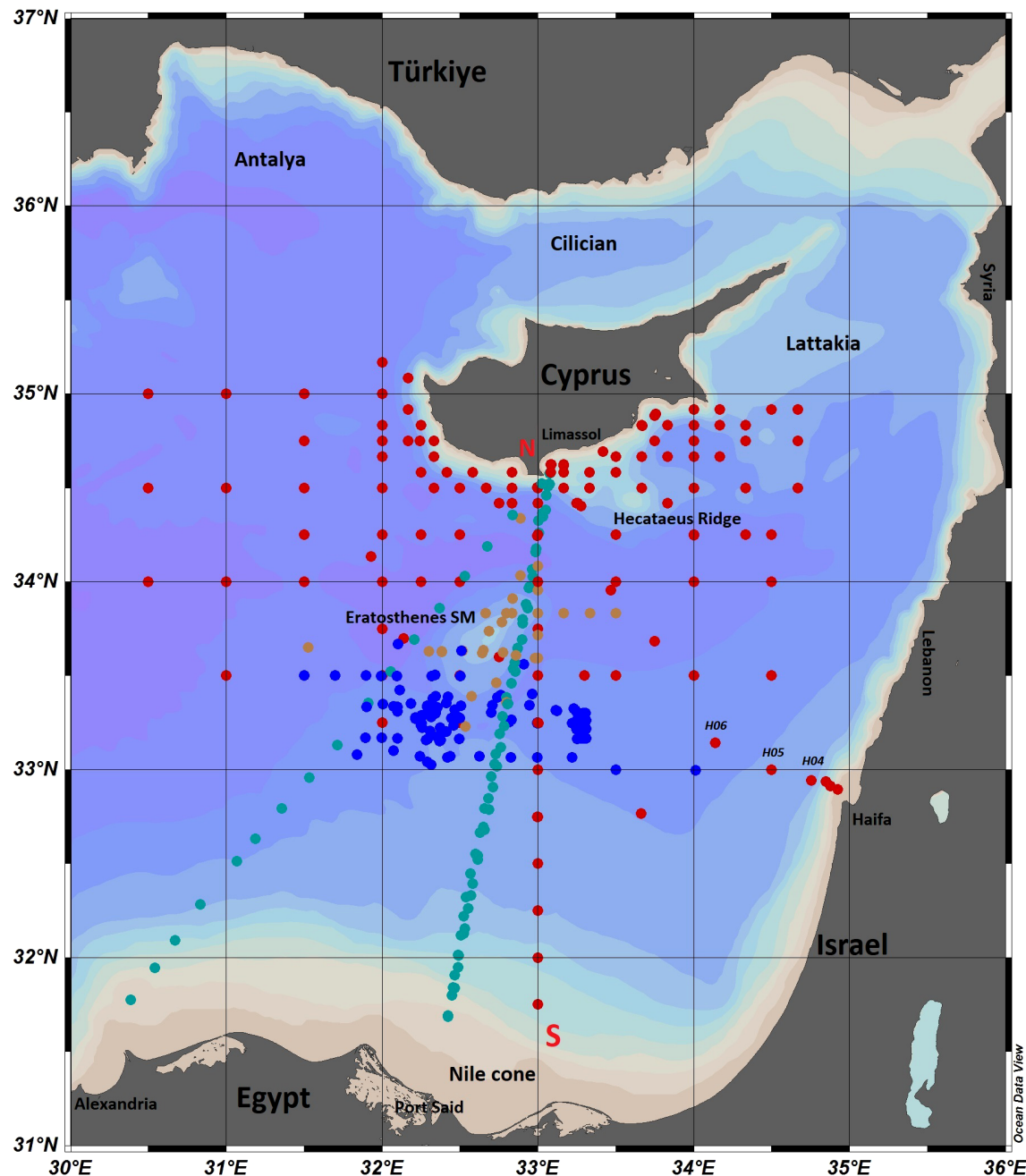
Physiography of the eastern Levantine Basin and locations of the CTD stations in the SE Levantine gathered during the CYBO and HaiSec (red dots), CYCLOPS (blue dots) and MSM14-1 (light brown dots) research cruises, and the XBT stations during the MFSPP-VOS and MFSTEP-VOS (light green) transects along Limassol (Cyprus) - Port Said (Egypt) and Limassol – Alexandria (Egypt). Stations H04-H06 across the Israeli shelf are also labeled.

Moreover, during the two CYCLOPS cruises on board the R/V "Aegaeo" and during the MSM14-1 cruise on board the R/V "Marian S. Merian", a total of 173 CTD profiles (Table 1A) were collected in the sea area of the Eratosthenes SM. The stations are indicated by the blue and light brown dots in Figure 1. Similarly, the CYCLOPS and MSM14-1 datasets, were processed following the same procedures as applied for the CYBO and HaiSec datasets.

Furthermore, within the framework of the MFSPP and MFSTEP projects a total of 35 XBT transects (Fusco et al., 2003) were carried out bi-weekly between September 1999 and June 2000 and monthly

between May 2004 to October 2005, along the transects Limassol (Cyprus) - Port Said (Egypt) and Limassol - Alexandria (Egypt), on board Volunteer Observing Ships (VOS) using cruise liners such as the "Princess Victoria" and "Princess Marissa" of the *Louis Cruise Lines*. A total of 348 XBT profiles, down to 460 m, were obtained during the MFSPP transects and 209 XBT profiles, down to 900 m, were obtained during the MFSTEP transects (Table 1B). Station locations are shown by the light green dots in Figure 1.

All of the pre-processed datasets gathered from the above CTD research cruises and VOS XBT transects (Tables 1A, B) were
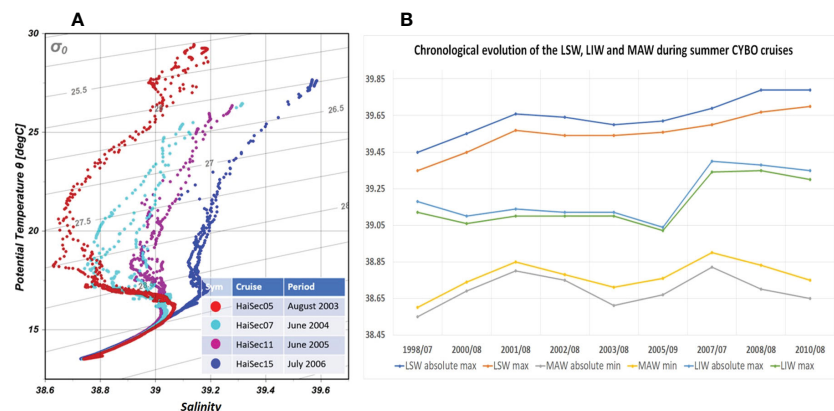
FIGURE 2
(A) T/S diagram of data from the 4 summer HaiSec cruises carried out from August 2003 to July 2006 at the stations H04–H06; **(B)** Evolution of the salinity extremes of the LSW (maximum), of the MAW (minimum) and of the LIW (maximum) during the summer CYBO cruises from 1998 to 2010.

converted to SeaDataNet ODV format for data Quality Control (QC) using the Ocean Data View software (ODV) (Schlitzer, 2002; https://odv.awi.de/). The QC criteria follow those recommended in the SeaDataNet Quality Control Procedures version 2.0 (https://www.seadatanet.org/Publications/Technical-documentation) and by Scory et al. (2018) since the datasets were submitted to and disseminated through the SeaDataNet portal (https://cdi.seadatanet.org/search). After the QC of the data, the ODV software was used to plot thematic maps, temperature and salinity cross sections, profiles, and T/S diagrams. The in-situ data were interpolated as necessary using the DIVA method (Troupin et al., 2010 - https://github.com/gher-uliege/DIVA) with automatic scaling length, which is embedded in the ODV software. Then, the maps of the dynamic height and the

cross sections with the geostrophic velocities were calculated and plotted with the same software using a reference level of 700 m.

3 Results and discussion

In this section the results are presented in two main subsections following the primary type and source of in situ, cruise data: (1) deep CTD casts, and (2) XBT transects. Each data set provides a broad overview of the spatial and temporal characteristic and variability of the circulation as assessed through the in-situ profiles, TS diagrams, vertical cross sections of temperature, salinity and geostrophic velocities, and horizontal maps of dynamic height.
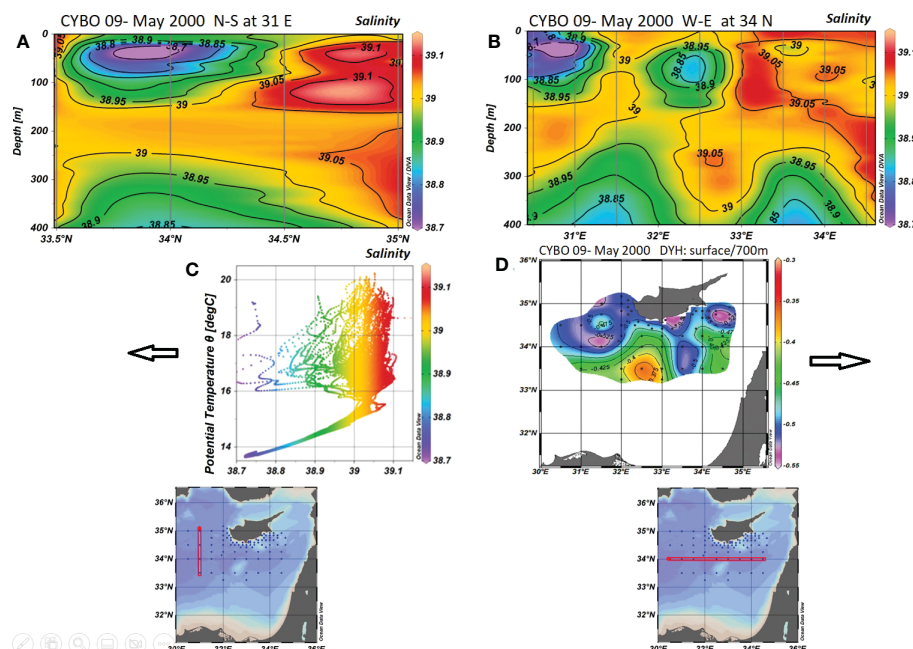
FIGURE 3
Results from CYBO 09 (May 2000): **(A)** N–S section along 31°E, **(B)** W–E section along 34°N, **(C)** T/S diagram, and **(D)** dynamic height topography relative to 700 dbar.

3.1 Deep CTD cast cruises in the SE Levantine

The post POEM long term, in-situ investigations in the SE Levantine from 1995 to 2015, within the framework of the CYBO and HaiSec cruises elucidated some answer and highlighted the issues regarding: a) the persistence and the seasonal-interannual spatial fluctuation of the anticyclonic Cyprus Eddy, b) the generation and the re-appearance of the anticyclonic Shikmona Eddy and gyre, c) the MMJ as an offshore cross basin flow transferring the MAW, d) the impact of the global warming on the water masses of the SE Levantine, and e) the characteristics of the EMTW in the deep cavities of the SE Levantine. These cruises were supplemented with data from several limited duration and site or process specific cruises - the two CYCLOPS cruises (Krom et al., 2005; Thingstad et al., 2005), which were devoted solely to investigating the biogeochemistry of the core of the Cyprus Eddy (Table 1A; Figure 1), and the MSM14-1 cruise (Christiansen et al., 2012), which focused on physical, biogeochemical and biological sampling at and around the Eratosthenes SM (Table 1A; Figure 1).

3.1.1 Main thermohaline characteristics

The high rates of the summer heating and evaporation transform the upper surface layer of the SE Levantine into the most saline (up to 39.6-39.79) and warmest (28-30.7°C) surface waters in the Mediterranean (LSW), as observed during the summer CYBO and HaiSec cruises from 1995 to 2015.

In general, the T/S diagrams from all the summer CYBO and HaiSec cruises (listed in Table 1A) show the well-known "S" shape of the temperature and salinity relationship characterizing the water mass distribution of the Levantine basin as shown for example in Figure 2A for four summer cruises. The four main water masses are visible - the warm, saline LSW, the less saline subsurface water attributed to the MAW, the maximum salinity in the intermediate water layer attributed to the LIW, and the less saline deep waters below. The superimposed T/S diagrams (Figure 2A) gathered during four summer HaiSec cruises at stations H04-H06 spanning the Israeli slope (Figure 1), which were

revisited repeatedly from 2003 to 2006, clearly demonstrates the rapid salinization of the main water masses in the eastern most part of the SE Levantine from the surface down to the intermediate water depths within a period of only 3 years. This is further emphasized in the 12-year evolution of the characteristic salinity extremes of the three water masses LSW, MAW, and LIW, for all CYBO summer cruises shown in Figure 2B where the LSW salinity maximum increased from an average of 39.35-39.45 in summer 1998 to an average of 39.70-39.79 in summer 2010, while the salinity of the subsurface MAW minimum increased from 38.55 in the summer of 1998 to 38.85 in the summer 2008. The salinization of the LIW (150-350 m) was observed to occur more rapidly from the year 2005 (Figure 2B) with an average maximum salinity in August 2010 between 39.30-39.35, while a decade earlier its maximum values varied on average between 39.08-39.1. This is consistent with the salinization of the water masses observed by Ozer et al. (2017) across the broader region of the southeastern quadrant of the Levantine basin.

MAW originates from the Atlantic water inflow through the upper layer of the Straits of Gibraltar while its salinity gradually increases as it is transported to the east due to net evaporation. MAW should appear near the surface throughout the Mediterranean, however surface heating and strong evaporation in the eastern basins from spring through autumn create the warm saline LSW which caps the MAW. Thus, MAW generally appears as subsurface salinity minimum between the more saline LSW and LIW. Nevertheless, on occasion MAW can be observed in the spring as a single layer extending from the surface down to 100 m depth in the western part of the SE Levantine basin as shown in Figure 3 for the CYBO 9 cruise (May 2000). This can be seen near the center of the N-S section of salinity along 31°E (Figure 3A), located to the west of Cyprus, with salinity values between 38.7-38.95. This is also seen at the western edge of the W-E section along 34°E (Figure 3B) as well as in the points falling in the upper left range of the T/S diagram (Figure 3C). As the MAW is transported eastward by the meandering MMJ (Figure 3D) the core of the MAW deepens and no longer reaches the surface as shown by the subsurface minimum near the
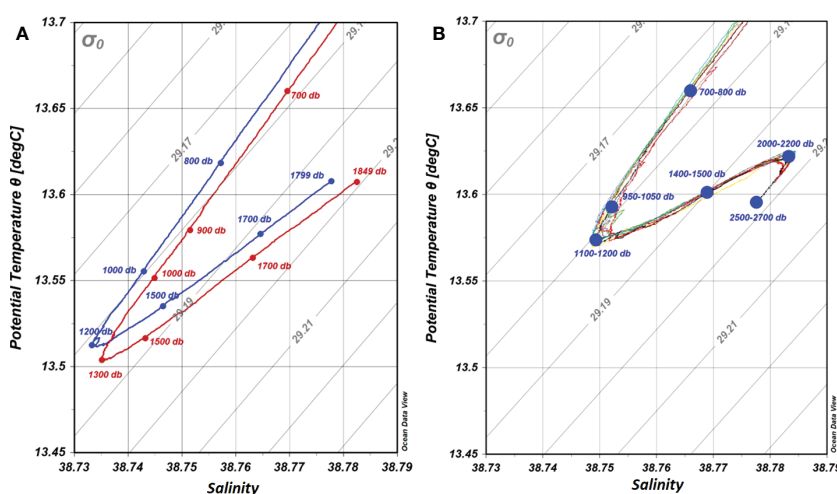

FIGURE 4
T/S diagrams of the EMTW in the SE Levantine: a) from a deep station south of Cyprus for CYBO 12 (Aug 2001) in blue and for CYBO 14 (Aug 2002) in red and b) from all deep stations (below 2000 dbar) for CYBO-HaiSec 25 (Dec 2012).
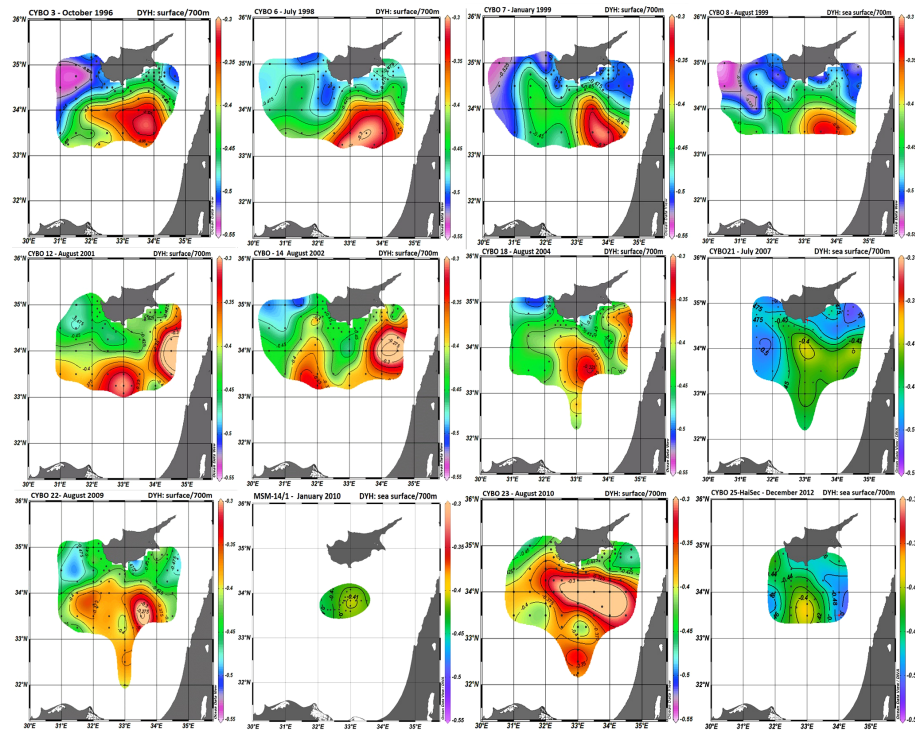
FIGURE 5
The dynamic height topography relative to 700 dbar during the cruises CYBO 3, 6, 7, 8 (top row); CYBO 12, 14, 18, 21 (middle row); and CYBO 22, MSM 14-1, CYBO 23, CYBO-HaiSec 25 (bottom row) corresponding to three active periods with: top row the dominance of the Cyprus Eddy (1996-1999), middle row the co-existence of the Cyprus and Shikmona eddies (2000-2007) and bottom row the dominance of the Cyprus Eddy (2009-2012).

center of Figure 3B where salinity values of 38.80-38.95 were observed.

During the CYBO cruises 12 (Aug 2001) and 14 (Aug 2002), the EMTW could be clearly identified in Figure 4A at depths below 1400 dbar with salinities of 38.74-38.78 and temperatures of 13.5-13.6°C, both increasing with depth. A decade later, during the CYBO-HaiSec 25 cruise in Dec 2012, the thermohaline characteristics of the EMTW changed noticeably as shown in Figure 4B. The transition depth from EMDW to EMTW (indicated by the turning point on the T/S curve) was lifted by roughly 100 dbar, while the water became warmer and saltier with typical increases of 0.05°C and 0.01 respectively. A similar shift in the characteristics of the deepest waters in the T/S diagrams was observed by Ozer et al. (2020) at station H06 of the HaiSec cruises during the period 2012-2019, thus indicating that the signal of changes in deep water characteristics is a long-term process, lasting for at least two decades. In addition, the T/S diagram in Figure 4B shows a second and deeper transition point, indicating that at depths below the 2000 dbar cooler and slightly less saline deep waters intruded into the deepest layers of the SE Levantine basin. The post EMT intrusion of this cooler, less saline deep water originating from the Adriatic Sea was observed in the eastern Levantine basin as early as 2008 (Gertman et al., 2010b; Gertman et al., 2016).

3.1.2 Main mesoscale circulation features

The two most prominent mesoscale circulation features in this region are the anticyclonic Cyprus and Shikmona eddies appearing in distinct geographic regions. The Cyprus Eddy appears in the vicinity of the Eratosthenes SM while the Shikmona Eddy appears to the

southeast of Cyprus. The location of the center of each eddy in a particular cruise was designated as (1) the point with the deepest depression of the isotherms at the base of the warm, saline thermostad forming the core of the eddy along a vertical cross section, or (2) the highest point in the horizontal map of the dynamic height topography. Criterion (1) was used by Brenner (1993). To be more precise, Gertman et al. (2007) proposed using the depression of the potential density surfaces rather than isotherms, although the differences are expected to be small as indicated by the respective temperature and salinity cross sections in Brenner (1993). The Cyprus Eddy was observed in 29 CTD cruises (CYBO, CYBO-HaiSec, CYCLOPS, MSM 14-1) as well as in 33 XBTs transects presented below in Section 3.2. Its center was located between 32°E to 34°E and fluctuating roughly +/- 50 km north and south around 33.5°N. The Shikmona Eddy was observed to co-exist with the Cyprus Eddy in only 9 of the CTD (CYBO) cruises, with its eddy center located between 34°E to 35°E and fluctuating less than +/- 50 km north and south around 34°N. In earlier studies (POEM and related cruises) these features were described as recurrent or persistent, which is corroborated by this study.

The in-situ dynamic height topography from winter 1996 to summer 1999 is shown in the top row of Figure 5 for four dates selected from the first eight CYBO cruises. These maps demonstrate that the anticyclonic Cyprus Eddy was quite well developed south of Cyprus, slightly east of the Eratosthenes SM, with its eddy center migrating seasonally in the longitudinal direction, between 33° 30'E and 33° 45' E, but remaining near latitude 33° 30' N. The geostrophic velocities at its periphery were up to 0.35-0.45 m/s. From spring 2000
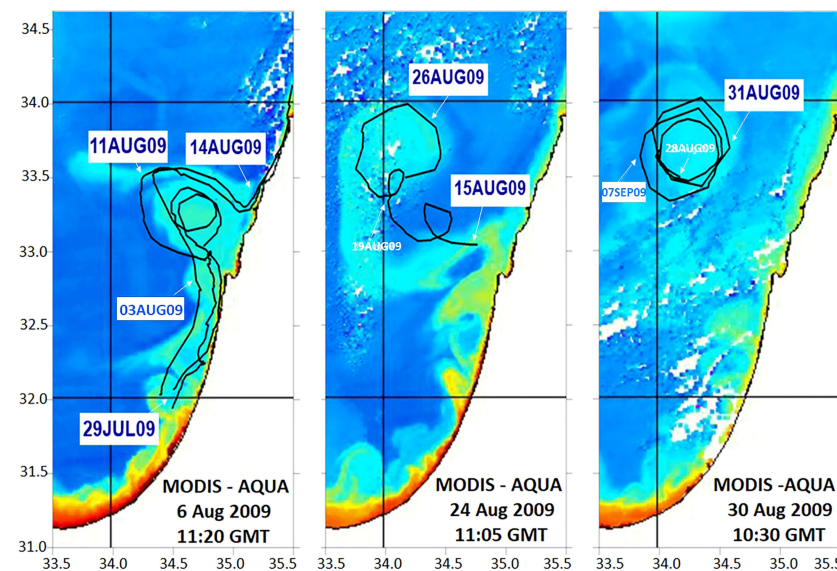
FIGURE 6
The NEMED SVP drifter trajectories superimposed on MODIS satellite images along the Israel-Lebanon shelf and slope from 29 Jul to 31 Aug 2009, showing the anticyclonic eddy formation starting as a meander in the northward flowing shelf-slope current, detaching from the current as an anticyclonic eddy and drifting out to the open sea towards the northwest. This eddy was simultaneously observed during the summer CYBO 22 cruise in late August 2009.

to summer 2007 (Figure 5 middle row), the dynamic height topography showed a more complicated flow structure south of Cyprus, with two well developed anticyclonic eddies, the Cyprus Eddy, which was shifted west of the Eratosthenes SM and a secondary anticyclonic eddy located in the eastern part of the surveyed area. The latter is attributed to the secondary eddy mentioned by the POEM group and named as the anticyclonic Shikmona Eddy by A. Hecht as reported in Robinson et al. (1991). During this period the Cyprus Eddy was shifted significantly westward or southwestward by 55-85 km, and in some cases by as much as 110 km. The eddy center migrated seasonally between longitudes 33° 00'E and 31° 45'E but in a very limited latitude range between 33° 15'N and 33° 30'N. The Shikmona Eddy was located east of the Cyprus Eddy, with its center migrating seasonally, between longitudes 34° 15'E to 34° 30'E but remaining close to latitude 34° 00'N. Around the time of the two CYCLOPS cruises in the springs of 2001 and 2002, the corresponding CYBO cruises 12 (Aug 2001) and 14 (Aug 2002) presented in the first and second panels in the middle row of Figure 5 revealed a significant seasonal spatial displacement of the Cyprus Eddy to the west from its initial position (Zodiatis et al., 2005a), leading to a complex flow path of the MMJ. During the CYBO 12 cruise in Aug 2001, three months after the first CYCLOPS cruise, the southward migration of the Cyprus Eddy resulted in the re-establishment of the eastward flowing MMJ, with geostrophic velocities up to 0.45 m s^{-1}, along the northern flank of the eddy (first panel in the middle row Figure 5). Concurrently the fluctuation of the northward current flowing along the shelf and slope of Israel and Lebanon resulted in the formation of the secondary anticyclonic eddy to the east. This prominent two eddy system persisted through the summer of 2004 and gradually weakened though the summer of 2007.

From summer 2009 to winter 2012 the dynamic height topography (Figure 5 bottom row), shows that the Cyprus Eddy once again became the dominant feature, shifting eastward close to its

previous location east of the Eratosthenes SM, with its center at 33° 30' E, 33° 30' N. The Shikmona Eddy disappeared. The circulation pattern, in the broader Eratosthenes SM region at the time of the MSM14-1 cruise in Dec2009 – Jan 2010 (second panel from the left in the bottom row of Figure 5) is dominated by a well-developed anticyclone, similar to the eddy observed during the CYBO and CYCLOPS cruises and identified as the Cyprus Eddy. The core of the Cyprus Eddy was located in the same geographical region as
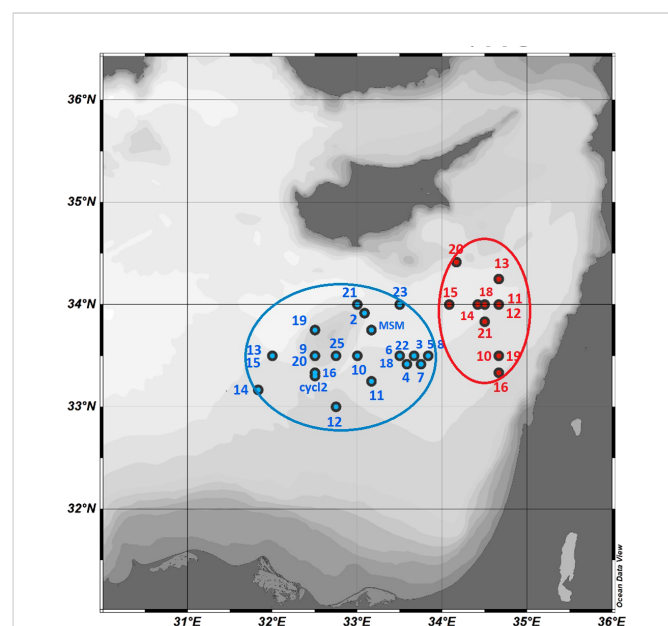

FIGURE 7
Seasonal and inter-annual migration of the Cyprus Eddy center (in blue) and of the Shikmona Eddy center (in red) from 1996 to 2012. Label next to each location indicates the cruise number listed in Table 1A.

during the CYBO cruises (Zodiatis et al., 2005a; Zodiatis et al., 2005b). The Cyprus Eddy, whose influence extends down to depths of roughly 450 m, constitutes one of the most intense (current speeds up to 0.35 m s^{-1}) circulation features in the SE Levantine Basin and undergoes strong temporal and spatial fluctuations as was found during the CYBO and CYCLOPS cruises as well as in historical data. During the MSM 14-1 cruise, shipborne ADCP and glider data were also collected in the same area at the beginning of Jan 2010 (Christiansen et al., 2012) and show good agreement with the pattern depicted in the relevant panel in Figure 5.

The secondary anticyclonic eddy in the southeastern most part of the domain was initially identified by the POEM group and years later it was named the Shikmona Eddy during the CYBO-HaiSec cruises. It appears to be generated at times when the strong northward current flowing along the Israel-Lebanese shelf and slope becomes unstable and detaches thus forming an anticyclonic eddy. During these events the Cyprus Eddy shifts westward or southwestward from the Eratosthenes SM. One example of the Shikmona Eddy formation in Aug 2009 is shown in Figure 6 where SVP drifter trajectories from the

NEMED project (Gertman et al., 2010a; Menna et al., 2012) are superimposed on MODIS SST images in the area along the shelf and slope of Israel-Lebanon. The drifter trajectories clearly show that the eddy detached from the northward flowing shelf-slope current (Rosentraub and Brenner, 2007) north of Haifa and drifted northwest to the area where the secondary eddy (the Shikmona Eddy) was observed during CYBO cruises and previously during the POEM cruises (Robinson et al., 1991). This secondary anticyclonic eddy was also observed at this time during the CYBO 22 cruise in late August 2009 (see Figure 5).

The analysis of the dynamic height topography during the period 1996-2011 reveals the significant migration of the Cyprus and Shikmona eddies' centers, as shown in Figure 7. The Cyprus Eddy center migrates eastward and south-eastward from the Eratosthenes SM, while during periods of the appearance of the Shikmona Eddy offshore along the Israel-Lebanon shelf and slope, the Cyprus Eddy is forced to migrate westward or south westward from the Eratosthenes SM. Similar migrations of these eddy centers were observed during the period 1985-1992 by Brenner et al. (1991) and Brenner (1993). In
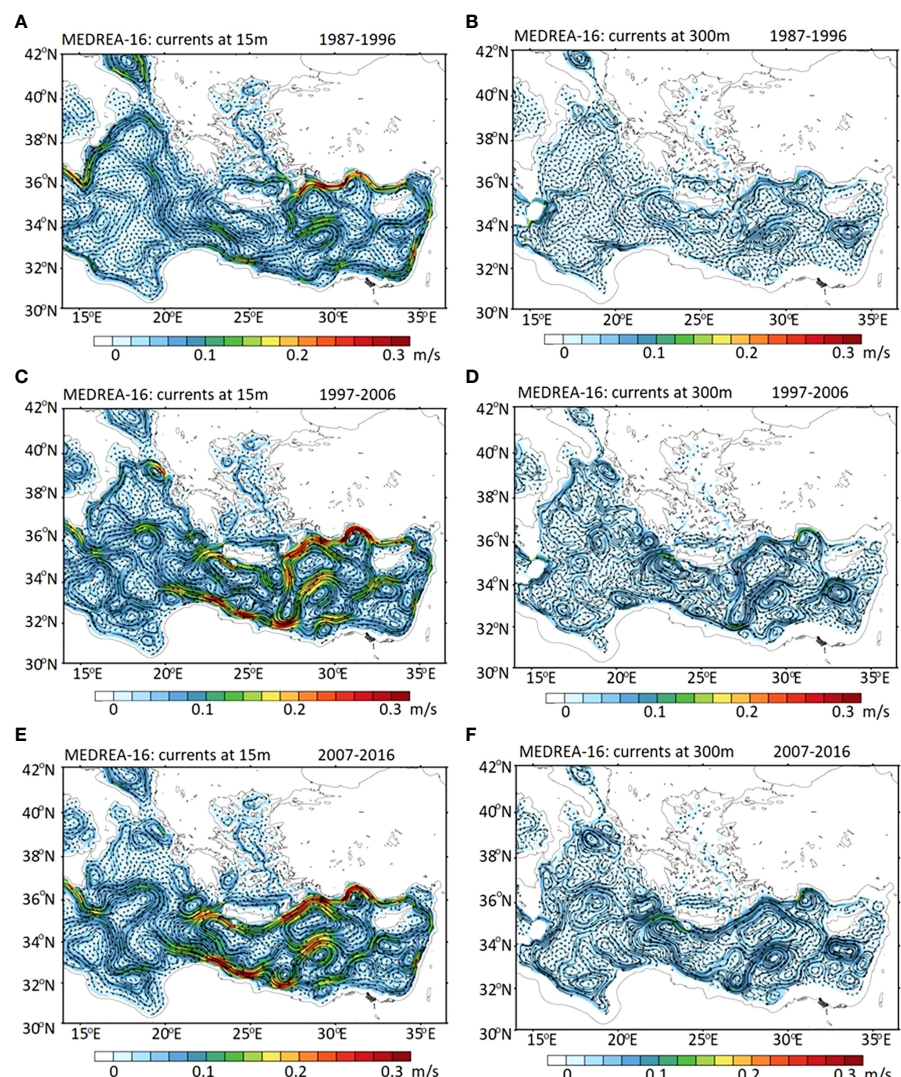

FIGURE 8
Surface decadal mean circulation in the Eastern Mediterranean from MEDREA16 reanalysis dataset (Simoncelli et al., 2014): **(A)** 1987-1996; **(C)** 1997-2006; **(E)** 2007-2016. Decadal mean circulation at intermediate depth of 300m: **(B)** 1987-1996; **(D)** 1997-2006; **(F)** 2007-2016.

a recent modeling study Egorova et al. (2022) suggested a mechanism for the Cyprus Eddy formation related to the growth of non-axisymmetric perturbations over complex bottom topography in the broader area of the Eratosthenes SM. They demonstrated that by imposing an eastward flow (attributed to the MMJ) at the western boundary of the Eratosthenes SM domain, it is possible to generate a dipolar vortex - an anticyclonic eddy attributed to the Cyprus Eddy, and a cyclonic eddy to the northwest of the Cyprus Eddy. Similar dynamical structures are visible in Figure 5.

The significant seasonal and inter-annual migration of the Cyprus Eddy can be explained based on the influence of other dynamical structures in the vicinity, such as the appearance of the Shikmona Eddy as noted above, or the significant fluctuations of the eastward flow in the central Mediterranean which transfers the MAW to the Levantine basin. Particularly, the periodic reversals of the North Ionian circulation (Gačić et al., 2010 and Gačić et al., 2011; Pinardi et al., 2015; Simoncelli et al., 2018) affect the eastward transfer of the MAW from the Ionian Sea to the Levantine basin as shown in Section 3.1 of von Schuckmann et al. (2016). However, further investigations are needed to examine if there is a dynamical relationship between the Northern Ionian circulation and the migration of the Cyprus Eddy.

With the development of the Mediterranean Sea reanalysis (MEDREA16, Simoncelli et al., 2014) within the framework of the MyOcean project (Simoncelli et al., 2016) and the Copernicus Marine Service (Section 3.1 in von Schuckmann et al., 2016; Simoncelli et al., 2018), as well as the downscaled, sub-regional, higher resolution CYCOFOS forecasting system (Zodiatis et al., 2018), an improved pattern of the circulation in the Levantine basin was depicted showing the co-existence of the anticlockwise flow along the north African (Egyptian) shelf and slope with the offshore cross basin current attributed to the MMJ. In order to emphasize the recurrence or persistence of the circulation features observed during the CTD cruises, several examples of the decadal mean circulation patterns near the surface and the 300 m depth from the MEDREA16 reanalysis

are shown in Figure 8 for comparison. The decadal mean circulation from 1987-1996 shows the reversal of the Northern Ionian Circulation (anti-cyclonic), while the following decade presents a cyclonic mean flow during 1997-2006. According to the analysis from Menna et al. (2021) based on observations, the last decade was characterized by several shorter period reversals of the Northern Ionian circulation, although this is not apparent in the decadal mean maps in Figures 8E, F. The main pathway of the AIS influences the thermohaline properties of the Levantine basin due to the eastward transport of MAW. Even during the last decade the AIS crosses the central Ionian at times and brings MAW to the Levantine basin. The decadal mean circulation in the Levantine clearly shows both a multipole Mersa Matruh Gyre system and the Cyprus Eddy near the surface and at intermediate depth. Furthermore, the MEDREA16 mean circulation during the first decade shows the Cyprus Eddy located east of the Eratosthenes SM, while during the second decade it was located west of the SM while co-existing with the Shikmona Eddy offshore Israel–Lebanon. During the third decade the Cyprus Eddy appears as a single, large eddy. Similarly, the decadal mean MEDREA16 circulation maps show the bifurcation of the MMJ southwest of Cyprus, with its eastward branch flowing along the periphery of the Cyprus Eddy. Despite the temporal differences between the circulation depicted from the CYBO-HaiSec cruises and the MEDREA16 mean circulation, there is a clear agreement between the flow patterns and their spatial distributions.

Menna et al. (2012) described this dual pathway eastward flowing current system with the offshore branch attributed to the MMJ, as well as the two anticyclonic features corresponding to the Cyprus and Shikmona eddies based on the analysis of hundreds of surface drifter trajectories. Recent numerical simulations conducted by Estournel et al. (2021) confirm the dominance of the Cyprus Eddy in the Levantine basin along with the periodic establishment of the Shikmona Eddy. Similarly, the results of the downscaled, high resolution CYCOFOS simulations confirm the prominence of the
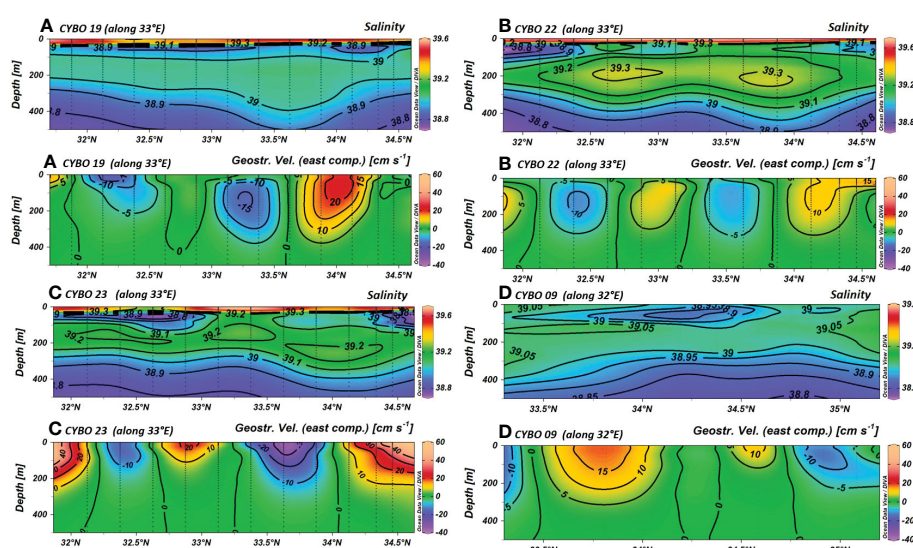

FIGURE 9
North-south cross sections along the 33°E meridian (see Figure 3) of salinity (top) and the eastward component of the geostrophic velocity (bottom) during: (A) CYBO 19 cruise (Sept 2005); (B) CYBO 22 cruise (Aug 2009); (C) CYBO 23 cruise (Aug 2010); (D) CYBO 9 cruise (May 2000). Positive geostrophic velocities indicate eastward flow, while negative velocities indicate westward flow.

Cyprus Eddy and the reappearance of the Shikmona eddy during the period 2013-2015.

3.1.3 The MAW and the MMJ

The analysis of the datasets obtained during the CYBO and HaiSec campaigns in the SE Levantine basin, particularly the salinity profiles gathered along the 33°E north-south cross sections, from Cyprus to Egypt (Figure 9), clearly reveal that the MAW is transported: a) eastward by a strong current flowing between the southern shelf of Cyprus and northern flank of the Cyprus Eddy, b) westward by a weaker flow along the southern flank of the Cyprus Eddy and c) eastward along the North African (Egyptian) shelf and slope. The CYBO and HaiSec in-situ data analysis regarding the pathway of the MAW confirms the POEM group's (Robinson et al., 1992) and Pinardi et al. (2015) description of the MMJ as a cross basin offshore current, as well as Nielsen (1912) description of an eastward flow following the North African coast. This contradicts the pattern suggested by Millot and Taupier-Letage (2005) who used only SST satellite imagery to claim that the MMJ was absent and was therefore an artifact of the POEM data analysis methodology. Here satellite SST images were used to complement our understanding of the variability of the general flow dynamics of the Levantine region during the CYBO and HaiSec cruises. While it is possible to define the main near surface flow features through remote sensing IR images, it is not possible to elucidate the true pathways of the MAW without the simultaneous use of in-situ data. The main reason is that the MAW mostly appears as a subsurface salinity minimum in the SE Levantine basin and SSTs especially in summer are quite high and therefore mask the signal of the MMJ at the sea surface.

In the summer of 2001 following the first CYCLOPS cruise, below the surface and MAW layers the Cyprus Eddy contained a well-defined lens of saline LIW below 120 m with a salinity of 39.10-39.14 with the 39 isohaline deflected downward below 400 m (not shown).

In contrast to this, the Shikmona Eddy contained a shallower, well-defined lens of lower salinity MAW with salinity of 38.85-38.90 extending down to 200 m. The latter suggests that after being transported eastward along the northern periphery of the Cyprus Eddy the MAW was then picked up by the Shikmona Eddy, which was more intense at the upper layers compared to the Cyprus Eddy. As noted above, the co-existence of these two anticyclones, was also observed during the CYBO 14 cruise in Aug 2002 (second panel in the middle row of Figure 5), after the second CYCLOPS experiment.

In summer 2005 during CYBO 19 cruise, the N-S salinity cross section between Cyprus and offshore Egypt shows the MAW transported eastward by the MMJ flowing close to Cyprus between the depths of 30-100 m (Figure 9A, upper panel) with salinity lower than 38.8. The eastward component of the geostrophic flow along the same section (Figure 9A, lower panel) shows the very pronounced MMJ flowing eastward along the northern flank of the Cyprus Eddy near 34° N, corresponding to the location of the core of MAW. In fact, eastward flow appears in general across most of the cross section except for two noticeable cores of westward flow, one is subsurface along the southern flank of the Cyprus Eddy near 33.3°N while the second is close to the surface offshore from Egypt near 32.2°N. These results confirm that during summer 2005 there was no significant eastward current offshore from Egypt. An additional shallower, thin, elongated patch of MAW was also found further south between 32.3°N and 33.5°N. The LIW occupies the depths between 100 to 250 m with salinity greater than 39.0, while in the core of the Cyprus eddy the higher salinity LIW appears as a salinity lens extending downward to 400 m. Comparison of these two sections indicates that some LIW is transported westward along the southern flank of the Cyprus Eddy although the lens of the highest salinity (S > 39.04) appears to be trapped in the core of the Cyprus Eddy. This is consistent with the results from Brenner (1993).

In the summers of 2009 and 2010, during the CYBO 22 (Figure 9B) and 23 (Figure 9C) cruises, the N-S cross sections between Cyprus and
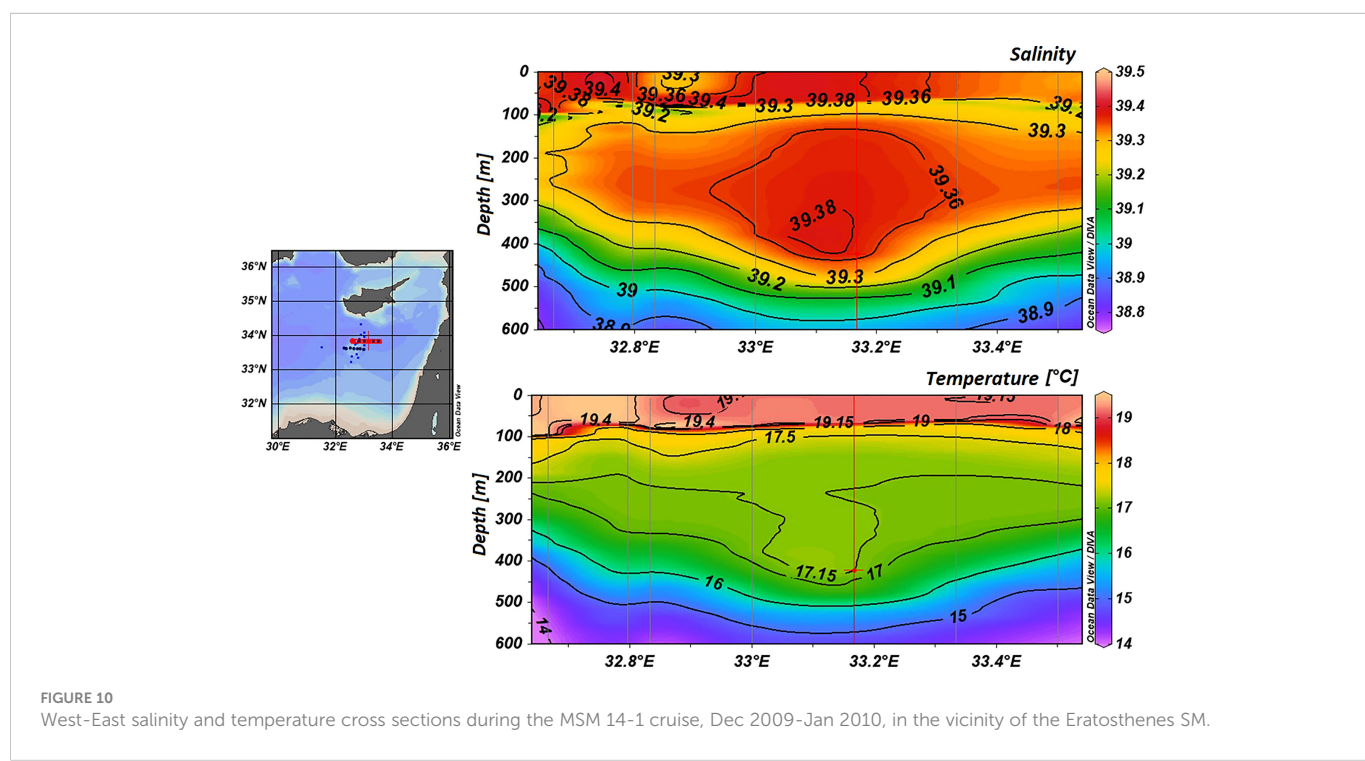
FIGURE 10
West-East salinity and reemperature cross sections during the MSM 14-1 cruise, Dec 2009-Jan 2010, in the vicinity of the Eratosthenes SM.

offshore Egypt show a similar salinity distribution of the MAW as observed during the summer of 2005 (Figure 9A) with two main patches of low salinity one in the north and one in the south. Furthermore, Figure 9B (summer 2009) demonstrates the classic concept that the main pathway of eastward flowing MAW follows the anticlockwise basin wide current along the shelf and slope of Egypt (North Africa). This is shown by the overlap of the most prominent patch of low salinity MAW, located south of 32°N, with the top layer of the eastward flowing jet. The second pathway of MAW appears near the northern end of the cross section where the low salinity lens overlaps with a strong MMJ. Figure 9C (summer 2010) also shows two main patches of MAW in the north and the south. However, the southern lens, centered near 32.7°N which is nearly 100 km north of the Egyptian coast appears to be trapped in the core of an offshore, anticyclonic eddy. In this case the main eastward flow of MAW is accomplished by the MMJ. These sections provide strong in-situ evidence regarding the important contributions of the MMJ and of the along shelf and slope North Africa current to transporting the MAW eastward, as was also found in results from numerical simulations (Pinardi et al., 2015; Section 3.1 in von Schuckmann et al., 2016; Zodiatis et al., 2018). They also show that the LIW layer typically contains several high salinity lenses, with values greater than 39.3 and 39.2 in 2009 (Figure 9B) and 2010 (Figure 9C), respectively. In summer 2009 the geostrophic velocity cross section (Figure 9B) suggests that two lenses of LIW are trapped in the cores of two anticyclonic eddies. The northern salinity lens can be attributed to the Cyprus Eddy while the southern salinity lens depression corresponds to an anticyclonic eddy offshore Egypt. In summer 2010 three lenses of LIW with salinity above 39.2 are present along the north-south cross section (Figure 9C). The northernmost lens, which is also the deepest, once again appears to be trapped in the core of the Cyprus Eddy as

suggested by the geostrophic velocity cross section. In early spring 2000, during the CYBO 9 cruise (5-12/5/2000), the N-S transect along longitude 32°E, to the west of Cyprus (Figure 9D) crossed a very pronounced lens of MAW as well as the eastward pathway of the MMJ. The low salinity lens, with salinity between 38.85-38.95, extended from the surface down to a depth of 90 m and has a north to south extent of about 75 km. The MMJ coincided with the southern part of this low salinity lens.

From December 2009 to January 2010 data gathered during the MSM14-1 cruise shown in Figure 10 reveal a surface mixed layer in the vicinity of the Eratosthenes SM extending down to depths of 50-80 m, with temperatures between 19.0-19.2°C and salinity of 39.30-39.4. Below the mixed layer, a thin layer of lower salinity water was found, with salinity values across most of the section slightly less than 39.3. Usually during winter, the sub-surface salinity minimum, which is attributed to the MAW, is eroded by mixing with the higher salinity surface water. However, due to milder winter conditions that prevailed before and during this cruise and because of the higher temperature and salinity of the surface water layer during the summer of 2009 prior to the cruise, the winter mixing could not completely eliminate the MAW but instead left a relatively higher salinity remnant of the combined surface water and MAW. The LIW observed over the Eratosthenes SM appeared as a warm and saline lens centered at a depth of 250-300 m with salinity and temperature values over 39.36 and 17.15°C, respectively. The deepest depression of the isotherms and isohalines below this lens, which extended down to 450 m, appeared at the eastern periphery of the Eratosthenes SM. This structure is remarkably similar to the one found by Brenner (1993) twenty years earlier although in comparison, here the LIW was warmer and more saline by 0.5°C and 0.1, respectively. In fact, the
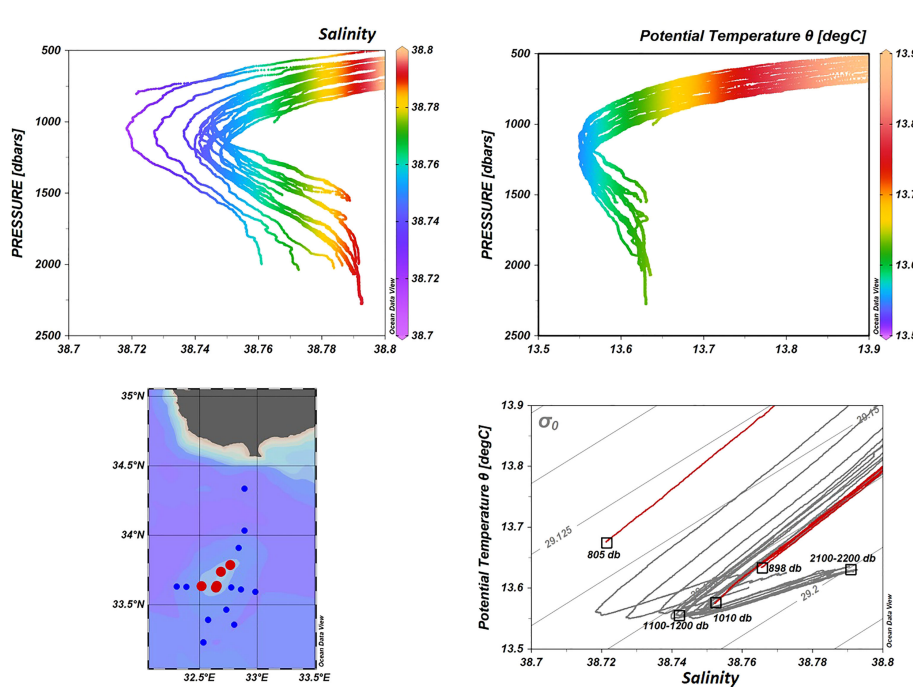
FIGURE 11
The EMTW salinity (upper left) and temperature (upper right) profiles and the T/S diagram (lower right) during the MSM14-1 cruise, Dec. 2009- Jan. 2010. Profiles and the T/S diagram include only stations sampled deeper than 1000 m where the bottom depth was about 2000 m. Red dots on the map and red lines on the T/S diagram represent the stations over the Eratosthenes SM where the bottom depth is shallower than 1000 m.
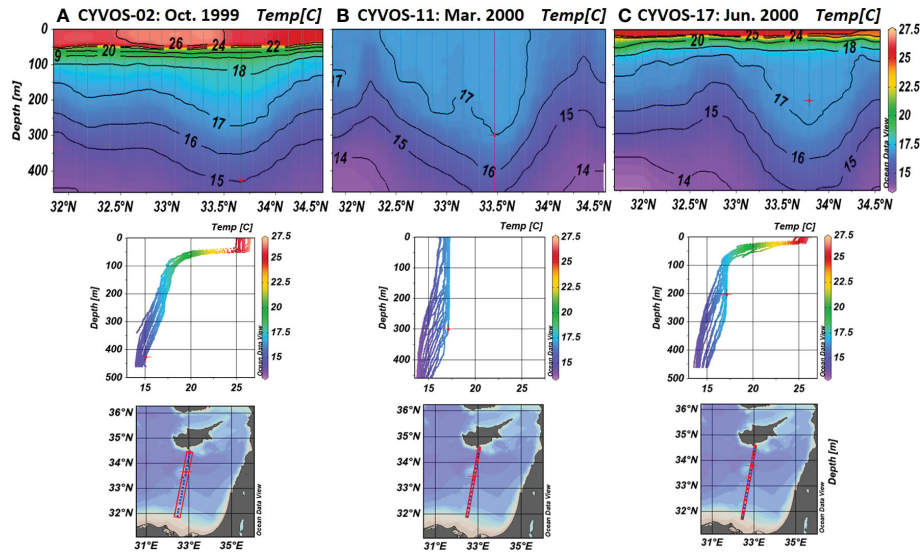
FIGURE 12
Temperature transects and composite profiles along the VOS transect from Limassol - Port Said: **(A)** Oct 1999 (CYVOS2); **(B)** Mar 2000 (CYVOS 11); **(C)** Jun 2000 (CYVOS17).

observations presented by Brenner et al. (1991) and Brenner (1993) suggest that the water in the core of the Cyprus Eddy retains its temperature and salinity characteristics for a period of 2.5-3 years and then jumps abruptly to new values.

In the deepest areas along the western boundary of the Eratosthenes SM, a clear signal of EMTW was found with increasing salinity and temperature below ~1100 dbar as shown in the salinity and temperature profiles in the two upper panels in Figure 11. The characteristic "tail" in the T/S curves (bottom right panel in Figure 11) pointing upward to the right from the transition point from EMDW between 1000-1100 m is also noticeable in the T/S diagram. It is similar to the one observed during the CYBO and HaiSec cruises in Figure 4. The temperature and salinity of the EMTW observed during MSM14-1 in early 2010 are consistent with the values observed during the CYBO-HaiSec 23 and 25

cruises which were conducted 8 months (Aug 2010) and two years (Dec 2012) later, respectively. The temperature and salinity values are also comparable to the EMTW observed during CYBO 13 (2001) and 14 (2002), except here the upper boundary of the EMTW was lifted to 1050 dbar on average, as compared to a depth of 1250 dbar on average, a decade earlier (compare to Figure 4).

3.4 MFSPP bi-weekly and MFSTEP monthly XBT transects in the SE Levantine: Limassol – Port Said and Limassol-Alexandria

The analysis of the bi-weekly and monthly XBT data gathered along the transects from Limassol (Cyprus) to Port Said (Egypt) and Limassol
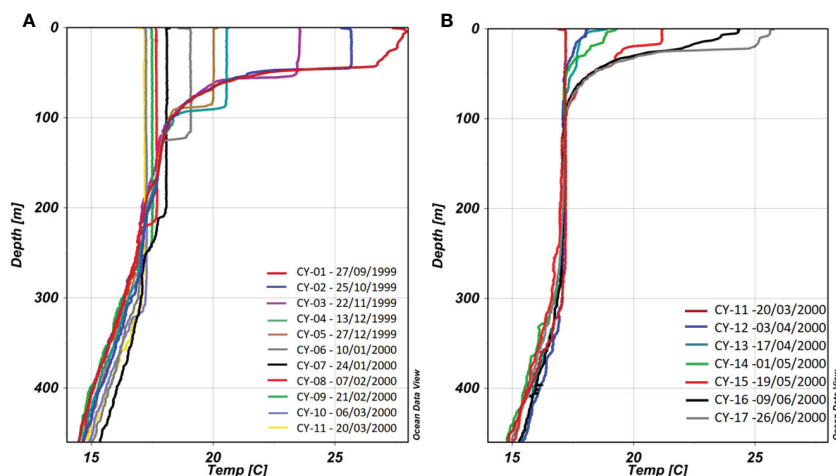
FIGURE 13
The bi-weekly evolution of the temperature profiles in the core of the Cyprus Eddy during the MFSPP project (Table 1B): **(A)** surface cooling erosion of the thermocline and deepening of the mixed from surface down to 320 m from Sep 1999 to Mar 2000; and **(B)** surface warming and restratification of the upper water column from Mar to June 2000.

to Alexandria (Egypt), shows a well stratified warm surface layer down to 40-60 m depth during autumn 1999 (Figure 12A) and in early summer 2000 (Figure 12C). The temperature of the surface water layer typically ranged from 27-28°C in September/October 1999 and decreased to 17-18°C in February-March 2000 (Figure 12B). A thermostad with temperature of 17-18°C centered near 33.5°N appears below the upper stratified layer. Below the thermostad the 15-17°C isotherms are noticeably depressed with the 15°C isotherm extending as deep as 400 m.

The surface cooling and the mixing in the winter of 1999-2000, led to a deepening of the mixed layer from 90 m down to 320 m from Sep 1999 to Mar 2000 (Figure 13A) in the center of the Cyprus Eddy. In Feb and Mar 2000 (Figure 13A) the water column was well mixed from surface down to at least 200 m with temperatures between 17-17.25°C. The deepest mixing, which most likely occurred near the center of the Cyprus Eddy is consistent with the deep mixing observed by Brenner et al. (1991) and Brenner (1993). The spring to early summer surface warming and restratification of the upper water column from Apr to Jun 2000 can be seen in Figure 13B. This deep mixing and restratification was observed at the eastern edge of the Eratosthenes SM. From Apr 2000 until the end of Jun 2000 surface heating led to the gradual re-establishment of the strong stratification of the upper layer, with temperatures as high as 25.5° C (Figure 13B). This led to the capping of the subsurface thermostad seen in Figure 12C.

The thermostad with a core temperature of 17-18°C appeared throughout the entire period of the XBT sampling along the eastern periphery of the Eratosthenes SM and is clearly associated with the core of the Cyprus Eddy. This is in agreement with the results of the CYCLOPS cruises and the CYBO cruises carried during late winter and in summer 2000. It is also consistent with results from the CYCOFOS (Zodiatis et al., 2018) and MFS (Pinardi et al., 2003) which assimilated XBT data from the Limassol-Port Said transect as well as the remotely sensed altimeter data from two satellites tracks in the same area. The CYBO in-situ data in winter and summer 2000 and the MFS (Pinardi et al., 2003) results during the periods of the Limassol-Port Said XBT transects, showed similar flow patterns in the broader area of the Eratosthenes SM. Both the in-situ data and numerical model results showed a well-established anticyclonic eddy with the eddy center coinciding with the subsurface thermostad for the period corresponding to the XBT transects.

The XBTs data provide strong evidence that the Cyprus Eddy as inferred from the isotherms, appears as a warm lens of water with a center that located between 33°- 33°30'N and 30°15'E. The data suggest that the core of the eddy also drifts north-south by about 30 km, although the location of the eddy center cannot be determined precisely from the north-south cross section alone. Moreover, during the MFSPP XBT transects it was found to be located as much as 55 km to the west of its position during the CYBO cruises between 1995-1999 and from the position reported by Brenner (1989); Brenner (1993) in late 1980s and in the early 1990's.

The MFSTEP XBT transects conducted during May 2004 and between Jun-Oct 2005 (not shown) intersected the core of the Cyprus Eddy while in Sep and Oct 2004, Feb, Apr, and May 2005, the transects intersected the western periphery of the Cyprus Eddy due to an eastward drift of its center. Nevertheless, the temperature distribution clearly shown a relatively deep depression of the 15-17°C isotherms, which is attributed to the Cyprus Eddy. In Dec 2004 and Jan 2005, the XBT transect from Limassol to Alexandria did not cross the eddy, however winter mixing of the surface waters down to about 100 m was observed with temperatures as low as 18.5°C. The
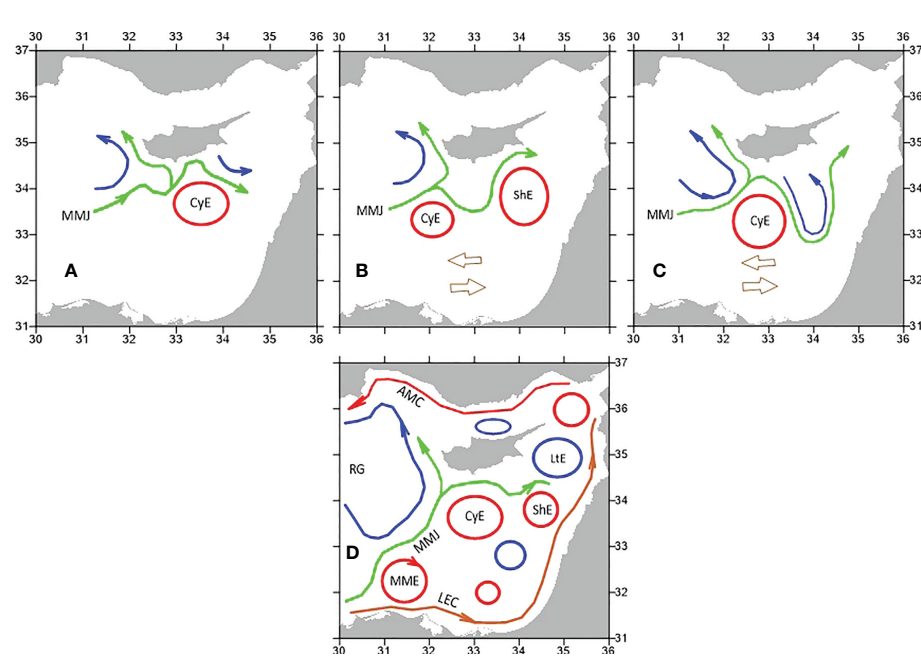
FIGURE 14
Schematic of the main flow features in the SE Levantine from 1995-2015 and the overall circulation based on in-situ data and downscaling numerical simulations. The three upper panels correspond to the three periods in Figure 5: **(A)** 1996-1999, **(B)** 2001-2007, and **(C)** 2009-2012 and the lower panel shows **(D)** summary of main features for the entire twenty year period. Anticyclonic eddies are shown in red (CyE, Cyprus Eddy; ShE, Shikmona Eddy; MME, Mersa Matruh Eddy), cyclonic eddies in blue (LtE, Lattakia Eddy; RG, Rhodes gyre), the MMJ in green, and the along the shelf-slope currents: LEC, Libyan-Egyptian Current in brown and AMC, Asia Minor Current in red.

overall picture provided by the MFSTEP XBT transects suggests that between Sep 2004-May 2005 the core of the Cyprus Eddy appears to have drifted eastward and then reversed course from Jun-Oct 2005 when it drifted westward back to near its previous position, as observed in May 2004. This is based on the temporal changes in the shape of the thermostad along the two transect tracks.

4 Conclusions

The in-situ data gathered in the SE Levantine Basin from 1995 to 2015 during 34 hydrographic, synoptic campaigns (CYBO, CYCLOPS, MSM14, CYBO-HaiSec, HaiSec cruises) and 35 XBTs transects (MSFPP-VOS, MFSTEP-VOS), along with data provided by the sub-basin, downscaled numerical simulation from CYCOFOS nested in the CMEMS Med MFC (Clementi et al., 2021) for the period from 2013-2015, have all provided new insight on the dominant, coherent mesoscale circulation features of the south-eastern Levantine basin and on the main water mass characteristics, including their bi-weekly, monthly, seasonal and interannual variability.

These data have confirmed and enhanced the POEM group's description of the mesoscale circulation, particularly regarding the anticyclonic Cyprus Eddy, the Shikmona Gyre and the pathway of the MMJ through this region. As in the historical data, the Cyprus Eddy is a persistent dynamical feature throughout these two decades of in-situ monitoring, located mainly east of the Eratosthenes SM. A recent modeling study has suggested that it is generated by the interaction of the MMJ and the complex topography in the vicinity of the SM. The occasional meandering and instability of the northward current flowing along the shelf and slope of Israel-Lebanon often initiates the growth of a secondary anticyclonic eddy, referred to as the Shikmona Eddy, after it detaches from the current and drifts offshore to the west. The intrusion of the less frequent Shikmona Eddy from the east may force the Cyprus Eddy to migrate westward from the Eratosthenes SM during periods when both eddies coexist. These extensive post POEM in-situ data sets provide incontrovertible evidence that the MMJ is indeed an offshore, cross basin current, which transports the MAW eastward from the Ionian Sea to the southwestern part of the Levantine. It continues its eastward path between the southern shelf and slope of Cyprus and the northern periphery of the Cyprus Eddy.

Occasional expansion of the Cyprus Eddy to the northwest can cause a diversion or bifurcation of the MMJ along the western shelf and slope of Cyprus. Consequently, the westward migration of the Cyprus Eddy affects the eastward transfer of MAW across the sub-basin. Analysis of the in-situ data gathered from numerous north-south transects from Cyprus to Egypt, confirms the co-existence of two eastward pathways for transporting MAW across the Levantine basin: (1) the MMJ flowing between the shelf and slope of Cyprus and the northern periphery of the Cyprus Eddy; and (2) the basin wide, anticlockwise current flowing eastward along the shelf and slope of Egypt, and then turning northward following the coasts of Israel and Lebanon. The periodic co-existence of the Cyprus and Shikmona eddies with a third eddy offshore from the shelf and slope of Egypt, combine to form the Shikmona Gyre, the multi-pole dynamical structure first observed by the POEM group in the late 1980s.

The spatial and temporal variability of the dominant flow features of the SE Levantine during these two decades of monitoring reveal

four active periods with distinct patterns as summarized in Figure 14: a) the dominance of the Cyprus Eddy from 1996 to 1999 with the eddy located east of the Eratosthenes SM; b) the co-existence of two anticyclonic eddies from 2001 to 2007 with the Cyprus Eddy west of the Eratosthenes SM and the Shikmona Eddy far east of the seamount; c) the dominance of the Cyprus Eddy from 2009 to 2012, with its center once again located east of the seamount. From 2013-2015 (not shown in Figure 14) the Shikmona Eddy reappeared and so this was also a period of co-existence of both eddies. Figure 14D shows the schematic summary of all of the major circulation features that appeared during the entire twenty-year period from 1995-2015.

The long-term trends in these datasets indicate summer warming and salinization of the water masses of the SE Levantine from the surface down to the upper boundary of the LIW. The bi-weekly XBTs transects passing through or near the center of the Cyprus Eddy provided a detailed chronological record of winter mixing and homogenization of the eddy center from surface down to 320 m depth. In addition, the deep profiles demonstrate that over time the upper boundary of the EMTW has been lifted on average from 1250 to 1050 m, while at water depths deeper than 2000 m the observed additional increase of the temperature and of the salinity is attributed to newest deep waters which intruded into the deep cavities of the SE Levantine in the vicinity the Eratosthenes SM.

Data availability statement

The datasets presented in this study can be found in online repositories. The names of the repository/repositories and accession number(s) can be found below:XBT data - https://cdi.seadatanet.org/search/welcome.php?query=2410&query_code={53081AD8-722D-4F4F-A8BC-18F0385F5336} CYBOdata - https://cdi.seadatanet.org/search/welcome.php?query=2409&query_code={C4AFECA2-B881-4336-AC17-761F797A09CE} HaiSec data - https://cdi.seadatanet.org/search/welcome.php?query=2408&query_code={30CC581C-1C48-4781-9D0C-DD4AA2315159}

Author contributions

GZ: data collection, data processing, data management, data analysis, manuscript co-writing, manuscript editing. SB: data analysis, manuscript co-writing, manuscript editing. IG: data collection, data processing, data management, data analysis. TO: data collection, data processing. SSi: data processing, data management, data analysis, manuscript co- writing, manuscript editing. MI: data collection, data processing. SSa: data collection, data processing. All authors contributed to the article and approved the submitted version.

Acknowledgments

Conflict of interest

The authors declare that the research was conducted in the absence of any commercial or financial relationships that could be construed as a potential conflict of interest.

Publisher's note

All claims expressed in this article are solely those of the authors and do not necessarily represent those of their affiliated organizations, or those of the publisher, the editors and the reviewers. Any product that may be evaluated in this article, or claim that may be made by its manufacturer, is not guaranteed or endorsed by the publisher.

References

Adani, M., Dobricic, S., and Pinardi, N.. (2011). Quality assessment of a 1985-2007 Mediterranean Sea reanalysis. *J. Atmos. Ocean. Tech.* 28, 569–589. doi: 10.1175/2010JTECHO798.1

Armi, L., Hebert, D., Oakey, N., Price, J., Richardson, P. L., Rossby, T., et al. (1988). The history and decay of a Mediterranean salt lens. *Nature* 333, 649–651. doi: 10.1038/333649a0

Armi, L., and Zenk, W. (1984). Large Lenses of highly saline Mediterranean water. *J. Phys. Oceanogr.* 14, 1560–1576. doi: 10.1175/1520-0485(1984)014<1560:LLOHSM>2.0.CO;2

Barboni, A., Lazar, A., Stegner, A., and Moschos, E. (2021). Lagrangian Eddy tracking reveals the Eratosthenes anticyclonic attractor in the eastern levantine basin. *Ocean Sci.* 17, 1231–1250. doi: 10.5194/os-17-1231-202

Brenner, S. (1989). Structure and evolution of warm core eddies in the Eastern Mediterranean levantine basin. *J. Geophys. Res.* 94, 12593–12602. doi: 10.1029/JC094iC09p12593

Brenner, S. (1993). Long term evolution and dynamics of a persistent warm core eddy in the Eastern Mediterranean Sea. *Deep Sea Res. II* 40, 1193–1201. doi: 10.1016/0967-0645(93)90067-W

Brenner, S., Rozentraub, Z., Bishop, J., and Krom, M. (1991). The mixed layer/thermocline cycle of a persistent warm core eddy in the eastern Mediterranean. *Dyn. Atmos. Oceans* 15, 457–476. doi: 10.1016/0377-0265(91)90028-E

Christiansen, B., Brand, T., Christiansen, H., Christiansen, S., Denda, A., Fischer, A., et al. (2012). *Structure and function of pelagic and benthic communities of the eastern Mediterranean in relation to physical drivers and bottom topography, MARIA s. MERIAN cruise No.14, leg 1* (Hamburg: Institut für Meereskunde der Universität Hamburg).

Clementi, E., Aydogdu, A., Goglio, A. C., Pistoia, J., Escudier, R., Drudi, M., et al. (2021). *Mediterranean Sea Physical Analysis and Forecast (CMEMS MED-Currents, EAS6 system) (Version 1) [Data set]* (Copernicus Monitoring Environment Marine Service (CMEMS)). doi: 10.25423/CMCC/MEDSEA_ANALYSISFORECAST_PHY_006_013_EAS6

Egorova, V. M., Zyryanov, V. N., and Sokolovskiy, M. A. (2022). The hydrodynamic theory of the Cyprus eddy. *Ocean Dynam.* 72, 1–20. doi: 10.1007/s10236-021-01484-7

Estournel, C., Marsaleix, P., and Ulses, C. (2021). A new assessment of the circulation of Atlantic and intermediate waters in the Eastern Mediterranean. *Prog. Oceanogr.* 198, 102673. doi: 10.1016/j.pocean.2021.102673

Fusco, G., Manzella, G. M. R., Cruzado, A., Gačic, M., Gasparini, G. P., Kovaĉevi·, V., et al. (2003). Variability of mesoscale features in the Mediterranean Sea fromXBT data analysis. *Ann. Geophys.* 21, 21–32. doi: 10.5194/angeo-21-21-2003

Gačić, M., Borzelli, G. L. E., Civitarese, G., Cardin, V., and Yari, S. (2010). Can internal processes sustain reversals of the ocean upper circulation? the Ionian Sea example. *Geophys. Res. Lett.* 37, L09608. doi: 10.1029/2010GL043216

Gačić, M., Civitarese, G., Eusebi Borzelli, G. L., Kovačević, V., Poulain, P.-M., Theocharis, A., et al. (2011). On the relationship between the decadal oscillations of the northern Ionian Sea and the salinity distributions in the Eastern Mediterranean. *J. Geophys. Res.* 116, C12002. doi: 10.1029/2011JC007280

García-Lafuente, J., Sammartino, S., Huertas, I. E., Flecha, S., Sánchez-Leal, R. F., Naranjo, C., et al. (2021). Hotter and weaker Mediterranean outflow as a response to basin-wide alterations. *Front. Mar. Sci.* 8. doi: 10.3389/fmars.2021.613444

Genin, A., Lazar, B., and Brenner, S. (1995). Vertical mixing and coral death in the red Sea following the eruption of mount pinatubo. *Nature* 377, 507–510. doi: 10.1038/377507a0

Gertman, I., Goldman, R., Rosentraub, Z., Ozer, I., Zodiatis, G., Hayes, D., et al. (2010a). Generation of shikmona anticyclonic eddy from an alongshore current. *Rapp. Commun. Int. Mer Medit. (CIESM Congress Proceedings)* 39, 114.

Gertman, I., Herut, B., and Kress, N. (2010b). Assessment of post transient changes in levantine basin deep waters. *Rapp. Commun. Int. Mer Medit. (CIESM Congress Proceedings)* 39, 113.

Gertman, I., Pinardi, N., Popov, Y., and Hecht, A. (2006). Aegean Sea Water masses during the early stages of the Eastern Mediterranean climatic transient (1988-90). *J. Phys. Oceanogr.* 36, 1841–1859. doi: 10.1175/JPO2940.1

Gertman, I., Zodiatis, G., Murashkovsky, A., Hayes, D., and Brenner, S. (2007). Determination of the location of southeastern levantine anticyclonic eddies from CTD data. *Rapp. Commun. Int. Mer Medit.* 38, 151.

Gertman, I., Zodiatis, G., Ozer, T., Goldman, R., and Herut, B. (2016). Renewal of deep water in vicinity of the eastern levantine slope. *Rapp. Commun. Int. Mer Medit. (CIESM Congress Proceedings)* 41, 124. abstract code 4405C.

Groom, S., Herut, B., Brenner, S., Zodiatis, G., Psara, S., Kress, N., et al. (2005). Satellite-derived spatial and temporal biological variability in the Cyprus eddy. *Deep Sea Res. II* 52, 2990–3010. doi: 10.1016/j.dsr2.2005.08.019

Hayes, D. R., Dobricic, S., Gildor, H., and Matsikaris, A. (2019). Operational assimilation of glider temperature and salinity for an improved description of the Cyprus eddy. *Deep Sea Res. II* 164, 41–53. doi: 10.1016/j.dsr.2019.05.015

Hayes, D. R., Hannides, A., Georgiou, G., Testor, P., Gildor, H., and Zodiatis, G. (2014). *Description of the long-lived subsurface mesoscale eddy south of cyprus. 6th EGO meeting and final symposium of the COST action ES0904* (Kiel, Germany: EGO).

Hayes, D. R., Zodiatis, G., Konnaris, G., Hannides, A., Solovyov, D., and Testor, P. (2011). *Glider transects in the levantine Sea: Characteristics of the warm core Cyprus eddy*. Spain: OCEANS 2011 IEEE. 1–9. doi: 10.1109/Oceans-Spain.2011.6003393

Hecht, A., and Gertman, I. (2001). Physical features of the eastern Mediterranean resulting from the integration of POEM data with Russian Mediterranean cruises. *Deep-Sea Res. I* 48, 1847–1876. doi: 10.1016/S0967-0637(00)00113-8

Hecht, A., Robinson, A., and Pinardi, N. (1988). Currents, water masses, eddies, and jets in the Mediterranean levantine basin. *J. Phys. Oceanogr.* 18, 1320–1353. doi: 10.1175/1520-0485(1988)018<1320:CWMEAJ>2.0.CO;2

Karlin, L. N., Kluikov, Y. Y., and Kutko, B. P. (1988). *The microscale structure of the hydrophysical fields at the upper layer of the ocean*. Gidrometeoizdat: Leningrad, 162. pp

Klein, B., Roether, W., Manca, B. B., Bregant, D., Beitzel, V., Kovacevic, V, et al. (1999). The large deep water transient in the Eastern Mediterranean. *Deep Sea Res. I* 46, 371–414. doi: 10.1016/S0967-0637(98)00075-2

Krom, M. D., Brenner, S., Kress, N., Neori, A., and Gordon, L. I. (1992). Nutrient dynamics and new production in a warm-core eddy from the Eastern Mediterranean Sea. *Deep Sea Res.* 39, 467–480. doi: 10.1016/0198-0149(92)90083-6

Krom, M. D., Thingstad, T. F., Carbo, P., Drakopoulos, P., Fileman, T. W., Flaten, G. A. F., et al. (2005). Overview of the CYCLOPS p addition Lagrangian experiment in the Eastern Mediterranean. *Deep Sea Res. II* 52, 3090–3108. doi: 10.1016/j.dsr2.2005.08.018

Lascaratos, A., Roether, W., Nittis, K., and Klein, B. (1999). Recent changes in deep water formation and spreading in the Mediterranean Sea: A review. *Progr. Oceanogr.* 44, 5–36. doi: 10.1016/S0079-6611(99)00019-1

Malanotte-Rizzoli, P., Manca, B. B., Marullo, S., Ribera d'Alcala, M., Roether, W., Theocharis, A., et al. (2003). The Levantine Intermediate Water Experiment (LIWEX) Group: Levantine basin—A laboratory for multiple water mass formation processes. *J. Geophys. Res.* 108 (C9), 8101–3108. doi: 10.1029/2002JC001643

Malanotte-Rizzoli, P., Manca, B. B., Riberad'Alcala, M., Theocharis, A., Brenner, S., Budillon, G., et al. (1999). The Eastern Mediterranean in the 80s and in the 90s: the big transition in the intermediate and deep circulations. *Dyn. Atmos. Oceans* 29, 365–395. doi: 10.1016/S0377-0265(99)00011-1

Manzella, G. M. R., Reseghetti, F., Coppini, G., Borghini, M., Cruzado, A., Galli, C., et al. (2007). The improvements of the ships of opportunity program in MFS-TEP. *Ocean Sci.* 3, 245–258. doi: 10.5194/os-3-245-2007

Manzella, G. M. R., Scoccimarro, E., Pinardi, N., and Tonani, M. (2003). Improved near real time data management procedures for the Mediterranean ocean forecasting system – voluntary observing ship program". *Ann. Geophys.* 21, 49–62. doi: 10.5194/angeo-21-49-2003

McDowell, S. E., and Rossby, H. T. (1978). A mesoscale lens of Mediterranean water off the Bahamas. *Science* 202, 1085–1087. doi: 10.1126/science.202.4372.1085

Menna, M., Gačić, M., Martellucci, R., Notarstefano, G., Fedele, G., Mauri, E., et al. (2022). Climatic, decadal, and interannual variability in the upper layer of the Mediterranean Sea using remotely sensed and in-situ data. *Remote Sens.* 14 (6), 1322. doi: 10.3390/rs14061322

Menna, M., Gerin, R., Notarstefano, G., Mauri, E., Bussani, A., Pacciaroni, M., et al. (2021). On the circulation and thermohaline properties of the Eastern Mediterranean Sea. *Front. Mar. Sci.* 8. doi: 10.3389/fmars.2021.671469

Menna, M., Poulain, P. M., Zodiatis, G., and Gertman, I. (2012). On the surface circulation of the levantine sub-basin derived from Lagrangian drifters and satellite altimetry data. *Deep Sea Res. I* 65, 46–58. doi: 10.1016/j.dsr.2012.02.008

Millot, C., and Taupier-Letage, I. (2005). Circulation in the Mediterranean Sea. In: A. Saliot eds. *The Mediterranean Sea. Handbook of Environmental Chemistry* (Berlin, Heidelberg: Springer) 5K, 29–66. doi: 10.1007/b107143

Nielsen, J. N. (1912). *Hydrography of the Mediterranean and adjacent water. report of Danish oceanographical expedition 1908-1910*. Copenhagen: Andr. Fred. Host & Son, 72–191.

Ovchinnikov, I. M., Plakhin, A., Moskalenko, L. V., Neglyad, K. V., Osadchiy, A. S., Fedoseyev, A. F., et al. (1976). *Hydrology of the Mediterranean Sea*. Gidrometeoizdat, Leningrad. 375.

Ozer, T., Gertman, I., Gildor, H., Goldman, R., and Herut, B. (2020). Evidence for recent thermohaline variability and processes in the deep water of the southeastern levantine basin, Mediterranean Sea. *Deep Sea Res. II* 171, 104651. doi: 10.1016/j.dsr2.2019.104651

Ozer, T., Gertman, I., Kress, N., Silverman, J., and Herut, B. (2017). Interannual thermohaline, (1979–2014) and nutrient, (2002–2014) dynamics in the levantine surface and intermediate water masses, SE Mediterranean Sea. *Glob. Planet. Change* 151, 60–67. doi: 10.1016/j.gloplacha.2016.04.001

Ozsoy, E., Hecht, A., Unluata, U., Brenner, S., Oguz, T., Bishop, J., et al. (1991). A review of the levantine basin circulation and its variability during 1985-1988, dyn. *Atmos. Oceans* 15, 421–456. doi: 10.1016/0377-0265(91)90027-D

Pinardi, N., Allen, I., De Mey, P., Korres, G., Lascaratos, A., Le Traon, P. Y., et al. (2003). The Mediterranean ocean forecasting system: first phase of implementation, (1998-2001). *Ann. Geophys.* 21, 3–20. doi: 10.5194/angeo-21-3-2003

Pinardi, N., and Coppini, G. (2010). Preface" operational oceanography in the Mediterranean Sea: the second stage of development". *Ocean Sci.* 6 (1), 263–267. doi: 10.5194/os-6-263-2010

Pinardi, N., Zavatarelli, M., Adani, M., Coppini, G., Fratianni, C., Oddo, P., et al. (2015). Mediterranean Sea Large-scale low-frequency ocean variability and water mass

formation rates from 1987 to 2007: A retrospective analysis. *Progr. Oceanogr.* 132, 318–332. doi: 10.1016/j.pocean.2013.11.003

Robinson, A. R., and Golnaraghi, M. (1993). Circulation and dynamics of the Eastern Mediterranean sea; quasi-synoptic data-driven simulations. *Deep Sea Res.* 40 (6), 1207–1246. doi: 10.1016/0967-0645(93)90068-X

Robinson, A. R., Golnaraghi, M., Leslie, W. G., Artegiani, A., Hecht, A., Lazzoni, E., et al. (1991). The eastern Mediterranean general circulation: features, structure and variability. *Dyn. Atmos. Oceans* 15, 215–240. doi: 10.1016/0377-0265(91)90021-7

Robinson, A. R., Malanotte-Rizzoli, P., Hecht, A., Michelato, A., Roether, W., Theocharis, A., et al. (1992). General circulation of the Eastern Mediterranean. *Earth Sci. Rev.* 32, 285–309. doi: 10.1016/0012-8252(92)90002-B

Roether, W., Manca, B. B., Klein, B., Bregant, D., Georgopoulos, D., Beitzel, V., et al. (1996). Recent changes in eastern Mediterranean deep waters. *Science* 271 (5247), 333–335. doi: 10.1126/science.271.5247.333

Rosentraub, Z., and Brenner, S. (2007). Circulation over the southeastern continental shelf and slope of the Mediterranean Sea: Direct current measurements, winds, and numerical model simulations. *J. Geophys. Res.* 112, C11001. doi: 10.1029/2006JC003775

Schlitzer, R. (2002). Interactive analysis and visualization of geoscience data with ocean data view. *Comput. Geosci.* 28 (10), 1211e1218. doi: 10.1016/S0098-3004(02)00040-7

Schroeder, K., and Chiggiato, J. (2022). *Oceanography of the Mediterranean Sea, An Introductory Guide. 1st Edition* (Elsevier), 561.

Schroeder, K., Chiggiato, J., Josey, S. A., Borghini, M., Aracri, S., and Sparnocchia, S.. (2017). Rapid response to climate change in a marginal sea. *Sci. Rep.* 7, 4065. doi: 10.1038/s41598-017-04455-5

Schroeder, K., Garcìa-Lafuente, J., Josey, S. A., Artale, V., Nardelli, B. B., Carrillo, A., et al. (2012). "Circulation of the Mediterranean Sea and its variability," in *Climate of the Mediterranean region*. Ed. P. Lionello (Amsterdam: Elsevier), 590, ISBN: . doi: 10.1016/B978-0-12-416042-2.00003-3

Scory, S., Simoncelli, S., Coatanoan, C., Bäck, Ö., Iona, S., and Myroshnychenko, V. (2018). *Data quality: why it is so important? the experience of the regional products managers and recommendations. SeaDataCloud training workshop (20-27 June 2018)* (Belgium: Ostend). Available at: https://www.seadatanet.org/content/download/3251/file/SDC_WP3_TRaining1%20_Importance_Quality_Control.pdf.

Simoncelli, S., Fratianni, C., Pinardi, N., Grandi, A., Drudi, M., Oddo, P., et al. (2014). *Mediterranean Sea physical reanalysis (MEDREA) (Version 1) [Data set]* (Copernicus Monitoring Environment Marine Service (CMEMS)). doi: 10.25423/MEDSEA_REANALYSIS_PHYS_006_004.

Simoncelli, S., Masina, S., Axell, L., Liu, Y., Salon, S., Cossarini, G., et al. (2016) *MyOcean regional reanalyses: overview of reanalyses sys- tems and main results. Mercator ocean j.* 54. special issue on main outcomes of the MyOcean2 and MyOcean follow-on projects. Available at: https://www.mercator-ocean.eu/wp-content/uploads/2017/04/Mercator-Ocean-newsletter-2015_54.pdf.

Simoncelli, S., Pinardi, P., Fratianni, C., Dubois, C., and Notarstefano, G. (2018). *Water mass formation processes in the Mediterranean Sea over the past 30 years. in Copernicus marine service ocean state report, issue 2*. Ed. K. von Schuckmann, et al. doi: 10.1080/1755876X.2018.1489208

Theocharis, A., Nittis, K., Kontoyiannis, H., Papageorgiou, E., and Balopoulos, E. (1999). Climatic changes in the Aegean Sea influence the Eastern Mediterranean thermohaline circulation. *Geophys. Res. Lett.* 26, 1617–1620. doi: 10.1029/1999GL900320

Thingstad, T. F., Krom, M. D., Mantoura, R. F. C., Flaten, G. A. F., Groom, S., Herut, B., et al. (2005). Nature of phosphorous limitation in the ultra oligotrophic Eastern Mediterranean. *Science* 309, 1068–1071. doi: 10.1126/science.1112632

Troupin, C., Machín, F., Ouberdous, M., Sirjacobs, D., Barth, A., and Beckers, J.-M. (2010). High-resolution climatology of the north-East Atlantic using data-interpolating variational analysis (Diva). *J. Geophys. Res.* 115, C08005. doi: 10.1029/2009JC005512

von Schuckmann, K., La Traon, P.-Y., Alvarez-Fanjul, E., Axell, L., Balmaseda, M., Breivik, L.-A., et al. (2016). The Copernicus marine environment monitoring service ocean state report. *J. Operational Oceanogr.* 9, s235–s320. doi: 10.1080/1755876X.2016.1273446

Zodiatis, G., Drakopoulos, P., Brenner, S., and Groom, S. (2005a). Variability of the Cyprus warm core eddy during the CYCLOPS project. *Deep Sea Res. II* 52, 2897–2910. doi: 10.1016/j.dsr2.2005.08.020

Zodiatis, G., Drakopoulos, P., and Gertman, I. (2004). Modified Atlantic water in the SE levantine basin, (1995-2003). *Rapp. Commun. Int. Mer Medit.* 37, 156.

Zodiatis, G., Drakopoulos, P., Gertman, I., Brenner, S., and Hayes, D. (2005b). The Atlantic water mesoscale hydrodynamics in the Levantine basin, CIESM, 2005. *Strategies for understanding mesoscale processes*. Monaco: CIESM Workshop Monographs n°27, 132. Monaco. Available at: https://www.ciesm.org/online/monographs/Villefranche.html.

Zodiatis, G., Galanis, G., Nikolaidis, A., Radhakrishnan, H., Emmanouil, G., Nikolaidis, G., et al. (2018). "Downscaling the Copernicus CMEMS med-MFC in the Eastern Mediterranean: The new CYCOFOS forecasting systems at regional and sub-regional scales, in Operational Oceanography serving Sustainable Marine Development," in *Proceedings of the Eight EuroGOOS International Conference*, Bergen, Norway, 3-5 October 2017, E. Buch, V. Fernández, D. Eparkhina, P. Gorringe and G. Nolan Eds. Brussels, Belgium: EuroGOOS. 516

Zodiatis, G., Gertman, I., Hayes, D., and Brenner, S. (2007). The Atlantic water in the levantine basin, (1995-2006). *Rapp.Comm. Int. Mer Medit.* 38, 215.

Zodiatis, G., Gertman, I., Poulain, P.-M., Menna, M., and Sofianos, S. (2016). Two decades of monitoring and forecasting of the circulation in the levantine, (1995-2016). *Rapp. Commun. Int. Mer Medit.* 41, 79.

Zodiatis, G., Hayes, D., Gertman, I., Poulain, P.-M., and Menna, M. (2013). The flow features of the SE levantine- long term in-situ monitoring 1995-2012. *Rapp. Commun. Int. Mer Medit.* 40, 141.

Zodiatis, G., Theodorou, A., and Demetropoulos, A. (1998). Hydrography and circulation south of Cyprus in late summer 1995 and in spring 1996. *Oceanol. Acta* 21 (3), 447–458. doi: 10.1016/S0399-1784(98)80029-7

Zohary, T., Brenner, S., Krom, M. D., Angel, D. L., Kress, N., Li, W. K. W., et al. (1998). Buildup of microbial biomass during deep winter mixing in a Mediterranean warm-core eddy. *Mar. Ecol. Progr. Ser.* 167, 47–57. doi: 10.3354/meps167047

Modelling distribution and fate of coralligenous habitat in the Northern Adriatic Sea under a severe climate change scenario

Maria Letizia Vitelletti[1]*, Elisabetta Manea[1], Lucia Bongiorni[1], Antonio Ricchi[2,3], Lorenzo Sangelantoni[3,4] and Davide Bonaldo[1]

[1]CNR – Consiglio Nazionale delle Ricerche, ISMAR – Istituto di Scienze Marine, Venice, Italy,
[2]Department of Physical and Chemical Sciences, University of L'Aquila, L'Aquila, Italy, [3]Center of
Excellence in Telesensing of Environment and Model Prediction of Severe Events (CETEMPS), University
of L'Aquila, L'Aquila, Italy, [4]Climate Simulation and Prediction (CSP), Fondazione Centro Euro-
Mediterraneo sui Cambiamenti Climatici (CMCC), Bologna, Italy

Due to their well-acknowledged capability in predicting habitat distributions, Habitat Suitability Models (HSMs) are particularly useful for investigating ecological patterns variations under climate change scenarios. The shallow coastal regions of the Northern Adriatic Sea, a sub-basin of the Mediterranean Sea, are studded with coralligenous outcrops recognized as important biodiversity hotspots exposed to the effects of climate change. In this research, we investigate the distributions of the Northern Adriatic Sea coralligenous habitats characterized by diverse species assemblages differently influenced by environmental factors, and provide a projection of how these might be impacted by climate change. Two models (Random Forest and MaxEnt), populated with occurrence data gathered from previous publications, environmental parameters' from online databases (CMEMS, Bio-Oracle), and a set of dedicated ocean model simulations, are applied in recent past conditions and under a future severe climate change scenario (RCP 8.5). The model performance metrics confirm the ability of both approaches for predicting habitat distribution and their relationship with environmental conditions. The results show that salinity, temperature, and nitrate concentration are generally the most relevant variables in affecting the coralligenous outcrops distribution. The environmental variations projected under climate change conditions are expected to favour the spreading of opportunistic organisms, more tolerant to stressful conditions, at the expense of more vulnerable species. This will result in a shift in the distribution of these habitats, with a consequent potential loss of biodiversity in the Northern Adriatic Sea.

KEYWORDS

coralligenous conservation, habitat suitability modelling, climate change, random forest, MaxEnt, machine learning

1 Introduction

Marine ecosystems play a key role in safeguarding the planet and in favoring human life. They host a large portion of the world's biodiversity and provide many fundamental benefits to humans, delivering resources and supporting maritime activities, such as fishery, tourism and transportation, and representing a driver of the world economy (Freeman et al., 2013; Barbier, 2017). They do also play a central role in stabilizing the Earth's climate system by contributing to buffer the effects of climate change on our planet (Melaku Canu et al., 2015). Nevertheless, the global climate change is deeply affecting oceanographic, biogeochemical, and hydrological processes that regulate the structure and functioning of marine systems (Leadley et al., 2014). In particular, starting from the 70s, abrupt shifts in current climate patterns (Cheung et al., 2009; Pereira et al., 2010; Cahill et al., 2012; Sloyan et al., 2016), alteration of frequency or intensity of environmental phenomena (Garcia-Reyes et al., 2015; Defforge and Merlis, 2017), increase in temperatures (IPCC, 2013b; Rhein et al., 2013) and ocean acidification (Hoegh-Guldberg et al., 2014) have been detected. These alterations lead to a higher probability and frequency of catastrophic events, mass mortality (IPCC, 2014; Pecl et al., 2017a; Pecl et al., 2017b), food webs alteration (Johnson et al., 2011), abrupt shifts in the seasonality of ecological processes (Deutsch et al., 2015; Lefort et al., 2015), and decline in ecosystem diversity and productivity (Short and Neckles, 1999; Behrenfeld et al., 2006; Hoegh-Guldberg et al., 2007; Polovina et al., 2008; Harley, 2011). As a cascade effect, shifts in marine organism populations, variations in species phenology, and interactions with serious impacts on ecosystem functioning have also been reported (Perry et al., 2005; Last et al., 2011; Doney et al., 2012).

The sensitivity of marine systems to climate change have been discussed in several Assessment Reports (hereby AR) of the Intergovernmental Panel on Climate Change (IPCC). Nevertheless, it was only since the fourth AR in 2007, that the impacts of climate change on marine ecosystems were addressed in deeper detail, with emphasis on the assessment of future ecosystems' response and through a recognition of the complexity of these environments (Gissi et al., 2021; Fraschetti et al., 2022).

Because global warming has been pinpointed to be one of the main elements of climate change, and temperature is expected to keep rising in the upcoming decades, marine species will be forced to either adapt to the new conditions or find new suitable ecological niches (Lawler et al., 2006; Coll et al., 2012; Marras et al., 2015; García Molinos et al., 2016), with consequent shifts in habitat distributions.

Developed to predict the distribution of habitat in response to a given set of environmental factors, Habitat Suitability Models (hereafter HSMs) have been applied in an increasingly number of contexts, becoming important tools to support biodiversity management (Lawler et al., 2006; Degraer et al., 2008; Glockzin et al., 2009; Gogina and Zettler, 2010; Bates et al., 2013; Freeman et al., 2013; Guisan et al., 2013). In particular, HSMs can have an important role in ecosystem-based management planning (Guisan and Thuiller, 2005; Heikkinen et al., 2006; Pompe et al., 2008; Elith and Leathwick, 2009; Kharouba et al., 2009; Lavender et al., 2021), by helping in i) identifying priority areas of conservation (Cañadas et al., 2005), ii) assessing the spatial distribution of suitable habitats for a

species or a community to live within protected areas (Monk et al., 2010), iii) predicting sites at risk of invasion by exotic species (Compton et al., 2010) and iv) investigating the distribution of possible diseases (Williams et al., 2010). These models can be grouped into two categories (Meineri et al., 2015): mechanistic methods aiming at reproducing the ecological dynamics by explicitly describing (and formalizing into equations to be solved by mean of numerical techniques) their driving processes (e.g. energy fluxes, biological interactions, dispersal); and correlative methods aiming instead at reproducing the distribution of species and habitats by addressing their probability of presence (or absence) under prescribed environmental parameters. By pursuing the emerging patterns instead of an explicit description of the ecological processes, the latter approach tends to be more efficient particularly in complex systems.

These tools are widely implemented in the Mediterranean Sea (Lauria et al., 2015; Giannoulaki et al., 2017), one of the worldwide biodiversity hotspots which has been predicted to be among the most impacted by global warming (Templado, 2014; Lionello and Scarascia, 2018) with many Mediterranean species at high risk of decline due to climate change (Vasilakopoulos et al., 2017). In particular, the growing and survival of calcifying organisms, such as corals and coralline algae, are threatened by the alteration of their optimal conditions (Freeman et al., 2013).

The coralligenous, a widespread habitat of the Mediterranean Sea, is recognized as a priority for conservation under the Habitats Directive (EU, 1992; 92/43/EEC) and the Marine Strategy Framework Directive (EU, 2008; 2008/56/EC) for its importance as a biodiversity hotspot (Gomes-Gras et al., 2019). It is the result of a balance between bioconstruction and bioeroding processes carried out by the associated organisms (Cerrano et al., 2001). These complex biogenic structures, characterized by holes and cavities, provide different microhabitats, microenvironments, and ecological gradients that host numerous species, especially coralline algae, mollusks, polychaetes, madrepores, and macroalgae (Ingrosso et al., 2018). Dim-light, narrow thermal oscillations and low water turbidity (influencing the filtering capacity of organisms) are among the main environmental conditions determining coralligenous growth and the number of associated species. The United Nations has identified this habitat as an ecosystem services provider (Action Plan for the protection of coralligenous and other calcareous bio-concretions in the Mediterranean Sea, 2017), and has remarked the need for its protection due to its vulnerability to climate change (Teixidó et al., 2013). At the European level, the EU Council (Regulation n°1967/2006) reported guidelines for sustainable fishery practices in the Mediterranean explicitly referring to the need to protect coralligenous habitat.

Coralligenous outcrops are scattered on the sandy-muddy seabed of the Northern Adriatic Sea (the northernmost region of the Mediterranean basin) and are locally known as *tegnùe*, *trezze* or *grèbeni* (Casellato and Stefanon, 2008). Differently from other bio-constructions, the *tegnùe* are observed to be associated with methane vents and hypothesized to be cemented by methane seeps mostly originating from microbial decomposition of fossil plant material, a characteristic that makes these outcrops unique in the Mediterranean Sea (Tosi et al., 2017 and references therein). Besides hosting highly diverse benthic communities, these outcrops play a fundamental role

as reproductive and nursery areas and attract and protect numerous demersal and pelagic fish species, thus representing sites of high local interest for divers and fishermen (Cenci and Mazzoldi, 2006; Casellato et al., 2007).

This habitat is subject to conservation by two Natura 2000 (N2K) sites, namely the SPA/SAC IT3330009 "Trezze di San Pietro e Bardelli" and the SAC IT3250047 "Tegnùe di Chioggia". The N2K network will likely expand in the Adriatic Sea to accomplish the conservation goals set up by global and European strategies - the Convention on Biological Diversity, the European Biodiversity Strategy 2030, the Global Sustainable Development Goals (de Francesco et al., 2020; Manea et al., 2021). As such, because of the potential effects of climatic change on this habitat, there is a need to implement durable conservation efforts in the area and guide the possible designation of new N2K sites for its protection.

In this direction, this study investigates the potential distribution of the coralligenous habitat in the Northern Adriatic Sea accounting for its species assemblages, and its possible shift under a future severe climate change scenario. Two methods of machine learning habitat suitability modelling are applied: Random Forest and Maximum Entropy (MaxEnt). Both of them are correlative approaches using the full spatial coverage of physical and biogeochemical variables to explore patterns of species distribution (Elith and Graham, 2009). They are both widely recognized as efficient tools for detecting and predicting habitat suitability distribution (Phillips et al., 2006; Thuiller and Münkemüller, 2010; Hijmans and Elith, 2013).

The study consists of two main modelling steps:

1. Habitat suitability analysis investigating the correlation between the distribution of different coralligenous habitat assemblages and the pattern of environmental variables (i.e. temperature, salinity, current velocity, light, nitrate, and phosphate concentration) during a historical period in the recent past (1999-2018, historical – "HIS" – run);

2. Habitat suitability analysis under future RCP 8.5 climate change scenario (2070-2099) and potential shift of the habitats assemblages by utilizing oceanic model simulations under the RCP 8.5 climate change scenario (Moss et al., 2010) (hereafter "SCE" run).

The results are discussed and interpreted in the light of the ecological properties of these systems and their implications for the coastal marine environment, aiming at providing usable information, alongside with some methodological remarks, for long-term planning, management and protection purposes.

2 Materials and methods

2.1 Analysis workflow overview

As a preparatory phase for the modelling activity, the collection of occurrence data was first carried out by georeferencing information obtained from the literature and partially classified under habitat assemblage categories. For those occurrences that were not classified in the literature, a classification phase was undertaken with a dedicated Random Forest and MaxEnt, using the occurrences already classified as a training dataset. This approach provided two distinct datasets (one for each method) with occurrences classified in habitat categories.

Subsequently, another set of Random Forest and MaxEnt based on the fully classified datasets was carried out for computing habitat suitability and its pattern under historical conditions. In this phase the datasets were split into training and test sets; the former was used to fit each of the HSMs on the available data and the latter was employed for the models skill assessment. The last modelling step addressed the prediction of coralligenous distribution under a climate change scenario. All data exploration, calculation, and model pre-processing were carried out using R software (R Development Core Team; version 4.0.5, https://www.r-project.org/), randomForest (version 4.6-14) (Liaw and Wiener, 2002) and dismo (version 1.3-3) (Hijmans et al., 2011) packages. The workflow of the investigation is reported in Figure 1.

2.2 Coralligenous occurrence data and habitat classification

Current coralligenous outcrops occurrences in the North Adriatic Sea were obtained by georeferencing (using ArcMap 10.2) the information contained in Falace et al. (2015) and Ponti et al. (2005) and combining them with the dataset compiled by Martin et al. (2014) in the framework of the projects MEDISEH and CoCoNET (Figure 2). In the study by Falace et al. (2015) the occurrences were clustered in three distinct habitat types (called A, B, and C) based on species


FIGURE 1
Workflow of the investigation process.

FIGURE 2
Geographical setting of the area of interest with the classified records according to the ML methods described in Paragraph 2.1. The filled ○ symbol means the occurrences already classified by Falace et al. (2015), while the unfilled ones represent occurrences from Ponti et al. (2005) and Martin et al. (2014). + symbol visualizes the records classified in the habitat typology with MaxEnt (M) and × stands for Random Forest (RF). Each color represents a habitat type.

compositions (a description of each habitat assemblage is reported in Table 1).

This habitat type classification was extended to all the coralligenous occurrences included in the present study to forecast the possible shift in communities' composition. The habitat types were attributed by measuring, through the potential of HSMs, the correlation between environmental variables and species assemblages reported in Falace et al. (2015). Specifically, both algorithms were trained using the outcrop occurrences already categorized, while, the remaining points were used as a test set to which were then attributed a habitat category to each entry (workflow in Figure 1). Random Forest is widely used for the classification process through the implementation of categorical variables; while the application of MaxEnt for this purpose has required the assessment of the suitability of each habitat based on the already classified points and the classification of the uncategorized occurrences based on the highest suitability value.

2.3 Environmental variables

Several environmental variables were identified in the literature as particularly relevant in influencing coralligenous growth. In this study, temperature, salinity, current velocity, and light (all evaluated at the sea bottom) were considered, alongside with phosphate and nitrate concentrations averaged over the water column (Casellato and Stefanon, 2008; Martin et al., 2014; Falace et al., 2015). Near-bottom quantities for most of the variables were selected considering that the coralligenous outcrops are benthic habitats mainly composed of encrusting organisms. Only the values of nitrate and phosphate characterized the whole water column since these variables, adopted as proxies of nutrients, strongly influence the filter feeder organisms associated with the coralligenous (Piazzi et al., 2011; Gómez-Gras et al., 2021). Data were extracted from different sources Table 2. Simulated temperature, salinity, and current velocity at the sea bottom were provided by the numerical model ROMS (Regional Ocean Modeling System, Haidvogel et al., 2008) reproducing 3-D hydrodynamics and thermohaline processes in the Adriatic Sea from 1987 to 2100. For this application, the Adriatic Sea was discretized into an orthogonal curvilinear grid with horizontal resolution ranging between approximately 2 km, in the northernmost part of the basin, and 10 km in the southeast. The water column was discretized into 15 terrain-following sigma levels progressively refined towards the sea surface to better describe air-sea heat and momentum exchanges. ROMS run was forced by 6-hourly atmospheric outputs from the Regional Climate Model SMHI-RCA4 (Strandberg et al., 2015), driven in turn by the General Circulation Model ICHEC-EC-EARTH (r3i1p1 ensemble member) retrieved from the EURO-CORDEX repository (Jacob et al., 2013). SMHI-RCA4 has been extensively used for regional-scale climate projections, well capturing the climate variability over Europe as represented by the CORDEX multi-model (Kotlarski et al., 2014). Driving atmospheric forcing has a horizontal resolution of approximately 12 km. Boundary conditions were prescribed at the Otranto Strait, at the southeastern end of the basin, based on monthly climatological values computed along the cross-section from the CMEMS reanalysis at 1/16° (Simoncelli et al., 2019) modulated following the anomalies computed from CMCC-CM (Centro Euro-Mediterraneo sui Cambiamenti Climatici Climate Model) profiles (Scoccimarro et al., 2011). Similarly, freshwater input from the mainland was prescribed as interannual modulations, based on the anomalies of SMHI-RCA4 precipitations on the Adriatic basin, of climatological values for 39 points sources along the coast following the estimates by Raicich (1994); Janeković et al. (2014), plus Zuliani et al. (2005) for the overall contribution from the Venice lagoon. In order to decouple the sea level modulation trends from the astronomical tide, no tidal forcing was included in this run. Although a thorough validation of the

TABLE 1 Habitat assemblages description extrapolated by Falace et al. (2015).

Habitat	Description	Species
A	Opportunistic and tolerant macroalgal species resistant to mud and organic matter	• Turf-dominant algae (*Cladophora* sp., *Antithammion* sp., *Pseudochlorodesmis furcellata*) • Encrusting Porifera (*Antho (Antho) incostans*, *Dictyonella incisa*, *Mycale (Mycale) massa*) • Bioeroders (*Cliona* spp., *Rocellaria dubia*)
B	Massive Porifera erect Tunicata and non-calcareous encrusting algae	• *Chondrosia reniformis*, *Tedania anhelans*, *Ircinia variabilis* • *Aplidium conicum*, *Aplidium tabarquensis* • *Peyssonnelia* spp.
C	Non-articulated calcareous macroalgae, tunicate	• *Polycitor adriaticus*

TABLE 2 Summary details of environmental variables.

Variable	Unit	Original resolution	Historical run	SCE run	Source
Temperature	°C	0.02°× 0.02°	1999-2018	2070-2099	ROMS
Salinity	PSU	0.02°× 0.02°	1999-2018	2070-2099	ROMS
Current Velocity	m/s	0.02°× 0.02°	1999-2018	2070-2099	ROMS
Light	E/m^2/year	0.083°× 0.083°	2000-2014	/	Bio-Oracle
Phosphate	Millimole/m^3	0.042° × 0.042°	1999-2018	/	CMEMS
Nitrate	Millimole/m^3	0.042° × 0.042°	1999-2018	/	CMEMS

ROMS run is beyond the scope of the present study, the most relevant quantities for our application were assessed against observational data and existing literature. In particular, sea surface temperature (SST) for the 1987-2016 period was compared with the L4 Optimal Interpolation (L4OI) Mediterranean SST Analysis L4, reprocessed using Pathfinder L3S (Pisano et al., 2016), available from the Copernicus Marine Service, whereas the main thermohaline and circulation patterns in the 1987-1996 decade were verified against the work by Artegiani et al. (1997a; 1997b). Modelled time-averaged SST in the Northern Adriatic Sea is characterized by a cold mean bias of approximately -0.75°C with moderate spatial variability (Figure 3A), and by an underestimation of the warming trend in the above-mentioned period by 0.02°C y^{-1}.

The vertical structure of the water column reproduces the space-averaged temperature and salinity seasonal profiles presented by Artegiani et al. (1997a), and the surface circulation pattern (Figure 3B) captures, at least qualitatively, the main features of the gyre system characterizing the basin-scale circulation in the area (Artegiani et al., 1997b).

Light at the sea bottom was retrieved from Bio-Oracle (Tyberghein et al., 2012; Assis et al., 2018). Phosphate and nitrate concentrations were extracted from the Copernicus Marine Service (hereafter CMEMS). For the first step of the modelling phase (HIS) data from ROMS and CMEMS were sampled and averaged for the period between 1999 and 2018, whereas data extracted from Bio-Oracle were averaged from 2000 to 2014. The SCE simulation was driven by projected data of temperature, salinity, and current velocity fields at the sea bottom from ROMS model

in the period between 2070 - 2099. For Random Forest and MaxEnt applications, all the variables were sampled on the same grid with 0.02° resolution, bracketing a geographical domain between 44.8-46 latitude and 23-14 longitude and projection (WGS84), interpolated when necessary using the "nearest neighbor" method. The patterns of the six environmental variables used in the study, with variations of temperature, salinity, and velocity in climate change scenarios, are reported in Figure 4.

2.4 Habitat Suitability Models set up and evaluation

Random Forest is an extension of single Classification Trees, in which multiple decision trees are built with random subsets of the data. This model can be employed for both classification and regression tasks (Vincenzi et al., 2011). Both modes were applied in this study, respectively for the identification of the unclassified habitats and for the computation of the suitability of each habitat, both in historical and climate change conditions. MaxEnt aims at assessing the suitability of a given habitat by pursuing a maximum entropy configuration (that is, closest to uniform) compatible with the available information (Freeman et al., 2013). Both models were populated with presence-only data of habitat-categorized coralligenous outcrops, using the six continuous environmental variables as predictors.

Before performing any suitability analyses, a tuning of hyperparameters in Random Forest (top parameters controlling the learning process and involved in understanding which parameters
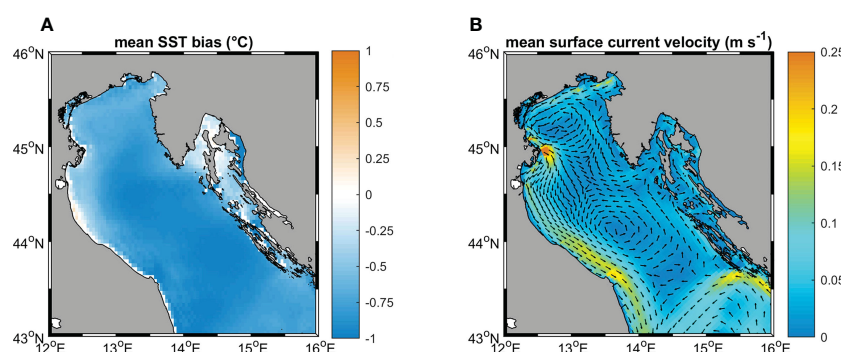
FIGURE 3
(A) mean SST bias; **(B)** surface circulation patterns, color map indicates the current speed, vectors (subsampled every 3 cell grids and normalized on the current speed) indicate the current directions.

can correctly map the features) and parameters in MaxEnt (internal to the model and estimated by the training process, that explicates the system variability) is strongly suggested to define the optimal model architecture. In this study, the default set up of Random Forest implemented in R appeared adequate, while for MaxEnt a specific investigation was conducted with the ENMeval R package (version 0.3.1, Muscarella et al., 2014) determining the best options balancing goodness-of-fit and model complexity.

In both models, the suitability analyses were carried out using training and testing datasets including respectively 70% and 30% of the whole occurrence data. The training set enabled the model to learn the relations between the environmental variables and occurrences, while the testing set was used to evaluate the model performance. The goodness-of-fit and performance were quantified by using the "Area Under the Curve" (hereafter AUC) and "True Skill Statistic" (hereafter TSS), two metrics that proved to be particularly indicated for Random Forest regression and MaxEnt applications (Shabani et al., 2018; Acharya et al., 2019; Rew et al., 2020). The AUC, related to the probability that a randomly chosen occurrence site ranks more suitable than a randomly chosen absence site (Elith et al., 2006), ranges between 0 and 1, where 1 means perfect matching, 0.5 represents matching not better than random, and 0 corresponds to completely wrong predictions. TSS considers omission and commission errors (related to false negatives and false positives respectively) and is not affected by the size of the validation set. It ranges between -1 and +1, where +1 indicates a perfect agreement and values of 0 or less indicate performance no better than random (Allouche et al., 2006).

The relative contribution to the model predictions from each variable is quantified in Random Forest as the Mean Decrease Accuracy (hereafter %IncMSE), and in MaxEnt as the Permutation Importance. In both cases, higher values correspond to the higher importance of the variable.

In MaxEnt the Jackknife analysis also allows the quantification of the individual effect of each variable by systematically excluding it from the dataset (Elith et al., 2011). The use of this function helped to identify also the variables that mainly affect the model fit.

For both models, the suitability is expressed as a probability ranging from 0 (worst suitability for the habitat) to 1 (best suitability for the habitat).

2.5 Habitat area calculation, distribution, and shift

The raster files produced by each model were used to estimate the suitability in the historical period and under climate change RCP 8.5 scenario. The calculation of the surface of each range of suitability was conducted by implementing basic functions in R. Furthermore, the SCE suitability values were extrapolated, for each occurrence point, to hypothesize which habitat could be the most likely to be found according to the predicted changes in environmental variables.

The model outputs, provided as ASCII raster files, were post-processed using Matlab (version MatlabR2018a) to identify spatial patterns of change in habitat suitability, shifts in dominant habitat,
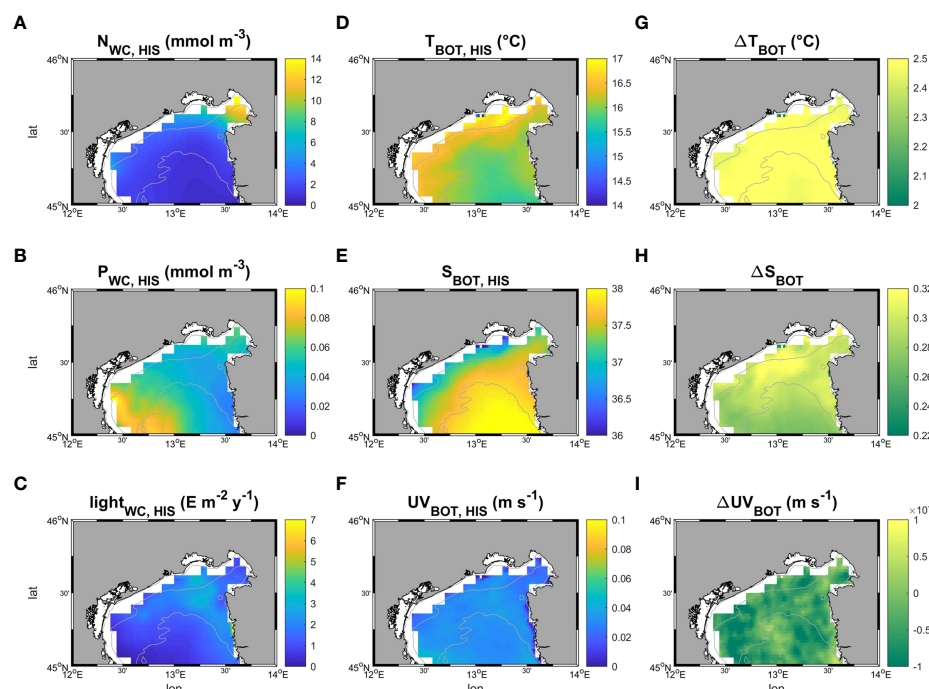
FIGURE 4
Patterns of the six environmental variables employed in this study. **(A–F)** show respectively the time averaged patterns of nitrate and phosphate concentration along the water column, and light, temperature, salinity and velocity at the sea bottom in the historical period (1999-2018). **(G–I)** map the difference (Δ) in bottom temperature, salinity and current velocity speed between future (under a severe climate change scenario RCP 8.5, 2070-2099 – SCE) and historical conditions (HIS).

and to produce maps for a visual representation of the results throughout the study area.

2.6 Sensitivity analysis

In order to explore how the uncertainty on the evolution of the environmental variables can affect the results of the present work, a sensitivity analysis was performed by running a set of additional HSM simulations in the future scenario, in which the projected values of each environmental variable were singularly increased and decreased by an estimate of the related uncertainty. The amount of this perturbation was defined based on existing large-scale modelling projections or, if unavailable, from information on basin-scale variability in present conditions (Bonaldo et al., 2014; Soto-Navarro et al., 2020; and Reale et al., 2022). For light radiation, in particular, the variation for the sensitivity analysis was chosen as the standard deviation of the present values restricted to a bathymetric range between -18 and -40m. A complete overview of the variations applied to each environmental factor is reported in Table 3. The overall sensitivity of the results was quantified in terms of consensus of the additional simulations with the SCE run. This was computed at each location as the fraction of sensitivity runs in which the projected evolution was consistent with the one computed in SCE. Larger values of consensus correspond to smaller sensitivity.

3 Results

3.1 Habitat classification

The classification of the reported occurrences into the three habitat assemblages results into two datasets differing from each other in only three occurrence points out of 85, reaching a 96% agreement rate. Figure 2 shows the distribution of the categorized record, while further details on the classification are provided in Supplementary Tables 1 and 2.

3.2 Models accuracy

Both Random Forest and MaxEnt exhibit high AUC values (the lowest, 0.88, was calculated by MaxEnt for habitat C), meaning that the models have a high prediction accuracy (Table 4). Although Random Forest seems slightly better performing than MaxEnt according to this metric (Figure 5), the difference between models' test AUC is very small (maximum 0.026 for habitat C). The models show high TSS values, indicating they were both reliable. Habitat A and B returned estimations of 0.95 for both in Random Forest and of 0.94 and 0.86 respectively in MaxEnt. Habitat C presents lower values with 0.73 and 0.72 in Random Forest and MaxEnt, respectively.

TABLE 3 Perturbation values for the sensitivity analysis.

Variable	Value of increase/decrease	Source
Temperature	± 1.5°C	Soto-Navarro et al. (2020)
Salinity	± 1.5 PSU	Soto-Navarro et al. (2020)
Current Velocity	± 0.05 m/s	Bonaldo et al. (2014)
Light	± 2 E/m^2/year	Standard deviation calculated by the environmental raster layer
Phosphate	± 37%	Reale et al. (2022)
Nitrate	± 11%	Reale et al. (2022)

TABLE 4 Models accuracy evaluation using AUC test and TSS metrics.

Random Forest		MaxEnt	
Habitat A			
AUC test	0.98	**AUC test**	0.97
TSS	0.95	**TSS**	0.94
Habitat B			
AUC test	0.98	**AUC test**	0.91
TSS	0.95	**TSS**	0.86
Habitat C			
AUC test	0.91	**AUC test**	0.88
TSS	0.73	**TSS**	0.72

3.3 Variable importance and contribution

The analysis of the contribution of each environmental variable quantifies their role in controlling the habitat distribution. The evaluation of Random Forest features under the historical period highlights that for both habitats A and B the highest decrease in % IncMSE is observed when salinity is removed by the system (11.84% and 12.57%, respectively), followed by phosphate (4.24%) and nitrate (2.87%) for habitat A, and temperature and light (11.56% and 8.06%, respectively) for habitat B. Regarding habitat C, it appears that nitrate is the most influencing (19.94%) variable, followed by salinity (16.21%), and temperature (16.15%).

The MaxEnt analysis of contribution shows that the historical distribution of habitat A is largely dependent on temperature (99.3%). Habitat B is mainly influenced by temperature (47.1%) and phosphate (45.3%). In habitat C salinity is reported as the most contributing variable (71.3%), followed by nitrate (12.8%) and light (9.1%). A complete variable ranking and related figures are in Supplementary Tables 3–8, and Supplementary Figure 2.

The Jackknife analysis built-in in MaxEnt (Figure 6) shows that temperature in habitat A, when taken individually, is the most influencing the goodness-of-fit (referred to in the model as "gain"); once this variable is cut out, the gain decreases, suggesting that temperature was the main source of system's variability. In habitat B, when considering each variable taken alone, light radiance appears as the one contributing the most, in turn, when individually removing each variable from the whole set, temperature emerges as the one mostly explaining the variability of the system. Salinity in habitat C is the most contributing variable when taken alone, but nitrate removal shows that this variable actually explains the variability of the system.

The response curves produced by MaxEnt reported for each habitat in Figures 7–9, represent the effect of each environmental variable on the model prediction. In habitat A, an increase in suitability is recorded as the light radiance increases and a similar trend is observed in habitat C where, however, the suitability curve

reaches a maximum and decreases up to a plateau. Light in habitat B presents a bell-shaped curve meaning that an optimal range of suitability is present corresponding to a defined interval of values with zero suitability at the extremes of the distribution. Nitrate shows a similar trend to light, both in habitat A and B, whereas in habitat C high suitability values were reached at low concentrations. In both habitats A and B suitability is inversely related to phosphate concentration; in habitat C the highest suitability is obtained in correspondence to intermediate concentration values. Habitats A and B exhibit comparable trends also in response to salinity, both reporting a decrease from the optimal suitability (1.00) to 0.55 and 0.60 respectively as long as the variable increases. Habitat C reaches the highest suitability around 38 followed a sudden decrease for higher values. Increasing temperature in habitats A and B lead to an increase in their suitability, while in habitat C the highest value is reached at about 16.5°C, followed by a steep decrease. Finally, the increase in bottom current velocity in habitats A and B causes a constant decrease in suitability, whereas habitat C reaches the highest suitability at the midpoint of the current velocity curve.

3.4 Coralligenous suitability mapping

Figures 10, 11 show the maps of historical suitabilities and the future variations computed respectively by Random Forest and MaxEnt for all habitat assemblages. In the historical run, Random Forest predicts patchy high suitability areas close to the occurrence point for all the three coralligenous habitat types, whereas MaxEnt predicts a wider suitable areas and smoother suitability patterns.

Random Forest for habitat A in SCE predicts an increase in the probability of having ideal conditions in the whole area of interest, in particular towards the Gulf of Trieste, the Slovenian and Croatian coasts. Variations between the historical and SCE are considered here as changes in total area of each habitat. Areas with "low" (equal to suitability values comprehended between 0 and 0.25) and "high" (0.50
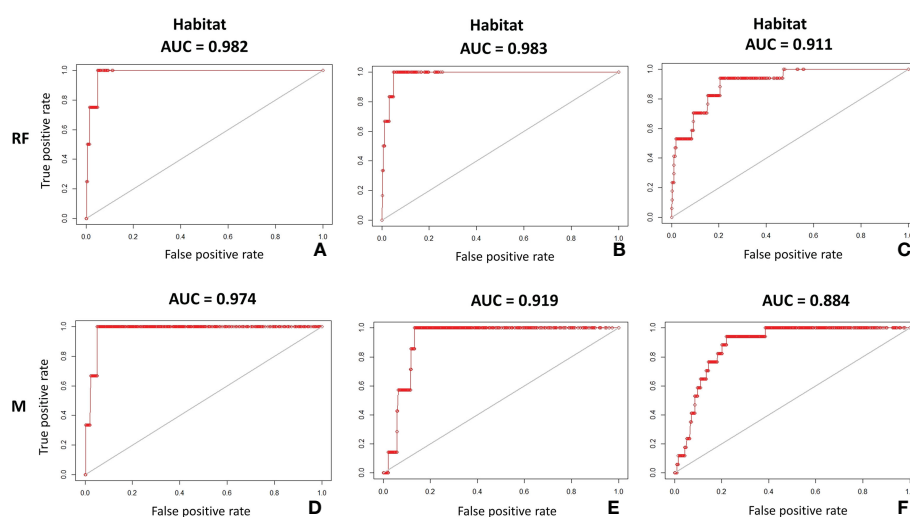
FIGURE 5

AUC plots on test dataset showing the accuracy of Random Forest (RF) and MaxEnt (M) in predicting the potential distribution of coralligenous: **(A)** Random Forest AUC on test dataset of habitat A; **(B)** Random Forest AUC on test dataset of habitat B; **(C)** Random Forest AUC on test dataset of habitat C; **(D)** MaxEnt AUC on test dataset of habitat A; **(E)** MaxEnt AUC on test dataset of habitat B; **(F)** MaxEnt AUC on test dataset of habitat C.

FIGURE 6
Jackknife analyses results derived from MaxEnt reporting the contribution and potential effects of variables on the model fit (referred in the system as "gain"): **(A)** Jackknife analysis of habitat A; **(B)** Jackknife analysis of habitat B; **(C)** Jackknife analysis of habitat C.
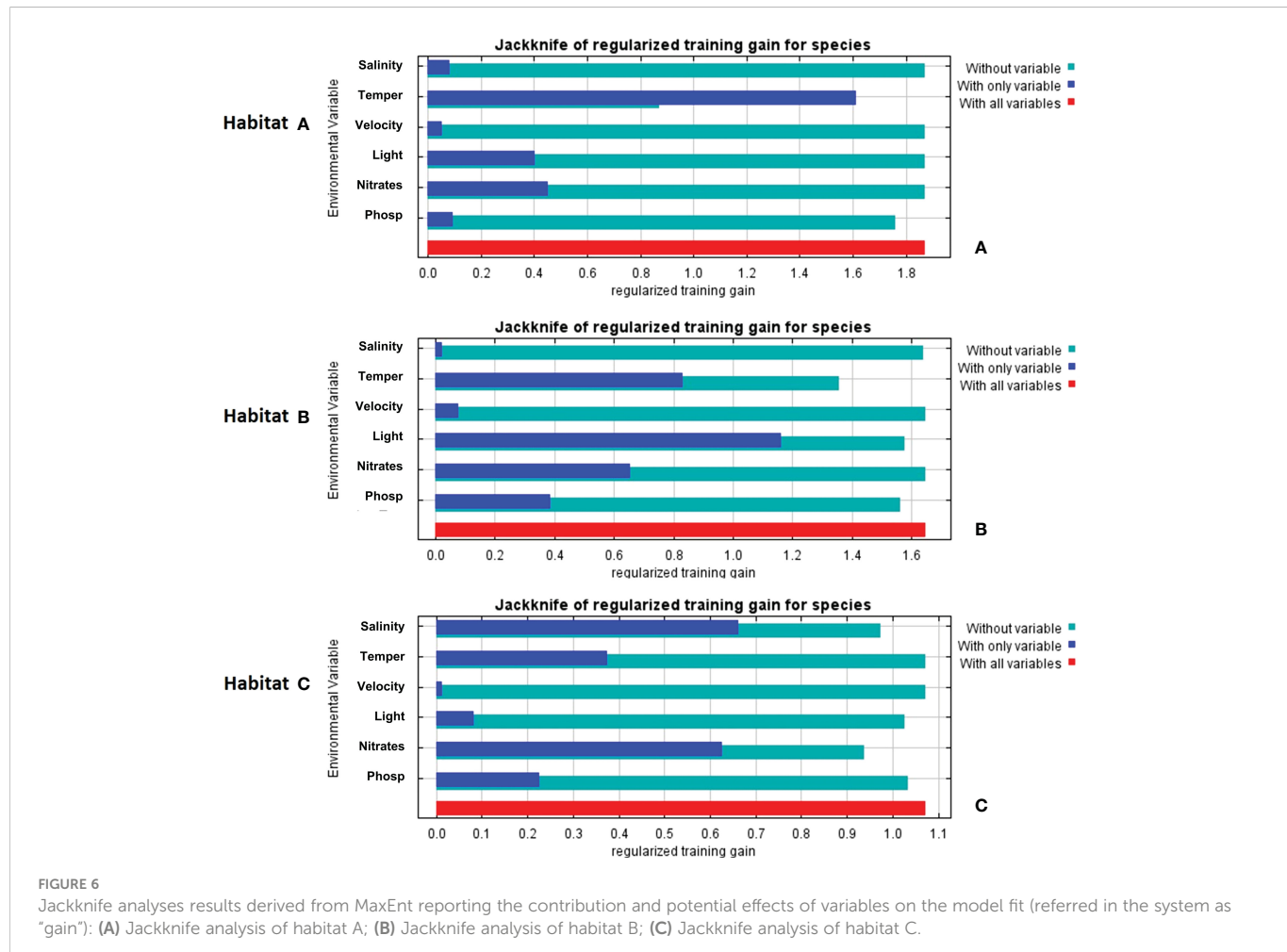
– 0.75) ranges experience an overall decrease of -801 km² (-10.46%) and -3 km² (-33.32%), whereas a very marked increase for the "moderate" (0.25 - 0.50) interval is reported with +805 km² (+2121.41%). An increment in the suitability is shown also for

habitat B. Random Forest reports an increase in the "moderate" interval with +117 km² (equal to +339.92%) whereas the "low" surface decreases by -79 km² (-1.04%) and "high" and "very high" (0.75 – 1.00) disappear in SCE. Lastly, in habitat C an overall decrease in
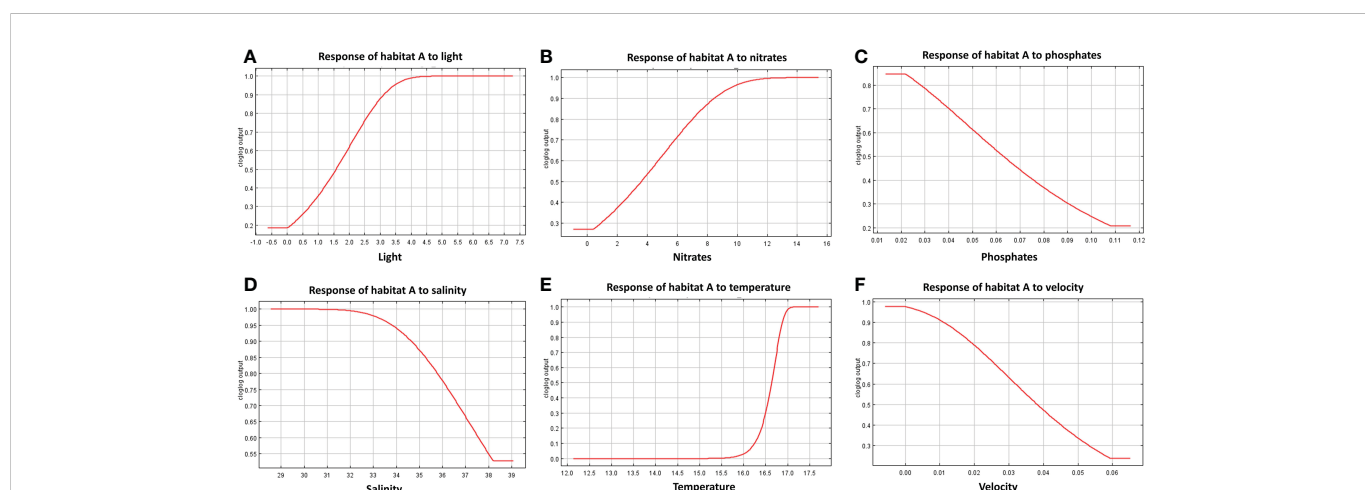
FIGURE 7
Response curves derived from MaxEnt reporting the relationship of predicted suitability of habitat A to environmental variables, with y-axis indicating the probability values and x-axis the concentration/intensity of the variables: **(A)** relationship between habitat A and light; **(B)** relationship between habitat A and nitrate concentration; **(C)** relationship between habitat A and phosphate; **(D)** relationship between habitat A and salinity; **(E)** relationship between habitat A and temperature; **(F)** relationship between habitat A and velocity.
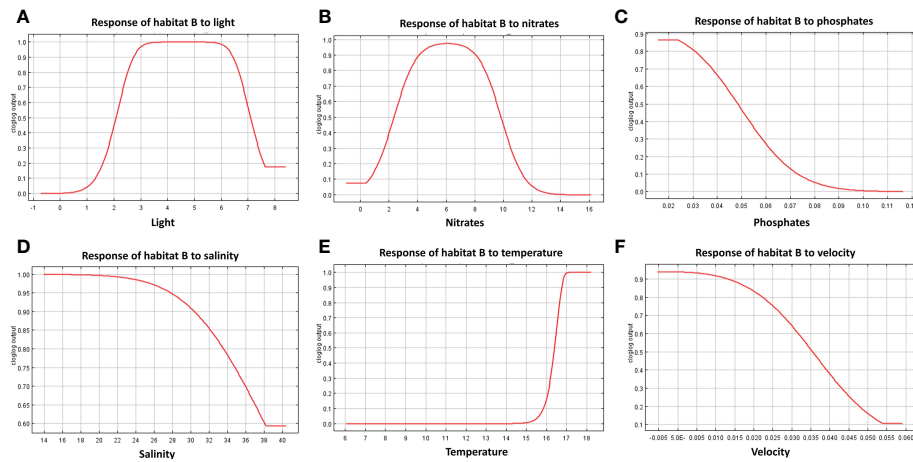
FIGURE 8
Response curves derived from MaxEnt reporting the relationship of predicted suitability of habitat B to environmental variables, with y-axis indicating the probability values and x-axis the concentration/intensity of the variables: **(A)** relationship between habitat B and light; **(B)** relationship between habitat B and nitrate concentration; **(C)** relationship between habitat B and phosphate; **(D)** relationship between habitat B and salinity; **(E)** relationship between habitat B and temperature; **(F)** relationship between habitat B and velocity.

suitability is observed in the SCE. Random Forest shows a decrease in the areas close to the occurrences and predicts a slight increase offshore. The variations between historical and SCE return an increment of +208 km^2 (+2.80%) in the "low" range, but an important decrease is reported for the "moderate" range with -114 km^2 (-65.99%), and the other two intervals set to zero.

Results from MaxEnt for habitat A exhibits a decrement in "low", "moderate" and "high" percentage by -7069 km^2 (99.56%), -228 km^2 (-100%), and -99 km^2 (-61.29%) respectively, whereas the "very high" increases by +7396 km^2 (+3348.69%). Habitat B has an increment in "high" and "very high" ranges with +130 km^2 and +4868 km^2 (+43.47% and +1740.95%) respectively. "low" and "moderate" decrease by -4835 km^2 and -164 km^2 (-73.90% and -27.89%). Then, for habitat C MaxEnt returns a reversed pattern: only the lowest range

reports an increase with +1213 km^2 (+22.12%), the others decreased by -395 km^2, -363 km^2, and -454 km^2 (-48.31%, -46.02%, -73.60%).

3.5 Habitat distribution and habitat shift

The comparison of the suitability values allows to identify the dominant (that is, the most suitable) habitat at each location, the habitat shift in future conditions, as well as the areas in which a minimum suitability threshold (in this case 0.5) is achieved (Figure 12).

The results from Random Forest returns suitability below 0.5 on the whole study area for all three habitats. Although with relatively low suitability values, in the historical period habitat C seems to dominate over a larger area, followed by B and A. The result reverses in SCE, with
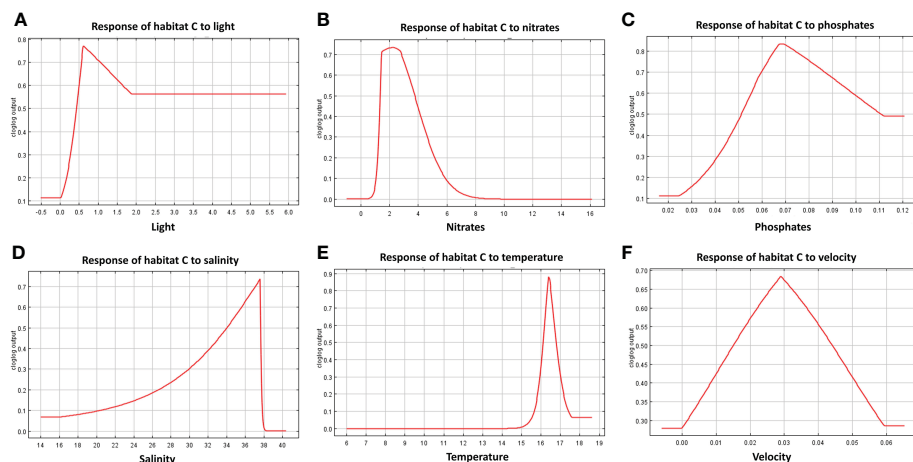
FIGURE 9
Response curves derived from MaxEnt reporting the relationship of predicted suitability of habitat C to environmental variables, with y-axis indicating the probability values and x-axis the concentration/intensity of the variables: **(A)** relationship between habitat C and light; **(B)** relationship between habitat C and nitrate concentration; **(C)** relationship between habitat C and phosphate; **(D)** relationship between habitat C and salinity; **(E)** relationship between habitat C and temperature; **(F)** relationship between habitat C and current velocity.
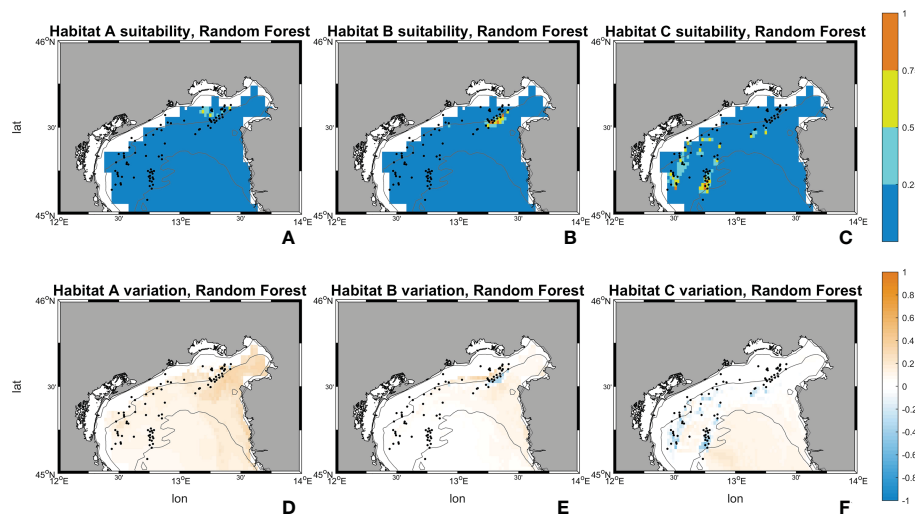
FIGURE 10
Suitability maps (horizontal resolution 0.02°) from Random Forest. Maps **(A−C)** represents Random Forest suitability for habitat A, B and C during the historical period (1999-2018). Maps **(D−F)** represents Random Forest future changes according to climate change RCP 8.5 scenario. First line scale legend: 0-0.25 = Low suitability; 0.25-0.5 = Moderate suitability; 0.5-0.75 = High suitability; 0.75-1 = Very high suitability (Thuiller and Münkemüller, 2010; Mousazade et al., 2019). Second line scale legend: -1 = prediction of a suitability decrement in comparison to historical period; 0 = no changes predicted; +1 = prediction of a suitability increment in comparison to historical period.

habitat A occupying a wider suitability surface, followed by C, and B. This change in dominant habitat patterns is associated with 14 occurrence points possibly shifting from habitat C to A, 3 from B to A, and 1 from A to B. MaxEnt maps returns suitability both below and above the 0.5 threshold in the historical period, with higher values near the coastal zone. The habitat that coveres most of the area is habitat C, followed by B and A. Once again, the picture changes in SCE, with a dominant presence of habitat A above the 0.5 threshold throughout the whole basin. In this perspective, MaxEnt predicts a potential shift of 50 occurrence points from C to A, 21 from B to A, and 4 from A to B.

3.6 Results from sensitivity analysis and consensus maps

The results of the sensitivity analysis are summarised in consensus maps showing, for every cell of the domain, the fraction of sensitivity runs in which the sign of the trend of the suitabilities (Figure 13) or the projected dominant habitats (Figure 14) confirm the results of the SCE run. Very high scores (yellow color) appear widespread for habitats A and B (Figures 13A, B, D, E) both in Random Forest and Maxent, suggesting a satisfactory robustness for
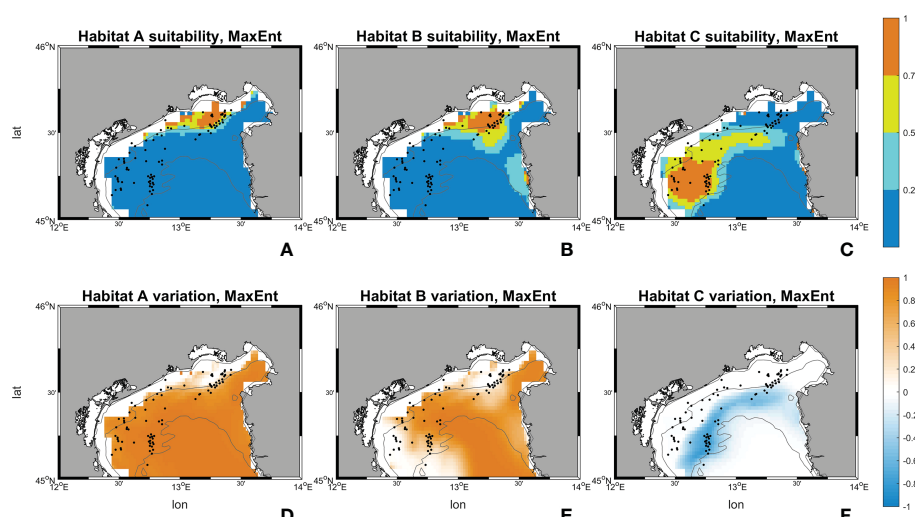
FIGURE 11
Suitability maps (horizontal resolution 0.02°) from MaxEnt. Maps **(A−C)** represents MaxEnt suitability for habitat A, B and C during the historical period (1999-2018). Maps **(D−F)** represents MaxEnt future changes according to climate change RCP 8.5 scenario. First line scale legend: 0-0.25 = Low suitability; 0.25-0.5 = Moderate suitability; 0.5-0.75 = High suitability; 0.75-1 = Very high suitability (Thuiller and Münkemüller, 2010; Mousazade et al., 2019). Second line scale legend: -1 = prediction of a suitability decrement in comparison to historical period; 0 = no changes predicted; +1 = prediction of a suitability increment in comparison to historical period.
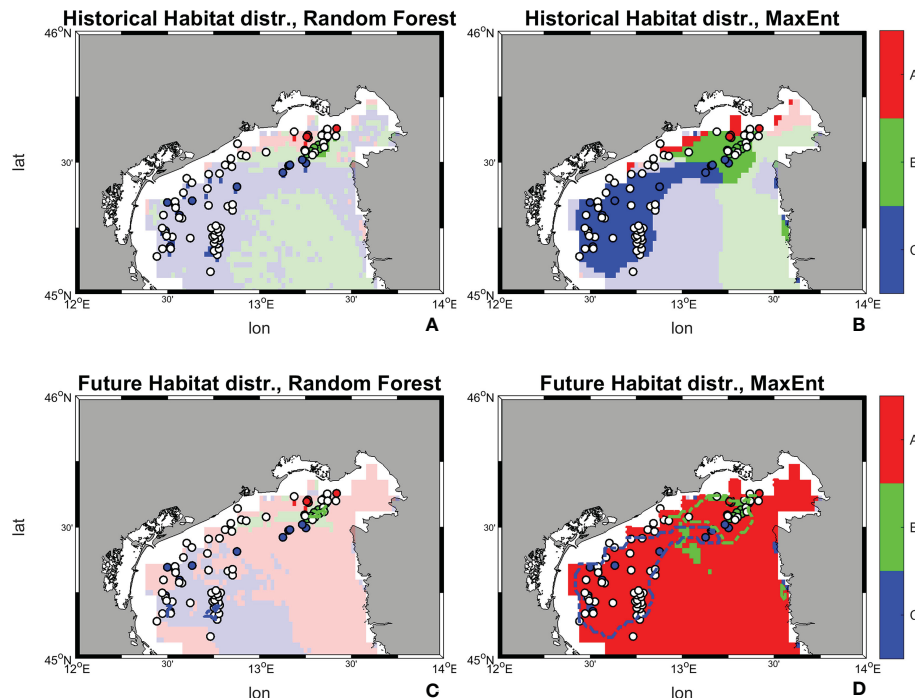
FIGURE 12
Historical and future distribution of dominant habitats (maximum suitability) according to Random Forest and MaxEnt models. **(A)** Historical distribution of habitats predicted by Random Forest; **(B)** Historical distribution of habitats predicted by MaxEnt; **(C)** Future distribution of habitats predicted by Random Forest; **(D)** Future distribution of habitats predicted by MaxEnt. Shaded colors indicate suitability values below a threshold of 0.5, therefore belonging to low-medium ranges, while marked ones stood for values above 0.5 and belonging to high range.

these predictions throughout the whole domain. Some larger sensitivity is found for habitat C (Figures 13C, F), appearing in Random Forest as a patchy pattern of low-agreement regions, and, to a smaller extent, in MaxEnt as a slight decrease in consensus along the coast.

The larger sensitivity of Random Forest in the calculation of the habitats suitabilites reflects on a smaller consensus in the prediction of the dominant habitat, whereas MaxEnt seems to confirm a larger robustness with respect to possible uncertainties in the environmental parameters (Figure 14).
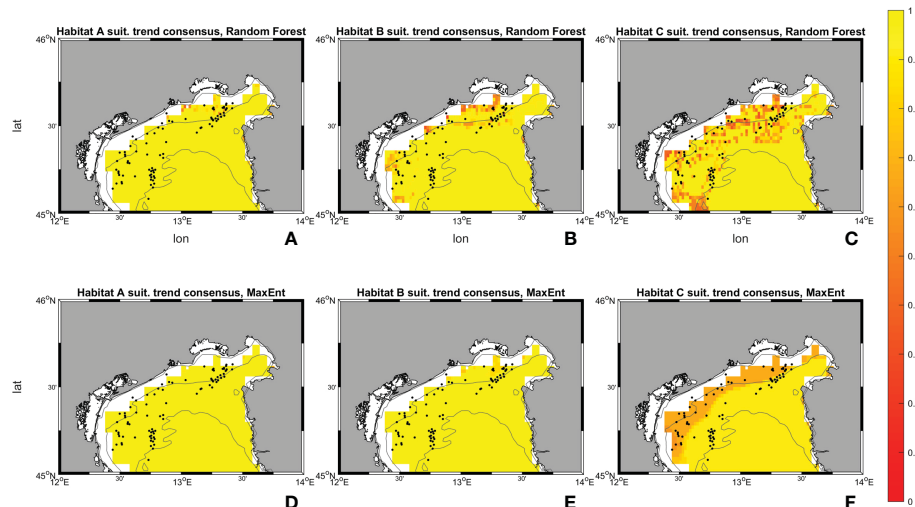
FIGURE 13
Consensus between trends sign in the sensitivity analysis and the SCE run for Random Forest **(A–C)** and for MaxEnt **(D–F)**. For each simulation, agreement is assessed based only on the sign (either increasing or decreasing) of the trend. The scale ranges from 0 (worst agreement, no simulation in the sensitivity analysis in agreement with SCE) to 1 (perfect agreement, all simulations in agreement with SCE).
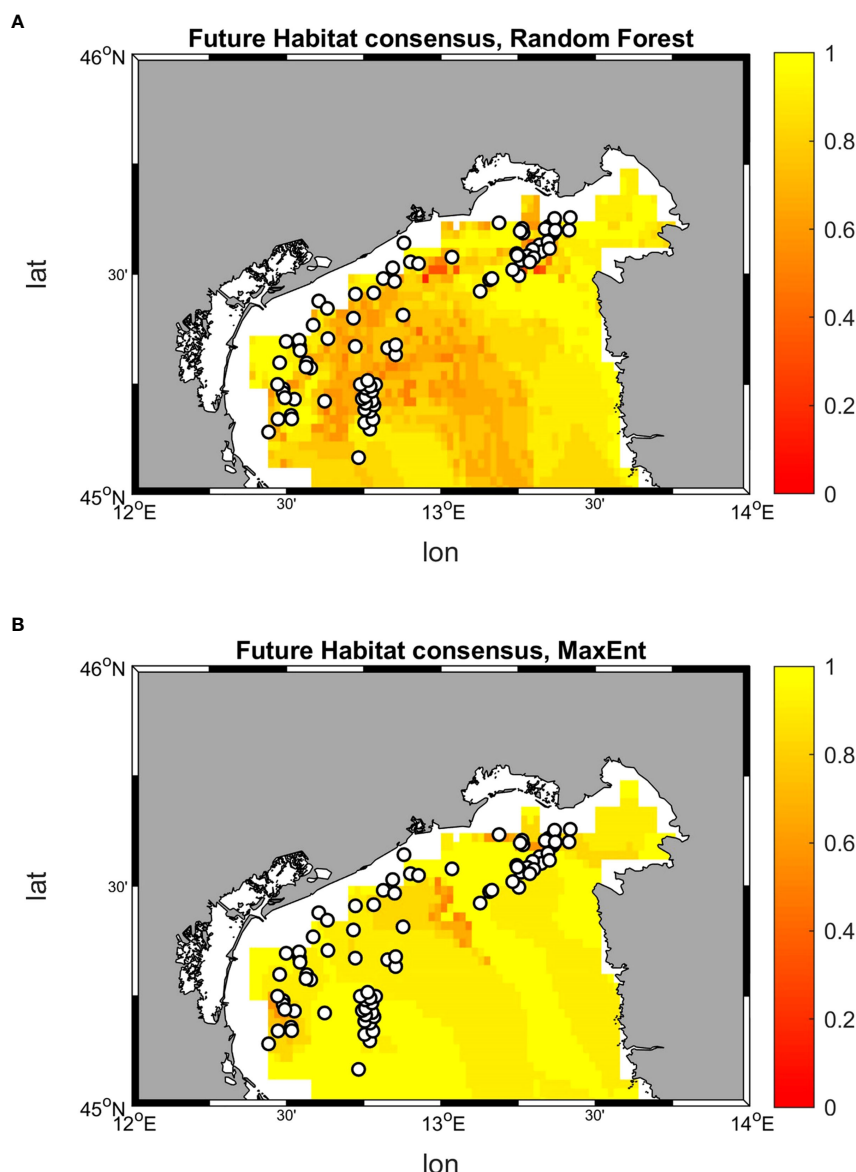
FIGURE 14
Consensus between projected habitat distribution in the sensitivity analysis and the SCE run for Random Forest **(A)** and MaxEnt **(B)**.

4 Discussion

The identification of areas of priority for conservation and the successful management of Marine Protected Areas (hereafter MPAs), are severely hindered by a lack of data on the distribution of habitats identified as vulnerable and threatened by environmental and anthropogenic effects at different scales, as it is the case of the coralligenous (Teixidó et al., 2013; Marshall et al., 2014). MPAs are recognized as excellent tools to counteract some threats that affect marine ecosystems and decrease their vulnerability by enhancing their resilience (Vitelletti and Bonaldo, 2020). The prediction of the effects of climate change on environmental conditions and communities can feed the adoption of anticipatory approaches, thus fostering the effective management and protection of marine areas (Elliott et al., 2017). The application of HSMs can provide forecast on the effects of environmental processes and possible human actions on the marine environment, facilitating the identification of areas of priority for conservation, and supporting the definition and implementation of MPA management plans (Robinson et al., 2011).

4.1 Remarks on models performance

The accuracy metrics calculated for Random Forest and MaxEnt confirm in principle the good performance of both models in predicting the probability of coralligenous presence in the Northern Adriatic Sea (Acharya et al., 2019 and reference therein). Nonetheless, the appearing discrepancies in terms of present and future habitat distribution show that accuracy metrics *per se* are not always sufficient for drawing conclusions on the validity of the results. In fact, due to the complexity of the ecological processes and the unavoidable need for simplified conceptualizations (be them mechanistic or correlative), HSMs are intrinsically prone to different sources of error. Several studies have investigated the different relations

between HSMs and input data characteristics concluding that models results and effectiveness vary according to the study system, data quality, and the scientific question addressed (Elith and Graham, 2008 and references therein). The implementation of at least two model techniques, with the comparison of their performances and the integration of the results, is typically adopted in HSM studies to better address the uncertainty related to the modelling approach.

The two models employed in this study predict higher habitats' suitability in areas close to the available occurrences, albeit with different distributions. While MaxEnt reports larger surfaces suitable for coralligenous presence with a gradual decrease as moving away from the occurrences, Random Forest, at a finer scale observation, showed narrower suitability ranges. In future conditions, both models predict some changes in habitat suitability and dominance with more marked variations in MaxEnt than in Random Forest, although with overall comparable spatial patterns. However, it is clear that a net loss of suitable areas of some habitat types is envisaged by both models and some associated species are more vulnerable than others to climate change (Boys et al., 2021). The difference between MaxEnt and Random Forest results can be ascribed to various reasons, from the implementation of different approaches eliciting differences in behavior of species distribution outputs to the choice of environmental variables (Shabani et al, 2018 and reference therein). In particular, the patchy pattern in Random Forest is probably due to an overfitted model, where the effects of environmental conditions on the location of occurrences exert a greater influence on the closest surrounding area and consequently lead to the presence of high probabilities of suitability in the neighbouring cells. The configuration of a built-in option called "regularization parameter" in MaxEnt permits to prevent overfitting although with a less localized prediction (Phillips and Dudik, 2008 and reference therein). The absence of this option in Random Forest model can be the reason for the greater influence of the environmental variables on the records' surrounding area and confirms the sensitivity of this model to spatial autocorrelation (Sinha et al., 2019). The size of the dataset might be another factor giving rise to different results between the models. Literature reports evidence of MaxEnt being capable of dealing with limited datasets (Kaky et al., 2020); whereas, Random Forest is more influenced by the quantity and spatial distribution of the available occurrences (Rahmati et al., 2016; Acharya et al., 2019), though possibly achieving satisfactory results also in the presence of a limited number of occurrence records (Mi et al., 2017 and reference therein). Even though the model skills of the two approachs are comparable, the tendency to overfitting in Random Forest, combined with its overall higher sensitivity to uncertainties in the input data, suggests that present and projected basin-scale patterns produced by this model should be treated with higher cautiousness.

4.2 Habitat shifts and ecological implications

The differentiation into the three habitat types and the application of HSMs allows to predict how each of them will be influenced by future climate changes.

Among the considered environmental variables temperature, salinity and nitrate are the strongest drivers for the distribution of the three habitats types. These variables are largely influenced by

atmospheric factors as well as by the terrestrial dynamics of the North Adriatic Sea that is subject to important river inputs (Degobbis et al., 2000). Alterations in environmental variables due to climate change have already been explored and have proved to be relevant in this sub-basin being able to change the characteristics and quality of the water body (Rizzi et al., 2016). However, a certain degree of correlation among variables, particularly in coastal environments dominated by cross-shore gradients, may have some spurious impacts on the results (Burbach, 2011) also considering that the distribution of habitats is influenced by overlapping and integrating factors. For this reason, during the setting up phase of any model, it is recommended to settle the correct resolution and spatial scale to capture the entire available environmental variability.

The results obtained in this study predict the shift from habitats B and C to habitat A, suggesting a more suitable growth conditions for habitat A species assemblages in the future. Opportunistic organisms (e.g. turf-forming macroalgae, encrusting Porifera, and bioeroders) dominate habitat A and are known to tolerate what is generally considered stressful environmental conditions, such as high temperature and organic loads (Piazzi et al., 2012; Falace et al., 2015). Indeed, the suitability distribution of this habitat was positively correlated with high nitrate concentrations and temperature, while a negative influence resulted from high salinity and phosphate levels. These results are in line with previous modeling findings (Falace et al., 2015). Habitat B is considered a transitional habitat, being composed of species characterizing habitat A together with massive Porifera, erect tunicate, and non-calcareous encrusting algae. Similarly to A, habitat B distribution appears influenced by temperature and salinity showing respectively positive and negative relationships. Both the increments of phosphate and nitrate concentrations have a negative influence on the potential presence of habitat B. These results are realistic considering the negative impact that high loads of nutrients and suspended sediment (which are highly correlated with dissolved nutrients) have on erect and filter-feeders organisms, by hindering their breathing and feeding habit (Lemly, 1982; Gibson et al., 2006 and reference therein). Finally, habitat C, distributed farther from the coast as compared to the other two, is characterized by the presence of calcareous algae and the tunicate *Polycitor adriaticus*, a species observed mainly in undisturbed environments and vulnerable to stressful conditions (Falace et al., 2015). Indeed, this habitat presents higher suitability in the Northern-Western Adriatic at low-medium concentrations of nutrients and medium-low temperatures (around 16.5°C). Light at the sea bottom (influenced by water turbidity) slightly influences the distribution of the different habitats, especially B and C. This result finds consistency in previous studies identifying light radiation as a factor that influences the distribution of mesophotic communities (Rossi et al., 2017; Coppari et al., 2020; Castellan et al., 2022), as the northern Adriatic rocky outcrops are defined (Fava et al., 2016; Ingrosso et al., 2018).

Under the climate change scenario, an average temperature increase of 2.48°C in the sub-basin is predicted. The changes in this environmental variable result in a sharp decline (Random Forest) or disappearance (MaxEnt) of habitat C (and partly of habitat B), which could be replaced by habitat A. The resulting pattern is opposite to what is depicted in the historical period. Since habitat A is dominated by opportunistic macroalgae, it is not surprising that it can benefit

from sea warming thus expanding its area at the expense of more temperature-vulnerable habitat-forming species, such as massive Porifera and erect tunicates (Ji et al., 2016; Ober, 2016). Extreme warming events caused by climate change have been observed to have major impacts on Mediterranean coralligenous assemblages, inducing the loss of engineering species characterized by key functional traits, which have a role in driving the biogeochemical cycles and the trophic chain that support biodiversity (Gómez-Gras et al., 2021).

It is interesting to know that contrasting observations have been reported about the effects of seawater warming on crustose coralline algae (associated with habitat C) (Cornwall et al., 2019). Unfortunately, in this study, it was not possible to discriminate the rocky outcrops based on their coralline algae species composition (mainly *Lithophyllum stictaeforme*, *Lithothamnion minervae*, and *Peyssonnelia polymorpha* according to Ponti et al., 2011).

An intensification of studies coupling long-term monitoring of coralligenous communities with habitat suitability and climate model predictions would be strongly beneficial in filling the present scarcity of an evidence-based insight in the effects of warming on these species (see, for example, Rodríguez-Prieto, 2016), Furthermore, in combination with warming, cumulative negative effects are expected on coralligenous. Indeed fast-growing turfs and invasive algae can overgrow on crustose coralline algae and trap and accumulate sediment preventing the recovery of filter feeders, leading then to the declining of these species due to high sedimentation rate (Filbee-Dexter et al., 2016 and references therein).

The projected scenario depicts a severe simplification in coralligenous habitat and a general loss of assemblages over the entire study area. Worth noting, the apparent underestimate of the SST increase rate in the ocean model simulation could imply, under the assumption that in shallow waters this reflects to some extent the behavior of the whole water column, that our projections underestimate the intensity of the climate change signal. As a result, the conditions discussed here for the end of this century could take place significantly sooner than depicted in this study. How climate change will alter the physical and chemical properties of the North Adriatic sub-basin and sedimentation loads is still unclear, even though changes in riverine inputs and runoff are expected, due to altered precipitations and snow-ice melting, together with increased frequency of storm surges (Castellan et al., 2022). The combined effect of all these events is uncertain, but surely it will alter the water quality and turbidity of the basin, with consequences on the species influenced by light radiation (Rizzi et al., 2016; Castellan et al., 2022), as those associated to habitat B and C. Nonetheless, the sensitivity analysis shows that the overall picture emerging from the present work can be confirmed even when accounting for the uncertainty affecting the values of the environmental parameters.

The biodiversity loss expected for the Northern Adriatic Sea in climate change conditions will likely lead to the loss of key ecological processes with important consequences on the entire food web and ecosystem functioning.

5 Conclusions

The use of HSMs is achieving a major role in estimating potential habitat distributions and informing conservation strategies. As such,

these modeling tools can support environmental surveys planning and management decisions and can suggest more suitable locations where conservation efforts should be focused. At present the available knowledge on HSM applications provides no striking evidence of one approach clearly outperforming the others for any application: for this reason, it is generally a good strategy to apply different approaches and critically evaluate the reliability of their results.

With reference to the present application, the following conclusions can be drawn:

- both Random Forest and MaxEnt achieved satisfactory accuracy metrics for the analysis of coralligenous habitats in the Northern Adriatic Sea. Nonetheless, some tendency to overfitting reported in the former, together with its higher sensitivity to uncertain input data, suggest some cautionsness in the interpretation of its results, particularly for spatial patterns far of the occurrence locations;
- the application of these HSMs showed that widespread modifications in coralligenous habitat distributions should be expected in a severe climate change condition (RCP 8.5). Tolerant and opportunistic species are expected to expand their distribution in the Northern Adriatic Sea, while calcareous species and organisms more vulnerable to environmental alterations might undergo a decrease in their suitable habitat;
- the projected shift in habitat distribution will result in a a potential net loss of biodiversity in the sub-basin;
- in this perspective, the use of HSMs can facilitate the identification of protection priorities for endangered areas. To this aim, the intensification of survey activities and the definition of long-term monitoring plans would provide valuable data for the model applications, collecting at the same time information on the evolution of marine habitats and on the results of management and protection actions put in place in these systems.

Data availability statement

Publicly available datasets were analyzed in this study. This data can be found here: Environmental data: - CMEMS data: Teruzzi, A., Di Biagio, V., Feudale, L., Bolzon, G., Lazzari, P., Salon, S., et al. (2021). Mediterranean Sea Biogeochemical reanalysis (CMEMS MED-biogeochemistry, MedBFM3 system) (Version 1) set. Copernicus Monit. Environ. Mar. Service (CMEMS). doi: 10.25423/CMCC/MEDSEA_MULTIYEAR_BGC_006_008_MEDBFM3 available at https://resources.marine.copernicus.eu/product-detail/MEDSEA_MULTIYEAR_BGC_006_008/INFORMATION - Bio-Oracle data: Tyberghein, L., Verbruggen, H., Pauly, K., Troupin, C., Mineur, F. and De Clerck, O. (2012), Bio-ORACLE: a global environmental dataset for marine species distribution modelling. Global Ecology and Biogeography, 21: 272-281. https://doi.org/10.1111/j.1466-8238.2011.00656.x; Assis, J, Tyberghein, L, Bosch, S, Verbruggen, H, Serrão, EA, De Clerck, O. Bio-ORACLE v2.0: Extending marine data layers for bioclimatic modelling. Global Ecol Biogeogr. 2018; 27: 277–284. https://doi.org/10.1111/geb.12693 - Occurrences data: Ponti, M.,

Colosio, F., Tumedei, M., and Abbiati, M. (2005). "Popolamenti Epibentonici Delle Tegnùe Chioggia", in Atti Del 1° Convegno Subacquea & Ambiente: Le Tegnùe Di Chioggia, 17-18 Settembre 2005, 33–41; Martin, C.S., Giannoulaki, M., De Leo, F., Scardi, M., Salomidi, M., Knittweis, L., Pace, M.L., Garofalo, G., Gristina, M., Ballesteros, E., Bavestrello, G., Belluscio, A., Cebrian, E., Gerakaris, V., Pergent, G., Pergent-Martini, C., Schembri, P. J., Terribile, K., Rizzo, L., Ben Souissi, J., Bonacorsi, M., Guarnieri, G., Krzelj, M., Macic, V., Punzo, E., Valavanis V., and Fraschetti, S. (2014). Coralligenous and maerl habitats: predictive modelling to identify their spatial distributions across the Mediterranean Sea. Science, Engineering and Humanities and Social Sciences references, 4, 5073. doi: 10.1038/srep05073; Falace, A., Kaleb, S., Curiel, D., Miotti, C., Galli, G., Querin, S., Ballesteros, E., Solidoro, C., and Bandelj, V. (2015). Calcareous bio-concretions in the Northern Adriatic Sea: Habitat types, environmental factors that influence Habitat distributions, and predictive modeling. PLoS ONE, 10(11), 1–21. doi: 10.1371/journal.pone.0140931.

Author contributions

Funding

Acknowledgments

Conflict of interest

The authors declare that the research was conducted in the absence of any commercial or financial relationships that could be construed as a potential conflict of interest.

Publisher's note

All claims expressed in this article are solely those of the authors and do not necessarily represent those of their affiliated organizations, or those of the publisher, the editors and the reviewers. Any product that may be evaluated in this article, or claim that may be made by its manufacturer, is not guaranteed or endorsed by the publisher.

Supplementary material

The Supplementary Material for this article can be found online at: https://www.frontiersin.org/articles/10.3389/fmars.2023.1050293/full#supplementary-material

References

Acharya, B. K., Chen, W., Ruan, Z., Pant, G. P., Yang, Y., Shah, L. P., et al. (2019). Mapping environmental suitability of scrub typhus in Nepal using MaxEnt and random forest models. *Int. J. Environ. Res. Public Health* 16 (23), 4845. doi: 10.3390/IJERPH16234845

Allouche, O., Tsoar, A., and Kadmon, R. (2006). Assessing the accuracy of species distribution models: prevalence, kappa and the true skill statistic (TSS). *J. Appl. Ecol.* 43 (6), 1223–1232. doi: 10.1111/J.1365-2664.2006.01214.X

Artegiani, A., Bregant, D., Paschini, E., Pinardi, N., Raicich, F., and Russo, A. (1997a). The Adriatic Sea general circulation. part I: Air–Sea interactions and water mass structure. *J. Phys. Oceanogr.* 27, 1492–1514. doi: 10.1175/1520-0485(1997)027<1492:TASGCP>2.0.CO;2

Artegiani, A., Bregant, D., Paschini, E., Pinardi, N., Raicich, F., and Russo, A. (1997b). The Adriatic Sea general circulation. part II: Baroclinic circulation structure. *J. Phys. Oceanogr.* 27, 1515–1532. doi: 10.1175/1520-0485(1997)027<1515:TASGCP>2.0.CO;2

Assis, J., Tyberghein, L., Bosch, S., Verbruggen, H., Serrão, E. A., and De Clerck, O. (2018). Bio-ORACLE v2.0: Extending marine data layers for bioclimatic modelling. *Global Ecol. Biogeogr.* 27, 277–284. doi: 10.1111/geb.12693

Barbier, E. B. (2017). Marine ecosystem services. *Curr. Biol.* 27 (11), R507–R510. doi: 10.1016/j.cub.2017.03.020

Bates, A. E., McKelvie, C. M., Sorte, C. J., Morley, S. A., Jones, N. A., Mondon, J. A., et al. (2013). Geographical range, heat tolerance and invasion success in aquatic species. *Proc. R. Soc. B: Biol. Sci.* 280 (1772), 20131958. doi: 10.1098/rspb.2013.1958

Behrenfeld, M. J., O'Malley, R. T., Siegel, D. A., McClain, C. R., Sarmiento, J. L., Feldman, G. C., et al. (2006). Climate-driven trends in contemporary ocean productivity. *Nature* 444, 752–755. doi: 10.1038/NATURE05317

Bonaldo, D., Benetazzo, A., Bergamasco, A., Falcieri, F. M., Carniel, S., Aurighi, M., et al. (2014). Sediment transport modifications induced by submerged artificial reef systems: A case study for the gulf of Venice. *Oceanological Hydrobiological Stud.* 43 (1), 7–20. doi: 10.2478/s13545-014-0112-4

Boys, W. A., Siepielski, A. M., Smith, B. D., Patten, M. A., and Bried, J. T. (2021). Predicting the distributions of regional endemic dragonflies using a combined model approach. *Insect Conserv. Diversity.* 14 (1), 52–66. doi: 10.1111/ICAD.12444

Burbach, T. (2011). The influence of environmental variables on predicting rare-plant habitat in the nez perce national forest. Master's thesis, University of Montana.

Cahill, A. E., Aiello-Lammens, M. E., Fisher-Reid, M. C., Hua, X., Karanewsky, C. J., Ryu, H. Y., et al. (2012). How does climate change cause extinction? *Procdings R. Soc. B: Biol. Sci.* 280 (1750).

Cañadas, A., Sagarminaga, R., Stephanis, R. D., Urquiola, E., and Hammond, P. S. (2005). Habitat preference modelling as a conservation tool: proposals for marine protected areas for cetaceans in southern Spanish waters. *Aquat. Conserv. Mar. Freshw. Ecosyst.* 15, 495–521. doi: 10.1002/aqc.689

Casellato, S., Masiero, L., Sichirollo, E., and Soresi, S. (2007). Hidden secrets of the northern Adriatic: "Tegnúe", peculiar reefs. *Cent. Eur. J. Biol.* 2, 122–136. doi: 10.2478/s11535-007-0004-3

Casellato, S., and Stefanon, A. (2008). Coralligenous habitat in the northern Adriatic Sea: An overview. *Mar. Ecol.* 29 (3), 321–341. doi: 10.1111/j.1439-0485.2008.00236.x

Castellan, G., Angeletti, L., Montagna, P., and Taviani, M. (2022). Drawing the borders of the mesophotic zone of the Mediterranean Sea using satellite data. *Sci. Rep.* 12 (1), 1–12. doi: 10.1038/s41598-022-09413-4

Cenci, E., and Mazzoldi, C. (2006). Le tegne di chioggia: Prima valutazione qualitativa e quantitativa della fauna ittica. *Biol. Marina Mediterr.* 13 (1), 840–843.

Cerrano, C., Bavestrello, G., Bianchi, C. N., Calcinai, B., Cattaneo-Vietti, R., Morri, C., et al. (2001). The role of sponge bioerosion in Mediterranean coralligenous accretion. *In Mediterr. Ecosyst.* (Milano) pp, 235–240.

Cheung, W. W. L., Lam, V. W. Y., Sarmiento, J. L., Kearney, K., Watson, R., and Pauly, D. (2009). Projecting global marine biodiversity impacts under climate change scenarios. *Fish Fisheries* 10, 235–251. doi: 10.1111/j.1467-2979.2008.00315.x

Coll, M., Piroddi, C., Albouy, C., Ben Rais Lasram, F., Cheung, W. W., Christensen, V., et al. (2012). The Mediterranean Sea under siege: spatial overlap between marine biodiversity, cumulative threats and marine reserves. *Global Ecol. Biogeogr.* 21 (4), 465–480. doi: 10.1111/j.1466-8238.2011.00697.x

Compton, T. J., Leathwick, J. R., and Inglis, G. J. (2010). Thermogeography predicts the potential global range of the invasive European green crab (*Carcinus maenas*). *Divers. Distrib.* 16, 243–255. doi: 10.1111/j.1472-4642.2010.00644.x

Coppari, M., Fumarola, L., Bramanti, L., Romans, P., Pillot, R., Bavestrello, G., et al. (2020). Unveiling asexual reproductive traits in black corals: Polyp bail-out in antipathella subpinnata. *Coral Reefs* 39 (6), 1517–1523. doi: 10.1007/s00338-020-02018-1

Cornwall, C. E., Diaz-Pulido, G., and Comeau, S. (2019). Impacts of ocean warming on coralline algal calcification: Meta-analysis, knowledge gaps, and key recommendations for future research. *Front. Mar. Sci.* 6, 186. doi: 10.3389/fmars.2019.00186

Council Regulation (EC)(2006) *Management measures for the sustainable exploitation of fishery resources in the Mediterranean Sea, amending regulation (EEC) no 2847/93 and repealing regulation (EC) no 1626/94, council regulation (EC) no 1967/2006 of 21 December.* Available at: http://data.europa.eu/eli/reg/2006/1967/2019-08-14 (Accessed 10/01/2022).

Defforge, C., and Merlis, T. (2017). Observed warming trend in sea surface temperature at tropical cyclone genesis. *Geophys. Res. Lett.* 44 (2), 1034–1040. doi: 10.1002/2016GL071045

de Francesco, M. C., Chiuchiarelli, I., Frate, L., Carranza, M. L., Pagliani, T., and Stanisci, A. (2020). "Towards new marine-coastal natura 2000 sites in the central Adriatic Sea," in *Eighth international symposium "Monitoring of Mediterranean coastal areas. problems and measurement techniques*. Eds. L. Bonara, D. Carboni and M. De Vincenzi Firenze University Press, 529–539.

Degobbis, D., Precali, R., Ivancic, I., Smodlaka, N., Fux, D., and Kveder, S. (2000). Long-term changes in the northern Adriatic ecosystem related to anthropogenic eutrophication. *Int. J. Environ. pollut.* 13, 495–533. doi: 10.1504/IJEP.2000.002332

Degraer, S., Verfaillie, E., Willems, W., Adriaens, E., Vincx, M., and Van Lancker, V. (2008). Habitat suitability modelling as a mapping tool for macrobenthic communities: an example from the Belgian part of the north Sea. *Cont Shelf Res.* 28, 369–379. doi: 10.1016/j.csr.2007.09.001

Deutsch, C., Ferrel, A., Seibel, B., Pörtner, H.-O., and Huey, R. B. (2015). Ecophysiology. Climate change tightens a metabolic constraint on marine habitats. *Science* 348 (6239), 1132–1135. doi: 10.1126/science.aaa1605

Doney, S. C., Ruckelshaus, M., Duffy, E. J., Barry, J. P., Chan, F., English, C. A., et al. (2012). Climate change impacts on marine ecosystems. *Annu. Rev. Mar. Science.* 4, 11–37. doi: 10.1146/annurev-marine-041911-111611

Elith, J., and Graham, C. (2008). Reasons for differing performances of species distribution models.

Elith, J., and Graham, C. H. (2009). Do they? how do they? WHY do they differ? on finding reasons for differing performances of species distribution models. *Ecography* 32, 66–77. doi: 10.1111/j.1600-0587.2008.05505.x

Elith, J., Graham, C. H., Anderson, R. P., Dudík, M., Ferrier, S., Guisan, A., et al. (2006). Novel methods improve prediction of species' distributions from occurrence data. *Ecography* 29, 129–151. doi: 10.1111/j.2006.0906-7590.04596.x

Elith, J., and Leathwick, J. R. (2009). Species distribution models: Ecological explanation and prediction across space and time. *Annu. Rev. Ecol. Evol. Syst.* 40, 677–697. doi: 10.1146/annurev.ecolsys.110308.120159

Elith, J., Phillips, S. J., Hastie, T., Dudík, M., Chee, Y. E., and Yates, C. J. (2011). A statistical explanation of MaxEnt for ecologists. *Diversity Distributions* 17 (1), 43–57. doi: 10.1111/j.1472-4642.2010.00725.x

Elliott, M., Burdon, D., Atkins, J. P., Borja, A., Cormier, R., De Jonge, V. N., et al. (2017). "And DPSIR begat DAPSI (W) r (M)!"-a unifying framework for marine environmental management. *Mar. pollut. Bull.* 118 (1-2), 27–40. doi: 10.1016/j.marpolbul.2017.03.049

European Commission (1992). Council directive 92/43/EEC of may 21 1992 on the conservation of natural habitats and of wild fauna and flora. *Off. J. Eur. Communities* 206, 22/07/1992, P. 0007-0050.

European Commission (2008). Directive 2008/56/EC of the European parliament of the council of 17 June 2008 establishing a framework for community action in the field of marine environmental policy (Marine strategy framework directive). *Off. J. Eur. Union* L164/19, 25/06/2008, P. 19-40.

Falace, A., Kaleb, S., Curiel, D., Miotti, C., Galli, G., Querin, S., et al. (2015). Calcareous bio-concretions in the northern Adriatic Sea: Habitat types, environmental factors that influence habitat distributions, and predictive modeling. *PloS One* 10 (11), 1–21. doi: 10.1371/journal.pone.0140931

Fava, F., Ponti, M., and Abbiati, M. (2016). Role of recruitment processes in structuring coralligenous benthic assemblages in the northern Adriatic continental shelf. *PloS One* 11 (10), e0163494. doi: 10.1371/journal.pone.0163494

Filbee-Dexter, K., Feehan, C. J., and Scheibling, R. E. (2016). Large-Scale degradation of a kelp ecosystem in an ocean warming hotspot. *Mar. Ecol. Prog. Ser.* 543, 141–152. doi: 10.3354/meps11554

Fraschetti, S., Fabbrizzi, E., Tamburello, L., Uyarra, M. C., Micheli, F., Sala, E., et al. (2022). An integrated assessment of the good environmental status of Mediterranean marine protected areas. *J. Environ. Manage.* 305, 114370. doi: 10.1016/j.jenvman.2021.114370

Freeman, L. A., Kleypas, J. A., and Miller, A. J. (2013). Coral reef habitat response to climate change scenarios. *PloS One* 8 (12), 1–14. doi: 10.1371/journal.pone.0082404

García Molinos, J., Halpern, B., Schoeman, D., Brown, C. J., Kiessling, W., Moore, P. J., et al. (2016). Climate velocity and the future global redistribution of marine biodiversity. *Nat. Clim Change* 6, 83–88. doi: 10.1038/nclimate2769

Garcia-Reyes, M., Sydeman, W., Schoeman, D., Rykaczewski, R., Black, B., Smit, A., et al. (2015). Under pressure: Climate change, upwelling, and eastern boundary upwelling ecosystems. *Front. Mar. Sci.* 2. doi: 10.3389/fmars.2015.00109

Giannoulaki, M., Pyrounaki, M. M., Bourdeix, J. H., Ben Abdallah, L., Bonanno, A., Basilone, G., et al. (2017). Habitat suitability modeling to identify the potential nursery grounds of the Atlantic mackerel and its relation to oceanographic conditions in the Mediterranean sea. *Front. Mar. Sci.* 4, 230. doi: 10.3389/fmars.2017.00230

Gibson, R. N., Atkinson, R. J. A., Gordon, J. D. M., and Taylor, E. (2006). Mediterranean Corralligenous assemblages: a synthesis of present knowledge. introduction and description. *Annu. Rev.* 44, 123–195.

Gissi, E., Manea, E., Mazaris, A. D., Fraschetti, S., Almpanidou, V., Bevilacqua, S., et al. (2021). A review of the combined effects of climate change and other local human stressors on the marine environment. *Sci. Total Environ.* 755, 142564. doi: 10.1016/j.scitotenv.2020.142564

Glockzin, M., Gogina, M., and Zettler, M. L. (2009). Beyond salty reins–modeling benthic species' spatial response to their physical environment in the pomeranian bay (southern Baltic Sea). *Balt Coast. Zone.* 13, 79–95.

Gogina, M., and Zettler, M. L. (2010). Diversity and distribution of benthic macrofauna in the Baltic Sea: Data inventory and its use for species distribution modelling and prediction. *J. Sea Res.* 64, 313–321. doi: 10.1016/j.seares.2010.04.005

Gómez-Gras, D., Linares, C., de Caralt, S., Cebrian, E., Frleta-Valić, M., Montero-Serra, I., et al. (2019). Response diversity in Mediterranean coralligenous assemblages facing climate change: Insights from a multispecific thermotolerance experiment. *Ecol. evolution.* 9 (7), 4168–4180.

Gómez-Gras, D., Linares, C., Dornelas, M., Madin, J. S., Brambilla, V., Ledoux, J. B., et al. (2021). Climate change transforms the functional identity of Mediterranean coralligenous assemblages. *Ecol. Lett.* 24 (5), 1038–1051. doi: 10.1111/ELE.13718

Guisan, A., and Thuiller, W. (2005). Predicting species distribution: offering more than simple habitat models. *Ecol. Lett.* 8, 993–1009. doi: 10.1111/j.1461-0248.2005.00792.x

Guisan, A., Tingley, R., Baumgartner, J. B., Naujokaitis-Lewis, I., Sutcliffe, P. R., Tulloch, A. I., et al. (2013). Predicting species distributions for conservation decisions. *Ecol. Lett.* 16 (12), 1424–1435. doi: 10.1111/ele.12189

Haidvogel, D. B., Arango, H., Budgell, W. P., Cornuelle, B. D., Curchitser, E., Di Lorenzo, E., et al. (2008). Ocean forecasting in terrain-following coordinates: Formulation and skill assessment of the regional ocean modeling system. *J. Comput. Phys.* 227 (7), 3595–3624. doi: 10.1016/j.jcp.2007.06.016

Harley, C. (2011). Climate change, keystone predation, and biodiversity loss. *Science* 334 (6059), 1124–1127. doi: 10.1126/science.121019

Heikkinen, R. K., Luoto, M., Araujo, M. B., Virkkala, R., Thuiller, W., and Sykes, M. T. (2006). Methods and uncertainties in bioclimatic envelope modelling under climate change. *Prog. Phys. Geogr.* 30, 751–777. doi: 10.1177/0309133306071957

Hijmans, R. J., and Elith, J. (2013). *Species distribution modeling with r* (R CRAN Project).

Hijmans, R. J., Phillips, S., Leathwick, J., and Elith, J. (2011) *Package 'dismo'*. Available at: http://cran.r-project.org/web/packages/dismo/index.html (Accessed 12/03/2021).

Hoegh-Guldberg, O., Cai, R., Poloczanska, E. S., Brewer, P. G., Sundby, S., Hilmi, K., et al. (2014). "The ocean in climate change 2014: Impacts, adaptation, and vulnerability," in *Part b: Regional aspects. contribution of working group II to the fifth assessment report of the intergovernmental panel on climate change*. Eds. V. R. Barros, C. B. Field, D. J. Dokken, M. D. Mastrandrea, K. J. Mach, T. E. Bilir, M. Chatterjee, K. L. Ebi, Y. O. Estrada, R. C. Genova, B. Girma, E. S. Kissel, A. N. Levy, S. MacCracken, P. R. Mastrandrea and L. L. White (Cambridge, United Kingdom and New York, NY, USA: Cambridge University Press), 1655–1731.

Hoegh-Guldberg, O., Mumby, P. J., Hooten, A. J., Steneck, R. S., Greenfield, P., Gomez, E., et al. (2007). Coral reefs under rapid climate change and ocean acidification. *Science* 318, 1737–1742. doi: 10.1126/SCIENCE.1152509

Ingrosso, G., Abbiati, M., Badalamenti, F., Bavestrello, G., Belmonte, G., Cannas, R., et al. (2018). "Mediterranean bioconstructions along the Italian coast. *Adv. Mar. Biol.* 79. doi: 10.1016/bs.amb.2018.05.001

IPCC (2013b). "Climate change 2013: The physical science basis," in *Contribution of working group I to the fifth assessment report of the intergovernmental panel on climate change*. Eds. T. F. Stocker, D. Qin, G. K. Plattner, M. Tignor, S. K. Allen, J. Boschung, A. Nauels, Y. Xia, V. Bex and P. M. Midgley (Cambridge, UK and New York, NY: Cambridge University Press), 1535.

IPCC (2014). "Climate change 2014: Impacts, adaptation, and vulnerability. part a: Global and sectoral aspects," in *Contribution of working group II to the fifth assessment report of the intergovernmental panel on climate change*. Eds. C. B. Field, V. R. Barros, D. J. Dokken, K. J. Mach, M. D. Mastrandrea, T. E. Bilir, M. Chatterjee, K. L. Ebi, Y. O. Estrada, R. C. Genova, B. Girma, E. S. Kissel, A. N. Levy, S. MacCracken, P. R. Mastrandrea and L. L. White. (Cambridge, UK and New York, NY: Cambridge University Press), 1132.

Jacob, D., Petersen, J., Eggert, B., Alias, A., Christensen, O. B., Bouwer, L. M., et al. (2013). EURO-CORDEX: New high-resolution climate change projections for European impact research. *Reg. Environ. Change* 14, 563–578. doi: 10.1007/s10113-013-0499-2

Janeković, I., Mihanović, H., Vilibić, I., and Tudor, M. (2014). Extreme cooling and dense water formation estimates in open and coastal regions of the Adriatic Sea during the winter of 2012. *J. Geophys Res. Oceans.* 119, 3200–3218. doi: 10.1002/2014JC009865

Ji, Y., Xu, Z., Zou, D., and Gao, K. (2016). Ecophysiological responses of marine macroalgae to climate change factors. *J. Appl. Phycol.* 28 (5), 2953–2967. doi: 10.1007/s10811-016-0840-5

Johnson, J. C., Banks, S. C., Barrett, N. S., Cazassus, F., Dunstan, P. K., Edgar, G. J., et al. (2011). Climate change cascades: Shifts in oceanography, species' ranges and subtidal marine community dynamics in eastern Tasmania. *J. Exp. Mar. Biol. Ecol.* 400 (1), 17–32. doi: 10.1016/j.jembe.2011.02.032

Kaky, E., Nolan, V., Alatawi, A., and Gilbert, F. (2020). A comparison between ensemble and MaxEnt species distribution modelling approaches for conservation: A case study with Egyptian medicinal plants. *Ecol. Inf.* 60, 101150. doi: 10.1016/J.ECOINF.2020.101150

Kharouba, H. M., Algar, A. C., and Kerr, J. T. (2009). Historically calibrated predictions of butterfly species' range shift using global change as a pseudo-experiment. *Ecology* 90, 2213–2222. doi: 10.1890/08-1304.1

Kotlarski, S., Keuler, K., Christensen, O. B., Colette, A., Déqué, M., Gobiet, A., et al. (2014). Regional climate modeling on European scales: A joint standard evaluation of the EURO-CORDEX RCM ensemble. *Geoscientific Model. Dev.* 7, 1297–1333. doi: 10.5194/gmd-7-1297-2014

Lauria, V., Gristina, M., Attrill, M. J., Fiorentino, F., and Garofalo, G. (2015). Predictive habitat suitability models to aid conservation of elasmobranch diversity in the central Mediterranean Sea. *Sci. Rep.* 5 (1), 1–16. doi: 10.1038/srep13245

Last, P. R., White, W. T., Gledhill, D. C., Hobday, A. J., Brown, R., Edgar, G. J., et al. (2011). Long-term shifts in abundance and distribution of a temperate fish fauna: a response to climate change and fishing practices. *Global Ecol. Biogeography* 20 (1), 58–72. doi: 10.1111/j.1466-8238.2010.00575.x

Lavender, E., Fox, C. J., and Burrows, M. T. (2021). Modelling the impacts of climate change on thermal habitat suitability for shallow-water marine fish at a global scale. *PloS One* 16 (10), e0258184. doi: 10.1371/journal.pone.0258184

Lawler, J. J., White, D., Neilson, R. P., and Blaustein, A. R. (2006). Predicting climate-induced range shifts: Model differences and model reliability. *Global Change Biol.* 12, 1568–1584. doi: 10.1111/j.1365-2486.2006.01191.x

Leadley, P., Proença, V., Fernández-Manjarrés, J., Pereira, H. M., Alkemade, R., Biggs, R., et al. (2014). Interacting regional-scale regime shifts for biodiversity and ecosystem services. *BioScience* 64 (8), 665–679. doi: 10.1093/biosci/biu093

Lefort, S., Aumont, O., Bopp, L., Arsouze, T., Gehlen, M., and Maury, O. (2015). Spatial and body-size dependent response of marine pelagic communities to projected global climate change. *Global Change Biol.* 21 (1), 154–164. doi: 10.1111/gcb.12679

Lemly, A. D. (1982). Modification of benthic insect communities in polluted streams: combined effects of sedimentation and nutrient enrichment. *Hydrobiologia* 87 (3), 229–245. doi: 10.1007/BF00007232

Liaw, A., and Wiener, M. (2002). Classification and regression by randomForest. *R News.* 2 (3), 18–22.

Lionello, P., and Scarascia, L. (2018). The relation between climate change in the Mediterranean region and global warming. *Regional Environ. Change* 18 (5), 1481–1493. doi: 10.1007/s10113-018-1290-1

Manea, E., Bergami, C., Bongiorni, L., Capotondi, L., De Maio, E., Oggioni, A., et al. (2021). A transnational marine ecological observatory in the Adriatic Sea to harmonize a fragmented approach to monitoring and conservation. *Adv. Oceanogr. Limnol.* 12, 9811. doi: 10.4081/aiol.2021.9811

Marras, S., Cucco, A., Antognarelli, F., Azzurro, E., Milazzo, M., Bariche, M., et al. (2015). Predicting future thermal habitat suitability of competing native and invasive fish species: from metabolic scope to oceanographic modelling. *Conserv. Physiol.* 3, cou059. doi: 10.1093/conphys/cou059

Marshall, C. E., Glegg, G. A., and Howell, K. L. (2014). Species distribution modelling to support marine conservation planning: the next steps. *Mar. Policy* 45, 330–332. doi: 10.1016/j.marpol.2013.09.003

Martin, C. S., Giannoulaki, M., De Leo, F., Scardi, M., Salomidi, M., Knittweis, L., et al. (2014). Coralligenous and maerl habitats: predictive modelling to identify their spatial distributions across the Mediterranean Sea. *Sci. Eng. Humanities Soc. Sci. References* 4, 5073. doi: 10.1038/srep05073

Meineri, E., Deville, A. S., Grémillet, D., Gauthier-Clerc, M., and Béchet, A. (2015). Combining correlative and mechanistic habitat suitability models to improve ecological compensation. *Biol. Rev. Camb Philos. Soc.* 90 (1), 314–329. doi: 10.1111/brv.12111

Melaku Canu, D., Ghermandi, A., Nunes, P. A., Lazzari, P., Cossarini, G., and Solidoro, C. (2015). Estimating the value of carbon sequestration ecosystem services in the Mediterranean Sea: An ecological economics approach. *Global Environ. Change* 32, 87–95. doi: 10.1016/j.gloenvcha.2015.02.008

Mi, C., Huettmann, F., Guo, Y., Han, X., and Wen, L. (2017). Why choose random forest to predict rare species distribution with few samples in large undersampled areas? three Asian crane species models provide supporting evidence. *PeerJ* 5, e2849. doi: 10.7717/peerj.2849

Monk, J., Ierodiaconou, D., Bellgrove, A., Harvey, E., and Laurenson, L. (2010). Remotely sensed hydroacoustics and observation data for predicting fish habitat suitability. *Continental Shelf Res.* Volume 31, Issue 2, Supplement, S17–S27. doi: 10.1016/j.csr.2010.02.012. ISSN 0278-4343.

Moss, R. H., Edmonds, J. A., Hibbard, K. A., Manning, M. R., Rose, S. K., Van Vuuren, D. P., et al. (2010). The next generation of scenarios for climate change research and assessment. *Nature* 463 (7282), 747–756. doi: 10.1038/nature08823

Mousazade, M., Ghanbarian, G., Pourghasemi, H. R., Safaeian, R., and Cerdà, A. (2019). MaxEnt data mining technique and its comparison with a bivariate statistical

model for predicting the potential distribution of astragalus fasciculifolius boiss. in fars, Iran. *Sustainability (Switzerland)* 11 (12), 3452. doi: 10.3390/su10023452

Muscarella, R., Galante, P. J., Soley-Guardia, M., Boria, R. A., Kass, J. M., Uriarte, M., et al. (2014). ENM eval: An r package for conducting spatially independent evaluations and estimating optimal model complexity for maxent ecological niche models. *Methods Ecol. Evol.* 5 (11), 1198–1205.

Ober, G. (2016). The effects of climate change on macroalgal growth, trophic interactions and community structure. *Doctoral dissertation* University of Rhode Island, 490.

Pecl, G. T., Araujo, M. B., Bell, J. D., Blanchard, J., Bonebrake, T. C., Chen, I. C., et al. (2017a). Biodiversity redistribution under climate change: Impacts on ecosystems and human well-being. *Science* 355 (6332), 1389–138+. doi: 10.1126/science.aai9214

Pecl, G. T., Araújo, M. B., Bell, J. D., Blanchard, J., Bonebrake, T. C., Chen, I. C., et al. (2017b). The universal impacts of species on the move. *Science* 355 (6332). doi: 10.1126/science.aai9214

Pereira, H. M., Leadley, P. W., Proença, V., Alkemade, R., Scharlemann, J. P. W., Fernandez-Manjarrés, J. F., et al. (2010). Scenarios for global biodiversity in the 21st century. *Science* 330, 1496–1501. doi: 10.1126/science.1196624

Perry, A. L., Low, P. J., Ellis, J. R., and Reynolds, J. D. (2005). Climate change and distribution shifts in marine fishes. *Science* 308, 1912–1915. doi: 10.1126/SCIENCE.1111322

Phillips, S. J., Anderson, R. P., and Schapire, R. E. (2006). Maximum entropy modeling of species geographic distributions. *Ecol. Model.* 190 (3-4), 231–259. doi: 10.1016/j.ecolmodel.2005.03.026

Phillips, S. J., and Dudík, M. (2008). Modeling of species distributions with MaxEnt: new extensions and a comprehensive evaluation. *Ecography* 31 (2), 161–175. doi: 10.1111/j.0906-7590.2008.5203.x

Piazzi, L., Gennaro, P., and Balata, D. (2011). Effects of nutrient enrichment on macroalgal coralligenous assemblages. *Mar. pollut. Bull.* 62 (8), 1830–1835. doi: 10.1016/j.marpolbul.2011.05.004

Piazzi, L., Gennaro, P., and Balata, D. (2012). Threats to macroalgal coralligenous assemblages in the Mediterranean Sea. *Mar. pollut. Bull.* 64 (12), 2623–2629. doi: 10.1016/J.MARPOLBUL.2012.07.027

Pisano, A., Buongiorno Nardelli, B., Tronconi, C. , and Santoleri, R. (2016). The new Mediterranean interpolated pathfinder AVHRR SST dataset, (1982-2012). *Remote Sens. Environ.* 176 (2016), 107–116. doi: 10.1016/j.rse.2016.01.019

Polovina, J. J., Howell, E. A., and Abecassis, M. (2008). Ocean's least productive waters are expanding. *Geophys. Res. Lett.* 35, L03618. doi: 10.1029/2007GL031745

Pompe, S., Hanspach, J., Badeck, F., Klotz, S., Thuiller, W., and Kühn, I. (2008). Climate and land use change impacts on plant distributions in Germany. *Biol. Lett.*, 4564–4567. doi: 10.1098/rsbl.2008.0231

Ponti, M., Colosio, F., Tumedei, M., and Abbiati, M. (2005). "Popolamenti epibentonici delle tegnùe chioggia," in *Atti del 1° convegno subacquea & ambiente: Le tegnùe di chioggia*, 33–41.

Ponti, M., Fava, F., and Abbiati, M. (2011). Spatial–temporal variability of epibenthic assemblages on subtidal biogenic reefs in the northern Adriatic Sea. *Mar. Biol.* 158 (7), 1447–1459. doi: 10.1007/s00227-011-1661-3

Rahmati, O., Pourghasemi, H. R., and Melesse, A. M. (2016). Application of GIS-based data driven random forest and maximum entropy models for groundwater potential mapping: A case study at mehran region, Iran. *Catena* 137, 360–372. doi: 10.1016/j.catena.2015.10.010

Raicich, F. (1994). Note on the flow rates of the Adriatic rivers. *Tech. Rep.* 561 RF 02/94, CNR Istituto Sperimentale Talassografico, Trieste.

Reale, M., Cossarini, G., Lazzari, P., Lovato, T., Bolzon, G., Masina, S., et al. (2022). Acidification, deoxygenation, and nutrient and biomass declines in a warming Mediterranean Sea. *Biogeosciences* 19 (17), 4035–4065. doi: 10.5194/bg-19-4035-2022

Rew, J., Cho, Y., Moon, J., and Hwang, E. (2020). Habitat suitability estimation using a two-stage ensemble approach. *Remote Sensing.* 12 (9). doi: 10.3390/RS12091475

Rhein, M., Rintoul, S. R., Aoki, S., Campos, E., Chambers, D., Feely, R. A., et al. (2013). "Observations: Ocean," in *Climate change 2013: The physical science basis. contribution of working group I to the fifth assessment report of the intergovernmental panel on climate change*. Eds. T. F. Stocker, D. Qin, G. K. Plattner, M. Tignor, S. K. Allen, J. Boschung, A. Nauels, Y. Xia, V. Bex and P. M. Midgley (Cambridge, United Kingdom and New York, NY, USA: Cambridge University Press).

Rizzi, J., Torresan, S., Critto, A., Zabeo, A., Brigolin, D., Carniel, S., et al. (2016). Climate change impacts on marine water quality: The case study of the northern Adriatic sea. *Mar. pollut. Bull.* 102 (2), 271–282. doi: 10.1016/j.marpolbul.2015.06.037

Robinson, L. M., Elith, J., Hobday, A. J., Pearson, R. G., Kendall, B. E., and Possingham, H. P. (2011). Pushing the limits in marine species distribution modelling: lessons from the land present challenges and opportunities. *Global Ecol. Biogeogr.* 20 (6), 789–802. doi: 10.1111/j.1466-8238.2010.00636.x

Rodríguez-Prieto, C. (2016). Light and temperature requirements for survival, growth and reproduction of the crustose coralline *Lithophyllum stictaeforme* from the Mediterranean Sea. *Botanica Marina* 59 (2-3), 95–104. doi: 10.1515/bot-2015-0070

Rossi, S., Bramanti, L., Gori, A., and Orejas, C. (2017). *Marine animal forests: the ecology of benthic biodiversity hotspots* (Cham: Springer International Publishing), 1–1366.

Scoccimarro, E., Gualdi, S., Bellucci, A., Sanna, A., Fogli, P., Manzini, E., et al. (2011). Effects of tropical cyclones on ocean heat transport in a high resolution coupled general circulation model. *J. Clim.* 24, 4368–4384. doi: 10.1175/2011JCLI4104.1

Shabani, F., Kumar, L., and Ahmadi, M. (2018). Assessing accuracy methods of species distribution models: AUC, specificity, sensitivity and the true skill statistic. *Global J. Hum. Soc. Science.* 18 (1), 6–18.

Short, F. T., and Neckles, H. A. (1999). The effects of global climate change on seagrasses. *Aquat. Bot.* 63, 169–196. doi: 10.1016/S0304-3770(98)00117-X

Simoncelli, S., Fratianni, C., Pinardi, N., Grandi, A., Drudi, M., Oddo, P., et al. (2019). Mediterranean Sea Physical reanalysis (CMEMS MED-physics) [Data set]. *Copernicus Monit. Environ. Mar. Service (CMEMS).* doi: 10.25423/MEDSEA_REANALYSIS_PHYS_006_004

Sinha, P., Gaughan, A. E., Stevens, F. R., Nieves, J. J., Sorichetta, A., and Tatem, A.J. (2019). Assessing the spatial sensitivity of a random forest model: Application in gridded population modeling. *Computers Environ. Urban Syst.* 75, 132–145. doi: 10.1016/j.compenvurbsys.2019.01.006

Sloyan, B., Ridgway, K., and Cowley, R. (2016). The East Australian current and property transport at 27°S from 2012 to 2013. *J. Phys. Oceanogr.* 46 (3), 993–1008. doi: 10.1175/JPO-D-15-0052.1

Soto-Navarro, J., Jordá, G., Amores, A., Cabos, W., Somot, S., Sevault, F., et al. (2020). "Evolution of Mediterranean Sea water properties under climate change scenarios in the med-CORDEX ensemble," in *Climate dynamics*, vol. 54, 2135–2165. doi: 10.1007/s00382-019-05105-4

Strandberg, G., Bärring, L., Hansson, U., Jansson, C., Jones, C., Kjellström, E., et al. (2015). CORDEX scenarios for Europe from the Rossby Centre regional climate model RCA4. *SMHI* 116.

Teixidó, N., Casas, E., Cebrián, E., Linares, C., and Garrabou, J. (2013). Impacts on coralligenous outcrop biodiversity of a dramatic coastal storm. *PloS One* 8 (1), e53742. doi: 10.1371/journal.pone.0053742

Templado, J. (2014). "Future trends of Mediterranean biodiversity," in *The Mediterranean Sea: Its history and present challenges*. Eds. S. Goffredo and Z. Dubinsky (Dordrecht, the Netherlands: Springer), 479–498.

Teruzzi, A., Di Biagio, V., Feudale, L., Bolzon, G., Lazzari, P., Salon, S., et al. (2021). Mediterranean Sea Biogeochemical reanalysis (CMEMS MED-biogeochemistry, MedBFM3 system) (Version 1) set. *Copernicus Monit. Environ. Mar. Service (CMEMS).* doi: 10.25423/CMCC/MEDSEA_MULTIYEAR_BGC_006_008_MEDBFM3

Thuiller, W., and Münkemüller, T. (2010). Habitat suitability modeling. effects of climate change on birds. A. P. Møller, W. Fiedler and P. Berthold (OUP Oxford), 77–85.

Tosi, L., Zecchin, M., Franchi, F., Bergamasco, A., Da Lio, C., Baradello, L., et al. (2017). Paleochannel and beach-bar palimpsest topography as initial substrate for coralligenous buildups offshore Venice, Italy. *Sci. Rep.* 7 (1), 1–10. doi: 10.1038/s41598-017-01483-z

Tybergbein, L., Verbruggen, H., Pauly, K., Troupin, C., Mineur, F., and De Clerck, O. (2012). Bio-ORACLE: A global environmental dataset for marine species distribution modelling. *Global Ecol. Biogeogr.* 21, 272–281. doi: 10.1111/j.1466-8238.2011.00656.x

UNEP-MAP-RAC, S. P. A.(2017). *Action plan for the conservation of the coralligenous and other calcareous bio-concretions in the Mediterranean Sea* (Tunis: UN Environment/MAP Athens).

Vasilakopoulos, P., Raitsos, D. E., Tzanatos, E., and Maravelias, C. D. (2017). Resilience and regime shifts in a marine biodiversity hotspot. *Sci. Rep.* 7 (1), 1–11. doi: 10.1038/s41598-017-13852-9

Vincenzi, S., Zucchetta, M., Franzoi, P., Pellizzato, M., Pranovi, F., De Leo, G. A., et al. (2011). Application of a random forest algorithm to predict spatial distribution of the potential yield of ruditapes philippinarum in the Venice lagoon, Italy. *Ecol. Model.* 222(8), 1471–1478. doi: 10.1016/j.ecolmodel.2011.02.007

Vitelletti, M. L., and Bonaldo, D. (2020). "Response to climate change in coastal and marine protected areas: Threats and opportunities," in *Governing future challenges in protected areas*. Eds. L. Alfaré and E. Ruoss (Roma, Italy: CNR Edizioni), 61-75.

Williams, G. J., Aeby, G. S., Cowie, R. O. M., and Davy, S. K. (2010). Predictive modelling of coral disease distribution within a reef system. *PloS One* 5, e9264. doi: 10.1371/journal.pone.0009264

Zuliani, A., Zaggia, L., Collavini, F., and Zonta, R. (2005). Freshwater discharge from the drainage basin to the Venice lagoon (Italy). *Environ. Int*, 31 (7), 929-938.

Climate risk assessment of the Tangier-Tetouan-Al Hoceima coastal Region (Morocco)

Kamal Agharroud[1]*, Manuela Puddu[2], Ante Ivčević[3,4], Alessio Satta[2], Alexander S. Kolker[5] and Maria Snoussi[6]

[1]GERN, Faculty of Sciences, Abdelmalek Essaadi University, Tetouan, Morocco, [2]Mediterranean Sea and Coast foundation, Cagliari, Italy, [3]Priority Actions Programme/Regional Activity Centre (PAP/RAC), UN Environment Programme/Mediterranean Action Plan (UNEP/MAP), Split, Croatia, [4]Department of Geography, Vrije Universiteit Brussel, Brussels, Belgium, [5]Louisiana Universities Marine Consortium, Chauvin, LA, United States, [6]Faculty of Sciences, University, Mohammed V, Rabat, Morocco

Coastal zones occupy a prominent position in the sustainable management perspective of Tangier-Tetouan-Al Hoceima (TTA) region because they accommodate a majority of the region's population and contribute to the economic wellbeing of local communities. High demographic and economic pressures associated to climatic and environmental factors increase and intensify the vulnerability of these coastal areas. The latter are severely affected by climate change implications in the course of time, which lead to damage and loss in coastal low-lying zones. In practice, the risks related to climate change, as coastal risks, are frequently addressed, and assessing coastal risk in the context of climate change is a research priority. The aim of this work is to evaluate the flooding risk of TTA coasts, taking into account the inundation level related to the conditions of extreme wave (return period of 100-year) and extreme sea level rise. We firstly defined the coastal hazard zone that corresponds to the maximum inundation level of 13 m for the whole area. We then applied a Coastal Risk Index application at the Local Scale (CRI-LS) methodology to calculate forcing, vulnerability, exposure and risk indices using nineteen physical, environmental and socioeconomical variables. Findings show that coastal hazard zone of Tangier-Tetouan-Al Hoceima region is extremely exposed to coastal forcing. More than 50% of the hazard zones indicates highly vulnerable zones and highest exposure is generally focused on the most populated urban zones. In the light of this, the coastal risk mapping shows hotspot zones in terms of climate change-related coastal risks located at Tangier Bay, south of Tangier city, Fnideq and Martil coasts, Tetouan city and north of Ksar El Kbir city. This paper corresponds to a useful support that can help policy-makers in decision-making to quietly follow coastal planning and management processes and participate in preserving coastal areas for future generations, which support the sustainable development goals of Agenda 2030 started by the United Nations with the goal of eradicating all kinds of poverty.

KEYWORDS

coastal risk index, northern Morocco, climate change, climate coastal hotspots, coastal adaptation policies

1 Introduction

The world is experiencing many climate, environmental and social change challenges, and coastal communities are engaged in an ongoing effort to tackle the impacts of this change. Particularly that is the case of the coastal areas that are severely affected by climate change that results in an increase in sea level rise, coastal storms, flooding, and erosion. (IPCC, 2022). The last report of the Intergovernmental Panel on Climate Change (IPCC) states that "climate change is widespread, rapid and intensifying" and that humankind's role in the climate crisis is unequivocal. The compound effects of extreme weather events are on the rise. The observed impacts from slow-onset processes of sea-level rise and regional decreases in precipitation are attributed to human-induced climate change with high confidence (IPCC, 2022). One of the mid to long-term projections (2041-2100) for coastal areas is that approximately one billion people will be at risk from coastal-related climate hazards under all IPCC scenarios. Scenarios exacerbated by population growth in low-lying coastal dwellings. The same report summarizes the concept of risk in the context of climate change as the one that derives from the interactions between climate-related hazards, and the exposure and vulnerability of human beings and ecological systems. The new aspect of the concept of risk is the risk that can be a consequence of human response to climate change (IPCC, 2022). However, understanding how natural and human-induced drivers will contribute to rising vulnerability and risks in coastal areas, requires a broader use of future projections capturing the spatiotemporal dynamics that drive changes in the different vulnerability dimensions, including the socio-demographic and economic spheres (Furlan et al., 2021).

The World Bank study (2011) on "*Climate Change Adaptation and Resilience to Natural Disasters in Coastal Cities of North Africa*," concluded that with a temperature of 4°C, 2.1 million people in Morocco will be affected by flooding. There is a high vulnerability to sea level rise in the coming decades that is related to the high concentration of populations and activities in coastal areas, and increased risks due to an increase in global sea levels, storms, and local coastal erosion. In this regard, the World Bank has ranked Morocco's coastal GDP in the Top 10 countries at risk with increasing storm surges (Dasgupta et al., 2009).

The climate-related risks for coastal communities are therefore worrying for Morocco. The country is quickly developing, and its coastal areas are facing rapid population growth and urban development, particularly the region of Tangier-Tetouan-Al Hoceima (Ivčević et al., 2020).

Like most of the Moroccan coastal areas, the coastline of the Tangier-Tetouan-Al Hoceima (TTA) region concentrates major societal and economic issues: population, industry and logistics, resort and tourism, fishing, agriculture, etc. (Haut-Commissariat au Plan, 2018). It is home to a large amount of biodiversity and provides many ecosystem services. However, the shift of populations and activities from the hinterland to the coast, since the beginning of the century, has contributed to a strong 'artificialization' of the coasts, making them more exposed to various meteorological and marine hazards, and consequently more vulnerable and less resilient to coastal risks (Snoussi et al., 2008; Snoussi et al., 2009; Khouakhi et al., 2013; Satta et al., 2016;

Aitali et al., 2020). Many coastal areas have already experienced a real estate boom and increased pressure on coastal dunes that are retreating or disappearing, exposing more and more property and people to flooding and coastal erosion (El Mrini et al., 2012; Kasmi et al., 2020; Flayou et al., 2021).

In this context of increasing anthropogenic pressures, climate change is expected to amplify the stresses on coastal areas, creating more and more assets exposed to hazards and thus posing a challenge for coastal decision-makers who are faced with the increasingly complex task of balancing development and the management of coastal risks, in particular submersion and coastal erosion (Cramer et al., 2018; Mastrocicco et al., 2021). One of the open questions is whether policymakers are aware of the gravity of these imminent risks in the coastal areas. Different coastal societies might not necessarily have the same risk perception level nor similar policy answers. The importance of local knowledge for sustainable disaster risk reduction and management is largely recognized by international policy, such as the Sendai Framework for Disaster Risk Reduction (United Nations, 2015). However, the extent to which this scientific knowledge is translated into concrete and practical measures, as well as the importance of risk awareness sessions, is still open to debate (Bwambale et al., 2020; Ivčević et al., 2021). To this end, public authorities have a growing demand for decision-making tools, such as coastal risk assessment, to help them prioritize hot spot areas. Different tools are suggested to assess coastal vulnerability and risk to climate change at different spatial and temporal scales and for different decision-making purposes (Mclaughlin and Cooper, 2010; ETC-CCA, 2011; Ramieri et al., 2011; Torresan et al., 2012; Gallina et al., 2020). More recently, a literature review of climate-related coastal risks in the Mediterranean in terms of methods, techniques and data platforms (Sarkar et al., 2022), showed that among the various types of techniques available, coastal risk assessment, coastal vulnerability assessment, and model-based and index-based approaches are the most preferred ones. However, despite the development of these many methods and tools, most of them cannot be easily applied because they require a lot of data, specialized knowledge and skills in using complex programs (Hinkel & Klein, 2009). Satta (2014), after the analysis of 26 existing methods, proposed an integrated approach to provide Mediterranean coastal managers with a coastal risk assessment tool that is simple, flexible, applicable at the local scale, and with lower costs, and therefore easier to use by managers with limited resources and data. This is why we have chosen to apply the Coastal Risk Index at the Local Scale (CRI-LS) proposed by Satta (2014) in this study, but with some considerations and improvements:

(i) The TTA region, which is a territorial authority with legal status, and administrative and financial autonomy, is characterized by strong territorial, bio-physical and socio-economic disparities, and is therefore subject to different degrees of climate change-related risks, requiring a global vision, equitable risk management and a coherent governance at the regional scale, even if adaptation measures will be carried out at a more local scale. This is why the coast of the whole TTA region has been considered in this study

(ii) The study was conducted as part of the ongoing development of the TTA Region Coastal Plan, which involves all coastal stakeholders. We believe that since the project is still in the formulation phase of the coastal plan, our results will have a much better chance of being considered in the plan implementation phase, since they integrate the needs of the local communities. Indeed, the vulnerability and risk assessment studies should be driven by bottom-up processes in which local stakeholders are involved.

(iii) Compared to previous application of the local scale index, the number of variables of the risk components have been increased to better describe the local climate change impacts and the lack of capacity to cope and adapt of the study area. Finally, we used the CRI-LS methodology to produce coastal risk map, a visual tool that provide a quick screening of risk hotspots. And here, we also improved the spatial resolution from 300-m- to 20-m- pixel size.

The main objective of this research is therefore to contribute to the identification of coastal areas at high risk to the combined climate and non-climate forcing in the TTA Region, considering their physical and social vulnerability. The final aim of this research is to provide decision-makers and coastal managers with climate risk maps that can help them define a sound coastal planning incorporating coastal adaptation. Considering how Moroccan territory administration is concerned, the potential study area choice benefits policymakers in deciding where flooding protection is necessary first and foremost (hotspot zones).

2 Materials and methods

2.1 Study area

Located at the crossroads of two maritime areas, the Atlantic and the Mediterranean, in the far northwest of Morocco, the region of Tangier-Tetouan-Al Hoceima (TTA) is the only one among the 12 administrative divisions of Morocco, which have two maritime facades. The coastline includes 51 municipalities, 34 of which have a maritime façade and 17 adjacent municipalities constitute the area of potential influence (Figure 1).

2.1.1 Physical setting

With approximately 447 km of coastline along the Atlantic Ocean, the Strait of Gibraltar, and the Mediterranean Sea, the coast of the TTA region has a specific geographical position and a geomorphological structure which make its landscape very rich and diverse, offering sites of great ecological value such as very steep coastal cliffs, creeks, coastal islets, bays, sandy beaches, coastal marshes, lagoons, etc.

Along the Mediterranean stretch, the region has a rugged coast with a succession of bays and capes. The shore is dominated by steep hills and cliffs (80%) isolating only beach pockets generally corresponding to the mouth of the rivers. This coastline is crossed by many rivers, the main ones being: Ghiss, Nekkor, Smir, Martil, Laou, and Amsa.

On the Atlantic side, the morphology is varied, ranging from low alluvial plains to beaches with or without dunes, sometimes preceding coastal marshes (Larache marsh, Tahaddart estuary
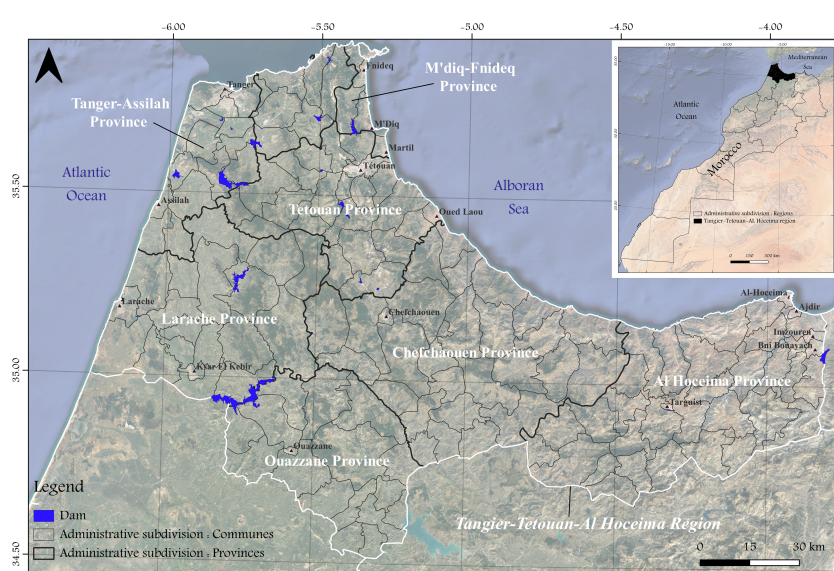

FIGURE 1
Geographical location of the TTA region and its administrative subdivisions. Background satellite imagery corresponds to google satellite of 2023, available as Basemap in QGIS v3.22.11 software.

complex), or rocky coasts or cliffs. This coastline is dominated by consolidated dunes forming alignments in the same direction as the coast itself. It is crossed by rivers, the main one being Oued Loukkos.

The coastline of the Strait of Gibraltar is rugged and dotted with rocks and beaches at the mouth of the wadis.

2.1.2 Climate

Overall, the region benefits from a Mediterranean-type climate with hot, dry summers and mild, wet winters. However, due to its geomorphological configuration, combining high Rif mountains and coastal plains, the TTA region is subject to very diverse climatic conditions. Indeed, the oceanic influence which characterizes the western basins of Loukkos and Tangier is gradually attenuated in the Mediterranean coastal basins, with an increasingly pronounced aridity from West to East. Between Larache and Oued Laou, rainfall can exceed 700 mm/year. While the eastern part of the region (particularly for the lower basins located between Jebha and Al Hoceima) receives barely 400 mm/year (CHIRPS data, https://www.chc.ucsb.edu/data/chirps).

Temperatures are generally mild, with an annual average of 17° C, but can vary from 0° C to 37° C depending on the season. However, it should be noted that in recent years, the region is subject to a higher occurrence of heat waves which further accentuates the negative impacts on people and natural resources (IPCC, 2022).

In terms of a marine climate, on the Mediterranean coast, the tides are microtidal, with a range that varies from 80-100 cm in spring to a few centimeters in neap tides (L.P.E.E, 1991). The intensity of tidal propagation, which comes from the Atlantic, gradually decreases to the east. The hydrodynamic conditions are characterized by dominant waves from the E to ENE, and a main longshore drift northward (El Mrini et al., 2012). The coastal area is very little fed with fluvial inputs, due to damming of the main watercourses, whose hydrological regime is typically Mediterranean with flash floods during the short-time high waters and an almost drying off in low waters (El Moutchou, 1995; Nachite et al., 2004; Anfuso et al., 2007; Niazi, 2007; El Mrini et al., 2012).

On the Atlantic side of the study area, the tides are classified as mesotidal with a maximum tidal range of about 3 m. Meteorological conditions generate W to NW swells. The strongest swells, of decadal frequency, can reach 7 to 9 m in amplitude during severe storms and are likely to mobilize sediments up to 100 m deep (Jaaidi and Cirac, 1987). The littoral drift is towards the south to SW (Taouati et al., 2011).

2.1.3 Hydrographic resources

The TTA region spans two hydrological domains: the Sebou basin and the Loukkos basin with an important hydrographic network. The renewable water potential is estimated at about 4 billion m^3/year as an average interannual supply, of which: 3,600 Mm^3/year of surface water and 460 Mm^3/year of groundwater (Agence du Bassin Hydraulique du Loukkos, 2018). Groundwater reserves remain quite modest given the dominance of impermeable geological formations in the region. The high intensity of rainfall

during short periods, the predominance of clayey facies and the rugged relief, promote runoff and limit the importance of groundwater resources. During major storms, rivers experience sudden and violent floods, causing heavy damages, especially in highly urbanized areas. The city of Tetouan, for example, has experienced catastrophic flooding over the past 15 years. Only the limestone mountains, the plains, the alluvial valleys and a few small isolated basins benefit from the infiltration of rainwater, which forms modest underground reservoirs whose importance varies from one unit to another. Seventeen dams, two of which are currently under construction, are used to regulate rivers and reduce the risk of flooding, as well as to satisfy the needs for irrigation, drinking and industrial water and to face the negative effects of droughts.

2.1.4 Socio-economic background

The coastline of the TTA Region is home to 2,479,578 inhabitants in 2020, 75% of whom live in urban areas. The average annual growth rate of the region increased at a rate of 1.47% between 2004 and 2014. The prefectures of M'diq-Fnideq and Tangier-Assilah recorded the highest growth rates, while the province of Al Hoceima recorded the lowest rate. The population density is on average 600 inhabitants per km^2 (three times the regional density) but can exceed 7000 inhabitants per km^2 in coastal cities such as Tangier and Tetouan (Haut-Commissariat au Plan, 2018).

The main contributors to the economy of the coastal area are port activities, trade, and services, fishing, tourism, and agriculture. The economies of Tetouan and M'diq-Fnideq are heavily dependent on trade and services, while the economy of Chefchaouen is more dependent on agriculture and fishing. In Tangier-Assilah, in addition to trade and services, the industry is an important component of the economy. 80% of the permanent industrial workforce and 92% of foreign trade is located in the major cities of the Tangier-Tetouan region along the coast (Haut-Commissariat au Plan, 2018).

Over the past two decades, the region's population has continually migrated to the coastal plains because of the natural, economic, and logistical resource potential they offer. The high demand for space and resources has resulted in extensive urban encroachment on natural and agricultural lands to meet all these needs. For example, a diachronic analysis of the Tangier coastline between 1995 and 2018 (Wahbi et al., 2019), showed that over the 23 years covered by the study, the built-up area has tripled in the coastal strip of 10 km from the shoreline. In the prefecture of Mdiq-Fnideq, the orographic constraint imposed a first extension on low-lying areas, which then continues on the hills around the two towns. Urbanization often encroaches on soils of great ecological value, such as wetlands, dunes, forests…, but also by occupying areas prone to flooding or landslides. On the Atlantic coast of the TTA region, the analysis of LULC changes in Tahaddart coast (Aitali et al., 2020) showed a decrease in almost all the land use units between 1999 and 2019 except the built-up area, which shows a sharp increase. These changes are linked to the fact that the Tangier-Asilah prefecture, has experienced significant

development in the last decade (Chattou, 2011), explaining the increase in the built-up area, to the detriment of the cultivated lands and the natural habitats (Rifai et al., 2018).

2.1.5 Environmental issues

Among the many pressures on the TTA coast, it seems that it is land pressure that dominates all along the coast, especially on the seafront, where linear urbanization is often carried out to the detriment of the coastal dunes, real beach regeneration reservoirs, the disappearance of which directly exposes the infrastructure to storm surges and other climate hazards.

In the bay of Tangier, while the extension of the port has boosted trade and economy in the region, it has also led to a significant erosion of the eastern beaches of the Bay of Tangier. According to numerous authors (El Arrim, 2001; Snoussi & Long, 2002; Bouzidi et al., 2004; Sedrati and Anthony, 2009), coastline retreat is estimated between 2 and 3 m per year in the eastern part of the bay.

Tetouan coast, which relies heavily on tourism, is also experiencing a strong retreat. Indeed, more than 95% of the dunes have been destroyed by residential and hotel infrastructure (Bello et al., 2006). In addition to coastal developments, the construction of dams on Smir and Martil, and of marinas (M'diq, Smir Marina and Kabila) have completely disrupted the coastal sedimentary budget, leading to severe coastal erosion. The historical shoreline changes, between 1958 and 2011 (Niazi, 2007; Snoussi et al., 2008; El Mrini, 2011; El Mrini et al., 2012) showed an overall erosive trend of the shoreline. Eroded beaches represent 70 to 86% of the coastline. Flayou et al. (2021) estimated the beach retreat to be between 20 and 24 m between 2004 and 2016, *i.e.*, an average annual rate of 1.83 m/year. In the eastern part of the study area, Khouakhi et al. (2013) estimated that about 60% of the Al Hoceima bay coastline showed an erosive trend between 1958 and 2013.

On the Atlantic coast of the TTA Region, the high wave energy beaches also show an erosive trend. For example, Charf el Akab beach retreated by approximately 70 m between 1985 and 1992 (in

Taouati et al., 2011). Amharak (2006) estimated the rate of erosion north of the Tahaddart estuary at 1.94 m/year, presumably due in part to sand mining and dam construction.

2.2 Methodology

The analysis performed in this research consists on the application of a multi-scale coastal risk index (MS-CRI) to the TTA region (Figure 2), based on the index-based approach developed by Satta (2014). This approach, as proposed by other indices in the scientific literature (Davidson and Lambert, 2001; Peduzzi et al., 2009), considers Risk (R) as a function of three factors: hazards, vulnerability and exposure as described in the simplified equation (1):

$$R = F \star V \star E \qquad (1)$$

In fact, the MS-CRI combines information on the potential effect of climate change on coastal hazards with physical, environmental, and socio-economic features (Greco and Martino, 2016; Satta et al., 2016; Satta et al., 2017; Torresan et al., 2020; Furlan et al., 2021), provides a simple numerical basis to identify the coastal areas where risks may be relatively high and displays these hotspots on geographic maps. This tool can easily be integrated into overall coastal management and adaptation strategies to support the implementation of the ICZM Protocol (Satta et al., 2016), and contribute both to coastal communities' protection and biodiversity conservation.

2.2.1 Multi-scale coastal risk index application at the local scale

This research proposes the application of the MS-CRI at the local scale of TTA region (CRI-LS) to define the coastal hazard zone and provide a wider spatial perspective of risk and vulnerability in 2100 at the local scale. The "hotspots", as well as the areas of relatively lower risk, emerge from the product of the different


FIGURE 2
Flowchart illustrating the materials and method used to calculate the coastal risk index. *Bibliography used to produce both HSC and DPCI is mentioned in (Table 2).
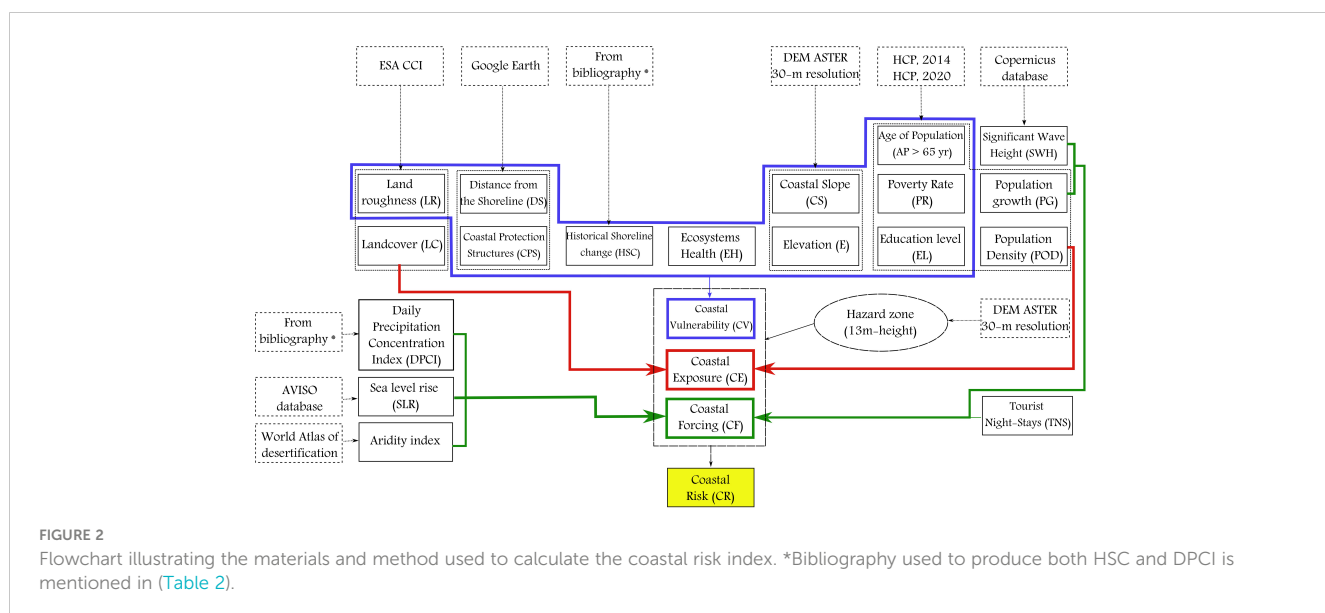
coastal risks components factors aggregated into the three sub-indices: the forcing index, dealing with climate and not climate drivers, the vulnerability index, dealing with the susceptibility and resilience of the coastal areas and local communities, and the exposure index, dealing with the human and environmental assets that could be adversely affected.

The process for implementing the CRI-LS methodology, is articulated around the following 5 steps: delineation of the coastal hazard zones; data collection and variables choice; assignation of scores and weights to risk variables; creation of raster spatial data; calculation of the sub-indexes and the final index.

2.2.2 Delineation of the coastal hazard zone

Identifying the coastal hazard zone is essential for efficient long-term coastal management, including the protection of both local populations and infrastructures (Satta, 2014). To do so, the estimation of the coastal hazard zone is based on an empirical approach of Hoozemans et al. (1993), taking into account the fact sea level rise 1.5 m in 2100. The later scenario was adopted as the upper limit for 2100 based on the precautionary principle. This claim is supported by the fact that sea levels can rise several tenths of a meter, during the 21st century, as sectors of Antarctica's marine-based ice sheets collapse (Satta et al., 2016 and reference therein). The value of 1.5 m was integrated in the Hoozemans equation and the results obtained for the study area are shown in Table 1. The Hoozemans equation also includes maximum flood level and storm surges with a 100-year return period (Table 1).

$$Dft = MHW + St + Wf + Pf \qquad (2)$$

where:

Dft: inundation level; MHW: mean high-water level; St: relative sea level rise; Wf: height of storm waves; Pf: sea level rise resulting from a decrease in atmospheric pressure (negligeable in TTA region).

In fact, the inundation level is higher in the Atlantic and relatively lower in the Mediterranean because of the higher value of MHW (higher tidal range) (Table 1). Based on these calculations, the extent of the coastal hazard zone is the maximum inundation level of 13 m, owing to the large study area (Figure 3). Thus, the coastal hazard zone was defined using a digital elevation model with a spatial resolution of 30-m (NASA/METI/AIST/Japan Space Systems, and U.S./Japan ASTER Science Team). From a technical viewpoint, all pixels corresponding to an altitude of between 0 and 13m were extracted. We obtained a coastal hazard zone that covers an area of 520 km^2 (Figure 3).

2.2.3 Variables selection and ranking

In order to construct the coastal risk index map, a series of variables (Table 1) associated with a coastal spatial unit was used, based on the equation of risk that integrates coastal forcing, coastal vulnerability, and coastal exposure indexes. Each component of the risk equation, including the final outcome, was produced with a concept of multi-criteria decision-making (MCDM) theory following the approach described in section 2.2.1. using the geographic information systems (GIS) platform. The method is widely employed in research studies for regions with similar characteristics (e.g., Bagdanavičiute et al., 2015; Satta et al., 2016; Satta et al., 2017; Aitali et al., 2020).

The selection of relevant variables was conducted in order to further describe forcing, vulnerability, and exposure indices (Table 2), and according to data availability referring to the TTA coastal zones.

Once the variables were selected, a ranking score was defined for each variable class according to its relative importance (Table 3) and based on literature review. A scale ranging from 1 to 5 was applied, with 1 being the lowest importance and 5 being the highest. Secondly, the weighting of each variable based on expert opinions as well as on stakeholder consultation during regional workshops, was carried out. In fact, variables deemed to have a higher impact on the final risk were given a weight close to 100%, while variables deemed to have a lower impact were given a weight close to 0% (Torresan et al., 2012). This way of weighting was widely adopted to assess coastal risks associated with climate change at the regional (Torresan et al., 2012; Zhou et al., 2015; Satta et al., 2017) and local scales (Satta et al., 2016; Aitali et al., 2020), and as a metric for ranking risk mitigation strategies (Zhou et al., 2015).

The coastal sub-indices are calculated according to the equation:

$$CSI = \frac{\left(\sum_{i=1}^{n} x_i W_i\right)}{\left(\sum_{i=1}^{n} W_i\right)} \qquad (3)$$

where:

CI = Coastal Sub-Index; n = number of variables; xi = scores related to variable i; Wi = weight related to variable i;

In order to convert the coastal sub-indices into the same standard scale ranging from 0 to 1, and facilitate the analysis of the values, a normalization procedure was applied to the variable xi as follows:

$$CSI' = \frac{\left(\sum_{i=1}^{n} x'_i W_i\right)}{\left(\sum_{i=1}^{n} W_i\right)} \qquad and \quad x' = \frac{x - x_{min}}{x_{max} - x_{min}} \qquad (4)$$

where CSI'= normalized Coastal Sub-Index ranging from 0 to 1;

TABLE 1 Description of parameters used in Hoozemans equation to calculate maximum inundation levels for the main facades of the TTA region (Laboratoire Central d'Hydraulique de France (1974); Snoussi et al., 2008; El Mrini, 2011; Taouati et al., 2011; Khouakhi et al., 2013).

Location	MHW	Storm waves (return period)	Inundation levels (Dft)
Mediterranean (Tetouan):	0.96	6.20 (1/100yr)	8 m
Strait of Gibraltar (Tangier)	2.60	8.5 (1/100yr)	12.6 m
Atlantic (Larache)	3.70	7.8 (1/100yr)	13 m

FIGURE 3
Coastal hazard zone (13m asl) for the TTA region. Background satellite imagery corresponds to google satellite of 2023, available as Basemap in QGIS v3.22.11 software.

TABLE 2 Description of variables used to create the coastal risk map and their sources.

Coastal risk components	Variables	Descriptions	Unit	Original Format of the dataset	Sources
Forcing	Aridity index (Ai)	Aridity is a measure of the "drought" of the climate expressed as the ratio of precipitation to evapotranspiration; the lower the ratio, the drier the climate. Ai less than 0.65 corresponds to an arid zone.	Mm	Raster	World Atlas of Desertification (EU Commission) https://wad.jrc.ec.europa.eu/geoportal
	Daily beach attendance	Number of people visiting and using the beach	x 10³ Pers.	Shapefile (by province)	Ministère de la Transition énergétique et du Développement Durable (2022)
	Daily precipitation concentration index (DPCI)	Index used as a measure of concentration. A high DPCI value of precipitation indicates that precipitation is more concentrated on a few rainy days during the year. DPCI could also be used to estimate precipitation erosivity and aggressiveness (REF).	mm/day	Shapefile	Salhi et al. (2019)
	Population Growth (PG)	Annual population growth rate of communes crossed hazardous zone.	%	Shapefile (by commune)	Haut-Commissariat au Plan, (2020), https://www.hcp.ma/
	Sea level rise (SLR)	Measures the annual trend of sea level rise between 1993 and 2021. Accurate measurements for a limited period are available through satellite altimetry data.	mm/yr	Shapefile	https://www.aviso.altimetry.fr/?id=1599
	Significant Wave Height (SWH)	Represents the number of detected waves exceeding the 95 percentile of daily wave heights on average per year (MSHx95p), over a long-term period (e.g., 100 years)	Cm	Shapefile	https://cds.climate.copernicus.eu/cdsapp#!/dataset/sis-ocean-wave-indicators?tab=overview
	Tourist night-stays (TNS)	Rate of tourist arrivals to the study site	x 103 Pers.	Shapefile (by province)	TTA Region Statistical Yearbook (2018)
Vulnerability	Land roughness (LR)	Using Manning coefficients, it represents the resistance of the terrestrial surface to surface erosion	–	Raster	https://2016africalandcover20m.esrin.esa.int/
	Distance from the shoreline (DS)	Related to the progression of the risk according to the inland penetration	M	Shapefile (coastline)	Calculated using the GIS platform
	Coastal protection structures (CPS)	Percent of coastline with protective structures (Groin, breakwaters, seawall…)		Shapefile	Google Earthimagery

(Continued)

TABLE 2 Continued

Coastal risk components	Variables	Descriptions	Unit	Original Format of the dataset	Sources
	Historical shoreline changes (HSC)	Evolution of shoreline change that locates eroded coast/Sediment budget	M	Shapefile (by location)	El Mrini (2011); Niazi (2007); Taouati et al. (2011); Khouakhi et al. (2013)
	Ecosystem health (EH)	Expresses the contribution of the ecosystem as protection against storm surges, flooding, and other coastal hazards.	–	Shapefile	Agence Nationale des Eaux et Forêts, Google earth imagery
	Elevation (E)	Coastal unit surface (pixel) within a specific elevation class Xi	M	Raster	ASTER DEM, NASA/METI/AIST/ Japan Space Systems, and U.S./Japan ASTER Science Team.
	Coastal slope (CS)	In relation to the relative risk of shoreline retreat.	%	Raster	ASTER DEM, NASA/METI/AIST/ Japan Space Systems, and U.S./Japan ASTER Science Team.
	Education level (EL)	Persons with a level at least equal to level 3 of the international standard	%	Shapefile (by commune)	Haut-Commissariat au Plan (2014), https://www.hcp.ma/
	Poverty rate (PR)	Persons with a low quality of life (poor people)	%	Shapefile (by commune)	Haut-Commissariat au Plan (2014), https://www.hcp.ma/
	Age of population (AP)	Number of people over 65	%	Shapefile (by commune)	Haut-Commissariat au Plan (2014), https://www.hcp.ma/
Exposition	LandCover (LC)	Land surface covered by different types of physical coverage (classes) in various places	–	Raster	https:// 2016africalandcover20m.esrin.esa.int/
	Population density (PoD)	Number of inhabitants per km2 in each commune crossed the study area	Inhab./ km2	Shapefile (by commune)	Haut-Commissariat au Plan (2020), https://www.hcp.ma/

TABLE 3 Variable selection and ranking for the CRI-LS index.

Coastal risk components	Variables	Unit	Score					Weight (%)
			1	2	3	4	5	
Forcing	Aridity index (AI)	–	No	–	–	–	Yes	15
	Daily Beach Attendance (DBA)	x 10³ pers.	< 1	1 – 5	5 – 10	10 – 20	> 20	10
	Daily precipitation concentration index (DPCI)	mm/yr	< 0.64	0.64 – 0.66	0.66 – 0.68	0.68 – 0.70	> 0.70	20
	Population Growth (PG)	%	≤ 0.1	0.1 – 0.5	0.5 – 1	1 – 2	> 2	10
	Sea level rise (SLR)	mm/y	< 1	1 – 1.6	1.7 – 2.4	2.5 – 3.2	> 3.2	10
	Significant Wave Height (SWH)	m	< 4.7	4.71 – 6.65	6.66 – 8.13	8.13 – 9.57	> 9.57	25
	Tourist Night-Stays (TNS)	x 10³ pers.	< 50	50 – 100	100 – 500	500 – 1000	> 1000	10
Vulnerability	Land Roughness (LR)	Manning coefficient	> 0.06	0.06 – 0.04	0.04 – 0.03	0.03 – 0.02	< 0.02	10
		m	< 300	300 – 900	900 – 2100	2100 – 4500	> 4500	12

(Continued)

TABLE 3 Continued

Coastal risk components	Variables	Unit	Score					Weight (%)
			1	2	3	4	5	
	Distance from the shoreline (DS)							
	Coastal Protection Structures (CPS)	%	> 50	50 – 30	30 – 20	20 – 5	< 5	7
	Historical Shoreline Changes (HSC)	m/yr	> +2	+1 to +2	+1 to -1	-1 to -2	> -2	10
	Ecosystem Health (EH)	–	No detectable change	Slight signs of disturbance	moderate disturbance with a 50% loss of species	major disturbances	severe disturbance with loss of most species	13
	Elevation (E)	m	6 – 4.8	4.8 – 3.6	3.6 – 2.4	2.4 – 1.2	< 1.2	13
	Coastal Slope (CS)	%	< 1	1 – 2	2 – 3	3 – 4	> 4	9
	Education Level (EL)	%	> 25	25 – 15	15 – 5	5 – 0.5	< 0.5	10
	Poverty Rate (PR)	%	< 5	5 – 10	10 – 20	20 – 30	> 30	9
	Age of Population (AP)	Pers.	< 3	3 – 7	8 – 13	14 – 20	> 20	7
Exposition	LandCover (LC)	–	Barelands	Shrubland, grasslands, sparse vegetation	Forest and Water bodies	Cultivated areas	Urban areas	52
	Population Density (PoD)	hab/km^2	< 50	50 – 1000	1000 – 2000	2000 – 3000	> 3000	48

Considering that $x_{min} = 1$; $x_{max} = 5$ $and \sum_{i=1}^{n} W_i = 1$ the equation becomes:

$$CSI' = \frac{(\sum_{i=1}^{n} x_i W_i) - 1}{4} \quad (5)$$

The equations to be applied to the three groups of raster images describing the various components of the sub-indices are:

$$CF' = \frac{(\sum_{a=1}^{n_{CF}} x_a W_a) - 1}{4} \quad (6)$$

$$CV' = \frac{(\sum_{b=1}^{n_{CV}} x_b W_b) - 1}{4} \quad (7)$$

$$CE' = \frac{(\sum_{b=1}^{n_{CE}} x_c W_c) - 1}{4} \quad (8)$$

Where: CH', CV' and CE' are the normalized weighted coastal sub-indices; nCF = number of CF variables; nCV = number of CV variables; nCE = number of CE variables; Wa = weight associated with the CF variables; Wb = weight associated with the CV variables; Wc = weight associated with the CE variables.

As the three sub-indices were normalized it is feasible to combine them into an overall index, which is calculated from the multiplication of the values obtained for each sub-index, as follows (Satta et al., 2016):

$$CRI - LS = CF' * CV' * CE' \quad (8)$$

2.2.4 Construction of the coastal risk map

The next operational steps require the application of GIS tools to process the data and to move from the numerical to the spatial dimension. To do so, variables were converted to a raster format assigning the scores defined in Table 2 to the pixels. The raster pixels were resampled to a similar spatial resolution of 20 m in order to minimize errors caused by different image resolutions. The resolution value was chosen because it is the most accurate data resolution available in available datasets (Landcover). The Eq. (6), (7) and (8) were used to produce the maps of forcing, vulnerability, and exposure indices, and then the Eq. (8) to calculate the CRI-LS in the GIS platform. In the end, the resulting values of each index were classified into five qualitative classes from "very low" to "very high".

3 Results & interpretations

The coastal risk assessment led to highlight the levels of risk that may affect the coastline of TTA and hinterland areas. The assessment is based on factors that reflect the implication of climate change through the climatic and non-climatic forcing, environmental and socioeconomic issues. Using the CRI-LS method, the coastal risk, forcing, vulnerability, and exposure levels for each cell along the hazard zone are visualized in Figure 4.
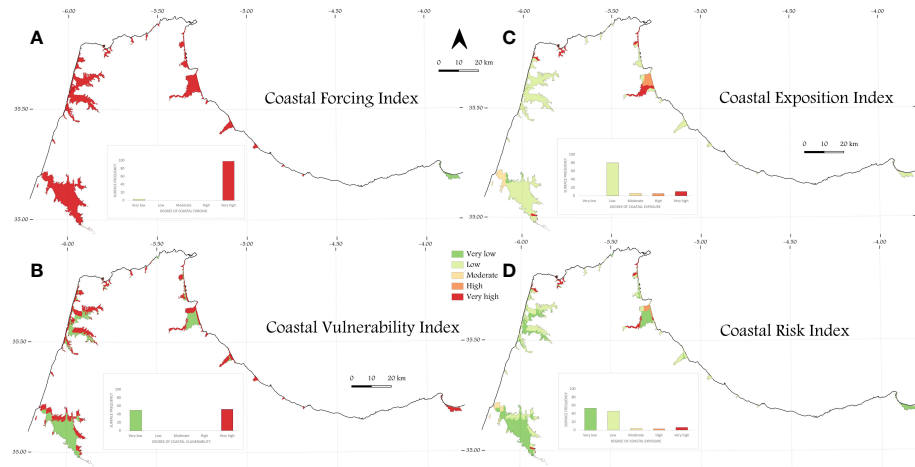
FIGURE 4
Result maps for coastal risk assessment of some selected coasts of the TTA region. **(A)** Coastal Forcing Index, **(B)** Coastal Vulnerability Index, **(C)** Coastal Exposure Index and **(D)** Coastal Risk Index.

3.1 Coastal forcing index

Seven climatic (Aridity index Ai, Daily precipitation concentration index DCPI, Sea Level Rise, Significant Wave Height SWH) and non-climatic (Daily Beach Attendance DBA, Population Growth, and Tourist night-stays TNS) variables were used to produce the coastal forcing index. Results indicate that, with the exception of the Al Hoceima site, which has a low coastal forcing, 97% of the study area is highly exposed to coastal forcing (Figure 4A). Due to long-term relative sea level changes brought on by sea level rise, coastal forcing is significant for most of the study area. In fact, the annual trend of the latter is greater than 2.9 mm/yr on the Atlantic coast, and increases to 3.3 mm/yr on the Mediterranean coast. A considerable amount of SHW is also linked to the sea level rise LR; along the Atlantic coast, it may reach 9.5 meters, whereas, along the Mediterranean coast, it may only reach 8 meters. This may explain the poor coastal forcing at the Al-Hoceima zone, as the SHW has a substantial amount of weight in comparison to other variables.

In addition, the population growth, associated with high anthropogenic activities in the coastal hazard zone's bordering cities, such as Tangier, Tetouan, Larache, and Assilah, also results in an increase in coastal forcing.

3.2 Coastal vulnerability index

To calculate the coastal vulnerability index, ten variables were combined including physical (LR, DS, HSC, E, and CS), environmental (CPS, and EH), and social (EL, PR, and AP) elements. A coastal hazard zone represents either very low or very high levels of vulnerability (Figure 4B), covering 48% and 52% of the total area, respectively. The coastal vulnerability map reveals that 'very high' vulnerabilities tend to be more concentrated nearby the coast, while 'very low' vulnerabilities tend to be farther from the coast.

The rise in vulnerability is solely due to physical variables. This claim is supported by the fact that: (1) the topographically low locations are those that seem to be more vulnerable; (2) the vulnerability rather decreases as the distance from the coast increases; and (3) the LR variable is crucial in determining vulnerability, particularly with regard to the risk of coastal flooding, because it varies according to the types of land cover (Satta et al., 2016).

Social vulnerability is also made evident in that high vulnerability zones extend over the cities and towns, which are relatively high in AP, EL, and PR. In addition, the vulnerability index may rise since there are not enough coastal protection structures along the TTA coastlines.

3.3 Coastal exposure index

This index reflects the level of exposure of the different stakes and assets located in the coastal hazard zone. Results show that 14% of the whole area corresponds to the highest exposure class (Figure 4C). The high exposure values are focused on the urbanized areas, which are characterized by high population density, such as Tangier, Tetouan, and Ksar El Kebir; along the coast of Fnideq and Martil (Figure 4C). In fact, all urban infrastructures, including buildings; highways, ports, marinas, and beach resorts, are concentrated in these cities. With the high population density, the potential damage related to the coastal hazard might be devastating. The rest of the area, 80% of the total area, has low exposure levels, with the exception of a few cells (6%), which consist of uninhabited or low-density territory.

3.4 Coastal risk hotspots

The coastal risk index was calculated from the three risk components discussed above. According to the coastal risk

mapping, the low coastal risk class dominates the study area with 89% of the total, 3% exhibit a moderate risk, and 8% is at high risk related to climate change (Figure 4D). It appears to be a cumulative effect of important exposure and vulnerability levels leading to high-risk levels. These areas, which correspond to the hotspot zones in terms of climate change-related coastal risks, are associated with the low-lying areas of the Bay of Tangier, Martil coast, Tetouan and Fnideq cities, and the Atlantic coastline of Tangier. Zooming in on the most economically and demographically important areas (Figure 3) better visualizes the areas at coastal risk.

(1) At Larache province, most of the hazard zone shows low to very low-risk levels (Figure 5A), despite the presence of the Loukkos estuarine valley. This is probably due to the low population rate of this area, devoted mainly to extensive agriculture. The moderate coastal risk concerns the north of the city of Larache, where human and port activities are concentrated. The very high coastal risk is identified to the west and northwest of Ksar El Kbir city, where the population density is high and socio-economic indicators are lower;

(2) From Assilah to the south of Tangier, the majority of the coastal hazard zone exhibit low to extremely low-risk classes (Figure 5B), probably due to the low density of the population and human activities. The only place where the coastal risk is very high relates to the free zone of Tangier where many industries are concentrated, and where the standard of living of rural populations is low;

(3) The Bay of Tangier is one of the most at-risk areas on the TTA coast. Figure 5C shows that the hazard zone with the high coastal risk extends particularly over the urbanized zones, including the port of Tanger city. This area consists of a big number of economic companies with large investments that employ thousands of people. Another hot spot of coastal risk is located in the industrial zone south of Tangier. This is an area, which already regularly experiences continental flooding due to its low elevation and the density of urbanization (Figure 5C);

(4) Tetouan city has an exceptionally high coastal risk towards the south of the city along the Martil river and in related hillslopes (Figure 5D). On the seafront, the level of coastal risk is generally high to very high, except for the steep
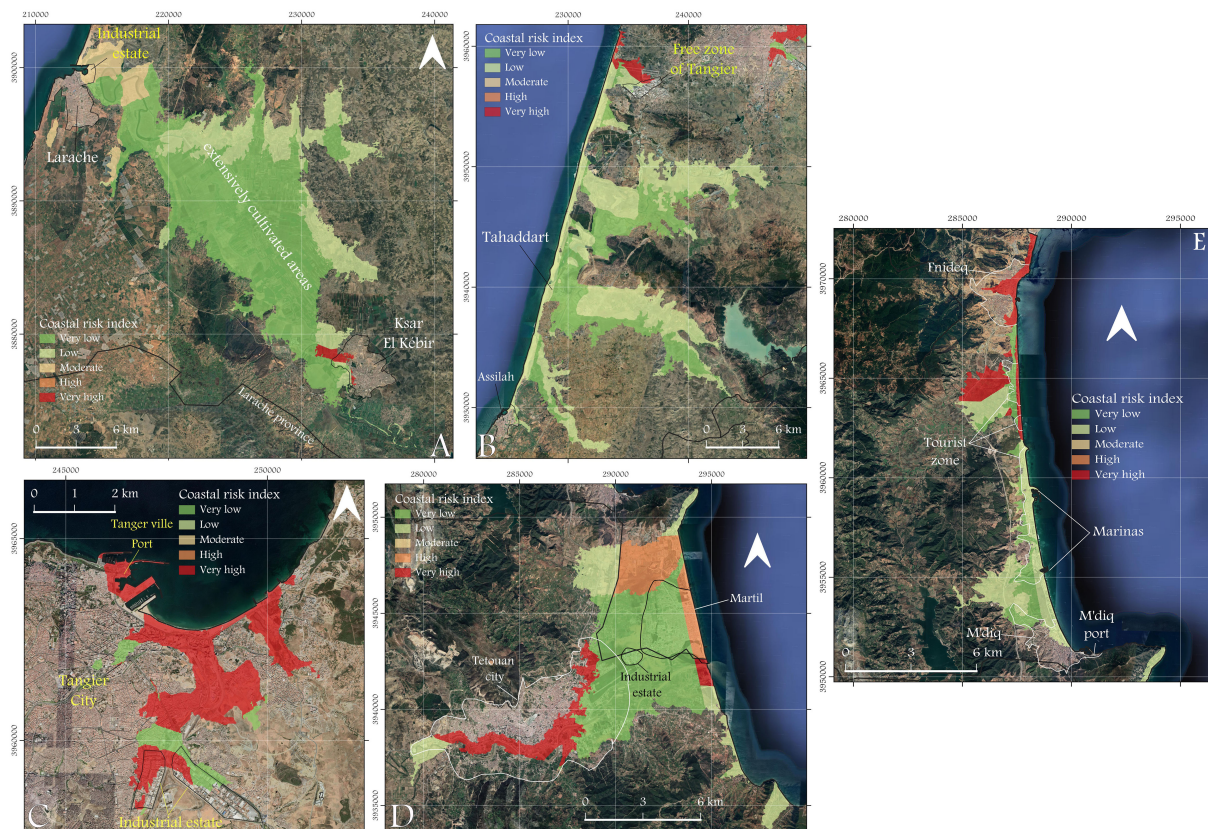

FIGURE 5
Maps focused on the most economically and demographically significant zones to define the hotspot locations in terms of coastal risk. **(A)** Larache, **(B)** Assilah-South of Tangier sector, **(C)** Bay of Tangier, **(D)** Tetouan, **(E)** Fnideq-M'diq.

coastline to the south. This coast is densely populated and highly urbanized, and has experienced a continuous retreat of the shoreline in recent years.;

(5) In Mdiq-Fnideq province, areas with very high coastal risk are concentrated in the urban area of Fnideq, including the port, and along the seafront, where several tourist resorts and infrastructure are located (Figure 3E). In some areas of the hinterland, coastal risk is also very high, due in part to the poverty and vulnerability of rural populations. M'diq is also known for its beach tourism. Yet, the coastal risk is low to moderate (Figure 5E), probably due to the higher standard of living of secondary residences here.

4 Discussion

The results of the coastal risk assessment in the TTA Region, performed using an index-based analysis, and visualized on risk maps, identified hot spot areas that require special attention in the development of the TTA Region's coastal plan.

For similar hazard conditions, a hot spot generally results from the combination or cumulative effect of high vulnerability and high exposure. These conditions are found in the Bay of Tangier and in the provinces of Tetouan and Mdiq-Fnideq. The factors that weighed most heavily in the assessment of risk in these hot spots are related to topography, population density and urbanization, and socio-economic indicators that reflect the resilience of the populations. The overall findings fully correspond to the existing literature in the region, as developed below.

In the Bay of Tangier, especially in its central part, the elevation is low, and the coastline is heavily urbanized with the largest agglomeration in the region, and one of the largest ports in Morocco. These assets of high economic value express the high exposure to coastal risks. In addition, the drastic reduction of sediment inputs by the few rivers flowing into the bay, the degradation of the lake's wetland (Snoussi et al., 2009), and the ineffectiveness of coastal erosion control structures (Sedrati and Anthony, 2009), make the area highly vulnerable to coastal hazards. According to Snoussi et al. (2009), 24% of the bay would be at risk of flooding with 11m inundation level scenario. The most exposed sectors are the urban area including the port, the coastal defenses, the tourist coastal infrastructures, and the industrial area. In addition, shoreline erosion would affect nearly 45% of the total beaches in 2100. These studies were based at that time only on the physical vulnerability component without considering the socio-economic or demographic parameters and therefore do not reflect all the aspects that can weigh in the assessment of coastal risks as this study has shown.

The Tetouan coast is also one of the Moroccan coasts that have been most rapidly and densely urbanized, mainly because of its tourist appeal. However, most of its beaches have an erosive trend, some of which might disappear in the next few decades (El Mrini et al., 2012; Flayou et al., 2021). Indeed, being a sand-deficient system, the coast will not be able to cope with the rise of the sea level, if no adaptation measures are undertaken. Satour et al. (2021) estimated the resilience index of this coast to flooding and showed that nearly 9000 households (18.4%) are in areas of very low to low resilience. Furthermore, Flayou et al. (2021) attempted a first assessment of the monetary losses that may be incurred by the tourism sector of the Tetouan coast, if the beaches were to disappear, which they estimated at 71.5 million US\$ annually. This amount is largely underestimated because it does not take into account the evaluation of other ecosystem services provided by these beaches such as the protection of settlements and coastal infrastructures against marine submersion. Our findings are consistent with these previous results and support the fact that areas falling under very high and high risks are linked to a combination of high erosion rates with high capital land use.

Another factor that seems to influence coastal risks in the study area is related to the socio-economic disparities that characterize the TTA region, with significant gaps between urban areas and rural municipalities, particularly in terms of education and access to public services and employment (Haut-Commissariat au Plan, 2018). Some rural territories in the hinterland have a high rate of illiteracy and poverty, often resulting in a lack of risk perception and awareness. In this regard, based on a field survey in the Tetouan coast Ivčević et al. (2020), rightly advocate risk awareness as a predictor of precautionary behavior and readiness of inhabitants to protect themselves and their belongings from natural risks. This coastal risk analysis revealed that rural areas display higher vulnerability index than urban areas and therefore have higher level of risks. In fact, poor socio-economic conditions can sometimes shift areas with low physical exposure to high or very high-risk classes, because of low population capacity to cope with these risks. Hence the importance of combining several variables in order to integrate environmental, social and economic aspects, as was done through the use of the composite CRI in this study. But the most important challenge is that these scientific results are properly and effectively used in the coastal plan currently under development and which involves all stakeholders of the TTA Region. Therefore, it is worth mentioning the need for a continuous effort to bridge the communication gap between science, coastal planners, risk managers, and civil society (Ivčević et al., 2021).

4.1 Policy instruments for coastal risks

At the national level, Morocco has committed to reconciling environmental protection and socio-economic development over the past decades. Several laws and reforms were initiated at the national and regional levels. Regarding the coastal zones, the main legislative and regulatory framework for their protection and sustainable development is the Coastal Law (Law No. 81-12) (2015), which advocates, among other things, to fight against coastal erosion and to consider the limit of the non-constructible area. This law requires the development of regional coastal plans, by adopting an integrated management approach that considers the coastal ecosystem and climate change.

In terms of climate change policy, several initiatives addressing adaptation measures and building resilience in coastal areas have been taken in the last decade. In 2009, within the National Plan to Combat Global Warming, a wide range of adaptation tools have been integrated into sectoral adaptation strategies, such as coastal planning, water, agriculture, fisheries, forestry, biodiversity protection and tourism. In 2016, the country launched its National Adaptation Plan (NAP) process. Furthermore, according to the National Strategic Adaptation Plan, which constitutes a roadmap for the implementation of an adaptation policy coordinated at national and territorial level, climate risks are now factored in investment decisions and development planning. Following this framework, the TTA Region has launched its Regional Climate Plan (PCR) in 2020. Moreover, in its United Nations Development Assistance Framework (UNDAF) 2017-2021, Morocco has expressed a number of specific outcomes related to climate change adaptation that can be enhanced through collaboration with the United Nations system, including sustainable territorial planning and reinforced resilience to climate change and natural risks, especially for vulnerable populations.

In terms of coastal risk management, the operational plan for implementing the National Risk Management Strategy 2021-2031, identified two projects relating to coastal areas: (i) Studies and scenarios of marine flooding and coastal erosion and mitigation measures for priority territories; and (ii) Tsunami risk studies and scenarios for priority territories.

At the TTA Region level, in addition to legislative and institutional strengthening, several management actions have been undertaken to reduce coastal hazards and protect coastal infrastructure from erosion. The most representative example is that of the Bay of Tangier. Indeed, in 1987, two groins and a breakwater were implemented in front of the eastern beaches of the bay to protect seaside resort infrastructure and to prevent further erosion (Laboratoire Central d'Hydraulique de France, 1974; Long et al., 1999). Ten years later, these structures have proven not very effective in stopping coastal retreat. In fact, given the advanced stage of erosion, only an integrated management strategy involving a good understanding of beach, dune and nearshore dynamics, within an Integrated Coastal Zone Management framework (Sedrati and Anthony, 2007), can effectively combat erosion and prepare for the unavoidable effects of climate change.

4.2 Climate change adaptation options

Adaptation plays a key role in reducing exposure and vulnerability to climate change. In general, there is no single solution for coastal areas, but at least basic principles to respect, including 'low regret' or 'no regret' measures, and actions that focus on the long term rather than the short term (UNEP/MAP/PAP, 2015). Nature-based solutions (NbS) have proven to be the most appropriate to meet these principles, through restoration and improving the conservation of ecosystems such as coastal wetlands, coastal dunes, forests, and seagrass meadows (Kumar et al., 2020; EC, 2021, Moraes et al., 2022). In addition, NbS are

expected to contribute to both adaptation and mitigation goals by protecting coastal environments from SLR and storms, and by storing substantial quantities of carbon (IPCC, 2022).

The coastline of the TTA Region, which is very diverse in terms of development, geomorphology, and biological diversity requires wider suite of adaptation measures either curative or preventive. The most appropriate solutions for the hotspots identified by the coastal risk analysis should combine hard structures such as seawalls, jetties, groins, and breakwaters to protect the most exposed coastal roads and settlements, with soft measures and NbS, including beach nourishment, and the fixation and revegetation of the coastal dunes. Coastal wetlands, like the Tahaddart tidal marshes or the Smir lagoon, provide a natural defense against coastal flooding and storm surges, and therefore should be restored and protected from urban expansion. The coastal defense structures built in the bay of Tangier to fight against beach erosion and protect the beachfront hotels will be exposed to more severe hydrodynamic conditions. Indeed, in shallow waters, with the rise in mean sea level and the potential intensification of offshore storms, the height of the waves will exceed the design values (Sergent et al., 2015; Almar et al., 2021; Bongarts Lebbe et al., 2021; Mohamed Rashidi et al., 2021). Most of the adaptation strategies proposed in the literature are based on coastal engineering and consist in: a) repairing the structures as they are b) reinforcing them c) demolishing and redesigning them d) accepting coastal realignment. According to Sergent et al. (2015), at very shallow depths (top of beach structures), if the mean water level rises by one meter, these structures will have to be raised by two to three meters to maintain the same crossing performance. In Tangier Bay, the breakwater and groyne will have to be either raised or reinforced, but this might be unsightly, or demolished and redesigned with the integration of softer measures like beach nourishment. However, this strategy might be costly and requires regular monitoring and maintenance.

4.3 Integrated coastal zone management: A proactive and effective process to implement adaptation

It is increasingly recognized that climate change challenges in coastal areas need to be addressed through integrated and ecosystem-based approaches, taking into consideration also other environmental and socioeconomic pressures (Cramer et al., 2018; IPCC, 2022). Moreover, the dynamic nature of climate risks means that a more proactive approach to adaptation planning is essential for coastal areas; otherwise, these risks could reach unacceptable levels (Nicholls et al., 2007; Rochette et al., 2010). The importance of anticipation, particularly in terms of providing knowledge and scientific data, essential at local scales, is also underlined, because of the many uncertainties on climate trends, which can constitute a major obstacle to the identification of coping strategies. Rochette et al. (2010) argued that beyond the conceptual convergences between the processes of ICZM and adaptation to climate change, synergies are possible at the operational level through common implementation tools, such as the setback zone.

At the national level, since the ratification of the ICZM Protocol to the Barcelona Conventions (Panayiotis and Paraskevi, 2020), Morocco has established a solid institutional, policy, and legal framework for ICZM, and hence has the capacity to effectively implement climate change adaptation strategies in coastal planning and management activities. In the TTA coast, the production of risk maps and the identification of hot spots on a regional scale will certainly help to i) better define the priority measures to be considered in the development phase of the coastal plan. The latter is a regulatory planning instrument, which must be based on robust scientific knowledge, provided that data are available, and on a participatory process; and ii) define a sound coastal planning integrating coastal adaptation measures during the implementation phase.

5 Conclusion

This research identifies hotspots and coastal areas at risk in the region of Tangier-Tetouan-Al Hoceima (TTA), Morocco. The main finding is that the coastal area of the TTA region is extremely exposed to coastal forcing, with more than 50% of the zone being highly vulnerable. This confirms that the TTA region is exposed to multiple and combined hazards, which in combination with high demographic and economic pressures intensify the vulnerability of the coastal areas. Compared to the previous study by Satta et al. (2016), we used the same Coastal Risk Index application at the Local Scale (CRI-LS) methodology, but we updated the vulnerability and exposure input data, we improved the spatial resolution from 300-m- to 20-m- pixel size, and we applied it to a whole TTA region.

The authors strongly recommend policy-makers to apply the outcomes of this research for current and future coastal planning and adaptation-related policies for the region of TTA. The process of preparation of the coastal plan of the TTA region is ongoing. It is a strategic document that reflects the vision of the region's coastal areas in the following twenty years and is elaborated by the regional stakeholders, the Regional Directorate of the Environment, and with the assistance of the UN Environment Programme/Mediterranean Action Plan (UNEP/MAP). Within this participatory process, more than sixty regional stakeholders are working on common objectives of sustainable development, to find ways how to mitigate the impact of climate change and to reduce coastal risks. In light of this process, the appearance of the present research is timely, so that the risk maps indeed can be applied in the new coastal plan of the TTA region. Since the coastal risk assessment identified hotspots in the region, this research facilitates the process of decision-making concerning the coastal adaptation to the ongoing processes of climate change, by making concrete decisions in coastal planning and management processes.

Although the human role in the climate crisis is unequivocal, the IPCC report (2021) gives us the power for change so it is important to know that we can still act and contribute to fighting the climate crisis and preventing the tipping points in our coastal areas.

Data availability statement

The original contributions presented in the study are included in the article/supplementary material. Further inquiries can be directed to the corresponding author.

Author contributions

The research, analysis, and manuscript were shaped by all authors, who provided critical feedback. A final version of the manuscript was written by all authors after discussing the results. All authors contributed to the article and approved the submitted version.

Funding

Acknowledgments

Conflict of interest

The authors declare that the research was conducted in the absence of any commercial or financial relationships that could be construed as a potential conflict of interest.

Publisher's note

References

Agence du Bassin Hydraulique du Loukkos (2018). *Projet. du plan directeur intégré des ressources en eau des bassins du loukkos, du tangérois et côtiers méditerranéens* (Royaume du Maroc: Rapport de synthèse), 74 p.

Aitali, R., Snoussi, M., and Kasmi, S. (2020). Coastal development and risks of flooding in Morocco: the cases of tahaddart and saidia coasts. *J. Afr. Earth Sci.* 164, 103771. doi: 10.1016/j.jafrearsci.2020.10377

Almar, R., Ranasinghe, R., Bergsma, E. W., Diaz, H., Melet, A., Papa, F., et al. (2021). A global analysis of extreme coastal water levels with implications for potential coastal overtopping. *Nat. Commun.* 12 (1), 3775. doi: 10.1038/s41467-021-24008-9

Amharak, M. (2006). "Evolution récente (occupation du sol et trait de côte) et impacts anthropiques au nivea' de l'Estuaire de tahaddart (Maroc nord occidental)," in *Mémoire de DESA, univ* (Tetouan, Morocco:Abdelmalek Essaadi, Faculté des Sciences Tétouan), 46.

Anfuso, G., Martinez del Pozo, A., Nachite, D., Benavente, J., and Macias, A. (2007). Morphological characteristics and medium-term evolution of the beaches between ceuta and cabo Negro (Morocco). *Environ. Geology 52* pp, 933–946. doi: 10.1007/s00254-006-0535-3

Bagdanavičiute, I., Kelpšaite, L., and Soomere, T. (2015). Multi-criteria evaluation approach to coastal vulnerability index development in micro-tidal low-lying areas. *Ocean Coast. Manage.* 104, 124–135. doi: 10.1016/j.ocecoaman.2014.12.011

Bello, E. A. G., Macias, A., Nachite, D., Benavente, J., and Barragán, J. M. (2006). *Études préliminaires en vue d'une proposition de gestion intégrée pour les côtes méditerranéennes du littoral marocain : la portion ceuta - cabo Negro*. 103 p, CA-123/2006 Cadiz, version française. (Cadiz -(Espagne): Servicio de publicación de la Univ.') Available at: https://www.researchgate.net/publication/315834261_Etudes_preliminaires_en_vue_d'une_proposition_de_gestion_integree_pour_les_cotes_mediterraneenne_du_littoral_marocain_la_portion_Ceuta-Cabo_Negro.

Bongarts Lebbe, T., Rey-Valette, H., Chaumillon, É, Camus, G., Almar, R., Cazenave, A., et al. (2021). Designing coastal adaptation strategies to tackle sea level rise. *Front. Mar. Sci.* 8, 740602. doi: 10.3389/fmars.2021.740602

Bouzidi, E. L. R., Labraimi, M., and Zourarah, B. (2004). Morphological evolution and spatio-temporal variability of the longshore drift system in the bay of tangier (Morocco). *J. Afr. Earth Sci.* 39, 527–534. doi: 10.1016/j.jafrearsci.2004.07.011

Bwambale, B., Nyeko, M., Muhumuza, M., and Kervyn, M. (2020). Questioning knowledge foundation: what is the best way to integrate knowledge to achieve substantial disaster risk reduction? *Int. J. Disaster Risk Reduct.* 51, 101850. doi: 10.1016/j.ijdrr.2020.101850

Chattou, Z. (2011). Tanger à la croisée de nouvelles recompositions territoriales et de mobilités transnationales. *Méditerranée* 1, 133–138. doi: 10.4000/mediterranee.5447

Cramer, W., Guiot, J., Fader, M., Garrabou, J., Gattuso, J. P., Iglesias, A., et al. (2018). Climate change and interconnected risks to sustainable development in the Mediterranean. *Nat. Climate Change* 8, 972–980. doi: 10.1038/s41558-018-0299-2

Dasgupta, S., Laplante, B., Murray, S., and Wheeler, D. (2009). Climate change and the future impacts of storm-surge disasters in developing countries. *Center Global Dev. Working Paper.* (182).

Davidson, R. A., and Lambert, K. B. (2001). Comparing the hurricane disaster risk of US coastal counties. *Natural Hazards Rev.* 2 (3), 132–142. doi: 10.1061/(ASCE)1527-6988(2001)2:3(132

EC. (2021). *Nature-based solutions | European commission. European commission - European commission.* Available at: https://ec.europa.eu/info/researchand-innovation/research-area/environment/nature-based-solutions_en.

El Arrim, A. (2001). "Contribution à l'étude du littoral de la baie de tanger (Rif nord occidental-maroc)," in *Approches sédimentologique, géochimique et impact de la dynamique sédimentaire* (Université Abdelmalek Essaadi: Tanger), 150 p. Thèse de Doctorat national.

El Moutchou, B. (1995). Dynamique côtière actuelle et évolution morphosédimentaire de la frange littorale méditerranéenne entre m'diq et oued laou (Région de tétouan, maroc nord-occidental). *Thèse 3ème Cycle Univ. Mohammed V. Rabat*, 131.

El Mrini, A. (2011). *Evolution morphodynamique et impact des aménagements sur le littoral tétounais entre ras mazari et fnideq (Maroc nord occidental)* (France: University Abdelmalek Essaadi, Morocco and Université de Nantes). PhD. thesis.

El Mrini, A., Maanan, M., Anthony, E. J., and Taaouati, M. (2012). An integrated approach to characterize the interaction between coastal morphodynamics, geomorphological setting and human interventions on the Mediterranean beaches of northwestern Morocco. *Appl. Geogr.* 35 (1), 334–344. doi: 10.1016/j.apgeog.2012.08.009

ETC-CCA. (2011). Methods for assessing coastal vulnerability to climate change. European topic centre on climate change impacts, vulnerability and adaptation. *Tech. Rep* 1, 1-93. Available at: https://dorsu.edu.ph/faculty/jscabrera/wp-content/uploads/2022/11/TP_1-2011.pdf

Flayou, L., Snoussi, M., and Raji, O. (2021). Evaluation of the economic costs of beach erosion due to the loss of the recreational services of sa–dy beaches - the case of

tetouan coast (Morocco). *J. Afr. Earth Sci.* 182, 104257. doi: 10.1016/j.jafrearsci.2021.104257

Furlan, E., Pozza, D., Michetti, P. M., Torresan, S., Critto, A., and Marcomini, A. (2021). Development of a multi-dimensional coastal vulnerability index: assessing vulnerability to inundation scenarios in the Italian coast. *Sci. Total Environ.* 772, 144650. doi: 10.1016/j.scitotenv.2020.144650

Gallina, V., Torresan, S., Zabeo, A., Critto, A., Glade, T., and Marcomini, A. (2020). A multi-risk methodology for the assessment of climate change impacts in coastal zones. *Sustainability* 12 (9), 3697. doi: 10.3390/su12093697

Greco, M., and Martino, G. (2016). Vulnerability assessment for preliminary flood risk mappingand management in coastal areas. *Nat. Hazards* 82, 7–26. doi: 10.1007/s11069-016-2293-1

Haut-Commissariat au Plan (HCP). (2014). Recensement général de population. Available at: https://rgph2014.hcp.ma/downloads/Resultats-RGPH2014_t18649.html

Haut-Commesariat au Plan (HCP). (2018). *Les Indicateurs sociaux au maroc, édition 2018.* Available at: https://www.hcp.ma/downloads/Indicateurs-sociaux_t11880.html.

Haut-Commissariat au Plan (HCP). (2020). *Projections de la population des provinces et préfectures de la région Tanger-Tétouan-Al Hoceima 2014-2030*. 66p.

Hinkel, J., and Klein, R. J. (2009). Integrating knowledge to assess coastal vulnerability to sea-level rise: the development of the DIVA tool. *Global Environ. Change* 19 (3), 384–395. doi: 10.1016/j.gloenvcha.2009.03.002

Hoozemans, F. M. J., Marchand, M., and Pennekamp, H. A. (1993). "Sea Level rise: a global vulnerability assessment – vulnerability assessments for population, coastal wetlands and rice production on a global scale," in *Delft hydraulics and rijkswaterstaat*, *2nd ed.* (Delft/The Hague: Deltares (WL)), 184.

IPCC. (2022). "Summary for policymakers," in *Climate change 2022: impacts, adaptation and vulnerability. contribution of working group II to the sixth assessment report of the intergovernmental panel on climate change.* Eds. H.-O. Pörtner, D. C. Roberts, E. S. Poloczanska, K. Mintenbeck, M. Tignor, A. Alegría, M. Craig, S. Langsdorf, S. Löschke, V. Möller and A. Okem (Cambridge, UK and New York, NY, USA: Cambridge University Press), 3–33. doi: 10.1017/9781009325844.001

Ivčević, A., Bertoldo, R., Mazurek, H., Siame, L., Guignard, S., Moussa, A. B., et al. (2020). Local risk awareness and precautionary behaviour in a multi-hazard region of north Morocco. *Int. J. Disaster Risk Reduct.* 50, 101724. doi: 10.1016/j.ijdrr.2020.101724

Ivčević, A., Mazurek, H., Siame, L., Bertoldo, R., Statzu, V., Agharroud, K., et al. (2021). Lessons learned about the importance of raising risk awareness in the Mediterranean region (north Morocco and west Sardinia, Italy). *Nat. Hazards Earth Syst. Sci.* 21 (12), 3749–3765. doi: 10.5194/nhess-21-3749-2021

Jaaidi, E. B., and Cirac, P. (1987). La couverture sédimentaire meuble du plateau continental atlantique marocain entre larache et agadir. *Bull. Inst Géol Bassin d'Aquitaine* 42, 33–51.

Kasmi, S., Snoussi, M., Khalfaoui, O., Aitali, R., and Flayou, L. (2020). Increasing pressures, eroding beaches and climate change in Morocco. *J. Afr. Earth Sci.* 164, 103771. doi: 10.1016/j.jafrearsci.2020.103796

Khouakhi, A., Snoussi, M., Niazi, S., and Raji, O. (2013). Vulnerability assessment of Al hoceima bay (Moroccan Mediterranean coast): a coastal management tool to reduce potential impacts of sea-level rise and storm surges. *J. Coast. Res.* 65, 968–973. doi: 10.2112/SI65-164.1. ISSN 0749-0208.

Kumar, P., Debele, S. E., Sahani, J., Aragão, L., Barisani, F., Basu, B., et al. (2020). Towards an operationalisation of nature-based solutions for natural hazards. *Sci. Total Environ.* 731, 138855. doi: 10.1016/j.scitotenv.2020.138855

Laboratoire Central d'Hydraulique de France (1974). Aménagement de la baie de tanger. protection de la plage. avant-projet détaillé. *Première partie. Société d'Aménagement la Baie Tanger*, 62. Unpublished report.

Long, B. F., Bencheikh, L., Boczar -Karakiewicz, B., Merzouk, A., and Romanczyk, W. (1999). "Beach protection at tangier by beach nourishment (Gandori-harbour)," in *Canadian Coastal Conference.* (Rabat: Rapport pour le Ministère de l'Equipement. Direction des Ports et du Domaine Maritime). 637–652pp.

L.P.E.E. (1991). Études maritimes sur le littoral de tétouan (Maroc) : étude de circulation sur modèle mathématique au port de martil 20.

Mastrocicco, M., Gervasio, M. P., Busico, G., and Colombani, N. (2021). Natural and anthropogenic factors driving groundwater resources salinization for agriculture use in the campania plains (Southern Italy). *Sci. Total Environ.* 758, 144033. doi: 10.1016/j.scitotenv.2020.144033

Mclaughlin, S., and Cooper, J. A. G. (2010). A multi-scale coastal vulnerability index: a tool for coastal managers? *Environ. Hazards* 9 (3), 233–248. doi: 10.3763/ehaz.2010.0052

Ministère de la Transition énergétique et du Développement Durable. (2022). "Surveillance de la qualité des eaux de baignade," in *Rapport analytique. Édition 2022* (Rabat: Ministère de la Transition énergétique et du Développement Durable), 274p.

Moraes, R. P., Reguero, B. G., Mazarrasa, I., Ricker, M., and Juanes, J. A. (2022). Nature-based solutions in coastal and estuarine areas of Europe. *Front. Environ. Sci.* 10, 928. doi: 10.3389/fenvs.2022.829526

Mohamed Rashidi, A. H., Jamal, M. H., Hassan, M. Z., Mohd Sendek, S. S., Mohd Sopie, S. L., and Abd Hamid, M. R. (2021). Coastal structures as beach erosion control and sea level rise adaptation in Malaysia: a review. *Water* 13 (13), 1741. doi: 10.3390/w13131741

Nachite, D., El Moutchou, B., Anfuso, G., Benavente, J., Bello, E., and Macias, A. (2004). Morphologie et évolution récente du littoral entre fnideq et m'diq (Tétouan, NE du maroc). *Geogaceta* 35, 43–46.

Niazi, S. (2007). *Évaluation des impacts des changements climatiques et de l'élévation du niveau de la mer sur le littoral de tétouan (Méditerranée occidentale du maroc): vulnérabilité et adaptation* (Rabat, Morocco:Faculty of sciences. Mohammed V university in Rabat). PhD Thesis.

Nicholls, R. J., Wong, P. P., Burkett, V. R., Codignotto, J. O., Hay, J. E., McLean, R. F., et al. (2007). "Coastal systems and low-lying areas," in *Climate change 2007: impacts, adaptation and vulnerability. contribution of working group II to the fourth assessment report of the intergovernmental panel on climate change*. Eds. M. L. Parry, O. F. Canziani, J. P. Palutikof, P. J. van der Linden and C. E. Hanson (Cambridge, UK: Cambridge University Press), 315–57RGPH. 2014. Recensement Général de la Population et de l'Habitat. Royaume du Maroc, Rabat 2014.

Panayiotis, P., and Paraskevi, D. (2020). "Implementation of the legal framework for the management of the marine environment of the Aegean Sea," in *The handbook of environmental chemistry* (Berlin, Heidelberg: Springer). doi: 10.1007/698_2020_693

Peduzzi, P., Dao, H., Herold, C., and Mouton, F. (2009). Assessing global exposure and vulnerability towards natural hazards: the disaster risk index. *Natural hazards Earth system Sci.* 9 (4), 1149–1159. doi: 10.5194/nhess-9-1149-2009

Ramieri, E., Hartley, A., Barbanti, A., Santos, F. D., Gomes, A., and Hilden, M. (2011). Methods for assessing coastal vulnerability to climate change. *ETC CCA Tech. paper* 1, 1–93.

Rifai, N., Khattabi, A., Moukrim, S., Arahou, M., and Rhazi, L. (2018). Évaluation de la dynamique de l'occupation du sol dans la zone humide RAMSAR de tahaddart (Nord-ouest du maroc). *Rev. d'Ecologie Terre Vie* 73 (2), 142–152. doi: 10.3406/revec.2018.1922

Rochette, J., Magnan, A., and Billé, R. (2010). "Gestion intégrée des zones côtières et adaptation au changement climatique en méditerranée," in *Le développement durable dans l'espace méditerranéen : enjeux et propositions*. Eds. Y. Lazzeri and E. Moustier (L'Harmattan), pp.99–pp120. Available at: https://www.torrossa.com/en/publishers/lharmattan.html.

Salhi, A., Martin-Vide, J., Benhamrouche, A., Benabdelouahab, S., Himi, M., Benabdelouahab, T., et al. (2019). Rainfall distribution and trends of the daily precipitation concentration index in northern Morocco: a need for an adaptive environmental policy. *SN Appl. Sci.* 1, 1–15.

Sarkar, N., Rizzo, A., Vandelli, V., and Soldati, M. (2022). A literature review of climate-related coastal risks in the Mediterranean, a climate change hotspot. *Sustainability* 14 (23), 15994. doi: 10.3390/su142315994

Satour, N., Raji, O., El Moçayd, N., Kacimi, I., and Kassou, N. (2021). Spatialized flood resilience measurement in rapidly urbanized coastal areas with a complex semi-arid environment in northern Morocco. *Nat. Hazards Earth Syst. Sci.* 21, 1101–1118. doi: 10.5194/nhess-21-1101-2021

Satta, A. (2014). "*An index-based method to assess vulnerabilities and risks of Mediterranean coastal zones to multiple hazards*," in Doctoral dissertation submitted in October 2014 (Venice, Italy: Department of Economics at Ca' Foscari University).

Satta, A., Puddu, M., Venturini, S., and Giupponi, C. (2017). International journal of disaster risk reduction assessment of coastal risks to climate change related impacts at the regional scale: the case of the Mediterranean region. *Int. J. Disaster Risk Reduct.* 24, 284–296. doi: 10.1016/j.ijdrr.2017.06.018

Satta, A., Snoussi, M., Puddu, M., Flayou, L., and Hout, R. (2016). An index-based method to assess risks of climate-related hazards in coastal zones: the case of tetouan. *Estuar. Coast. Shelf Sci.* 175, 93–105. doi: 10.1016/j.ecss.2016.03.021

Sedrati, M., and Anthony, E. J. (2007). Storm-generated morphological change and longshore sand transport in the intertidal zone of a multi-barred macrotidal beach. *Mar. geology* 244 (1-4), 209–229.

Sedrati, M., and Anthony, E. J. (2009). A brief overview of plan-shape disequilibrium in embayed beaches: tangier bay (Morocco). *Méditerranée* 108, 2007. doi: 10.4000/mediterranee.190

Sergent, Ph., Prevot, G., Mattarolo, G., Brossard, J., Morel, G., Mar, F., et al. (2015). Adaptation of coastal structures to mean sea level rise. *La Houille Blanche* 2014 (6), 54–61. doi: 10.1051/lhb/2014063

Snoussi, M., and Long, B. (2002). Historique de l'évolution de la baie de tanger, in : Érosion littorale en méditerranée : dynamique, diagnostic et remèdes. *CIESM Workshop Ser.*, 39–42.

Snoussi, M., Ouchani, T., Khouakhi, A., and Niang-Diop, I. (2009). Impacts of sea-level rise on the Moroccan coastal zone: quantifying coastal erosion and flooding in the tangier bay. *Geomorphology* 107, 32–40. doi: 10.1016/j.geomorph.2006.07.043

Snoussi, M., Ouchani, T., and Niazi, S. (2008). Vulnerability assessment of the Moroccan coastal zone to the impacts of sea-level rise: the case of the Eastern Mediterranean coast. *Estuar. Coast. Shelf Sci.* 77, 206–213. doi: 10.1016/j.ecss.2007.09.024

Taouati, M., Nachite, D., Benavente, J., and Elmrini, A. (2011). Seasonal changes and morphodynamic behavior of a high-energy mesotidal beach: case study of charf el akab beach on the north Atlantic coast of Morocco. *Environ. Earth Sci.* 64, 1225–1236. doi: 10.1007/s12665-011-0937-8

Torresan, S., Critto, A., Rizzi, J., and Marcomini, A. (2012). Assessment of coastal vulnerability to climate change hazards at the regional scale: the case study of the north Adriatic Sea. *Natural Hazards Earth System Sci.* 12 (7), 2347–2368.

Torresan, S., Furlan, E., Critto, A., Michetti, M., and Marcomini, A. (2020). Egypt's coastal vulnerability to sea level rise and storm surge: present and future conditions. *Integr. Environ. Assess. Manage.* 16, 761–772. doi: 10.1002/ieam.4280

TTA Region Statistical Yearbook. (2018). The annual statistical bulletin of the Tangier-Tetouan-Al Hoceima region for 2018. Haut-Commissariat au Plan (in arabic). Available at: https://www.hcp.ma/reg-alhoceima/attachment/1868511/.

UNEP/MAP/PAP. (2015). Guidelines for adapting to climate variability and change along the Mediterranean coast. split. *Priority Actions Programme*, 70.

United Nations. (2015). *Sendai Framework for disaster risk reduction 2015–2030*.

Wahbi, M., Boulaassal, H., Maatouk, M., El Kharki, O., and Yazidi Alaou, O. (2019). Dynamique de l'artificialisation des surfaces de la ville de tanger à partir des images spot et sentinel 2. Scientific conference on coastal risks, Rabat. Available at: https://www.scolamar.com/fr/conference-rabat-wahbi.pdf.

Zhou, Y., Liu, Y., Wu, W., and Li, N. (2015). Integrated risk assessment of multi-hazards in China. *J. Nat. Hazards* 78, 257–280. doi: 10.1007/s11069-015-1713-y

Present and future flooding and erosion along the NW Spanish Mediterranean Coast

Xavier Sánchez-Artús[1]*, Vicente Gracia[1], Manuel Espino[1], Joan Pau Sierra[1], Jordi Pinyol[2] and Agustín Sánchez-Arcilla[1]

[1]Laboratori d'Enginyeria Marítima (LIM), Departament d'Enginyeria Civil i Ambiental (DECA), Universitat Politècnica de Catalunya (UPC), Barcelona, Spain, [2]Institut Cartogràfic i Geològic de Catalunya, Unitat de Processos Actius i Servei d'Informació de Riscos Geológics (SIRG), Barcelona, Spain

Coastal flooding and eros-ion caused by extreme events are the main factors responsible for beach hazards. This effect will be exacerbated by the sea level rise induced by climate change. The present work determines the vulnerability to erosion and flooding along 55 beaches grouped in different coastal archetypes, representative of the Catalan coast. The vulnerability assessment has been done through the numerical simulation of different combinations for projected waves and mean water levels under present conditions and the climate change scenarios RCP4.5 and RCP8.5 for the year 2100. A storm event approach has been used to determine coastal flooding and erosion with return periods of 50, 100, and 500 years using the XBeach numerical model. Results show that shoreline retreat is not the best proxy to characterize the erosion. The low-lying nature of the coast, the non-presence of well-developed berms, and the existence of river mouth and torrents govern the coastal flooding. The sea level rise appears to be a dominant variable in coastal hazards.

KEYWORDS

climate change, XBeach, flooding, erosion, sea level, modeling, sandy beaches

1 Introduction

Climate change and its associated sea level rise are expected to increase the risk of flooding in coastal regions (Zhang et al., 2004; Nicholls et al., 2007; Condon and Peter Sheng, 2012) where much of the population is concentrated (Nicholls and Misdorp, 1993; Small and Nicholls, 2003) and an important portion of the global gross domestic product is produced (Turner et al., 1996; Nordhaus, 2006). In Europe, about 13 million people would be threatened by coastal flooding (Nicholls and Klein, 2005). According to Hinkel et al. (2010), the Mediterranean coast appears to be one of the most vulnerable regions due to the rapid growth of the coastal population and the boom of tourism, which has become an important economic driver (P. B. UNEP and MAP, 2016). This surge in population is the primary cause of the coastal landscape reshaping, with the occupation of the first hundreds of meters in front of beaches by houses and associated transport infrastructures. In these areas, coastal flooding and erosion have significant economic consequences (Gracia and

Jiménez, 2004; Sánchez-Arcilla et al., 2014; García-León et al., 2015) and beaches represent the last natural defense.

Coastal vulnerability at a regional scale, here understood as of hundreds of kilometers, is commonly assessed by the definition of vulnerability indices. Roukounis and Tsihrintzis (2022) present a critical review of such approach. The use of an index requires the simplification of the problem through the selection of few fundamental variables, which roughly reflects the specifications of the analyzed coastal stretch but permits a regional view of the hazard. Coastal flooding and erosion indices are typically parameterized by wave energy and run-up, mean water level, and the morphological characteristics of the area such as land elevation and emerged beach slope [(Ozyurt et al., 2008; Bosom and Jiménez, 2011a; Yin et al., 2012; Tatui et al., 2019) among many others] The common metrics used are the shoreline retreat and the temporary inundated area (Ranasinghe, 2016a; Ranasinghe et al., 2021). However, the real detailed magnitude of such hazards depends not only on the existing hydrodynamic forcing but also on the interactions with the existing beach morphology, which are not usually reflected in the aggregated indices.

The development of numerical models has allowed us to obtain a detailed description of coastal flooding and erosion and has been applied at the local scale by many authors [e.g (Martinelli et al., 2010; Villatoro et al., 2014; Barnard et al., 2019; Orejarena-Rondon et al., 2019), among many others] There are few examples in which numerical models have been used on a regional scale or global scale (Athanasiou et al., 2019; Agulles et al., 2021). Ranasinghe (2016b) pointed out the inability of models to provide sufficient reliable predictions that integrate climate change effects. A solution for that conundrum is the characterization of the hazards induced by episodic events with a predefined time horizon (Li et al., 2014; Ranasinghe and Callaghan, 2017; Ranasinghe et al., 2021). However, the computational costs that such numerical approach requires when dealing with large coastal stretches have prevented them from being widely used. A simplification of such complexity is the use of the coastal archetype concept (Sánchez-Arcilla et al., 2016a; Haasnoot et al., 2019), i.e., a coastal stretch that shares some morphohydrodynamic and land use commonalities. The use of coastal archetypes allows researchers to catch the 2D effects over the hydrodynamics and morphodynamics by incorporating spatial changes in the bathymetry and topography.

The goal of this article is to determine the coastal vulnerability to flooding and erosion at a regional scale under extreme events with return periods of 50, 100, and 500 years for present, RCP4.5, and RCP8.5 scenarios (IPCC, 2022). The analysis is performed along the Catalan coast for a set of selected coastal archetypes representative of a highly urbanized littoral. The use of coastal archetypes permits the identification of coastal response patterns making the results much more extrapolated to other coastal stretches. This work is organized as follows: *Section 2* presents the study area and presents hydrodynamic conditions, future climate for RCP8.5 scenarios, and the modeling framework. *Section 3* shows the erosion and flooding results by extracting the coastal response patterns. Finally, *Section 4* summarizes the main conclusions of the work.

2 Materials and methods

2.1 Study area

The Catalan coast, an autonomous region located at the northwestern Spanish Mediterranean, is about 920 km long. It comprises a wide variety of coastal types from sandy and gravel beaches, cliffs, to armored coastal stretches. During the last decades, it experienced an intense urban development (Jiménez et al., 2012; Jiménez et al., 2017). The present coastal socioeconomic activities in the area, similar to other Mediterranean highly developed regions, are mainly governed by commerce, tourism, agriculture, and residential housing (Sardà et al., 2005) that have shaped the current coastal landscape.

We select a series of beaches trying to fulfill the whole diversity of coastal archetypes, as described in (Sánchez-Arcilla et al., 2016b; Haasnoot et al., 2019), present at the Catalan region. They go from low-lying to high coasts and from semi-natural environments to urban beaches, where the vast majority of population and economic activities are situated. Moreover, we define the studied beaches following the criterion for the littoral cells described in (CIIRC, 2010). We group the beaches with this standard in nine different sections, covering the three littoral provinces of Catalonia (Tarragona, Girona and Barcelona). We split some of these sections in the simulation process to reduce computational time due to grid density, but to show the results in a graphical way, they were combined again. We use data from (CIIRC, 2010) to obtain the granulometry. A representative sample was taken at the center of each beach near the shoreline and subjected to analysis in a laboratory setting. The sediment was washed, dried, and then separated through a mechanical sieve. The granulometric parameters were obtained using the Gradistat software (Blott and Pye, 2001). Table 1 shows the basic characteristics of the analyzed beaches. We consider a total of about 58 km of coast covering 55 different beaches. We define the sediment as uniform and uni-layered since the entire area is occupied by sand with non-cohesive sediment observed.

We denominate the units using the same criterion as (CIIRC, 2010) to make our results comparable and establish a correlation between both studies. Unit 4, at the south, corresponds to the coastal stretch from Vandellòs harbor to Hospitalet Infant-Salou. The main use is recreational tourism with a high-medium rate of occupation. It is surrounded by urban cores with some natural areas. The municipalities have reported some sediment loss problems and occasional damages on the promenade and the beach furniture associated with extreme events. Unit 7 includes some representative beaches of the Cubelles-Garraf littoral cell. It is mainly a recreational area with an intensive degree of occupation with the back beach covered by secondary houses, campsites, and some industrial areas. The reported problems are mainly related to the general loss of emerged beach surface, which has forced the administration to nourish some coastal sections when the emerged width is very narrow. Unit 8, from Ginesta harbor to Barcelona harbor, shares a recreational use with a semi-natural landscape with a low degree of occupation. Again, problems related to loss of

TABLE 1 Description of the studied units.

Provinces	Littoral cell name	Cell number (CIIRC, 2010)	Length of sandy beaches (m)	Mean emerged beach width (m)	Number of sandy beaches	D50 (mm)	Coastal Description
Tarragona	H. Infant Salou harbor–Salou	4	5,173	49.2	5	0.5	Long open low-lying coast with wide emerged beach width and a seafront promenade with a street and secondary houses at the backshore.
Barcelona	Cubelles harbor–Garraf	7	3,002	27.4	10	0.2	Short compartmentalized narrow beaches by breakwaters with a high seafront promenade with a street and secondary houses. Both ends are low-lying.
	Port Ginesta–Port Barcelona	8	16,843	126.4	5	0.2–0.35	Deltaic urbanized coast with some torrents (ancient courses) and very wide beaches with a seafront promenade and secondary houses.
	Barcelona city	9	1,695	59.5	2	0.5	Urban compartmentalized coast with coastal infrastructures. Low-lying at the south and with a high seafront promenade at the North. Limited by ports at both ends and by commerces at the back.
	Badalona harbor–Masnou harbor	10	3,338	34.6	9	1	Long open wide beaches with a seafront promenade. Land at the back moderately high and crossed by some torrents. Road and railway at the backside.
	Masnou harbor–Premià harbor	11	2,850	100	1	1	Open coast with a very wide beach leaning at the south in a marina and crossed by several torrents. Road and railway in the backside defended by a revetment.
	Arenys harbor–Blanes harbor	15	12,587	57.4	12	1.3	Long exposed beaches mostly wide crossed by torrents and with a small river delta at the North. Semi-urbanized with agriculture land in some areas and with a road and railway in the backside defended by a revetment.
Girona	Blanes harbor–Llosa des Llevador	16	2,990	38	2	1.3	Urban narrow beaches with a river mouth at the south and land moderately high with a seafront promenade.
	Tamariu beach–Salou	19	9,105	67.7	9	0.3	Natural low-lying coast with very wide beaches with a river mouth at the center and a well-developed fore-dune at the South. Slightly urbanized. Mostly wave exposed.
	TOTAL		57,583		55		

sediments are reported added to some coastal flooding events during storms, especially at two active torrents. The emerged beach slope is gentle at the south of the unit with values ranging from 0.06 to 0.1 and steep values up to 0.2 at the north, which indicates a protection of the shoreline against energetic waves. At the south, the east–west shoreline orientation is less exposed to the most energetic wave conditions from the east whereas the northern sector with a northeast–southwest orientation is fully exposed to wave action. Unit 9 is an example of urban compartmentalized coast with coastal infrastructures (Barcelona). It is a low-lying coast at the south with a high seafront promenade at the north, limited by ports at both ends with commerces at the back. The area also presents high damages to the promenade and beach infrastructures when huge storm events appear. Unit 10 covers Badalona harbor to Masnou harbor. This is constituted by long open wide beaches with a seafront promenade. The land at the back is moderately high and the beaches are crossed by some torrents. A main road and railway

are present next to the beach. The ministry has intervened occasionally in the area after the impact of severe storms; however, no coastal flooding events have been reported. A uniform emerged beach slope up to 0.25 exists together with a well-developed high berm. Unit 11, from Masnou harbor to Premià harbor, is represented by a single exposed beach, very wide, leaning at the south in a marina and crossed by several torrents. A road and a railway at the back is defended by a revetment. It presents steep slopes of 0.21–0.25 with a berm up to 1.51–2 m. This beach is fully recreational with an intense–moderate occupation and some problems of loss of beach width at the northern side. Unit 15 corresponds to Arenys harbor–Blanes harbor and is an example of long exposed beaches, mostly wide crossed by torrents and limited with a small river delta at the north. This is a semi-urbanized coast with agriculture land at the back and with a road and a railway defended by a revetment. This coastal stretch shows an intense degree of occupation sharing urban cores with industrial,

agricultural, and natural areas. The emerged beach shows steep slopes up to 0.25 with again well high-developed berms indicating the existence of coarse sediment and important beach widths. No significant flooding events are reported. Unit 16, corresponding to Blanes harbor until Llosa des Llevadors, is an urban narrow coast with a river mouth at the south and moderately high lands at the north occupied by a seafront promenade. Severe coastal flooding episodes are reported at the north close to the Tordera river mouth (Gracia and Jiménez, 2004). Finally, Unit 19, from Tamariu beach to Escala harbor, is an example of a natural low-lying coast with very wide beaches and a river mouth at the center with a well-developed fore-dune at the south. The area is slightly urbanized and mostly exposed to wave action. The slope in this area is gentle, with values ranging from 0.05 to 0.1. Figure 1 shows the location of the analyzed units.

2.2 Present conditions and future climate

We aim to study the problems for both present and possible future climate change scenarios. To do so, we use the years 1985–2005 as reference for the actual state, defining the associate hydrodynamic conditions; meanwhile, in order to test climate change scenarios, we select the period from 2081 to 2100. This range represents long-term projections where we test different scenarios following Intergovernmental Panel on Climate Change (IPCC) predictions, which are called Representative Concentration

Pathways (RCPs) (IPCC, 2022). First, we study RCP4.5, a scenario which establishes a stabilization of the greenhouse gases to 650 ppm at the second half of the century, among other variables (Thomson et al., 2011). Then, we also cover the worst and most aggressive predictions, which represent the RCP8.5. This scenario assumes that there will be a continuation in the use of fossil fuels, together with an increment of the greenhouse gas emissions without implementing mitigation actions (Schwalm et al., 2020).

The three selected scenarios (actual, RCP4.5, and RCP8.5) have been combined with the conditions of representative storms with associated return periods (hereinafter RP) of 50, 100, and 500 years resulting in nine different states for each study case. We define the storm wave regime using data developed by "Instituto de Hidráulica Ambiental de Cantabria" (IHC) in the framework of the project "Elaboración de la metodologia y bases de datos para la proyeccion de impactos de cambio climático a lo largo de la costa española" granted by Ministerio para la Transición Ecologica (MITECO) (IH Cantabria, 2019). It can be accessed *via* a server at http://thredds.ihcantabria.com/PRME/catalog.html. The wave data are organized into nodes spaced 0.08° apart, covering the entire study area. The selected hydrodynamic parameters, including significant wave height, peak period, and direction, are recorded hourly in the database and used to calculate the extreme regime of each node using the Peak Over Threshold (POT) method (Ferreira. and Soares, 1998) for both current and projected conditions, as derived from various climatic models.
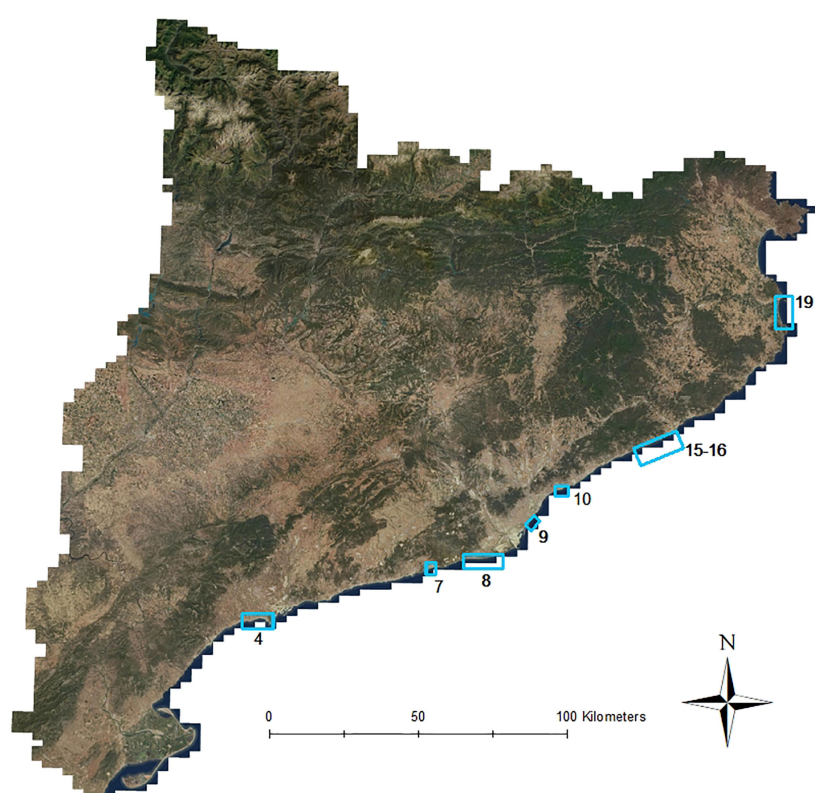

FIGURE 1
Map of Catalonia. Blue rectangles represent the different study units.

To define when we consider that a storm starts, we select a threshold value of 2 m (Bosom and Jiménez, 2011b) for the wave height. Then, to guarantee that the event is a real storm, in some moment, the wave height has to reach 2.3 m, what we call minimum threshold for extreme events. Finally, to take only the storms that are considered extreme and that are important for our analysis, we define a threshold for extreme events, which in our case is 2.6 m. With the parameters corresponding to the data that meet these conditions, we fit a probability distribution using Weibull and Gumbel for the methods of maximum likelihood, momentum, and least squares (Goda, 1988; Castillo and Sarabia, 1994; Coles, 2001). To guarantee a minimum of values in the fit, we do not take into account the wave direction, following a scalar approach for the extreme analysis. Then, we define the coefficients of directionality to better reproduce the fit for these directions. In the next step, we select the central band of the fit to take the values of the wave height for the different RPs. Finally, we choose the best fits for each node and climate model, with the final values being representative of the ensemble of all values. We match the periods using an exponential fit of the form Tp = a*Hs*b, where Tp is the Peak Period and Hs is the Significant Wave Height. We pick the final conditions as the ones that follow the pattern of the highest Hs with the most perpendicular direction to the coast on deep waters.

For the definition of the mean water level (MWL), two processes have been considered: first, the meteorological tide or storm surge, which has been fixed to 0.3 m for all cases and scenarios since the analyzed conditions are storms and the local punctual increase of the level is considered invariable (Bolaños et al., 2009; Lin-Ye et al., 2020); second, the sea level rise (SLR), induced by climate change, that we set to 0.55 m (ranging from 0.39 to 0.72 m) for the RCP4.5 scenario and 0.84 m (ranging from 0.6 to 1.1 m) for the RCP8.5 scenario, following the recommendations proposed by the "Oficina Catalana del Canvi Climatic" (OCCC) (Generalitat de Catalunya, 2016; IPCC, 2022). The combination of both processes results in three different MWL conditions, which are 0.3 m for the present state, 0.85 m for the RCP4.5 scenario, and 1.14 m for the RCP8.5 scenario.

2.3 Modeling

The hydromorphodynamical model XBeach was selected for this study. It is a two-dimensional model that allows one to study wave propagation, sediment transport, and morphology changes on beaches, among others (Roelvink et al., 2010; McCall et al., 2014). For the study area of this work, the model has been previously validated in (Gracia et al., 2013; Sanuy and Jiménez, 2019; Grases et al., 2020). The needs of the model include information based on the topobathymetry of the study area as well as the wave characteristics of the simulated event. We generate the different grids using the same methodology for all the study cases, combining topography and bathymetry from different resources. For the topographies, Institut Cartogràfic i Geològic de Catalunya (ICGC) provides a 5 × 5-m-resolution Digital Elevation Model (DEM) while the bathymetries are generated from digitization of high-resolution

screenshots taken from nautical charts of the web page "Navionics" using Geographic Information Systems (GIS) software. The combination of both derives in a 10 × 10-m-resolution grid whose resulting files are modified to have the correct XBeach formats. With these conditions, the final mesh begins at a depth of 30 m for the offshore limit, which is sufficient for the model to function optimally. We complete the model setup with the parameters extracted in *Section 2.2*, finally referencing the data in ETRS89 coordinate system to easily represent the results on the resources provided by ICGC.

For each study area, we simulate the nine different scenarios, one for each combination of 50, 100, and 500 years of RP and the mean water level corresponding to present or future conditions. The study considers storms as a 12-h duration event with constant characteristics, helping to reduce computational time while focusing on the peak of the storm, which corresponds to the point of highest impact (Mendoza and Jiménez, 2008; Mendoza et al., 2011). Since the increase of simulation velocity is a crucial factor, we use the Message Passing Interface (MPI) module from XBeach, which allows one to parallelize the code and simulate with simultaneous processors, which is four in our case (Clarke et al., 1994; Rautenbach et al., 2022). This strategy helps to speed up the process, resulting on an average computational time of 1 h per case, while if serial computing was used, the average time could go up to 5–6 h per case. We visually represent coastal flooding as polygons generated from the results of the model that contain the wet zones, i.e., the inundated areas, of the simulated domains during the event. The model sometimes classify low levels as flooded when it is not true due to errors on the definition of the output variables combined with the structure of the grid, so we decide to only count a point as wet when it surpasses 0.005 m of water level for the node. Moreover, to deem an area as inundated, we also determine that the point of the grid has to be considered wet by the model for more than 4 h over all the 12-h simulation as seen in Equation 1. This decision relies on the fact that once the model detects that the water touches a cell even if it is only a few centimeters, all the 10 × 10 m node is considered flooded. With this strategy, we expect to minimize these situations of false positives and only represent those areas that remain inundated for extended periods.

$$\sum_{t=1}^{t=12} wet_{i,j,t} > 4s \qquad (1)$$

On the other hand, we represent erosion in terms of coastline retreat. Since we only study the storm event, for the present scenarios, we fix the reference level of the coastline to 0.3 m due to the storm surge effect. Then, for the simulations involving climate change scenarios, we redefine the coast baseline to reflect the levels associated with the SLR and the storm surge, which are 0.85 m and 1.14 m, respectively, for RCP4.5 and RCP8.5. The coastline retreat is characterized as the difference between this level and the final position of the same line at the end of the event. The comparison between final state coastlines between different simulated scenarios is also treated as changes in the coastline retreat.

Finally, we present the visualization of the results in a graphical way through a viewer developed by Institut Cartogràfic i Geològic

de Catalunya (ICGC). The web viewer https://visors.icgc.cat/PIMA-AdaptaCostas/includes part of the vector information prepared for the PIMA Adapta Costas project. The objective of the web viewer is to make cartographic information available to the public about the impacts of coastal dynamics on the coast of Catalonia, including climate projections that take climate change into account. The information is organized in tabs, the content of which is internally structured in layers. Among other interesting information from other studies, the results obtained from this paper can be accessed through the "Escenarios" tab, going to "Inundación por oleaje" for the flooding results and "Línea de la costa final despues de un temporal de 12 horas" for the erosion. Then, all the combinations of scenarios presented in the study can be selected and visualized into the map. Background cartography, both topographic and hybrid orthophoto, are ICGC own products for Catalonia and OSM for the rest of the world.

3 Results and discussion

3.1 Flooding

Following the methodology described in *Section 2.3*, we perform an analysis of the inundation for all the nine different scenarios, combining storms and sea level rise, but to easily compare, define patterns, and better understand the figures, we decide to show only the results for the lowest and highest RPs (50 and 500 years) combined with the actual conditions and the worst scenario corresponding to RCP8.5. From now to the end of this section, the figures match the color light blue to actual conditions and 50 years of RP, dark blue to actual conditions and 500 years of RP, light lilac to RCP8.5 and 50 years of RP, and dark lilac to RCP8.5 and 500 years of RP. We classify the units depending on the impacts we observe, creating three different groups.

3.1.1 Low-flooded beaches

We consider in this group beaches that do not experience flooding impacts regardless of the scenario. Figure 2 corresponds to Unit 10 where we observe little changes depending on the scenario but none of them represents a serious risk of flooding. This matches with the expected results regarding the information provided in *Section 2.1* where the coast is classified as high with steep slopes and a well-developed berm, and no episodes of flooding were reported. We can also observe a little bit of inconsistency on the matching between the coastline and the flooding polygons. This will happen through all the cases because the orthophoto was not taken at the same time as the topobathymetry. Moreover, it is highly difficult for the interpolation through the grid generation to fit perfectly with the baseline. In Figure 3, we observe Unit 11. As with the previous one, although some changes are observed, the areas of interest corresponding to the whole beach environment and the promenade are unaffected. Again, we detect consistency related to
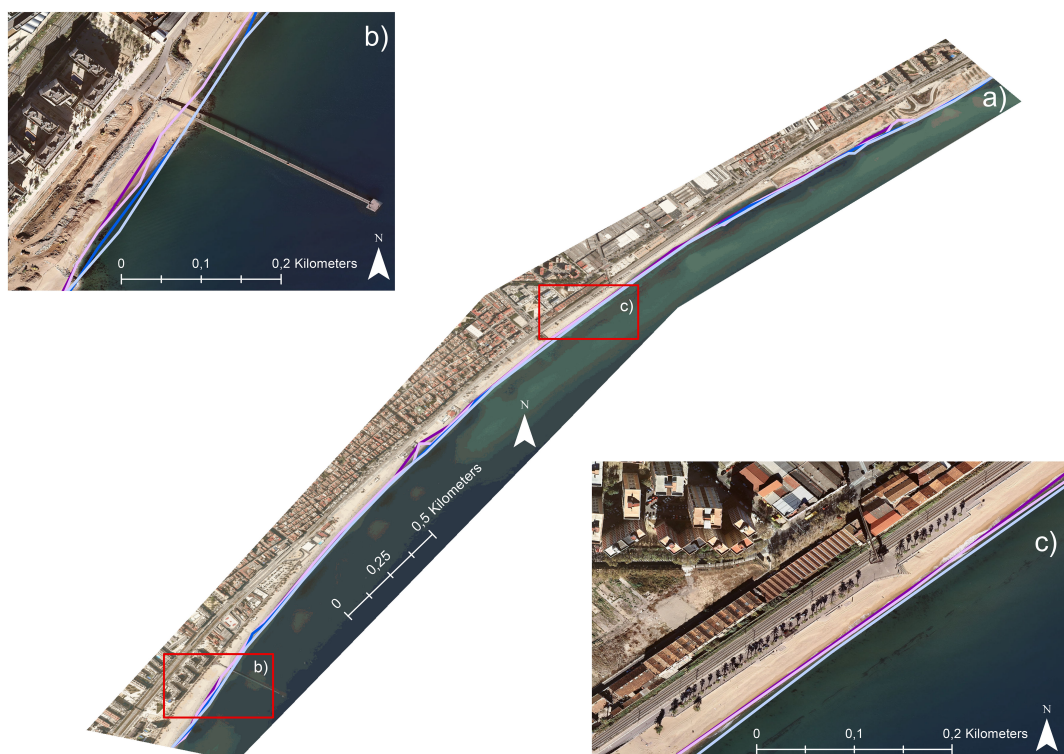
FIGURE 2
Flooding lines distribution of Unit 10. **(A)** General view of the unit. **(B, C)** Close-up view. Light blue = actual conditions, RP = 50 years; dark blue = actual conditions, RP = 500 years; light lilac = RCP8.5, RP = 50 years; and dark lilac = RCP8.5, RP = 500 years.
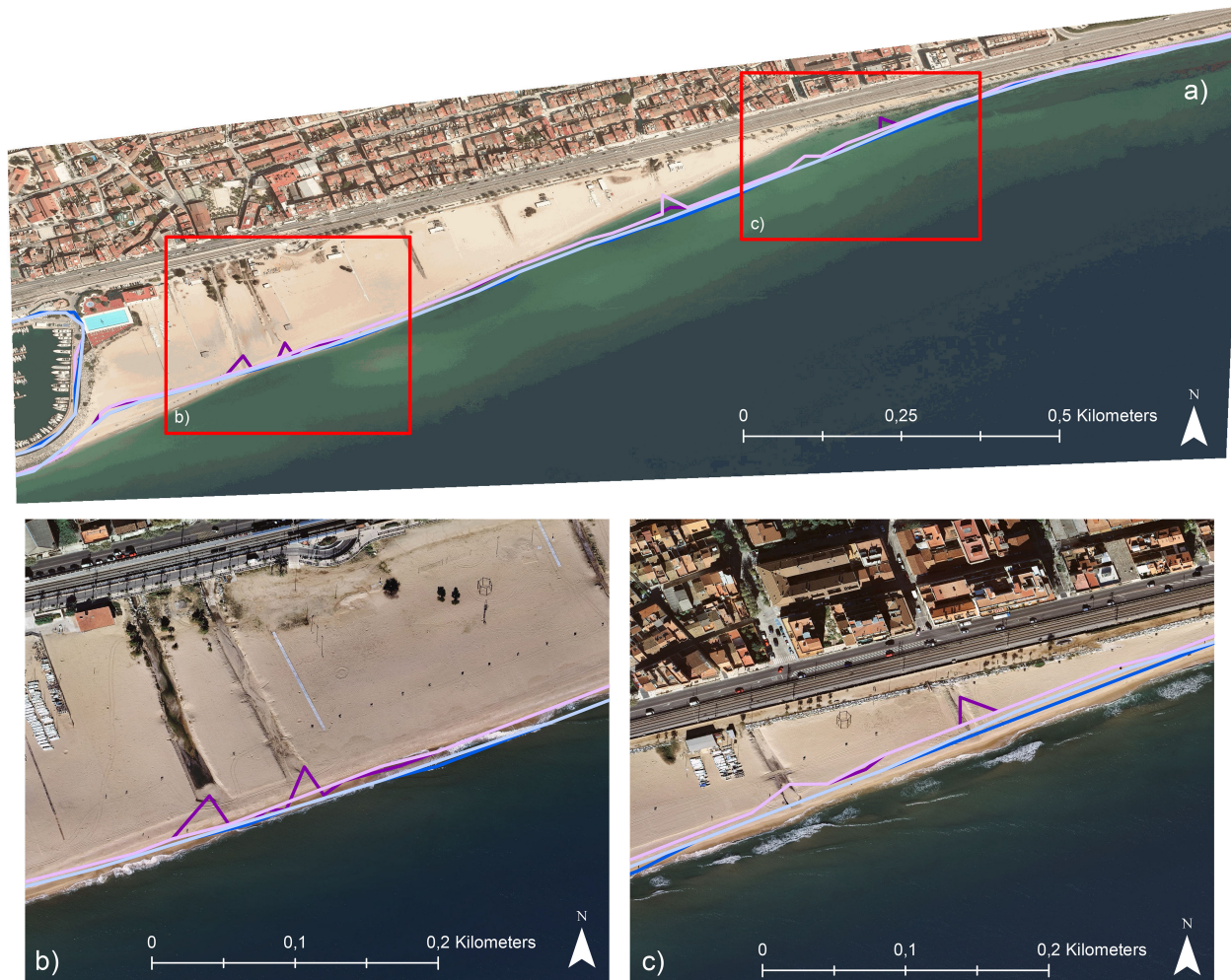
FIGURE 3
Flooding lines distribution of Unit 11. **(A)** General view of the unit. **(B, C)** Close-up view. Light blue = actual conditions, RP = 50 years; dark blue = actual conditions, RP = 500 years; light lilac = RCP8.5, RP = 50 years; and dark lilac = RCP8.5, RP = 500 years.

the description of the unit where a well-developed berm together with high slopes stops the water from inundating the area. Finally, in Figure 4, we see the section corresponding to Units 15 and 16, and in this case, although we divided this section into subsections to correctly generate hydrodynamic conditions and optimize computational time when simulating, we show the units together as they are correlated. We observe the same low impacts for the beach environment, and once more, these areas present well-developed berms and steep slopes that can reduce the energy of the waves and reduce the flooding hazards. Specifically for the northern part of Unit 16, which corresponds to the northern part of Figure 4, flooding areas can be observed as described in *Section 2.1*. We also find a pattern that will be consistent for all the sections with these characteristics. When a river mouth is present as in this case (corresponding to La Tordera), the sea water enters the river. As we increase the sea level, this effect becomes more relevant.

Generally, in the presented units, the same pattern has been observed where all of them are high coasts, due to steep slopes and to well-developed berms preventing the water to enter many meters into the beaches. Moreover, and as it can also be observed in Table S1

of the Supplementary Materials, climate change has a higher flooding effect than the intensity of the storm for these areas.

3.1.2 Medium-flooded beaches

We consider in this group beaches that experience flooding impacts at the beach but the promenade remains intact or barely impacted. In Figure 5, we see Unit 8. With the present conditions, the impacts are not important, but when we simulate the climate change scenarios, practically all the beach is inundated, turning sea level rise as the main variable responsible for major flooding events in this region (see Table S1). We do not classify this unit as highly flooded because the water is unable to reach the promenade. As described in *Section 2.1*, some coastal flooding events were reported and the southern part presents gentler slopes than the northern part, matching with our observation of the simulations where we see less flooded area at the upper part. The presence of vegetated dunes at the back of the beach that can be easily visualized in Figure 5 produces changes on the topography that may lead to the stop of the water before the promenade. Also, in this section, we observe the pattern of the river mouth explained in *Section 3.1.1* four more

FIGURE 4
Flooding lines distribution of Units 15 and 16. **(A)** General view of the unit. **(B, C)** Close-up view. Light blue = actual conditions, RP = 50 years; dark blue = actual conditions, RP = 500 years; light lilac = RCP8.5, RP = 50 years; and dark lilac = RCP8.5, RP = 500 years.


FIGURE 5
Flooding lines distribution of Unit 8. **(A.1, A.2)** General views of the unit. **(B)** Close-up view. Light blue = actual conditions, RP = 50 years; dark blue = actual conditions, RP = 500 years; light lilac = RCP8.5, RP = 50 years; and dark lilac = RCP8.5, RP = 500 years.

times. Figure 6 corresponds to Unit 4 and follows the same pattern with climate change having the highest impact on the flooded area as can be also observed in Table S1. The unit is characterized in Table 1 as low-lying; this has gentle slopes, and for this reason, both the storm event and even more the increase of the sea level affect a lot of the beaches. Furthermore, the northern part of the unit has a highly flooded area even entering the city for the worst scenarios. Checking the slopes published in (CIIRC, 2010),we observed that this is one of the beaches with less inclination on the unit, giving strength to the fact that it is the most affected.

3.1.3 Highly flooded beaches

We consider in this group beaches that experience flood impacts both at the beach itself and at the promenade or even inside the city or village. The Barceloneta beach, corresponding to Unit 9 (Figure 7), with present conditions experiences flooding during severe episodes as described in *Section 2.1*. This situation has also been reported for extreme events such as the Gloria storm (year 2020) (Sancho-García et al., 2020; De Alfonso et al., 2021). Its low-lying nature and the high level of urbanization imply that when climate change scenarios are simulated, the resulting flooding area is much higher due to the fact that the rigid bottom (the urban area) is reached, and there is less sediment available to create a submerged

bar that would lessen the impact of incoming waves. Furthermore, the low elevation of the backshore makes it easier for water to advance, allowing the waves to reach the urban non-erodible bottom, inducing a much more inundated surface that can extend up to 200 m inland. When analyzing the flooding within the storm, it can be seen that sea water enters, as expected, through the lowest points of the emerged beach and backshore, finally resulting in a complete homogeneous inundated area. Table S1 supports these interpretations as it can be seen from the flooded area under the highly energetic storm in the unit, which reaches all the beach and even beyond for all scenarios. Additionally, it can be seen how the problem will worsen with the rise of MWL, and even less intense storms will cause more damage. Unit 19 (Figure 8) presents the highest impact of all the studied cases. In the present conditions, we do not observe heavy impacts, but when climate change conditions are induced, the low-slope component of the area, together with the absence of a high promenade or any barrier that would prevent water from entering the land, results in an intense flooding rate, as seen in Unit 9, but in this case, the flat backshore is due to the presence of campsites and farmlands (see Table S1). The unique area where no flooding is present corresponds to the southern part that coincides with the presence of a well-developed fore-dune as stated in *Section 2.1*. Moreover, the preferential path of the water
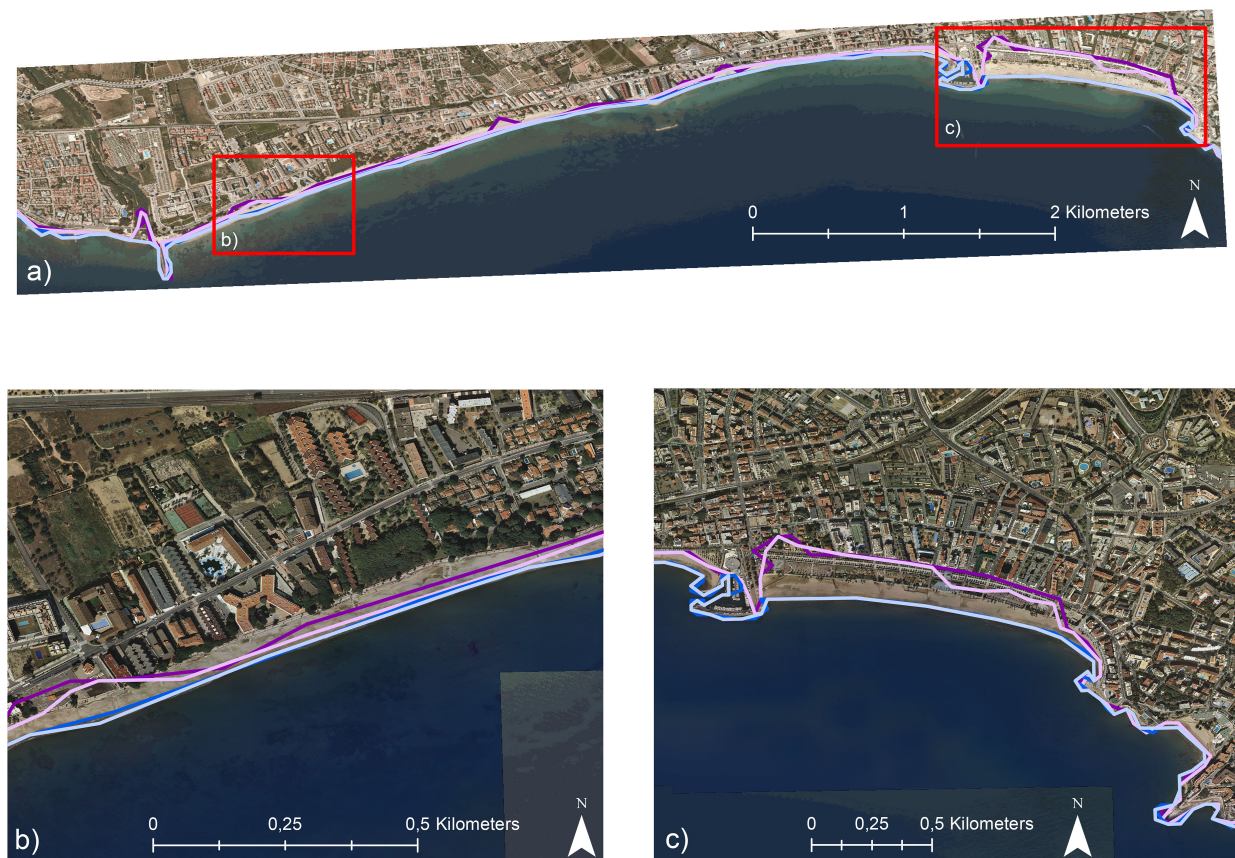
FIGURE 6
Flooding lines distribution of Unit 4. **(A)** General view of the unit. **(B, C)** Close-up view. Light blue = actual conditions, RP = 50 years; dark blue = actual conditions, RP = 500 years; light lilac = RCP8.5, RP = 50 years; and dark lilac = RCP8.5, RP = 500 years.

FIGURE 7
Flooding lines distribution of Unit 9. **(A)** General view of the unit. **(B, C)** Close-up view. Light blue = actual conditions, RP = 50 years; dark blue = actual conditions, RP = 500 years; light lilac = RCP8.5, RP = 50 years; and dark lilac = RCP8.5, RP = 500 years.

through the mouth rivers is also observed in this unit. Finally, in Unit 7 (Figure 9), a great part of the area could be classified as medium-flooded since the water stops at the seafront and does not enter the city, which is consistent with the explanation given in Table 1, classifying the coast as narrow with high promenades. However, the description also states that the ends of the beaches are low-lying, and as we can see in Figure 9, one of these zones presents the highest inundated ratio, with the water entering the city. This situation led us to finally classify the unit as highly flooded beaches.

To summarize, the units categorized in this section are characterized by a low-lying coast with a flat backshore, which permits water to enter the land. These units lack any form of developed berm and feature gentle slopes. Despite the fact that the storms in the present state cause significant damages, the majority of the impacts are produced by the influence of climate change.

3.2 Erosion

As stated in *Section 2.3*, we study erosion using the retreat of the coastline as an indicator. After checking all the simulated cases, we find a common pattern for all the sections. First, and as we observe in Figure 10, selected arbitrarily to avoid preference, the retreat of the coastline derived from the storm is very low compared with the

retreat due to the increasing of the mean water level. Furthermore, we have found that this increment is higher on low-steep beaches, as expected. In the specific case of Figure 10, the retreat after the pass of the RP 500 years' storm in actual conditions is 3 m, while with the climate change conditions, it is nearly 30 m. This proportion has been observed in all the other cases. Although the retreat derived from the storms is not negligible when studying scenarios of high RPs, when graphed on a map, this change is barely visible, as we see in Figures 11, 12. We also find that while the increase on the mean water level causes the coastline to directly retreat, the erosion and sedimentation processes maintain its balance on the 0-m level. Since the equilibrium of the beach does not change between scenarios, the behavior is the same but with different intensities due to the quantity of water hitting the area. We propose that when using climate change scenarios and beaches in equilibrium for present conditions, some other modeling strategies could have been used in order to avoid changes in the 0-m baseline and more balances on the new water level (in these cases, 0.85 and 1.14 m). We have discussed the use of long simulations during the study, using the increase of the mean water level without storm conditions until the new equilibrium is reached and then the storm scenario is repeated, but this strategy was rejected because of computational constrains, lack of knowledge about the human interventions in the future, and specifications of the model.
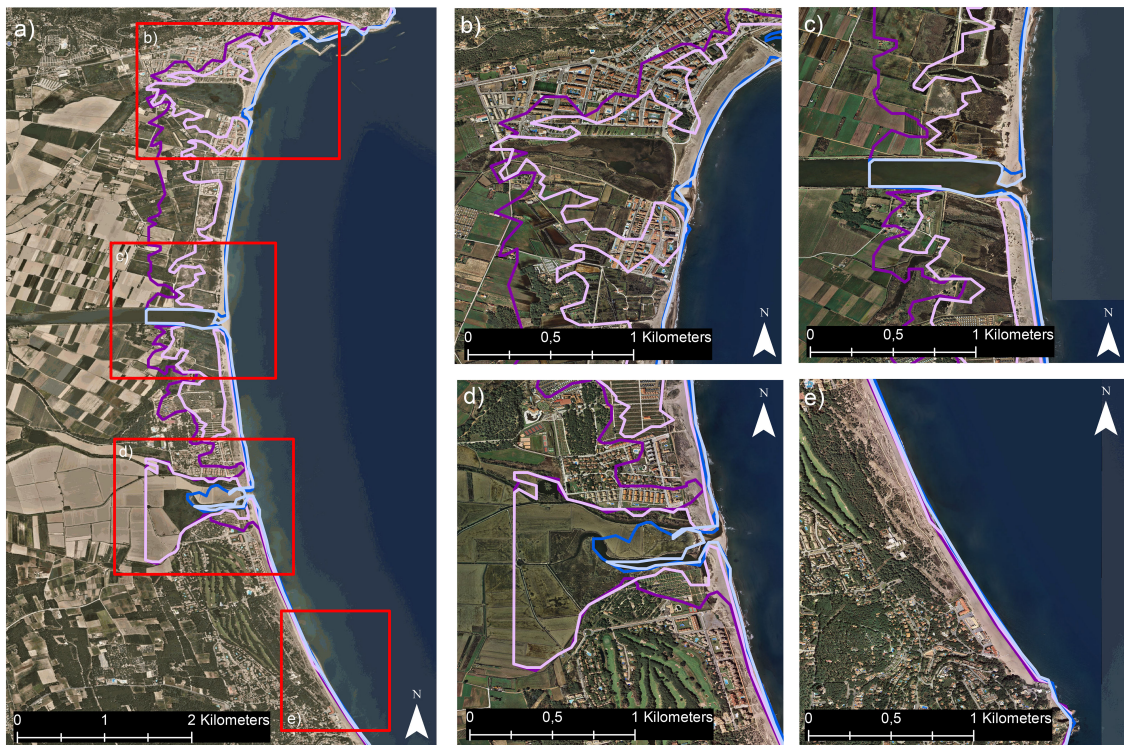
FIGURE 8
Flooding lines distribution of Unit 19. **(A)** General view of the unit. **(B–E)** Close-up view. Light blue = actual conditions, RP = 50 years; dark blue = actual conditions, RP = 500 years; light lilac = RCP8.5, RP = 50 years; and dark lilac = RCP8.5, RP = 500 years.

Figures 11, 12 show the explained behavior. The correlation of the modeled coastline with the one presented in the map is not exact because, again, the times when the topobathymetry and the orthophoto were taken are different and so the beach forms due to changes on the dynamics of the littoral cell. Furthermore, the importance lies in the magnitudes of coastline retreat where, on both figures, the retreat due to the storm pass is a lot less than for the mean water level introduction.

4 Summary and conclusion

The modeling approach has demonstrated its efficacy in describing the flooding and erosion impacts on the studied beaches caused by different storm scenarios and climate change conditions. A characterization of the most common and important archetypes of the Catalan coast has been done, finding that the low-lying coasts with gentle slopes are the most affected by, while the high coasts with well-developed berms are the most protected from, flooding events. We have achieved a good computational time from trial and error, taking into account the needs of the study since it is not time-limited. The MPI strategy gives a good performance and we do not expect that the incorporation of clustering computing can give us enough improvement to test it. Some trials done with interpolating grids with more resolution (5 × 5 m and 2 × 2 m) resulted in an increase of the computational time without

improving the accuracy of the results, due to the limitation of the topobathymetry resolution. All these factors enhance the use of the selected strategy. The flooding rate, as expected, increases with the storm intensity for all the studied cases, as it could be seen in Table S1, while the archetype and characteristics of the beach, for example, the slopes, the presence of berms or dunes, and the existence of mitigation zones like vegetation or high promenades, define the final pattern of inundation. Nevertheless, climate change is the driving factor, with more affected areas in all the scenarios as the water level rises. We observe that the characterization of some parts of the Catalan coast using morphodynamical models results in an interesting tool to predict the possible consequences that could be seen in the future for the suggested predictions. The observed behavior for the different analyzed cases shows how low-lying coastal stretches are the most vulnerable to flooding. Furthermore, on low urban coasts, when the incident waves reach the non-erodible surface, the beach configuration is not enough to stop them and waves can penetrate more than 200 m inland. We conclude that the maintenance of an enough emerged beach width and the generation of a backshore coastal room are necessary strategies to cope with these effects. Another interesting process that has been observed relates to the streams and channels that connect the lagoons. These areas are not well characterized by the topobathymetric data and are classified as a low-lying dry region. Adding this to the fact that they present levees on both sides of the entrances makes them susceptible to flooding, especially in the face
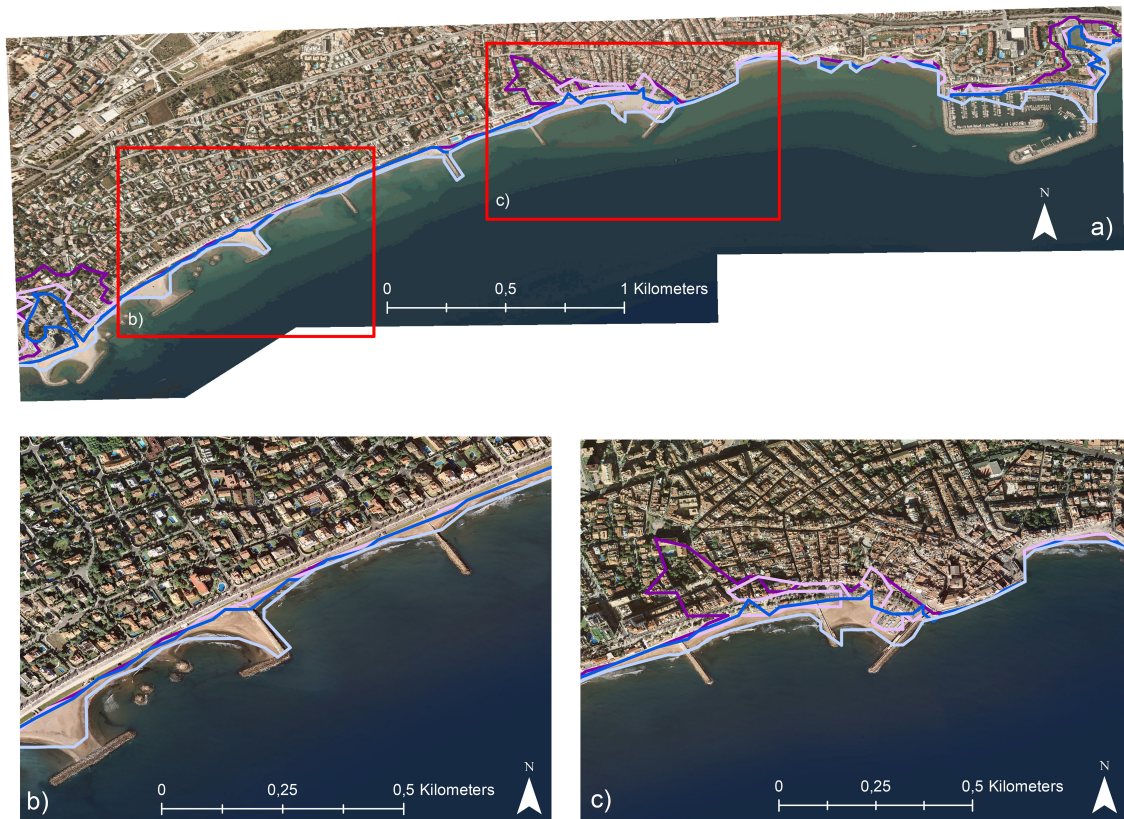
FIGURE 9
Flooding lines distribution of Unit 7. **(A)** General view of the unit. **(B, C)** Close-up view. Light blue = actual conditions, RP = 50 years; dark blue = actual conditions, RP = 500 years; light lilac = RCP8.5, RP = 50 years; and dark lilac = RCP8.5, RP = 500 years.
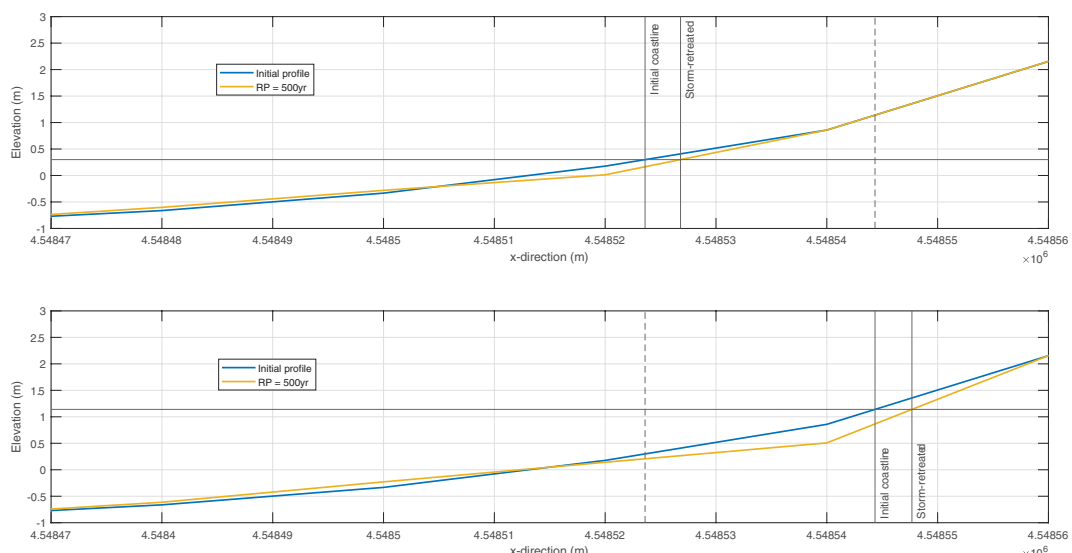
FIGURE 10
Profile evolution corresponding to the middle of Unit 4. The top image shows the evolution in actual conditions and the bottom image shows that for the RCP8.5 scenario. The blue line shows the initial profile and the yellow line shows the final profile after the pass of an RP = 500 years' storm. Vertical lines represent the initial coastline and the coastline retreat due to the storm pass. Dashed vertical lines help to compare between scenarios.

FIGURE 11
Map of Catalonia and close-up map of coastline retreat of Unit 4. Blue rectangle on the top map shows the position of the unit. Light blue = actual conditions, RP = 50 years; dark blue = actual conditions, RP = 500 years; light lilac = RCP8.5, RP = 50 years; and dark lilac = RCP8.5, RP = 500 years.

of climate change conditions. This behavior has been previously studied in the Ebro delta river mouth under different sea level rise scenarios, as described by Grases et al. (2020). Unit 8 also strengthens the arguments since a similar flooding pattern has been observed compared with the description of CIIRC (2010), which finds inundation in the torrents. Although the condition of dry rivers is not realistic at the present time, this may become a more plausible scenario under climate change conditions, with the region expected to experience a significant reduction in rainfall rates (Dore, 2005).

FIGURE 12
Map of Catalonia and close-up map of coastline retreat of Unit 11. Blue rectangle on the top map shows the position of the unit. Light blue = actual conditions, RP = 50 years; dark blue = actual conditions, RP = 500 years; light lilac = RCP8.5, RP = 50 years; and dark lilac = RCP8.5, RP = 500 years.

As regards the erosion impacts, we conclude that coastline retreat does not seem to be the best proxy. First, storm conditions surprisingly have a minimal effect due to redistribution processes. Even if there are huge changes in the sand position due to high-intensity storm events, the most common movements are the erosion of the part where the waves arrive, which normally corresponds to an area above the coastline. This sand then goes to the formation of a submerged bar as described in (Guillén and Palanques, 1993; Eichentopf et al., 2020), especially on dissipative beaches (Bowman and Goldsmith, 1983; Aagaard et al., 2013). This generates a scenario where the hypothetical 0-m baseline corresponding to the coastline remains invariable or barely changed but does not provide enough interesting information to the study. Moreover, SLR has a direct impact on the coastline retreat. As expected, the results show that gentle beach slopes, which correspond to fine sand fractions, are more sensitive to climate change, resulting in greater shoreline retreats, but the impacts derived from the combination of SLR and storms have to face the same problem described before. Additionally, the fact that the coastline directly changes its position even before the storm event starts if climate change scenarios are included makes it impossible to compare the present and future conditions. Finally, a proposal to modify the topobathymetry using long-term simulations to reach equilibrium with sea level rise conditions has been questioned due to concerns about its necessity during the study. However, this strategy was turned down for various reasons. Firstly, as stated by in (Simmons et al., 2017; Matheen et al., 2021), the model's free parameters have a greater impact on the final results than the used profile. Secondly, updating the bathymetry would be highly computationally demanding, adding to the rejection of the proposed method. Last, the bathymetry projection for the year 2100 is highly uncertain and can only be evaluated with some confidence in the absence of human intervention. Currently, all of the analyzed scenarios are subject to management control, so the expected bathymetry for 2100 is unclear. This paper proposes a solution to this uncertainty by assuming that the present coastal layout will be maintained. The methodology used in this study presents how we can obtain high-resolution results of the impacts to define management policies on a large scale. It opens the door to implement operational strategies based on the shown concepts to prevent future impacts on the beaches along Catalonia. The work also defines common patterns that could be used to study other possible areas with the same patterns. The definition of the flooding impacts as polygons would help the administration to easily understand and situate the problem, facilitating the decision about which mitigation actions they have to implement; meanwhile, another strategy to characterize the erosion has to be defined since the coastline retreat is not a good proxy to mitigate the loss and accumulation of sediments on the beach and the promenade. A more detailed and updated version of the topographies and especially bathymetries on the Catalan coast would further improve the obtained results and performance. This, added to a constant flux of hydrodynamic data, would be the last step in creating a good early warning system to reduce the actual impacts and even prepare the affected areas for future problems.

Data availability statement

The original contributions presented in the study are included in the article/Supplementary Material, further inquiries can be directed to the corresponding author/s.

Author contributions

VG and XS-A led the manuscript drafting with the contribution of JP, JPS, ME, and AS-A. VG, AS-A, JPS, ME, and JP contributed to the organization of the study. JPS contributed to the generation of the hydrodynamic conditions. XS-A contributed to the modeling simulations and the generation of results. JP contributed to the implementation of the viewer and the supply of the topographies. All authors contributed to the article and approved the submitted version.

Conflict of interest

The authors declare that the research was conducted in the absence of any commercial or financial relationships that could be construed as a potential conflict of interest.

Publisher's note

All claims expressed in this article are solely those of the authors and do not necessarily represent those of their affiliated organizations, or those of the publisher, the editors and the reviewers. Any product that may be evaluated in this article, or claim that may be made by its manufacturer, is not guaranteed or endorsed by the publisher.

Supplementary material

The Supplementary Material for this article can be found online at: https://www.frontiersin.org/articles/10.3389/fmars.2023.1125138/full#supplementary-material

References

Aagaard, T., Greenwood, B., and Hughes, M. (2013). Sediment transport on dissipative, intermediate and reflective beaches. *Earth-Sci Rev.* 124, 32–50. doi: 10.1016/j.earscirev.2013.05.002

Agulles, M., Jordà, G., and Lionello, P. (2021). Flooding of sandy beaches in a changing climate. The case of the Balearic Islands (NW Mediterranean). *Front. Mar. Sci.* 8. doi: 10.3389/fmars.2021.760725

Athanasiou, P., Van Dongeren, A., Giardino, A., Vousdoukas, M., Gaytan-Aguilar, S., and Ranasinghe, R. (2019). Global distribution of nearshore slopes with implications for coastal retreat. *Earth System Sci. Data* 11, 1515–1529. doi: 10.5194/essd-11-1515-2019

Barnard, P., Erikson, L., Foxgrover, A., Hart, J., Limber, P., and Neil, A. (2019). Dynamic flood modeling esential to assess the coastal impacts of climate change. *Sci. Rep.* 4309, 9. doi: 10.1038/s41598-019-40742-z

Blott, S. J., and Pye, K. (2001). Gradistat: a grain size distribution and statistics package for the analysis of unconsolidated sediments. *Earth surface processes Landforms* 26 (11), 1237–1248. doi: 10.1002/esp.261

Bolaños, R., Jordà, G., Cateura, J., Lopez, J., Puigdefabregas, J., Gómez, J., et al. (2009). The xiom: 20 years of a regional coastal observatory in the spanish catalan coast. *J. Mar. Syst.* 77 (3), 237–260. doi: 10.1016/j.jmarsys.2007.12.018

Bosom, E., and Jiménez, J. (2011a). Probabilistic coastal vulnerability assessment to storms at regional scale - application to catalan beaches (nw mediterranean). *Natural Haz. Earth System Sci.* 11 (1), 475–484. doi: 10.5194/nhess-11-475-2011

Bosom, E., and Jiménez, J. (2011b). Probabilistic coastal vulnerability assessment to storms at regional scale– application to catalan beaches (nw mediterranean). *Natural haz. Earth system Sci.* 11 (2), 475–484. doi: 10.5194/nhess-11-475-2011

Bowman, D., and Goldsmith, V. (1983). "Bar morphology of dissipative beaches: an empirical model,". *Mar. Geol.* 51 (1-2), 15–33. doi: 10.1016/0025-3227(83)90086-5

Castillo, E., and Sarabia, J. (1994). "Extreme value analysis of wave heights,". *J. OF Res. Natl. INSTITUTE OF STANDARDS AND Technol.* 99, 445–445. doi: 10.6028/jres.099.042

CIIRC (2010). *Estat de la zona costanera a catalunya* (International Centre for Coastal Resources Research). Technical Report. Available at: https://territori.gencat.cat/ca/01_departament/documentacio/territori-i-urbanisme/ordenacio_territorial/llibre_verd_estat_de_la_zona_costanera/.

Clarke, L., Glendinning, I., and Hempel, R. (1994). "The MPI message passing interface standard," in *Programming Environments for Massively Parallel Distributed Systems: Working Conference of the IFIP WG 10.3, April 25–29, 1994* (Birkhäuser Basel: Springer), 213–218.

Coles, S. (2001). An introduction to statistical modeling of extreme values, in: *Springer Series in Statistics* (London, UK: Springer). doi: 10.1007/978-1-4471-3675-0

Condon, A. J., and Peter Sheng, Y. (2012). Evaluation of coastal inundation hazard for present and future climates. *Natural haz.* 62 (2), 345–373. doi: 10.1007/s11069-011-9996-0

De Alfonso, M., Lin-Ye, J., García-Valdecasas, J. M., Perez-Rubio, S., Luna, M. Y., Santos-Muñoz, D., et al. (2021). Storm gloria: sea state evolution based on *in situ* measurements and modeled data and its impact on extreme values. *Front. Mar. Sci.* 8,646873. doi: 10.3389/fmars.2021.646873

Dore, M. H. (2005). "Climate change and changes in global precipitation patterns: what do we know?". *Environ. Int.* 31 (8), 1167–1181. doi: 10.1016/j.envint.2005.03.004

Eichentopf, S., van der Zanden, J., Cáceres, I., Baldock, T. E., and Alsina, J. M. (2020). Influence of storm sequencing on breaker bar and shoreline evolution in large-scale experiments. *Coast. Eng.* 157, 103659. doi: 10.1016/j.coastaleng.2020.103659

Fereirra., J. A., and Soares, C. G. (1998). An application of the peaks over threshold method to predict extremes of significant wave height. *J. Offshore Mechanics Arctic Eng.* 120, 165–176. doi: 10.1115/1.2829537

García-León, M., Gracia, V., Robichaux, L., Kroger, A., Gault, J., and Sánchez-Arcilla, A. (2015)Evaluation of transient defence measures against storms (Accessed Proceedings of the Coastal Sediments).

Generalitat de Catalunya. (2016). *Tercer informe sobre el canvi climàtic a Catalunya*. Institut d'Estudis Catalans i Generalitat de Catalunya. Available at: https://cads.gencat.cat/ca/detalls/detallarticle/Tercer-informe-sobre-el-canvi-climatic-a-Catalunya-00003.

Goda, Y. (1988). "On the methodology of selecting design wave height,". *Coast. Eng. Proc.*, 67. doi: 10.9753/icce.v21.67

Gracia, V., García, M., Grifoll, M., and Sánchez-Arcilla, A. (2013). "Breaching of a barrier under extreme events. the role of morphodynamic simulations". *J. Coast. Res.* 65 (10065), 951–956. doi: 10.2112/SI65-161.1

Gracia, V., and Jiménez, J. (2004)Unexpected response of infrastructures and beaches along the spanish mediterranean coast to the extreme storm of november of 2001 (Accessed Proceedings of the 29th International Conference on Coastal Engineering).

Grases, A., Gracia, V., García-León, M., Lin-Ye, J., and Sierra, J. P. (2020). "Coastal flooding and erosion under a changing climate: implications at a low-lying coast (ebro delta)". *Water* 12 (2), 346. doi: 10.3390/w12020346

Guillén, J., and Palanques, A. (1993). "Longshore bar and trough systems in a microtidal, storm-wave dominated coast: the ebro delta (northwestern mediterranean)". *Mar. Geol.* 115 (3-4), 239–252. doi: 10.1016/0025-3227(93)90053-X

Haasnoot, M., Brown, S., Scussolini, P., Jiménez, J. A., Vafeidis, A. T., and Nicholls, R. J. (2019). Generic adaptation pathways for coastal archetypes under uncertain sea-level rise. *Environ. Res. Commun.* 1 (7), 071006. doi: 10.1088/2515-7620/ab1871

Hinkel, J., Nicholls, R. J., Vafeidis, A. T., Tol, R. S., and Avagianou, T. (2010). Assessing risk of and adaptation to sea-level rise in the european union: an application of diva. *Mitigation Adaptat. Strategies Global Change* 15 (7), 703–719. doi: 10.1007/s11027-010-9237-y

IH Cantabria. (2019). *Elaboración de la metodología y bases de datos para la proyección de impactos de cambio climático a lo largo de la costa española* (Gobierno de España: Ministerio para la Transición Ecológica). Technical Report. Available at: https://adaptecca.es/sites/default/files/documentos/2019_metodologia_y_bbdd_proyeccion_impactos_de_cc_costa_espanola.pdf.

IPCC (2022). *Climate change 2022: impacts, adaptation and vulnerability* (Policymakers, Cambridge, UK and New York, USA: Cambridge University Press).

Jiménez, J. A., Sancho-Garcıa, A., Bosom, E., Valdemoro, H. I., and Guillén, J. (2012). Storm-induced damages along the catalan coast (nw mediterranean) during the period 1958–2008. *Geomorphology* 143, 24–33. doi: 10.1016/j.geomorph.2011.07.034

Jiménez, J. A., Valdemoro, H. I., Bosom, E., Sánchez-Arcilla, A., and Nicholls, R. J. (2017). Impacts of sea-level rise-induced erosion on the catalan coast. *Regional Environ. Change* 17 (2), 593–603. doi: 10.1007/s10113-016-1052-x

Li, F., van Gelder, P., Ranasinghe, R., and Callaghan, D. (2014). Probabilistic modelling of extreme storms along the dutch coast. *Coast. Eng.* 86, 1–13. doi: 10.1016/j.coastaleng.2013.12.009

Lin-Ye, J., García-León, M., Gracia, V., Ortego, M. I., Lionello, P., Conte, D., Sánchez-Arcilla, A., et al. (2020). "Modeling of future extreme storm surges at the nw mediterranean coast (spain),". *Water* 12 (2), 472. doi: 10.3390/w12020472

Martinelli, L., Zannuttigh, B., and Corbau, C. (2010). Assessment of coastal flooding hazard along the emilia romagna littoral, it. *Coast. Eng.* 57 (11-12), 1042–1158. doi: 10.1016/j.coastaleng.2010.06.007

Matheen, N., Harley, M. D., Turner, I. L., Splinter, K. D., Simmons, J. A., and Thran, M. C. (2021). Bathymetric data requirements for operational coastal erosion forecasting using xbeach. *J. Mar. Sci. Eng.* 9 (10), 1053. doi: 10.3390/jmse9101053

McCall, R., Masselink, G., Poate, T., Roelvink, J., Almeida, L., Davidson, M., et al. (2014). Modelling storm hydrodynamics on gravel beaches with xbeach-g. *Coast. Eng.* 91, 231–250. doi: 10.1016/j.coastaleng.2014.06.007

Mendoza, E. T., and Jiménez, J. (2008). Clasificación de tormentas costeras para el litoral catalán (mediterráneo no). *Ingeniería hidráulica en México* 23 (2), 21–32.

Mendoza, E., Jimenez, J., and Mateo, J. (2011). "A coastal storms intensity scale for the catalan sea (nw mediterranean)". *Natural Haz. Earth System Sci.* 11 (9), 2453–2462. doi: 10.5194/nhess-11-2453-2011

Nicholls, R., and Klein, R. J. (2005). Climate change and coastal management on europe's coast. *Managing Eur. Coasts*, 199–226. doi: 10.1007/3-540-27150-3_11

Nicholls, R. J., and Misdorp, R. (1993). Synthesis of vulnerability analysis studies. In: *Proceedings of WORLD COAST*. (The Netherlands: Ministry of Transport, Public Works and Water Management) pp. 181–216.

Nicholls, R., Tol, R. S., and Hall, J. (2007). "Assessing impacts and responses to global-mean sea-level rise," in *Human-induced climate change: an interdisciplinary assessment* (Cambridge University Press), 119–134. doi: 10.1017/CBO9780511619472.013

Nordhaus, W. D. (2006). Geography and macroeconomics: new data and new findings. *Proc. Natl. Acad. Sci.* 103 (10), 3510–3517. doi: 10.1073/pnas.0509842103

Orejarena-Rondón, A., Sayol, J., Marcos, M., Otero, L., Restrepo, J., and Hernández-Carrasco, I. (2019). Coastal impacts driven by sea-level rise in cartagena de indias. *Front. Mar. Sci.* 450, 6:614. doi: 10.3389/fmars.2019.00614

Ozyurt, G., Ergin, A., and Esen, M. (2008)Indicator based coastal vulnerability assessment model to sea level rise (Accessed Proceedings of the 7th International Conference on Coastal and Port Engineering in Developing Countries (COPEDEC)).

P. B. UNEP and MAP (2016). *Tourism and sustainability in the Mediterranean: key facts and trends*. Plan Blue. Regional Activity Centre, Valbonne.

Ranasinghe, R. (2016a). Assessing climate change impacts on open sandy coasts: a review. *Earth-science Rev.* 160, 320–332. doi: 10.1016/j.earscirev.2016.07.011

Ranasinghe, R. (2016b). On the need for a new generation of coastal change models for the 21st century. *Sci. Rep.* 10 (1), 1–6. doi: 10.1038/s41598-020-58376-x

Ranasinghe, R., and Callaghan, D. (2017). "Assessing storm erosion hazards,". *Coast. storms: processes impacts*, 241–256. doi: 10.1002/9781118937099.ch12

Ranasinghe, R., Ruane, A. C., Vautard, R., Arnell, N., Coppola, E., Cruz, F. A., et al. (2021). Climate change information for regional impact and for risk assessment. In: *Climate Change 2021: The Physical Science Basis. Contribution of Working Group 1 to the Sixth Assessment Report of the Intergovernmental Panel on Climate Change.* (Cambridge: Cambridge University Press), pp. 1767–1926.

Rautenbach, C., Trenham, C., Benn, D., Hoeke, R., and Bosserelle, C. (2022). Computing efficiency of xbeach hydro-and wave dynamics on graphics processing units (gpus). *Environ. Model. Software* 157, 105532. doi: 10.1016/j.envsoft.2022.105532

Roelvink, D., Reniers, A., Van Dongeren, A., Van Thiel de Vries, J., Lescinski, J., and McCall, R. (2010). "XBeach model description and manual," in *Unesco-IHE institute for water education*. (Deltares and Delft University of Tecnhology), 21.

Roukounis, C. N., and Tsihrintzis, V. A. (2022). Indices of coastal vulnerability to climate change: a review. *Environ. Processes* 9 (2), 1–25. doi: 10.1007/s40710-022-00577-9

Sánchez-Arcilla, A., García, M., Gracia, V., Devoy, R., Stanica, A., and Gault, J. (2016a). Managing coastal environments under climate change: pathways to adaptation. *Sci. Total Environ.* 572, 1336–1352. doi: 10.1016/j.scitotenv.2016.01.124

Sánchez-Arcilla, A., García-León, M., Gracia, V., Devoy, R., Stanica, A., and Gault, J. (2016b). Managing coastal environments under climate change: pathways to adaptation. *Sci. total Environ.* 572, 1336–1352. doi: 10.1016/j.scitotenv.2016.01.124

Sánchez-Arcilla, A., Gómez, M., Gracia, V., Gironella, X., and García-León, M. (2014). Reliability analysis of beaches as defenses against storm impacts under a climate change scenario (Accessed Proceedings of the 35th International Conference on Coastal Engineering).

Sancho-García, A., Guillén, J., and Rubio-Nicolás, B. (2020). *"Coastal damages caused by an extreme storm (gloria event) along the spanish mediterranean coast"*.

Sanuy, M., and Jiménez, J. A. (2019). "Sensitivity of storm-induced hazards in a highly curvilinear coastline to changing storm directions. the tordera delta case (nw mediterranean)". *Water* 11 (4), 747. doi: 10.3390/w11040747

Sardà, R., Ávila, C., and Mora, J. (2005). A methodological approach to be used in integrated coastal zone management processes: the case of the catalan coast (catalonia, spain). *Estuarine Coast. Shelf Sci.* 62 (3), 427–439. doi: 10.1016/j.ecss.2004.09.028

Schwalm, C. R., Glendon, S., and Duffy, P. B. (2020). "Rcp8.5 tracks cumulative co2 emissions,". *Proc. Natl. Acad. Sci.* 117 (3), 19656–19657. doi: 10.1073/pnas.2007117117

Simmons, J. A., Harley, M. D., Marshall, L. A., Turner, I. L., Splinter, K. D., and Cox, R. J. (2017). Calibrating and assessing uncertainty in coastal numerical models. *Coast. Eng.* 125, 28–41. doi: 10.1016/j.coastaleng.2017.04.005

Small, C., and Nicholls, R. J. (2003). A global analysis of human settlement in coastal zones. *J. Coast. Res.* 19 (3), 584–599. Available at: http://www.jstor.org/stable/4299200.

Tâtui, F., Pîrvan, M., Popa, M., Aydogan, B., Ayat, B., Görmüs, T., et al. (2019). "The black sea coastline erosion: index-based sensitivity assessment and management-related issues". *Ocean Coast. Manage.* 182, 104949. doi: 10.1016/j.ocecoaman.2019.104949

Thomson, A. M., Calvin, K. V., Smith, S. J., Kyle, G. P., Volke, A., Patel, P., et al. (2011). "Rcp4.5: a pathway for stabilization of radiative forcing by 2100". *Climatic Change* 109, 77–94. doi: 10.1007/s10584-011-0151-4

Turner, R. K., Subak, S., and Adger, W. N. (1996). Pressures, trends, and impacts in coastal zones: interactions between socioeconomic and natural systems. *Environ. Manage.* 20, no. 2, 159–173. doi: 10.1007/BF01204001

Villatoro, M., Silva, R., Mendez, F., Zanuttigh, B., and Pan, S. (2014). And E.E.A. Trifonov, "An approach to assess flooding and erosion risk for open beaches in a changing climate". *Coast. Eng.* 87 (1), 50–76. doi: 10.1016/j.coastaleng.2013.11.009

Yin, J., Yin, Z., Wang, J., and Xu, S. (2012). National assessment of coastal vulnerability to sea-level rise for the chinese coast. *J. Coast. Conserv.* 16 (1), 123–133. doi: 10.1007/s11852-012-0180-9

Zhang, K., Douglas, B., and Leatherman, S. (2004). Global warming and coastal erosion. *Climatic Change* 64 (1), 41–58. doi: 10.1023/B:CLIM.0000024690.32682.48

Climate change - induced hazards on touristic island beaches: Cyprus, Eastern Mediterranean

Isavela N. Monioudi[1]*, Adonis F. Velegrakis[1],
Dimitris Chatzistratis[1], Michalis I. Vousdoukas[1], Christos Savva[1],
Dandan Wang[2], Gerald Bove[3], Lorenzo Mentaschi[4],
Dominik Paprotny[5], Oswaldo Morales-Nápoles[6],
Antonis E. Chatzipavlis[1], Thomas Hasiotis[1]
and Evangelia Manoutsoglou[1]

[1]Department of Marine Sciences, University of the Aegean, Mytilene, Greece, [2]School of Information
Engineering, Zhejiang Ocean University, Zhoushan, Zhejiang, China, [3]Biological Field Station on
Otsego Lake, State University of New York at Oneonta, Oneonta, NY, United States, [4]Department of
Physics and Astronomy, University of Bologna, Bologna, Italy, [5]Research Department Transformation
Pathways, Potsdam Institute for Climate Impact Research, Potsdam, Germany, [6]Department of
Hydraulic Engineering, Faculty of Civil Engineering and Geosciences, Delft University of Technology,
Delft, Netherlands

This contribution presents an assessment at a regional (island) scale of the beach erosion due to storm events under Climate Change. The approach adopted to assess beach erosion at the island scale consisted of three modules. First, the location, dimensions and other attributes of the Cypriot beaches were recorded on the basis of widely-available satellite imagery. Secondly, sea levels and waves were modeled along the coast under different climatic scenarios and dates in the 21st century. Finally, using these projections beach retreat due to the relative mean sea level rise (RSLR) and extreme sea levels (ESLs) was estimated using ensembles of analytical and numerical cross-shore morphodynamic models, respectively. Extreme sea levels (ESLs) were projected to (a) increase by up to 60% in 2100 from their baseline (2000) levels, and (b) vary along the coast, with the highest ESLs (and corresponding waves) projected for the southern and western coasts. The mostly narrow Cypriot beaches (91% recorded maximum widths of < 50 m) showed increased exposure to erosion. In 2100, about 47% and 72% (based on the median model estimates) of the 241 unprotected Cypriot beaches will be permanently eroded, due to mean sea level rise (SLR), to 50% of their present maximum width, depending on the scenario. In addition to the long-term erosion due to SLR, severe storm erosion is projected by 2050 even under the RCP4.5 scenario; the 100-year extreme sea level event (ESL100) may overwhelm (at least temporarily) 49% of the currently unprotected Cypriot beaches without effective adaptation responses, with the most exposed beaches located along the northern coast. As the beach carrying capacity and hedonic value will be severely compromised, effective adaptation policies and technical measures will be urgently required.

KEYWORDS

beach erosion, shoreline retreat, island beaches, extreme sea levels, sea level rise, climate change impacts

1 Introduction

Beaches (sandy shorelines) are critical coastal ecosystems. They constitute a substantial fraction of the global coastline (e.g. Luijendijk et al., 2018), are important habitats in their own right (e.g. Ackerman, 2017), have a high hedonic value (Boto-García and Leoni, 2022) and provide protection from coastal flooding to their backshore ecosystems, assets and infrastructure (e.g. Ciavola et al., 2018). At the same time, many beaches are under retreat/erosion (Wong et al., 2014), manifested as: (i) shoreline retreat due to relative mean sea level rise (RSLR) and negative sedimentary budgets (Nicholls and Cazenave, 2010); and/or (ii) short-term retreat caused by storm events, which although might not result in permanent erosion, it could be, nevertheless, devastating (Di Paola et al., 2023). Shoreline retreat in beaches backed by natural and/or artificial features, such as coastal cliffs and infrastructure/ assets could result in beach 'drowning'.

Assessments are determined by the spatial (global, regional, local) and temporal (short- or long-term) scales of the study and the available information and resources (Ranasinghe, 2016). These involve (a) evaluations of the current trends (e.g. Mentaschi et al., 2018), and/or (b) future projections using analytical, numerical and/or empirical models (e.g. Hinkel et al., 2013; de Winter and Ruessink, 2017; Vousdoukas et al., 2020). Assessments at the regional scale (100s of km of coastline) are particularly important for integrated adaptation policies and efficient allocation of the requisite resources (e.g. Monioudi et al., 2016; Toimil et al., 2017; Giardino et al., 2018).

Erosion can be particularly threatening for island beaches, as these commonly have limited dimensions and sediment supply (Monioudi et al., 2017). At the same time, in many cases, island beaches are major tourism destinations (e.g. Alvarez et al, 2022). Tourism, which has been increasingly associated with beach recreation according to the 'Sun, Sea and Sand - 3S' model (Monioudi and Velegrakis, 2022) accounts for about 33.5% (on average) of the Gross Domestic Product (GDP) of the Caribbean Small Island Developing States (SIDS) (ILO, 2020), with many Mediterranean islands being also dependent on beach tourism (UNWTO, 2019). In the period 2010 - 2021, the majority of the 246.5 million arrivals (20.1 million annual average) in Greece had a Greek island destination (SETE, 2023), whereas about 23% of the 71.6 million arrivals in Spain in 2022 had a Balearic destination (IBESTAT, 2023; INE, 2023).

In the future, the accelerating mean sea level rise, coupled with potential changes in the magnitude and recurrence frequency of storm events (e.g. Vitousek et al., 2017; IPCC, 2019) will inevitably Intensify beach erosion and coastal flooding, with severe impacts on the natural and human coastal systems (e.g. Bellard et al., 2014; Anderson et al., 2018; Toimil et al., 2018; Rodella et al., 2020). Therefore, although projecting the beach morphodynamics under a variable and changing climate is not an easy exercise due to inherent uncertainties in both forcing and the beach response (Le Cozannet et al., 2019), beach erosion assessment and mitigation should be decidedly important components in all sustainable development plans of the coastal zone (e.g. Summers et al., 2018).

The present contribution presents an approach for the assessment of beach retreat/erosion at a regional (island) scale under mean sea level and storm events and its application at the touristic island of Cyprus (Eastern Mediterranean). The spatial characteristics and other attributes of the Cypriot beaches were recorded from widely available satellite imagery. Projections of mean and extreme sea levels (ESLs) and corresponding waves under different climatic scenarios were then used to force cross-shore morphodynamic model ensembles to obtain estimates of beach erosion for the island beaches.

2 Cypriot beaches: environmental setting and socio-economic significance

Cyprus is the third largest Mediterranean island, with an area of 9,250 km^2, a total population of about 1.25 million (2022) and a coastline length of about 740 km. The island is located in a tectonically active region and can be divided in 4 main geological zones (Figure 1): the northern Keryneia Terrane, comprising thrusted Cenozoic sedimentary sequences; (ii) the Troodos massif comprising uplifted, Cretaceous ophiolites; (iii) the Mesozoic sedimentary/basaltic Mamonia terrane in the west; and (iv) the Circum–Troodos sedimentary succession. Cyprus climate exhibits hot dry summers and changeable winters characterized by short-lived wet events that provide most of the annual precipitation (Price et al., 1999). The seasonal precipitation and the burgeoning summer water needs have prompted the construction of 108 river dams with a total capacity of about 332 million m^3 (WDD, 2017) diminishing the sediment supply at their downstream beaches.

The coast of Cyprus is microtidal (Wolff et al., 2018) and its wave regime varies, with the most energetic waves observed along the western and southern coastline (Galanis et al., 2012). The regional sea level rise has accelerated to 2.4 – 3.8 mm/year since the late 1990s (Tsimplis et al., 2013). Regarding the extreme sea levels, their storm surge components (Section 3.2) have a seasonal footprint and heights that have rarely exceeded 0.4 m (e.g. Tsimplis and Shaw, 2010).

In recent decades, beach (3S) tourism has become a most significant economic activity in Cyprus that requires efficient and integrated coastal management. However, coastal governance, management and regulation in Cyprus are fragmented. The northern part of the island and about half of its coastline are administered by the self–declared Turkish Republic of Northern Cyprus (TRNC) (https://www.securitycouncilreport.org/un-documents/cyprus/). The Republic of Cyprus, an EU Member State since 2004, administers only the island's southern and western coasts where there are also parts of the coast located in the UK Sovereign Base Areas (Akrotiri and Dhekelia) and the UN Buffer Zone (Figure 1).

In 2019, 4.0 million international tourists visited the Republic of Cyprus contributing about €2.7 billion to the economy, a contribution forecasted to reach up to about 27% of GDP by 2027 (CYSTAT, 2017; CYSTAT, 2019). Tourism infrastructure
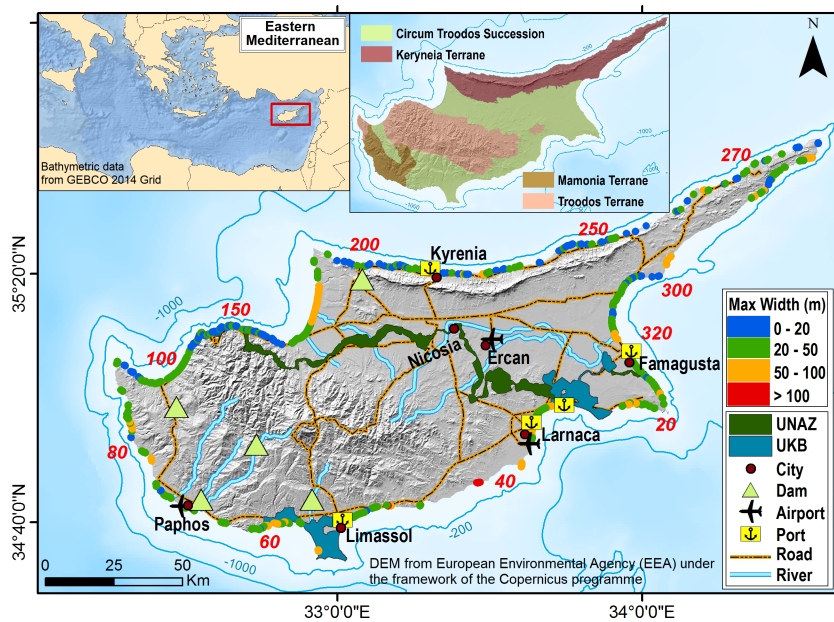
FIGURE 1
Cyprus: Major administrative boundaries, cities, transport network, rivers and major dams. The 322 beaches with their maximum widths recorded in this study are numbered clockwise from the eastern UNAZ border. Inset shows the generalized geology http://www.moa.gov.cy/moa/gsd/gsd.nsf/All/F9B6C7484AFDCADCC2258363003BE7C5?OpenDocument. Key: UNAZ, United Nations Administered Buffer Zone (https://unficyp.unmissions.org/); UKB, UK Sovereign Base Areas (https://www.army.mod.uk/deployments/cyprus/).

and activities are concentrated at the coast. In 2013, 94% of the hotel beds were located at the coast (Lemesios et al., 2016) whereas, in 2016, 91% of the international tourists stated that they had a coastal vacation (CYSTAT, 2017). The situation is similar in northern Cyprus (TRNC), where the vast majority of the tourism facilities/flows are also found at the coast (Farmaki et al., 2015; Safakli and Kutlay, 2016)

3 Methods

The approach adopted to assess beach erosion at the island scale consisted of three modules. First, the location, dimensions and other attributes of the Cypriot beaches were recorded on the basis of widely-available satellite imagery. Secondly, sea levels and waves were modeled along the coast under different climatic scenarios and dates in the 21st century. Finally, using these projections beach retreat due to the relative mean sea level rise (RSLR) and extreme sea levels (ESLs) was estimated using ensembles of analytical and numerical cross-shore morphodynamic models, respectively. A concise flow chart of the approach is presented as Figure 2.

3.1 Characteristics of Cyprus beaches

The beach inventory was created using the satellite images and related optical information and tools available in the Google Earth Pro application. To facilitate consistency, a standard operating procedure (SOP) for capturing beaches from the images was used. The subaerial ('dry') beaches were digitized as polygons (Figure 3),

with their: (i) landward boundaries defined by either backshore natural features (vegetated dunes and/or cliffs), or permanent artificial structures (e.g. coastal embankments, roads and buildings); (ii) lateral extent delimited by promontories, rocky coasts or coastal works; and (iii) seaward boundaries defined by the shoreline, i.e., the median line of the foaming swash zone in the imagery.

Geo-spatial characteristics and other attributes of the beach database include: beach location, dimensions (e.g. area and beach maximum width, BMW) and orientation; imagery acquisition dates; the presence of natural and artificial features (backshore sand dunes and cliffs, coastal defenses); the coverage of the infrastructure/assets at the immediate backshore as a fraction of its length; road accessibility; and a qualitative classification of the beach sediment texture (e.g. gravel, sand) based on the available optical information (e.g. Wolff et al., 2018). Very small beaches (lengths< 30 m) were not recorded. Digitization was carried out by a unique analyst who followed consistently the SOP rules, whereas production of metadata from the digitized polygons was carried out in a GIS environment. The database includes characteristics of the 322 recorded beaches (beach location in Figure 1).

In order to assess historical changes, images from Google Earth historical image tool were used; in total 2363 images spanning the period 2003 – 2022 were examined. However, comparisons were carried out between images from the 2010 – 2014 and 2020 – 2022 periods for 317 beaches (no available images for beaches 284 – 288 from the period 2010 – 2014). This was due to the lack of concurrent images of appropriate quality covering the whole Cyprus coastline; thus, the time span of the comparisons differs along the coast. Since in an interannual scale longshore transport

FIGURE 2
Flow chart of the methodology used in the present study. Key 1: Athanasiou (2019); 2: Bujan et al. (2019).
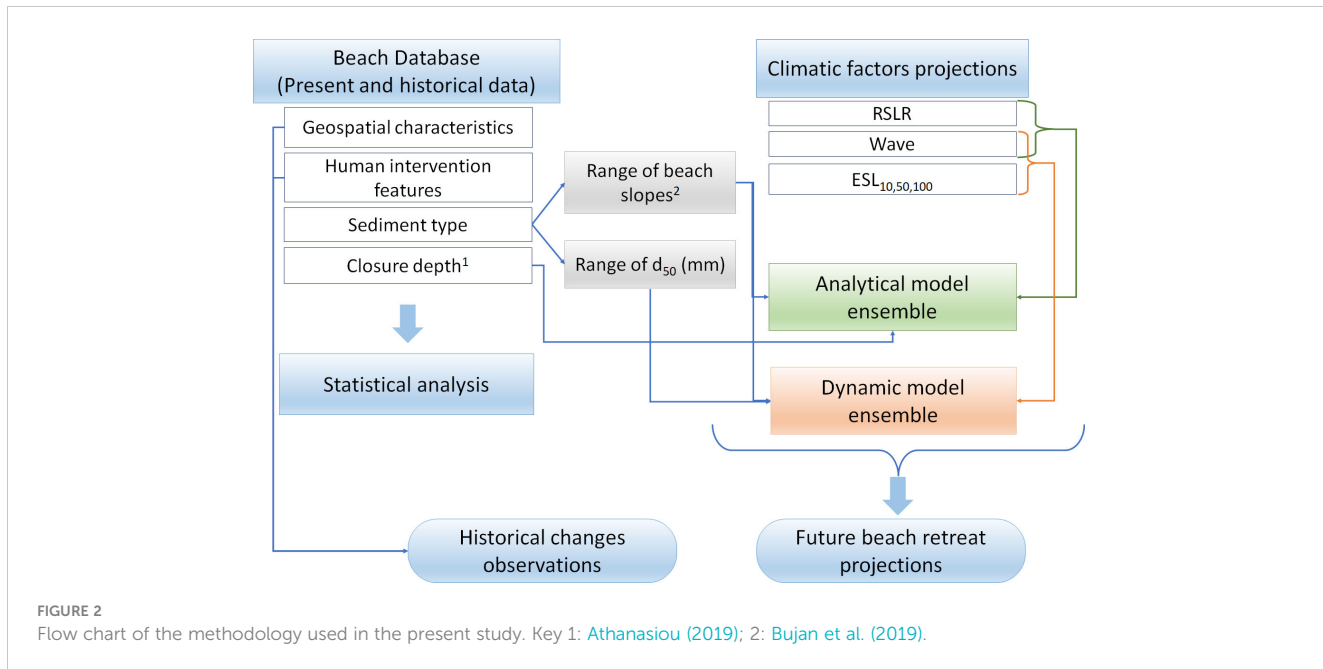
processes can affect beach morphology altering positions of accreted and eroded parts alongshore it can be assumed that a decrease in the recorded BMW implies erosion for the total beach area.

Constraints of the approach in terms of capturing the beach features and their dynamics can stem from the accuracy/resolution of the images from which the information was extracted. Moreover, the available satellite imagery has not been synoptic over the island, having been collected in different times and under different hydrodynamic conditions preceding image acquisition. Although tidal effects on the shoreline position in the microtidal Cyprus coast can be considered small and care was taken to compare images from the same season (when possible) and under low hydrodynamic conditions, recorded beach dimensions may not represent the 'mean' conditions as there could be considerable short-term variability in response to the nearshore hydrodynamics (e.g. Chatzipavlis et al., 2019). This, however, cannot be avoided in comparisons of historical coastal satellite imagery (e.g. Mentaschi et al., 2018).

3.2 Sea level and waves

The Projections for the 21st century under the IPCC representative concentration pathway scenarios RCP4.5 and RCP8.5 were obtained from the dataset presented in Vousdoukas et al. (2018b) for every 25 km along the coastline. Extreme sea levels at the coast are due to mean sea level, the astronomical tide (η_{tide}) and the episodic coastal water levels (η_{CE}) due to storm surges and wave set ups. Projections have been derived using dynamic models, namely the DFLOW-FM (Muis et al., 2016) for the storm surges and the WAVEWATCH III (Tolman, 2009) for the offshore wave characteristics while mean sea level (RSLR) projections are according to Jevrejeva et al. (2016). As detailed information on the nearshore bathymetry has not been available to provide a

precise estimation of the wave set ups, these were assessed using the generic approximation (0.2 x H_s) of CEM (2002). The dataset combined all ESL components and their uncertainties in a probabilistic fashion through Monte Carlo simulations. https://www.aviso.altimetry.fr/en/data/products/auxiliary-products/global-tide-fes.html

In addition to the ESLs, beach response during the extreme sea level events is controlled by the corresponding waves (Toimil et al., 2017). This was assessed by bivariate copulas, i.e., joint distributions on the unit square with uniform [0,1] margins (e.g. Oswaldo et al., 2017; Li et al., 2018). In this study, the variables involved were transformed to [0,1] margins through their empirical margins and the correlation of total water level with the wave parameters (H_s, T and direction) was investigated with Spearman's rank correlation coefficient. The pairs of transformed margins were then fitted to 7 copula types (Gaussian, Gumbel, Clayton, Frank, Plackett, t and Joe-Clayton BB7), representing various dependency structures (Joe, 2014). For each pair, the type best fitting the data was chosen by goodness-of-fit statistics (Genest et al., 2009):

$$M_n(u) = n\sum_{|u|}\left\{C_{\hat{\theta}_n}(u) - B(u)\right\}^2, u \in [0,1]^2 \qquad (1)$$

where $B(u) = 1/n\sum 1(U_i \le u)$ is the empirical copula, and $C_{\hat{\theta}_n}(u)$ is a parametric copula with parameter $\hat{\theta}_n$ estimated from the sample of length n.

For a given ESL value, the probability of exceedance on the marginal distribution of total water levels was computed. However, when this was lower than $1/n$, indicating that the selected margin values could not include such an extreme case, the margins were amended using parametric distributions of extreme values for each margin (except wave direction); generalized Pareto distribution, fitted to values above the 98.5th percentile threshold, was employed for this purpose. Finally, the conditional marginal distribution of each wave parameter given $P(ESL)$ was computed, providing both the expected

(mean) value of the wave parameters and the uncertainty bounds. The copula dependency analysis, which was based on the reanalysis data, allowed to obtain for every η_{CE} the corresponding most likely significant wave height (H_s), period (T) and wave direction. These waves were used to force the morphodynamic models.

3.3 Beach erosion projections

Two ensembles of cross-shore (1-D) morphodynamic models were used: (a) an analytical ensemble consisting of the models Bruun (Bruun, 1988), Dean (Dean, 1991) and Edelman (Edelman, 1972) which was used to assess beach retreat due to mean sea level rise (RSLR) and (b) a numerical model ensemble comprising the models SBEACH (Larson and Kraus, 1989), Leont'yev (Leont'yev, 1996), Xbeach (Roelvink et al., 2010) and Boussinesq (Karambas and Koutitas, 2002) which was used to assess beach retreat under ESLs. Ensemble methods in coastal modelling have been found to perform generally better than individual models and their application have been predicted to increase in the future (Sherwood et al., 2022). As the sensitivity to different forcing factors varies among individual morphodynamic models, ensemble techniques exploit each model's strength and mitigate its weaknesses (Simmons and Splinter, 2022). In the present case, a validation exercise involving the same model ensembles, the results of which were compared with results of physical experiments (Monioudi et al., 2017), showed that ensemble modeling improves considerably the comparisons between the projected beach retreats with those recorded in the physical experiments under both the mean sea level rise and extreme sea levels.

The Bruun model is based on the equilibrium profile concept with its results controlled by the beach slope and the closure depth which was abstracted from the database of Athanasiou (2019). The Edelman model can deal with temporally variable sea level changes and realistic beach profiles, whereas the Dean model assigns a greater significance on wave hydrodynamics than the previous models. The Leont'yev (1996) model uses the energetic approach to simulate the hydrodynamic conditions and estimates sediment transport separately for the surf and swash zones, whereas the SBEACH model contains descriptions of the wave transformation in shoaling waters and estimates sediment transport through the coastal wave energy flux. The Xbeach model contains a time dependent, wave action balance equation and simulates sediment transport using a depth-averaged advection/diffusion equation. Finally, the Boussinesq model computes nonlinear wave transformation involving high-order equations (Karambas and Koutitas, 2002) and its sediment transport module estimates sheet flow as well as bed and suspended load over uneven sea beds (e.g. Karambas, 2006). The numerical models were run from 20 m depth to the beach (up to a 10 m elevation above the mean level), with the simulation duration controlled by beach profile stabilization. Further details on the models used and their comparison with experimental data can be found elsewhere (e.g. Vousdoukas et al., 2009; Monioudi et al., 2016; Monioudi et al., 2017).

For each of the 322 recorded beaches, the nearest mean sea level, ESL and corresponding waves (at 20 m water depth) were selected

from their available projections along the coastline (Section 3.2) and were used to force the models. Given the spatial and temporal scales of the application, the input seabed slope and sediment data could not be based on observations or on open source nearshore bathymetric datasets (e.g. GEBCO or EMODnet products) due to their coarse resolution. Instead, the models, used in a stationary mode, were set up using a range of linear beach profiles; this was justified, since the validation of the models against physical experiments has shown that, at least for the conditions tested, the beach retreats projected from the model ensembles set up with equivalent linear profiles were reasonably close to those by the physical experiments with natural profiles (Monioudi et al., 2017).

Regarding the bed slopes and sediments, it has been widely suggested that beach face slopes and sediment size can be interdepended, with coarser sediment sizes associated with steeper slopes (e.g. Reis and Gama, 2010). Based on the slope-grain size relationship presented by Bujan et al. (2019) and on the recorded (qualitative) sediment texture (Section 3.1) a plausible range of beach slopes and median gain sizes were selected for each beach. Beaches were grouped in 3 categories based on their sediment texture: sandy, mixed (sandy gravels) and gravel beaches. The models were run for various combinations of bed slopes and median sediment sizes (d_{50}): bed slopes between 1/20 – 1/30 and sediment sizes between 0.2 and 0.8 mm for sandy beaches; (ii) bed slopes between 1/10 – 1/15 and sediment sizes between 0.8 and 1 mm for mixed texture beaches; and (iii) bed slopes between of 1/10 and sediment sizes (d_{50}) between 2 – 5 mm.

Cross-shore beach retreat was assessed for the 1-10, 1-50 and 1-100 year ESLs projected for the years 2050 and 2100 under the IPCC RCP4.5 (moderate) and RCP8.5 scenarios. Due to the different conditions used in the model set ups, each model produced a range of beach erosion projections. The minimum, maximum and median values of the projections of the ensembles were then calculated to project the minimum (most conservative), median and maximum beach retreat, respectively, for each beach (Supplementary Table 1). These retreats were then compared to the recorded beach maximum widths (BMWs) (Section 3.1) to assess the future impacts on each beach. The change in beach maximum width was selected as it is a conservative indicator regarding the impacts of the beach retreat on the safety of the (frontline) backshore infrastructure/assets and the beach carrying capacity, since a decrease in the recorded BMW implies even worse erosion and impacts for the rest of the beach. Projections are not provided for about 25% of the Cypriot beaches recorded as being 'perched' and/or protected by various coastal protection schemes (Velegrakis et al., 2016); nevertheless, these beaches will also experience impacts in the future, as most coastal defenses have not been designed to mitigate erosion under mean sea level rise (e.g. Arns et al., 2017). Finally, it is noted that beach retreats due to episodic extreme sea levels and waves may be reversible.

4 Results

4.1 Beach characteristics

In Cyprus, 322 beaches were recorded (Figure 1), with a total area of approximately about 2.9 km^2 that indicates a total beach

carrying capacity, i.e. the number of visitors that can be simultaneously hosted, of about 131,800 users (22 m^2 per user, Chen and Teng 2016). Regarding coastal management, the Republic of Cyprus administers 142 beaches (with an area of 1.24 km^2), whereas 163 (1.46 km^2), 10 (0. 2 km^2) and 7 beaches (0.01 km^2) are located in northern Cyprus, the UK Bases and the UN Administered Zone, respectively.

Most Cypriot beaches are narrow: almost 42% recorded maximum 'dry' beach widths (BMWs) of less than 20 m and 91% of less than 50 m, with only 0.6% recording maximum widths exceeding 100 m in the most recent images. Regarding the sediment texture, the majority of the beaches have been classified as sandy beaches (166 beaches, 52% of the total); this finding is in broad agreement with that presented in the Mediterranean coastal database of (Wolff et al., 2018). Mixed texture (sand- gravel beaches) was allocated to 103 beaches (32%), whereas about 16% were classified as gravel beaches. Very few beaches were found associated with active river mouths, whereas about half of the Cypriot beaches are backed directly by cliffs and/or coastal infrastructure and assets; such beaches have a high 'coastal squeeze' risk from increasing sea levels (Nicholls and Cazenave, 2010).

Statistical tests (a Levene's test followed by a Kruskal-Wallis test, p< 0.05) showed that beaches facing the northern sector (NW, N and NE, 53% of all beaches) recorded mean (per direction) BMWs of less than 20.5 m, whereas mean BMWs for the other directions were exceeding 36 m; the largest mean BMWs were found at the S and SW facing beaches (about 39 m). As the northern beaches are affected by less energetic waves (Section 4.2), these findings indicate that beach dimensions may have been controlled by the geology, antecedent topography and sediment supply rather than the wave energetics. For example, it appears that the northern beaches associated with the Troodos and Kyreneia terranes are generally narrower than those built in coastal areas associated with the other major geological units (Figure 1). A significant correlation (p< 0.05) was also found between BMWs and sediment texture: sandy beaches were found to be wider than those built on sand-gravel and, particularly, gravels. In addition to natural and geological factors, human interventions have been found to impact beach width (BMW). Beaches associated with coastal protection structures have an average BMW of 37.3 m, whereas unprotected beaches have an estimated average BMW of 24.6 m. This finding suggests that the presence of hard structures may have a positive effect on beach stability.

Most (63%) Cypriot beaches do not show any significant backshore development, which is an interesting finding, as Cyprus has a mature 3S tourism industry, with the majority of its beaches (85%) easily accessible by road (49% directly connected to the main road network) and there are also 45 'Blue Flag' beaches. The remainder of the beaches (37%) were found to directly front coastal infrastructure/assets, without any construction line 'set-back'; on these beaches there is a high/intense beach tourism during summer, manifested by the beach umbrellas and the presence of watersport facilities in many of them.

The density of the backshore frontline assets (where any) is variable, ranging from few houses observed in remote beaches to the heavy concentrations of public and private assets found behind the beaches of Larnaca, Limassol, Kyrenia and Famagusta (Figure 1). Frontline backshore asset coverage (expressed as a percentage of the beach length) is higher than 30% for about 13% of the Cyprus beaches, and higher than 80% for about 2% of the beaches. Finally, 77 beaches (24%) were observed to host coastal protection schemes, most of them (46) located in the Republic of Cyprus. Groynes were found to be the dominant schemes (14% of beaches) either alone or in mixed schemes that may also include offshore breakwaters or jetties. It should be noted that in the area of Limassol most beaches (no 29-54) are fronted by detached breakwaters that cover the entire beach length.

Analysis of the changes in BMWs (Figure 3) showed discernible decreases for 152 (48%) beaches and increases for 164 (52%) beaches (Figure 4A); interestingly these results appear comparable to those of the global assessment of Luijendijk et al. (2018). It is noted that in the present study manual mapping was carried out using high resolution Google Earth images, whereas in the global Luijendijk et al. (2018) assessment an automated mapping technique on coarser 30 m Landsat images was applied. Concerning the frontline backshore development (urbanization) (Figure 4B), 46 beaches showed discernible changes in the coverage of the frontline backshore assets (as a percentage of the beach length), with fast development detected mostly along the southern and the eastern coast.

4.2 Mean and extreme sea levels and waves

Mean sea levels are projected to rise considerably in the course of the century, with the rate of rise increasing with the time and the RCP scenario; small spatial RSLR variability (0.01-0.05 m) is also projected along the coastline (Table 1). In comparison, ESLs are projected to be more variable and consistently higher along the southern and western Cyprus coast (Table 1 and Figure 5). For the baseline (2000) year, the 1 in a 100 years extreme sea level (ESL$_{100}$), was found to range along the coast between 0.83 and 1.29 m above the mean sea level. Future ESLs will also exhibit spatial variability, with the differentials between the highest and the lowest ESLs$_{100}$ projected along the coastline (at beaches 73-86 and 225-235, respectively) varying between 23 and 35%, depending on the date and climatic scenario.

ESLs are projected to rise in the course of the century, being increasingly controlled by the emission scenario (Table 1). For example, the maximum ESL$_{100}$ along the Cyprus coastline in 2050 is projected as 1.47 and 1.54 m higher than the baseline mean sea level under RCP4.5 and RCP8.5, respectively, whereas in 2100 the spread between the two climatic scenarios has increased threefold (1.74 - 2.04). It also appears that the ESL increases are controlled by the RSLR (Table 1). Considering the corresponding to the baseline ESL$_{100}$ waves (Section 3.2), their heights and periods were projected to also differ along the coastline, varying between 1.1 and 2.35 m and 4.1 and 7.3 s, respectively (Table 1). More energetic waves were consistently projected along the western and southern coasts (Figure 5), but heights appear to be overall slightly decreasing
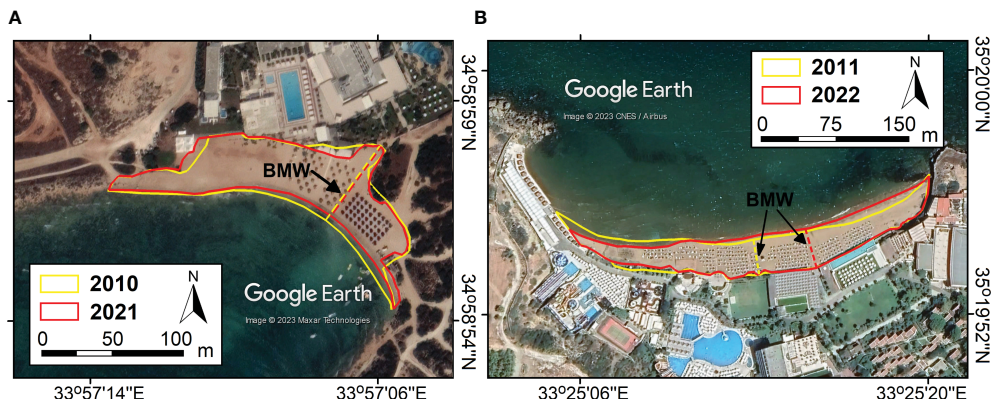
FIGURE 3
Beach delimitation in the historical imagery of **(A)** a southern beach (ID 27) and **(B)** a northern beach (ID 223) (for location see Figure 1). The differing landward boundary position in **(A)** is due to changes in vegetation coverage. Note that there are apparent area losses in both embayed beaches, but the maximum beach widths (BMWs, stippled lines) of the 'dry' beaches have not changed significantly.

during the century under most tested scenarios (see also Camus et al., 2017).

Regarding the contributions of the different ESL components and their temporal evolution (Table 1), no changes are projected for the tidal range/maxima. It also appears that although the episodic η_{CE} is the primary contributor of the baseline period, its dominance will decrease in the future as it will change little compared with the accelerating RSLR (e.g. Androulidakis et al., 2015).
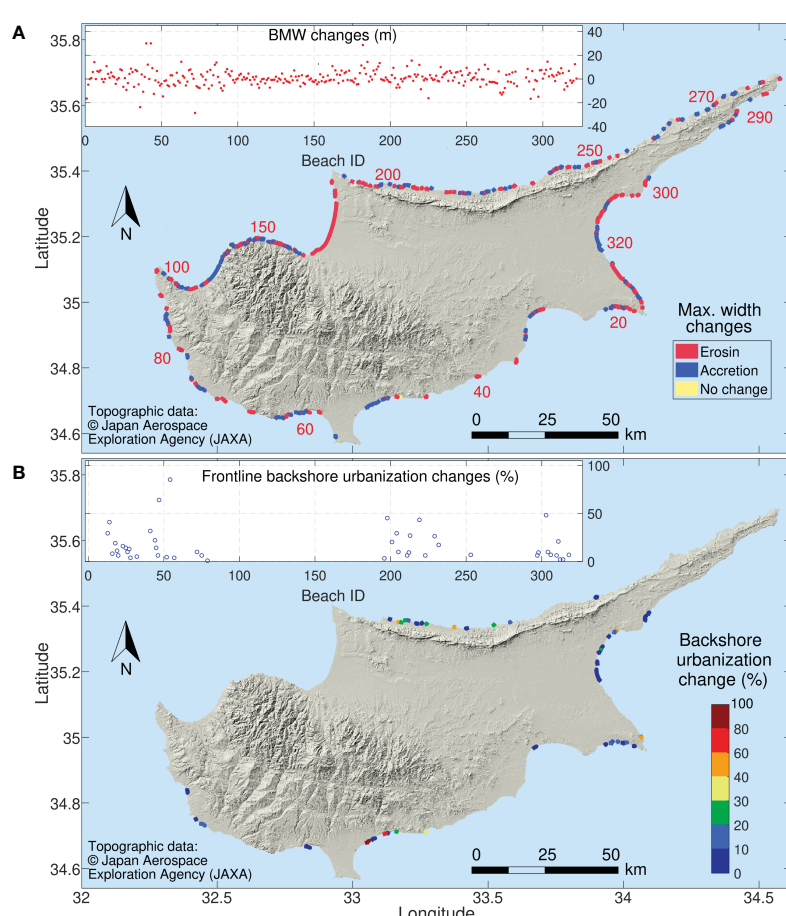
FIGURE 4
Historical changes in the **(A)** recorded BMWs and **(B)** frontline backshore urbanization, i.e. in the coverage of the frontline assets as a percentage of the beach length (only the 46 beaches recording changes are shown). Changes shown are between the periods 2010-2014 and 2020-2022.

The return periods of ESL events with particular magnitudes will significantly decrease over time (Table 1 and Figure 6); for example, depending on the location along the Cypriot coastline, the baseline (2000) ESL_{100} will be occurring in 2050 every about 9 – 27 (RCP4.5) and 2.5 – 13 years (RCP8.5). respectively. By 2100, and under the RCP8.5 scenario, the baseline ESL_{100} will occur many times annually. These projections may have significant implications for the design of coastal works.

Changes in the intensity/direction of (extreme) coastal wave energy fluxes (*WEFs*) under CV&C could also impact the Cypriot coastal natural and human environment. Global simulations for the extreme *WEFs* (Mentaschi, 2017), suggest that Cypriot coastline is currently characterized by relatively low to moderate extreme *WEFs*, with the highest intensities found in the western Cyprus. Our analysis shows that the 100-year significant wave height ranges between 0.95 and 2.16 m with higher waves observed at the W and SW coast of Cyprus and less energetic waves at the NE and E coast; no significant changes are observed through the course of the century (Figure 5)

4.3 Beach retreat

Models generally displayed differential behavior for almost all tested conditions, showing varying shoreline retreats and profile changes (Figure 7). At the same time, each model gave a range of results, reflecting the varying bed slopes and sediment sizes used; thus, the median value and minimum and maximum projections for each condition and scenario tested are considered (see also Section 3.3). The beach slope and hydrodynamics were found to represent major controls. Beach retreat projections decreased with increasing Iribarren number ($\xi = (\beta/(H/L)^{1/2}$, where β the seabed slope and H and L the wave height and length, respectively), for the range of bed slopes and wave conditions considered.

The most sensitive models were found to be the Edelman and the SBEACH models and the least sensitive the XBeach model. Regarding the sediment texture, a weak decreasing trend in beach retreat was observed (for the numerical models) with increases in the sediment size. Generally, Xbeach provided the most 'pessimistic' predictions (Figure 7), whereas the Leont'yev and SBEACH models projected similar retreats. With regard to the analytical models, the Dean model gave the highest erosion predictions, whereas the Bruun and Edelman models projected mostly similar retreats.

RSLR was projected by the analytical model ensemble to lead to beach retreats (Table 2). By 2050, according to the projection median values, about 2% of the tested beaches will retreat by more than 100% and about 11 and 16% by 50% of the current BMW under the RCP4.5 (Figure 8) and RCP8.5, respectively.

By 2100, beach retreat has been projected to be very significant: between 9 and 30% of the (currently unprotected) Cypriot beaches will retreat by > 100% of their current BMW under RCP4.5 and RCP8.5, respectively, whereas between 47 and 72% will retreat by

TABLE 1   Ranges of the 10-, 50- and 100-year extreme sea levels (ESLs₁₀, ESLs₅₀ and ESLs₁₀₀) and their components (RSLR, η_{tide}, and η_{CE}) and corresponding wave conditions along the Cypriot coastline (Figure 4) for different dates (2000-baseline, 2050 and 2100) and under the IPCC RCP4.5 and RCP8.5 scenarios.

		Extreme Sea Level (ESL) ranges along the Cyprus coastline				
	T_r	Baseline	RCP 4.5		RCP 8.5	
		2000	2050	2100	2050	2100
RSLR (m)	–	0	0.21-0.23	0.47-0.52	0.27-0.29	0.78-0.83
η_{tide} (m)	–	0.12-0.15	0.12-0.15	0.12-0.15	0.12-0.15	0.12-0.15
η_{CE} (m)	10	0.52-0.90	0.49-0.85	0.48-0.83	0.51-0.87	0.49-0.83
	50	0.63-1.07	0.58-1.02	0.58-1.00	0.61-1.03	0.59-0.99
	100	0.69-1.16	0.64-1.11	0.64-1.10	0.66-1.12	0.65-1.08
ESL(m)	10	0.66-1.02	0.85-1.21	1.09-1.47	0.92-1.28	1.42-1.78
	50	0.77-1.19	0.94-1.38	1.19-1.64	1.02-1.45	1.52-1.95
	100	0.83-1.29	1.00-1.47	1.25-1.74	1.08-1.54	1.57-2.04
H_s (m)	10	0.83-1.87	0.77-1.81	0.78-1.77	0.80-1.83	0.78-1.77
	50	0.97-2.17	0.91-2.08	0.91-2.03	0.90-2.08	0.94-2.03
	100	1.06-2.35	0.97-2.23	1.02-2.21	1.02-2.27	0.98-2.17
T (s)	10	4.07-6.79	4.10-6.70	4.11-6.77	4.07-6.75	4.10-6.75
	50	4.12-7.12	4.13-7.00	4.12-7.03	4.12-7.11	4.12-7.03
	100	4.11-7.33	4.06-7.23	4.07-7.22	4.09-7.26	4.08-7.07

Key: T_r, extreme event return period (years); RSLR, mean sea level rise relative to the baseline mean sea level; η_{tide}, max. tidal level; η_{CE}, storm sea level component; H_s, significant wave height; T, wave period.
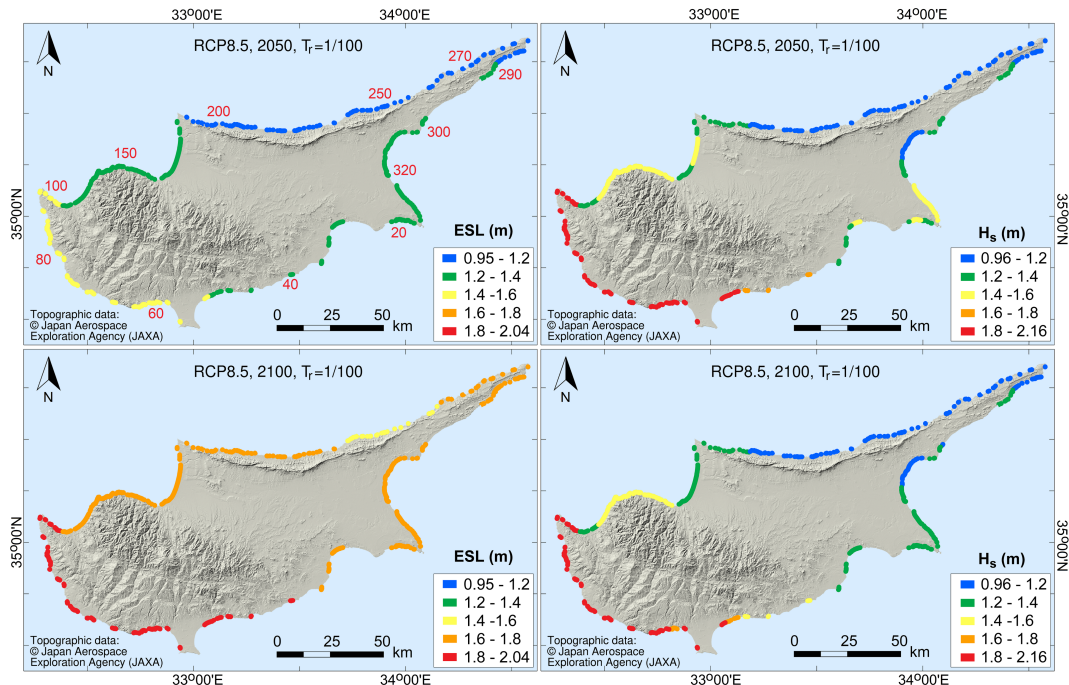
FIGURE 5
Extreme sea levels (T_r 1/100, $ESLs_{100}$) and corresponding wave heights (H_s) at the Cypriot beaches for different dates under RCP8.5.

50% of their current BMW. As many of these beaches lack the accommodation space to retreat landwards (Table 2), such retreats may translate to coastal squeeze and permanent erosion (Nicholls and Cazenave, 2010). In this case, appropriate beach replenishment schemes would be required to avoid damage to the backshore

assets/infrastructure and maintain the beach carrying capacity (e.g. Monioudi and Velegrakis, 2022).

Cypriot beaches are also threatened by the extreme events (Table 2). According to the median projections of the numerical model ensemble, the 10-, 50- and 100-year events (ESL_{10}, ESL_{50} and
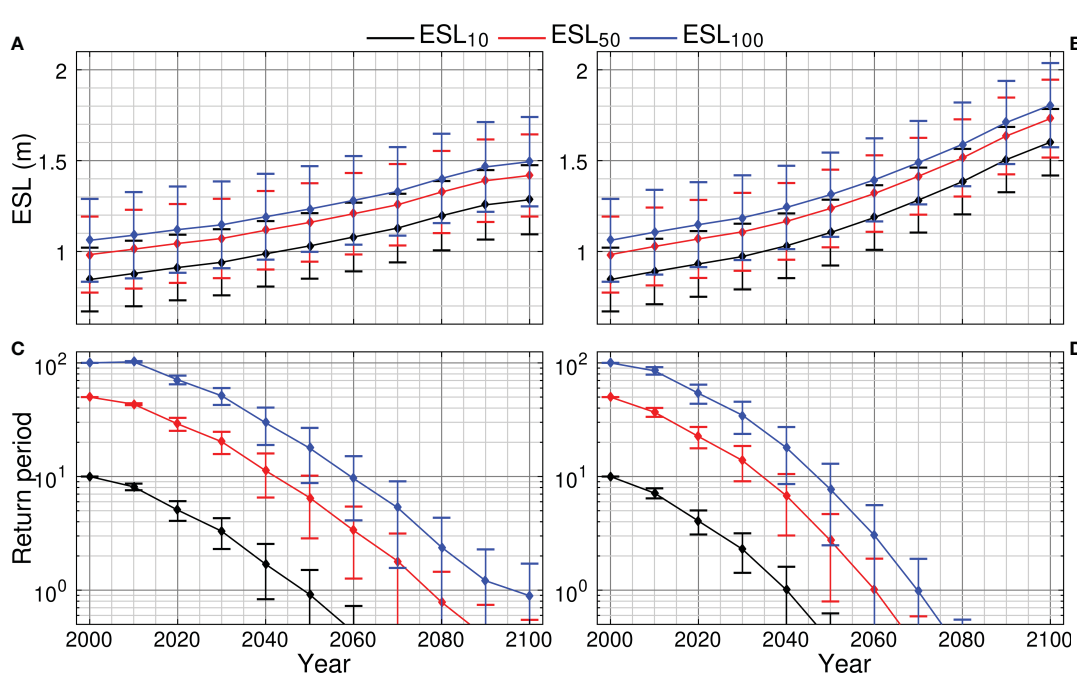
FIGURE 6
Time evolution of ESLs, i.e., the sum of the RSLR, the maximum astronomical tide and the episodic level rise due to storm surges and wave set ups (A, B) and of their corresponding return periods (C, D) compared to their baseline return periods for the 10- 50- and 100-year events, under RCP4.5 (A, C) and RCP8.5 (B, D). Predictions are for all beaches which explains the result spread.
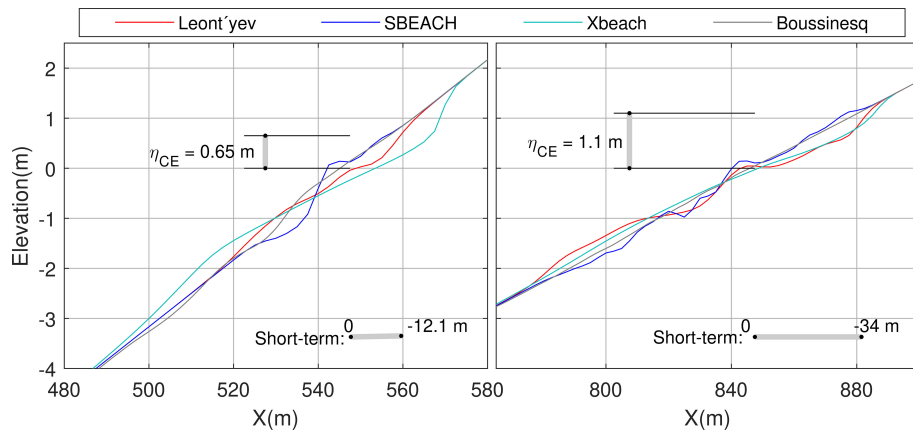
FIGURE 7
Morphodynamic changes in the upper beach profile of a northern beach (left, ID 238, equivalent linear bed slope: 1/15, d_{50}: 1 mm) and a southern beach (right, ID 73, 1/30, 0.5 mm) projected by the numerical (short-term) model ensemble. Projections are for the ESL_{100}. Models are forced by waves (at 20 m water depth, origin of x axis) with heights of 1 and 2 m and periods of 6 and 7 s, respectively. Mean shoreline retreats for 2050 (RCP4.5) are shown as horizontal bars. Key: η_{CE}, episodic level rise.

ESL_{100}) in 2050 (RCP4.5) will result in storm beach retreats of up to about 30, 34 and 37 m, respectively; under RCP8.5, retreat is projected to be slightly greater (up to about 32, 36 and 39 m); the difference in the projections between the two RCP scenarios will increase by 2100 (Table 2). Although these retreats can be temporary and the beaches could in time partially or totally recover, there could be very significant impacts on the backshore frontline infrastructure/assets. By 2050 and under RCP4.5, about 37, 45 and 47% of the beaches tested are projected to temporarily retreat by more than 100% of their current BMW, under the ESL_{10},

ESL_{50}, and ESL_{100}, respectively, whereas under RCP 8.5, more beaches (43, 49 and 54%, respectively) will retreat more than their current BMWs. By 2100, shoreline retreats under extreme events could be devastating for the backshore assets/infrastructure under both tested scenarios (Table 2). Concerning the spatial distribution of the projections, the most impacted beaches will be also along the northern and eastern Cyprus coast (Figure 9).

It appears that in the next decades, many Cyprus beaches and their backshore infrastructure/assets will be seriously impacted by extreme events. It should be noted that these projections are

TABLE 2 Model ensembles' estimates of the range of median beach retreat (S_{median}) along the Cyprus coast under mean sea level rise and extreme events.

Sea Level				S_{median} (Range-all beaches) (m)	Retreat to 50% of max. width (%)	Retreat to max. width (%)	Beaches with assets affected	
	Year	RCP	(m)				N	%
RSLR	2050	4.5	0.21-0.23	2.8-9.0	11.2	1.7	1	1.9
		8.5	0.27-0.29	3.4-10.4	16.2	2.1	1	1.9
	2100	4.5	0.47-0.52	5.3-16.1	46.9	8.7	5	9.4
		8.5	0.78-0.83	8.5-23.9	72.2	29.9	13	24.5
ESL_{10}	2050	4.5	0.85-1.21	8.9-30.1	80.1	36.9	17	32.1
		8.5	0.92-1.28	9.6-32.0	83.4	42.7	18	34.0
	2100	4.5	1.09-1.48	11.4-36.7	88.4	50.6	23	43.4
		8.5	1.42-1.78	14.8-44.3	94.2	67.6	31	58.5

(Continued)

TABLE 2 Continued

Sea Level				S_{median} (Range-all beaches) (m)	Retreat to 50% of max. width (%)	Retreat to max. width (%)	Beaches with assets affected	
	Year	RCP	(m)				N	%
ESL$_{50}$	2050	4.5	0.94-1.38	9.8-34.3	84.6	45.2	18	34.0
		8.5	1.02-1.45	10.7-36.2	86.7	48.5	21	39.6
	2100	4.5	1.19-1.64	12.4-41.1	92.9	57.7	27	50.9
		8.5	1.52-1.95	15.8-48.7	95.0	70.5	33	62.3
ESL$_{100}$	2050	4.5	1.00-1.47	10.4-36.7	87.1	49.0	20	37.7
		8.5	1.08-1.54	11.3-38.6	90.9	53.9	24	45.3
	2100	4.5	1.25-1.74	13.0-43.5	92.9	29.0	29	54.7
		8.5	1.57-2.04	16.3-51.0	95.4	71.8	33	62.3

Percentages refer to 241 Cypriot beaches (perched/protected beaches were excluded) that are projected to retreat by more than 50% of their current BMW and more than their current BMW. Numbers (N) and percentages of beaches where (current) frontline backshore infrastructure/assets are projected to be impacted are also shown.

considered conservative as: a) they refer to retreats relative to the recorded beach maximum widths; and b) they do not account for other beach retreat/erosion contributing factors such as potential beach sediment losses from the extreme events (and their sequencing) during the intervening time and the diminishing river sediment supply due to the many Cyprus riverine dams (Section 2).

5 Discussion

Most approaches for regional and large-scale assessments of shoreline retreats under climate change have limitations stemming from, amongst others, their requirements for detailed coastal topographic information (e.g. Rueda et al., 2017). In the present approach, ranges of shoreline retreats under the mean and extreme sea levels (and corresponding waves) are projected for different plausible bed slopes and sediment sizes; thus, it can account for the lack of specific information on the slope of the active beach profile (Ranasinghe et al., 2012) and sediments when such information is not available which is commonly the case for the present and, certainly, for the future beaches. Nevertheless, there are also several constraints.

Regarding the historical trends, in addition to the difficulty to extract probabilistic estimates of shoreline retreat required in coastal management/planning frameworks (Ranasinghe, 2016), there are also geo-referencing issues in the imagery comparisons, as well as issues associated with the varying hydrodynamic conditions during the image collection that can affect shoreline delimitation (e.g. Chatzipavlis et al., 2019). Although the former is

not a large issue as the 'dry' beach maximum widths are used in the comparisons, the latter may introduce uncertainties which, however, cannot be avoided in large-scale studies (e.g. Mentaschi et al., 2018).

Some processes are inevitably neglected in the modeling. These include, amongst others, cumulative storm impacts, the effects of storm duration/spacing, as well as the potential effects of a changing wave regime on multi-decadal mean sea level changes (Callaghan et al., 2008; Melet et al., 2018). Moreover, predictions are based on the assumption that the Cyprus (mostly 'pocket') beaches comprise sediment reservoirs with no lateral sediment exchanges and/or other sediment sinks/sources (e.g. Dean and Houston, 2016). In addition, although perched/protected beaches were excluded from the beach retreat projections to avoid uncertainties from the influence of the natural and/or artificial coastal protection structures (e.g. Velegrakis et al., 2016; Stripling et al., 2017), the implications of potential nearshore benthic ecosystems (e.g. seagrasses) on wave attenuation (e.g. Twomey et al., 2020; Peduzzi et al., 2022) have not been considered. Finally, the results are based on cross-shore modelling which cannot account for longshore sedimentary processes/transport; this issue, however, cannot be resolved without incorporating full 2D (or 3D) modeling that requires detailed topographic/sedimentary information for meaningful set up and high computational resources, which are prohibitively expensive endeavors for other than local scale assessments (Le Cozannet et al., 2014; Toimil et al., 2017).

Notwithstanding these constraints, the study provides the first comprehensive assessment of the Cypriot beach retreat/erosion hazard under climate change on the basis of easily obtainable
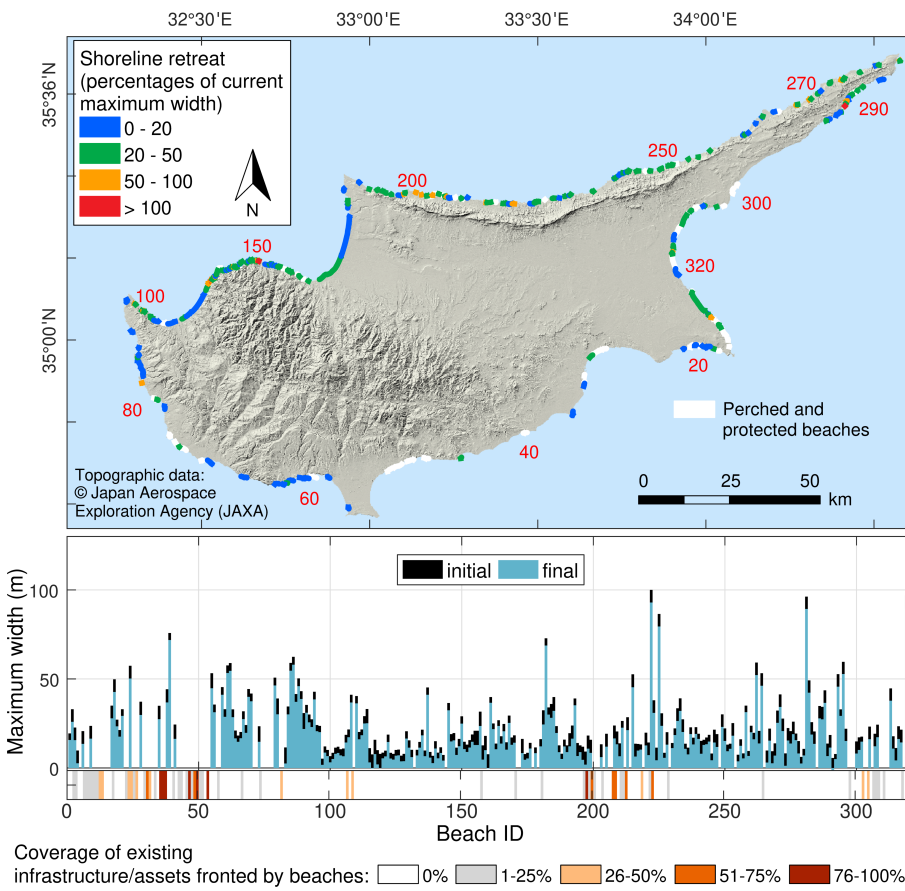
FIGURE 8

Projection of the impacts of the RSLR under RCP4.5 on the 241 currently unprotected Cypriot beaches in 2050. The impacts are shown on the map as reductions (%) in the current BMW due to the median beach retreats projected by the analytical model ensemble (Section 3.3). In the lower panels, the projected median retreats are shown together with the recorded coverage of frontline backshore assets (as a percentage of the beach length); the current (initial) BMWs (black bars) are compared with those resulting from the beach retreats (blue bars).

information and modest investment in resources. Results could be fine-tuned, if high resolution coastal topographies/bathymetries (DEMs) were to become available. In any case, the aim of the exercise has not been to replace detailed local studies for individual beaches (Ranasinghe, 2016).

Under the RSLR alone, beach retreat/erosion has been projected to become an issue after 2050. By comparison, the projected increases in ESLs combined with the corresponding storm waves will have severe impacts on Cyprus beaches; by 2100, impacts could be devastating (Table 2). It is noted that the present projections refer to shoreline retreat/erosion and cannot deal with the implications of the potential increases in coastal flooding and/or wave runup. Regarding the former, a study on the European coastal flood risk has estimated that the Expected Annual Damages (EADs) in Cyprus will range from 0.6 to 0.8% and 1.7 to 8.3% of Cyprus GDP in 2050 and 2100, respectively, depending on the scenario (Vousdoukas et al., 2018a). Concerning the latter, although wave runup (i.e., the wave incursion length (or height) onto the dry beach under extreme waves) is a critical factor for shoreline change (e.g. Chatzipavlis et al., 2019) as well as a very significant boundary for the legal demarcation of the beach (Velegrakis et al., 2021), its

assessment requires detailed/accurate nearshore bathymetric information (e.g. Gomes da Silva et al., 2020; Almar et al., 2021).

The findings of the present study strongly indicate that plans to respond effectively to projected beach erosion/retreat should be urgently drawn up in Cyprus with different adaptation options considered. First, effective policies and regulation should be introduced. The allocation of buffer ('set-back') zones, such as those prescribed in Art. 8.2 of the 2008 ICZM Protocol to the Barcelona Convention (ICZM, 2008), behind retreating shorelines where no future development shall be allowed, could be a critical regulatory development (e.g. Summers et al., 2018). Nevertheless, since many Cypriot beaches show minimal (or no) backshore development (Section 4.1), both sustainable policies and coastal development might still be possible.

Secondly, several adaptation options should be considered, although given the dire nature of the problem costly 'hard' engineering schemes might be, in many cases, inevitable (e.g. Narayan et al., 2016). Projections on the future magnitude and recurrence frequency of ESLs and waves along the island's coast can provide vital information for the selection, design, timing, costs and benefits of the requisite technical responses (Arns et al., 2017); in
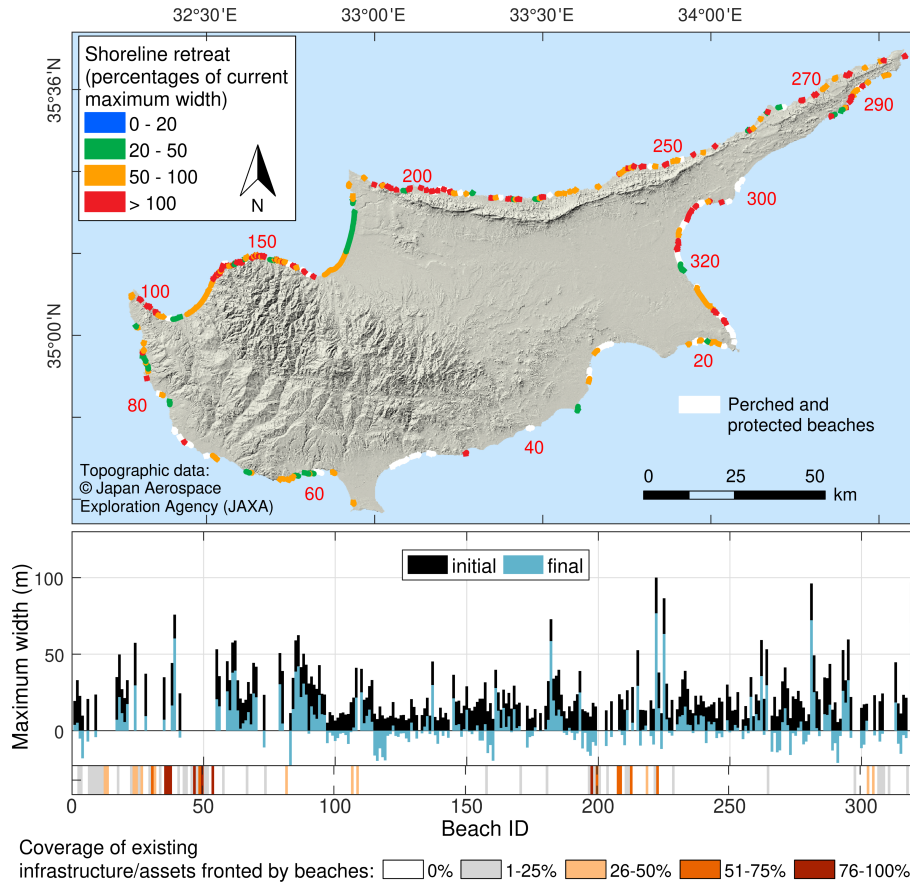
FIGURE 9
Projection (RCP4.5) of the ESL$_{100}$ impacts on the 241 currently unprotected Cypriot beaches in 2050, shown as decreases (%) in the current BMW due to the median projections by the numerical model ensemble (Section 3.3). In the lower panels, the projected median retreats are shown together with the recorded coverage of the frontline backshore assets (as a percentage of the beach length); the current (initial) BMWs (black bars) are compared with those resulting from the beach retreat projections (blue bars); negative values indicate beach retreat more than the current BMW.

any case, such assessments are prescribed by the European Directive 2014/52/EU for all future coastal projects in the EU Members States.

The importance of the beaches as socio-economic resources and the low effectiveness of the hard coastal defenses (groynes, offshore breakwaters and seawalls/revetments) to protect them under increasing mean sea levels (Semeoshenkova and Newton, 2015; Beuzen et al., 2018), suggest that beach replenishment schemes will be required, at least for beaches which function as "armors" to valuable backshore infrastructure and assets, serve as important environments of leisure and/or have particular environmental significance (e.g. marine turtle nesting beaches, Mavris, 2011). The results of our analysis indicate that the presence of hard structures may have a positive effect on beach stability. However, it is important to note that the effectiveness of these coastal protection structures cannot be definitively concluded due to the fact that beach nourishment projects are also commonly implemented in the most touristic beaches of the southern sector, where the majority of coastal works have been implemented. As marine aggregates form the most suitable (but often scarce) material for beach replenishment (Velegrakis et al., 2010), the sustainability of such deposits, should be ensured in the marine spatial planning of Cyprus (see also EU Directive 2014/89/EU), as a matter of

priority. Moreover, and considering that the intense dam construction in Cyprus have been found in past studies to cause recession of adjacent beaches and delta areas through sediment trapping (Toumazis et al., 2008), efficient management of terrestrial sediments is required.

6 Conclusion

This study represents the first comprehensive effort to record the characteristics of the beaches of the island of Cyprus and provide an assessment of their exposure to erosion due to Climate Change. Cypriot beaches were found to be mostly sandy and narrow with 91% recording maximum widths of less than 50 m and only 0.6% of more than 100 m. Analysis of the historical changes showed (a) discernible erosion and accretion in 152 and 164 beaches, respectively and (b) increases in backshore urbanization at 46 beaches, which are mostly located along the southern and eastern coast. Substantial increases in the magnitude of RSLR and ESLs were projected for the 21st century, which will vary along the Cyprus coast with the highest ESLs (and waves) projected for its western and southern sectors.

In terms of beach erosion, even under a moderate emission scenario (RCP4.5) and as early as 2050, the one in 100-year extreme sea level event (ESL_{100}) could completely (at least temporarily) overwhelm 49% of the 241 unprotected Cyprus beaches in the absence of effective technical responses. In 2100 impacts will be devastating, with 72% of (currently unprotected) beaches projected to be completely (at least temporarily) eroded under the business as usual (i.e. RCP8.5) scenario, with the most exposed beaches located along the western and northern coast. These results suggest that the primary natural resource of the island's booming 3S tourism is under a clear and increasing risk. Plans to respond effectively to the projected risk should be urgently drawn up with different regulatory (shoreline development) and technical adaptation (coastal fortification) options examined.

The approach adopted in the present study can provide a framework for regional assessments of the beach erosion under climate change and produce vital information for the selection, design and timing of the requisite technical adaptation options. In this context, it may assist managers and policy makers at island settings to identify beaches under increased risk, estimate losses in beach carrying and hedonic value, and plan and prioritize effective adaptation responses.

Data availability statement

The raw data supporting the conclusions of this article will be made available by the authors, without undue reservation.

Author contributions

IM, AV, and TH contributed to the conception, scope and design of the study. IM assembled the models, performed the simulations to assess beach erosion under mean and extreme sea levels and wrote sections of the manuscript. AV contributed to the results interpretation and discussion and wrote sections of the manuscript. MV and LM performed the dynamic simulations for the projections of the extreme sea levels, their components and the waves. DP and OM-N performed the bivariate copula statistics to obtain the corresponding most likely wave characteristics for the episodic sea level rise. DC and CS studied/selected the satellite images to be analyzed, and assembled the beach inventory. AC performed the statistical analysis of the database and wrote the relevant sections of the manuscript. DW, EM, and GB collated the information regarding the environmental setting, wrote the

corresponding sections of the manuscript and prepared the relevant figures. All authors contributed to the article and approved the submitted version.

Conflict of interest

The authors declare that the research was conducted in the absence of any commercial or financial relationships that could be construed as a potential conflict of interest.

Publisher's note

All claims expressed in this article are solely those of the authors and do not necessarily represent those of their affiliated organizations, or those of the publisher, the editors and the reviewers. Any product that may be evaluated in this article, or claim that may be made by its manufacturer, is not guaranteed or endorsed by the publisher.

Supplementary material

The Supplementary Material for this article can be found online at: https://www.frontiersin.org/articles/10.3389/fmars.2023.1188896/full#supplementary-material

References

Ackerman, R. A. (2017). "The nest environment and the embryonic development of sea turtles," in *The biology of Sea turtles*. Eds. P. L. Lutz and J. A. Musick (Boca Raton: CRC Press), 83–106.

Almar, R., Ranasinghe, R., Bergsma, E. W. J., Diaz, H., Melet, A., Papa, F., et al. (2021). A global analysis of extreme coastal water levels with implications for potential coastal overtopping. *Nat. Commun.* 12, 3775. doi: 10.1038/s41467-021-24008-9

Alvarez, S., Bahja, F., and Fyall, A. (2022). A framework to identify destination vulnerability to hazards. *Tour. Manag.* 90, 104469. doi: 10.1016/j.tourman.2021.104469

Anderson, T. R., Fletcher, C. H., Barbee, M. M., Romine, B. M., Lemmo, S., and Delevaux, J. M. S. M. S. (2018). Modeling multiple sea level rise stresses reveals up to twice the land at risk compared to strictly passive flooding methods. *Sci. Rep.* 8, 14484. doi: 10.1038/s41598-018-32658-x

Androulidakis, Y. S., Kombiadou, K. D., Makris, C. V., Baltikas, V. N., and Krestenitis, Y. N. (2015). Storm surges in the Mediterranean Sea: variability and trends under future climatic conditions. *Dynamics. Atmospheres. Oceans.* 71, 56–82. doi: 10.1016/j.dynatmoce.2015.06.001

Arns, A., Dangendorf , S., Jensen, J., Talke, S., Bender, J., and Pattiaratchi, C. (2017). Sea-Level rise induced amplification of coastal protection design heights. *Sci. Rep.* 7, 40171. doi: 10.1038/srep40171

Athanasiou, P. (2019). *Global distribution of nearshore slopes*. Version 1, dataset. Internet: 4TU.Centre for Research Data. doi: 10.4121/uuid:a8297dcd-c34e-4e6d-bf66-9fb8913d983d

Bellard, C., Leclerc, C., and Courchamp, F. (2014). Impact of sea level rise on the 10 insular biodiversity hotspots. *Glob. Ecol. Biogeogr.* 23, 203–212. doi: 10.1111/geb.12093

Beuzen, T., Turner, I. L., Blenkinsopp, C. E., Atkinson, A., Flocard, F., and Baldock, T. E. (2018). Physical model study of beach profile evolution by sea level rise in the presence of seawalls. *Coast. Eng.* 136, 172–182. doi: 10.1016/j.coastaleng.2017.12.002

Boto-García, D., and Leoni, V. (2022). *The hedonic value of coastal amenities in peer-to-peer markets* (DEA WP no.94. Palma, Ballearic Islands, Palma, Ballearic Islands: Departament d'Economia Aplicada, Universitat de Les Illes Balears).

Bruun, P. (1988). The bruun rule of erosion by Sea-level rise: a discussion on Large-scale two- and three-dimensional usages. *J. Coast. Res.* 4, 627–648.

Bujan, N., Cox, R., and Masselink, G. (2019). From fine sand to boulders: examining the relationship between beach-face slope and sediment size. *Mar. Geol.* 417, 106012. doi: 10.1016/j.margeo.2019.106012

Callaghan, D. P., Nielsen, P., Short, A., and Ranasinghe, R. (2008). Statistical simulation of wave climate and extreme beach erosion. *Coast. Eng.* 55, 375–390. doi: 10.1016/j.coastaleng.2007.12.003

Camus, P., Losada, I. J., Izaguirre, C., Espejo, A., Menéndez, M., and Pérez, J. (2017). Statistical wave climate projections for coastal impact assessments. *Earths. Future* 5, 918–933. doi: 10.1002/2017EF000609

CEM (2002). *Coastal engineering manual* (Washington, DC: U.S. Army Corps of Engineers).

Chatzipavlis, A., Tsekouras, G. E., Trygonis, V., Velegrakis, A. F., Tsimikas, J., Rigos, A., et al. (2019). Modeling beach realignment using a neuro-fuzzy network optimized by a novel backtracking search algorithm. *Neural Comput. Appl.* 31 (6), 1747–1763. doi: 10.1007/s00521-018-3809-2

Chen, C.-L., and Teng, N. (2016). Management priorities and carrying capacity at a high-use beach from tourists' perspectives: a way towards sustainable beach tourism. *Mar. Policy* 74, 213–219. doi: 10.1016/j.marpol.2016.09.030

Ciavola, P., Harley, M. D., and den Heijer, C. (2018). The RISC-KIT storm impact database: a new tool in support of DRR. *Coast. Eng.* 134, 24–32. doi: 10.1016/j.coastaleng.2017.08.016

CYSTAT (2017) *Tourism statistics 2016* (Nicosia, Cyprus: Statistical Service of Cyprus). Available at: https://library.cystat.gov.cy/Documents/Publication/TOURISM_STATISTICS-2016-141117.pdf (Accessed February 2, 2023).

CYSTAT (2019) *Tourism statistics 2017-2019* (Nicosia, Cyprus: Statistical Service of Cyprus). Available at: https://library.cystat.gov.cy/Documents/Publication/TOURISM_%20STATISTICS-2017_19-EN-120820.pdf (Accessed February 2, 2023).

Dean, R. G. (1991). Equilibrium beach profiles: characteristics and applications. *J. Coast. Res.* 7, 53–84.

Dean, R. G., and Houston, J. R. (2016). Determining shoreline response to sea level rise. *Coast. Eng.* 114, 1–8. doi: 10.1016/j.coastaleng.2016.03.009

de Winter, R. C., and Ruessink, B. G. (2017). Sensitivity analysis of climate change impacts on dune erosion: case study for the Dutch Holland coast. *Clim. Change* 141, 685–701. doi: 10.1007/s10584-017-1922-3

Di Paola, G., Rodríguez, G., and Rosskopf, C. M. (2023). Shoreline dynamics and beach erosion. *Geosciences* 13 (3), 74. doi: 10.3390/geosciences13030074

Edelman, T. (1972). "Dune erosion during storm conditions," in *13th conference on coastal engineering* (Vancouver, Canada: ASCE), 1305–1312. doi: 10.1061/9780872620490.073

Farmaki, A., Altinay, L., Botterill, D., and Hilke, S. (2015). Politics and sustainable tourism: the case of Cyprus. *Tour. Manage.* 47, 178–190. doi: 10.1016/j.tourman.2014.09.019

Galanis, G., Hayes, D., Zodiatis, G., Chu, P. C., Kuo, Y.-H., and Kallos, G. (2012). Wave height characteristics in the Mediterranean Sea by means of numerical modeling, satellite data, statistical and geometrical techniques. *Mar. Geophys. Res.* 33, 1–15. doi: 10.1007/s11001-011-9142-0

Genest, C., Rémillard, B., and Beaudoin, D. (2009). Goodness-of-fit tests for copulas: a review and a power study. *Insur. Math. Econ.* 44, 199–213. doi: 10.1016/j.insmatheco.2007.10.005

Giardino, A., Schrijvershof, R., Nederhoff, C. M., de Vroeg, H., Brière, C., Tonnon, P.-K., et al. (2018). A quantitative assessment of human interventions and climate change on the West African sediment budget. *Ocean. Coast. Manage.* 156, 249–265. doi: 10.1016/j.ocecoaman.2017.11.008

Gomes da Silva, P., Coco, G., Garnier, R., and Klein, A. H. F. (2020). On the prediction of runup, setup and swash on beaches. *Earth Sci. Rev.* 204, 103148. doi: 10.1016/j.earscirev.2020.103148

Hinkel, J., Nicholls, R. J., Tol, R. S. J., Wang, Z. B., Hamilton, J. M., Boot, G., et al. (2013). A global analysis of erosion of sandy beaches and sea-level rise: an application of DIVA. *Glob. Planet. Change* 111, 150–158. doi: 10.1016/j.gloplacha.2013.09.002

IBESTAT (2023) *Turismo. flujo de turistas (FRONTUR)*. Available at: https://www.caib.es/ibestat/estadistiques/043d7774-cd6c-4363-929a-703aaa0cb9e0/ed5d4d88-cb17-46bd-b7b0-29fbaa5dba19/es/I208002_n101.px (Accessed February 25, 2023).

ICZM (2008) *Protocol to the Barcelona convention on integrated coastal zone management (ICZM) in the Mediterranean*. Available at: https://www.unep.org/unepmap/who-we-are/contracting-parties/iczm-protocol (Accessed February 25, 2023).

ILO (2020) *Tourism sector in the English- and Dutch speaking Caribbean: an overview and the impact of COVID-19 on growth and employment* (Port of Spain: International Labour Organization, Office for the Caribbean). Available at: http://www.ilo.int/wcmsp5/groups/public/—americas/—ro-lima/—sro-port_of_spain/documents/publication/wcms_753077.pdf (Accessed February 15, 2023).

INE (2023). *Tourist movements at borders (FRONTUR) December 2022 and 2022 year. provisional data* (Madrid, Spain: Instituto Nacional de Estadística. Madrid, Spain).

IPCC (2019). "Summary for policymakers," in *IPCC special report on the ocean and cryosphere in a changing climate*. Eds. H.-O. Pörtner, D. C. Roberts, V. Masson-Delmotte, P. Zhai, M. Tignor, E. Poloczanska, et al. (Cambridge, UK and New York, NY, USA: Cambridge University Press), 3–35. doi: 10.1017/9781009157964.001

Jevrejeva, S., Jackson, L. P., Riva, R. E. M., Grinsted, A., and Moore, J. C. (2016). Coastal sea level rise with warming above 2 °C. *Proc. Natl. Acad. Sci.* 113, 13342–13347. doi: 10.1073/pnas.1605312113

Joe, H. (2014). *Dependence modeling with copulas. 1st ed* (New York: Chapman and Hall/CRC). doi: 10.1201/b17116

Karambas, T. V. (2006). Prediction of sediment transport in the swash-zone by using a nonlinear wave model. *Cont. Shelf. Res.* 26, 599–609. doi: 10.1016/j.csr.2006.01.014

Karambas, T. V., and Koutitas, C. (2002). Surf and swash zone morphology evolution induced by nonlinear waves. *J. Waterw. Port. Coast. Ocean. Eng.* 128, 102–113. doi: 10.1061/(ASCE)0733-950X(2002)128:3(102

Larson, M., and Kraus, N. C. (1989). *SBEACH: numerical model for simulating storm-induced beach change; report 1: empirical foundation and model development* (Washington, DC: US Army Coastal Engineering Research Center).

Le Cozannet, G., Bulteau, T., Castelle, B., Ranasinghe, R., Wöppelmann, G., Rohmer, J., et al. (2019). Quantifying uncertainties of sandy shoreline change projections as sea level rises. *Sci. Rep.* 9, 42. doi: 10.1038/s41598-018-37017-4

Le Cozannet, G., Garcin, M., Yates, M., Idier, D., and Meyssignac, B. (2014). Approaches to evaluate the recent impacts of sea-level rise on shoreline changes. *Earth Sci. Rev.* 138, 47–60. doi: 10.1016/j.earscirev.2014.08.005

Lemesios, G., Giannakopoulos, C., Papadaskalopoulou, C., Karali, A., Varotsos, K. V., Moustakas, K., et al. (2016). Future heat-related climate change impacts on tourism industry in Cyprus. *Reg. Environ. Change* 16, 1915–1927. doi: 10.1007/s10113-016-0997-0

Leont'yev, I. O. (1996). Numerical modelling of beach erosion during storm event. *Coast. Eng.* 29, 187–200. doi: 10.1016/S0378-3839(96)00029-4

Li, F., Zhou, J., and Liu, C. (2018). Statistical modelling of extreme storms using copulas: a comparison study. *Coast. Eng.* 142, 52–61. doi: 10.1016/j.coastaleng.2018.09.007

Luijendijk, A., Hagenaars, G., Ranasinghe, R., Baart, F., Donchyts, G., and Aarninkhof, S. (2018). The state of the world's beaches. *Sci. Rep.* 8, 6641. doi: 10.1038/s41598-018-24630-6

Mavris, C. (2011). Sustainable environmental tourism and insular coastal area risk management in Cyprus and the Mediterranean. *J. Coast. Res.* 61, 317–327. doi: 10.2112/SI61-001.32

Melet, A., Meyssignac, B., Almar, R., and Le Cozannet, G. (2018). Under-estimated wave contribution to coastal sea-level rise. *Nat. Clim. Change* 8, 234–239. doi: 10.1038/s41558-018-0088-y

Mentaschi, L., Vousdoukas, M. I., Voukouvalas, E., Dosio, A., Feyen, L., Lionello, P., et al. (2017). Global changes of extreme coastal wave energy fluxes triggered by intensified teleconnection patterns. *Geophys Res Lett* 44, 2416–2426. doi: 10.1002/2016GL072488

Mentaschi, L., Vousdoukas, M. I., Pekel, J.-F., Voukouvalas, E., and Feyen, L. (2018). Global long-term observations of coastal erosion and accretion. *Sci. Rep.* 8, 12876. doi: 10.1038/s41598-018-30904-w

Monioudi, I. N., Karditsa, A., Chatzipavlis, A., Alexandrakis, G., Andreadis, O. P., Velegrakis, A. F., et al. (2016). Assessment of vulnerability of the eastern Cretan beaches (Greece) to sea level rise. *Reg. Environ. Change* 16, 1951–1962. doi: 10.1007/s10113-014-0730-9

Monioudi, I. N., and Velegrakis, A. F. (2022). Beach carrying capacity at touristic 3S destinations: its significance, projected decreases and adaptation options under climate change. *J. Tourism. Hospit.* 11, 500. doi: 10.35248/2167-0269.22.11.500

Monioudi, I. N., Velegrakis, A. F., Chatzipavlis, A. E., Rigos, A., Karambas, T., Vousdoukas, M. I., et al. (2017). Assessment of island beach erosion due to sea level rise: the case of the Aegean archipelago (Eastern Mediterranean). *Nat. Hazards. Earth Syst. Sci.* 17, 449–466. doi: 10.5194/nhess-17-449-2017

Muis, S., Verlaan, M., Winsemius, H. C., Aerts, J. C. J. H., and Ward, P. J. (2016). A global reanalysis of storm surges and extreme sea levels. *Nat. Commun.* 7, 11969. doi: 10.1038/ncomms11969

Narayan, S., Beck, M. W., Reguero, B. G., Losada, I. J., van Wesenbeeck, B., Pontee, N., et al. (2016). The effectiveness, costs and coastal protection benefits of natural and nature-based defences. *PloS One* 11, e0154735. doi: 10.1371/journal.pone.0154735

Nicholls, R. J., and Cazenave, A. (2010). Sea-Level rise and its impact on coastal zones. *Science* 328, 1517–1520. doi: 10.1126/science.1185782

Oswaldo, M.-N., Dominik, P., Daniël, W., Linda, A.-B., and Wim, C. (2017). Characterization of precipitation through copulas and expert judgement for risk assessment of infrastructure. *ASCE. ASME. J. Risk Uncertain. Eng. Syst. A. Civ. Eng.* 3, 04017012. doi: 10.1061/AJRUA6.0000914

Peduzzi, P., Velegrakis, A., Chatenoux, B., Estrella, M., and Karambas, T. (2022). Assessment of the role of nearshore marine ecosystems to mitigate beach erosion: the case of Negril (Jamaica). *Environments* 9 (5), 62. doi: 10.3390/environments9050062

Price, C., Michaelides, S., Pashiardis, S., and Alpert, P. (1999). Long term changes in diurnal temperature range in Cyprus. *Atmos. Res.* 51, 85–98. doi: 10.1016/S0169-8095 (99)00022-8

Ranasinghe, R. (2016). Assessing climate change impacts on open sandy coasts: a review. *Earth Sci. Rev.* 160, 320–332. doi: 10.1016/j.earscirev.2016.07.011

Ranasinghe, R., Callaghan, D., and Stive, M. J. F. (2012). Estimating coastal recession due to sea level rise: beyond the bruun rule. *Clim. Change* 110, 561–574. doi: 10.1007/s10584-011-0107-8

Reis, A. H., and Gama, C. (2010). Sand size versus beachface slope [[/amp]]mdash; an explanation based on the constructal law. *Geomorphology* 114, 276–283. doi: 10.1016/j.geomorph.2009.07.008

Rodella, I., Madau, F., Mazzanti, M., Corbau, C., Carboni, D., Simeoni, U., et al. (2020). Carrying capacity as tool for beach economic value assessment (case studies of Italian beaches). *Ocean. Coast. Manage.* 189, 105130. doi: 10.1016/j.ocecoaman.2020.105130

Roelvink, D., Reniers, A., Van Dongeren, A., Van Thiel De Vries, J., Lescinski, J., and Report, R. M. (2010). *XBeach model description and manual* (Delft: Unesco-IHE Institute for Water Education, Deltares and Delft University of Technology).

Rueda, A., Vitousek, S., Camus, P., Tomás, A., Espejo, A., Losada, I. J., et al. (2017). A global classification of coastal flood hazard climates associated with large-scale oceanographic forcing. *Sci. Rep.* 7, 5038. doi: 10.1038/s41598-017-05090-w

Safakli, O. V., and Kutlay, K. (2016). Potential multiplier effect of tourism sector in northern Cyprus. *Int. J. Acad. Res. Accounting. Financ. Manage. Sci.* 6, 44–51. doi: 10.6007/IJARAFMS/v6-i4/2293

Semeoshenkova, V., and Newton, A. (2015). Overview of erosion and beach quality issues in three southern European countries: Portugal, Spain and Italy. *Ocean. Coast. Manag.* 118, 12–21. doi: 10.1016/j.ocecoaman.2015.08.013

SETE (2023) *Key figures of incoming tourism in greece. Greek tourism confederation*. Available at: https://insete.gr/districts/?lang=en (Accessed February 24, 2023).

Sherwood, C. R., van Dongeren, A., Doyle, J., Hegermiller, C. A., Hsu, T.-J., Kalra, T. S., et al. (2022). Modeling the morphodynamics of coastal responses to extreme events: what shape are we in? *Ann. Rev. Mar. Sci.* 14, 457–492. doi: 10.1146/annurev-marine-032221-090215

Simmons, J. A., and Splinter, K. D. (2022). A multi-model ensemble approach to coastal storm erosion prediction. *Environ. Model. Software.* 150, 105356. doi: 10.1016/j.envsoft.2022.105356

Stripling, S., Panzeri, M., Blanco, B., Rossington, K., Sayers, P., and Borthwick, A. (2017). Regional-scale probabilistic shoreline evolution modelling for flood-risk assessment. *Coast. Eng.* 121, 129–144. doi: 10.1016/j.coastaleng.2016.12.002

Summers, A., Fletcher, C. H., Spirandelli, D., McDonald, K., Over, J.-S., Anderson, T., et al. (2018). Failure to protect beaches under slowly rising sea level. *Clim. Change* 151, 427–443. doi: 10.1007/s10584-018-2327-7

Toimil, A., Díaz-Simal, P., Losada, I. J., and Camus, P. (2018). Estimating the risk of loss of beach recreation value under climate change. *Tour. Manage.* 68, 387–400. doi: 10.1016/j.tourman.2018.03.024

Toimil, A., Losada, I. J., Camus, P., and Díaz-Simal, P. (2017). Managing coastal erosion under climate change at the regional scale. *Coast. Eng.* 128, 106–122. doi: 10.1016/j.coastaleng.2017.08.004

Tolman, H. L. (2009). *User manual and system documentation of WAVEWATCH III version 3.14* (Camp Springs, MD: U. S. Department of Commerce National Oceanic and Atmospheric Administration, National Weather Service, National Centers for Environmental Prediction).

Toumazis, A., Kyrou, K., Iacovou, N., Sophos, J., Zervos, S., and Anastasakis, G. (2008). Pre – reservoirs: a sustainable solution for eroding beaches/deltas of dammed rivers. *WIT. Trans. Built. Environ.* 99, 179–188. doi: 10.2495/CENV080171

Tsimplis, M. N., Calafat, F. M., Marcos, M., Jordà, G., Gomis, D., Fenoglio-Marc, L., et al. (2013). The effect of the NAO on sea level and on mass changes in the Mediterranean Sea. *J. Geophys. Res. Oceans.* 118, 944–952. doi: 10.1002/jgrc.20078

Tsimplis, M. N., and Shaw, A. G. P. (2010). Seasonal sea level extremes in the Mediterranean Sea and at the Atlantic European coasts. *Nat. Hazards. Earth Syst. Sci.* 10, 1457–1475. doi: 10.5194/nhess-10-1457-2010

Twomey, A. J., O'Brien, K. R., Callaghan, D. P., and Saunders, M. I. (2020). Synthesising wave attenuation for seagrass: drag coefficient as a unifying indicator. *Mar. pollut. Bull.* 160, 111661. doi: 10.1016/j.marpolbul.2020.111661

UNWTO (2019). *International tourism highlights* (Madrid: United Nations World Tourism Organisation). doi: 10.18111/9789284421152

Velegrakis, A. F., Ballay, A., Poulos, S., Radzevicius, R., Bellec, V., and Manso, F. (2010). European Marine aggregates resources: origins, usage, prospecting and dredging techniques. *J. Coast. Res.* 51, 1–14. doi: 10.2112/si51-002.1

Velegrakis, A. F., Hasiotis, T., and Papadatou, K. (2021). Coastal climate resilience: review of policies and regulations. deliverable 2.2 – ECFAS project (GA 101004211). *Zenodo.* doi: 10.5281/zenodo.6538546

Velegrakis, A. F., Trygonis, V., Chatzipavlis, A. E., Karambas, Th., Vousdoukas, M. I., Ghionis, G., et al. (2016). Shoreline variability of an urban beach fronted by a beachrock reef from video imagery. *Nat. Hazards.* 83, 201–222. doi: 10.1007/s11069-016-2415-9

Vitousek, S., Barnard, P. L., Fletcher, C. H., Frazer, N., Erikson, L., and Storlazzi, C. D. (2017). Doubling of coastal flooding frequency within decades due to sea-level rise. *Sci. Rep.* 7, 1–9. doi: 10.1038/s41598-017-01362-7

Vousdoukas, M. I., Mentaschi, L., Voukouvalas, E., Bianchi, A., Dottori, F., and Feyen, L. (2018a). Climatic and socioeconomic controls of future coastal flood risk in Europe. *Nat. Clim. Change* 8, 776–780. doi: 10.1038/s41558-018-0260-4

Vousdoukas, M. I., Mentaschi, L., Voukouvalas, E., Verlaan, M., Jevrejeva, S., Jackson, L. P., et al. (2018b). Global probabilistic projections of extreme sea levels show intensification of coastal flood hazard. *Nat. Commun.* 9, 2360. doi: 10.1038/s41467-018-04692-w

Vousdoukas, M. I., Ranasinghe, R., Mentaschi, L., Plomaritis, T. A., Athanasiou, P., Luijendijk, A., et al. (2020). Sandy coastlines under threat of erosion. *Nat. Clim. Change* 10, 260–263. doi: 10.1038/s41558-020-0697-0

Vousdoukas, M. I., Velegrakis, A. F., and Karambas, T. V. (2009). Morphology and sedimentology of a microtidal beach with beachrocks: vatera, Lesbos, NE Mediterranean. *Cont. Shelf. Res.* 29, 1937–1947. doi: 10.1016/j.csr.2009.04.003

WDD (2017)Catalogue of reservoirs, list of water reservoirs (dams). In: *Water development department (WDD), Cyprus ministry of agriculture*. Available at: http://www.moa.gov.cy/moa/wdd/wdd.nsf/All/25041A3BAC14BC48C22583D800396FF5? OpenDocument (Accessed February 25, 2023).

Wolff, C., Vafeidis, A. T., Muis, S., Lincke, D., Satta, A., Lionello, P., et al. (2018). A Mediterranean coastal database for assessing the impacts of sea-level rise and associated hazards. *Sci. Data* 5, 180044. doi: 10.1038/sdata.2018.44

Wong, P. P., Losada, I. J., Gattuso, J.-P., Hinkel, J., Khattabi, A., McInnes, K. L., et al. (2014). "Coastal systems and low-lying areas," in *Climate change 2014: impacts, adaptation, and vulnerability. part a: global and sectoral aspects. contribution of working group II to the fifth assessment report of the intergovernmental panel on climate*. Eds. C. B. Field, V. R. Barros, D. J. Dokken, K. J. Mach, M. D. Mastrandrea, T. E. Bilir, et al (Cambridge, United Kingdom and New York, NY, USA: Cambridge University Press), 361–409.

Climate projections of meteotsunami hazards

Cléa Denamiel[1], Danijel Belušić[2,3], Petra Zemunik[4]
and Ivica Vilibić[1*]

[1]Department for Marine and Environmental Research, Ruđer Bošković Institute, Zagreb, Croatia,
[2]Department of Geophysics, Faculty of Science, University of Zagreb, Zagreb, Croatia, [3]Swedish
Meteorological and Hydrological Institute, Rossby Centre, Norrköping, Sweden, [4]Physical
Oceanography Laboratory, Institute of Oceanography and Fisheries, Split, Croatia

Global climate models, indispensable for projecting the human-driven climate change, have been improving for decades and are nowadays capable of reproducing multiple processes (e.g., aerosols, sea-ice, carbon cycle) at up to 25 km horizontal resolution. Meteotsunami events – tsunami waves generated by mesoscale atmospheric processes – are properly captured only by sub-kilometre-scale downscaling of these models. However, the computational cost of long-term high-resolution climate simulations providing accurate meteotsunami hazard assessments would be prohibitive. In this article, to overcome this deficiency, we present a new methodology allowing to project sub-kilometre-scale meteotsunami hazards and their climate uncertainties at any location in the world. Practically, the methodology uses (1) synoptic indices to preselect a substantial number of short-term meteotsunami episodes and (2) a suite of atmospheric and oceanic models to downscale them from an ensemble of global models to the sub-kilometre-scale. Such approach, using hundreds of events to build robust statistics, could allow for an objective assessment of the meteotsunami hazards at the climate scale which, on top of sea level rise and storm surge hazards, is crucial for building adaptation plans to protect coastal communities worldwide.

KEYWORDS

meteotsunami hazard assessments, synoptic index, downscaling, climate uncertainty, climate projections

1 Introduction

Meteorological tsunamis, or meteotsunamis, are tsunami-like ocean long waves driven by intense, fast-propagating and low-dispersive atmospheric disturbances capable of transferring their energy to the ocean (Monserrat et al., 2006). Extreme meteotsunami events can be associated with coastal flooding, structural damage and human losses, as illustrated in Figure 1 for one of the highest meteotsunami waves ever witnessed (with conservative estimate of up to 6 m in height) which took place in Vela Luka (Adriatic Sea, Croatia) on the 21st of June 1978. Two processes are preconditioning the generation of these extreme events: (1) offshore resonance (Vilibić, 2008) occurring when the speed of the

FIGURE 1
Compilation of photos and newspaper clips illustrating the catastrophic sea level oscillations and floods during the 21st of June 1978 meteotsunami event in Vela Luka, Croatia (after Vučetić and Barčot, 2008).

atmospheric waves is equal to either the speed of the ocean long waves over a flat bathymetry (i.e., Proudman resonance; Proudman, 1929) or the speed of the edge waves along a coastline (Greenspan resonance; Greenspan, 1956), and (2) nearshore amplification, for example, through shoaling and harbour resonance (Pattiaratchi and Wijeratne, 2015; Rabinovich, 2020). Consequently, meteotsunamis mostly occur in known hotspot locations (e.g., the Balearic Islands and the Adriatic Sea in the Mediterranean region or the Great Lakes in the USA) favourable to the amplification of the long waves (Vilibić et al., 2016; Vilibić et al., 2021) and during weather events generating atmospheric disturbances travelling at speeds that trigger the Proudman or Greenspan resonances.

The most common weather conditions driving meteotsunami events are associated with mesoscale processes such as atmospheric mesoscale gravity waves (MGWs), convective storms, frontal passages/ squall lines and tropical cyclones. Atmospheric MGWs may be generated by unbalanced jet streaks through the so-called spontaneous balance adjustment (Ruppert et al., 2022) and may be preserved over long distances via wave ducting in the lower troposphere (Lindzen and Tung, 1976; Monserrat and Thorpe, 1996). Consequently, MGWs can generate meteotsunamis due to rapid surface pressure oscillations up to >5 hPa in less than an hour (e.g., Sheremet et al., 2016). Individual convective storms can be generated locally in unstable atmospheric situations and are typically associated with surface pressure perturbations that, when propagating at appropriate speeds, can cause meteotsunamis (e.g., Belušić and Strelec Mahović, 2009). Squall lines, or lines of thunderstorms, often form along or ahead of cold fronts and can extend laterally for hundreds of kilometres. Long-lived strong squall lines, also called "derechos" (Spanish for 'straight'), can travel many hundreds of

kilometres and are associated with air pressure disturbances that can generate meteotsunamis through resonance (e.g., Šepić and Rabinovich, 2014; Wertman et al., 2014). Finally, meteotsunamis can also be driven by either tropical cyclone rainbands – i.e., the regions of heaviest precipitation outside of the tropical cyclone eyeball – that can develop squall-line-like characteristics or by atmospheric internal gravity waves produced by tropical cyclones (e.g., Shi et al., 2020).

In the last decade, numerical modelling and forecast of meteotsunami events has been a pressing issue for the development of meteotsunami early warning systems (Vilibić et al., 2016). Despite the many challenges posed by accurately simulating both the localized mesoscale atmospheric processes and the nearshore amplifications driving the meteotsunami events, more and more early warning systems and high-resolution modelling suites are nowadays capable to capture these processes (e.g., Renault et al., 2011; Anderson and Mann, 2021; Angove et al., 2021; Sun and Niu, 2021; Tojčić et al., 2021; Kim et al., 2022; Rahimian et al., 2022). Historically, three complementary avenues have been explored: (1) synoptic indices, (2) high-resolution numerical models and (3) ensemble or stochastic approaches. Synoptic indices – connecting atmospheric patterns with meteotsunami events – have only been successfully used in the Balearic Islands, Spain (Ramis and Jansà, 1983; Šepić et al., 2016; Vich and Romero, 2021). They also have recently been derived worldwide and strong connections between meteotsunami events and synoptic patterns have been found along most of the world's coastlines, but particularly at mid-latitudes (Šepić et al., 2015; Vilibić and Šepić, 2017; Zemunik et al., 2022). The advantage of the approach is that no additional numerical cost is required, as synoptic indices – identifying meteotsunami events up to a week in advance – can be derived and used with relatively coarse weather models (30-80 km in resolution). The major drawback is the impossibility to quantify the intensity of the events due to the important contribution of mesoscale processes not captured by the synoptic indices, which can be exacerbated for locally generated atmospheric disturbances, such as convective storms, that can be completely missed. Consequently, the implementation of operational coupled atmosphere-ocean modelling suites at the sub-kilometre scale is an unavoidable necessity in early warning systems. To this date, they have only been implemented in the Balearic Islands (Renault et al., 2011) and the Adriatic Sea (Denamiel et al., 2019a; Denamiel et al., 2019b). In both systems the presence of meteotsunamigenic disturbances triggering the event mode of the early warning systems are nearly always detected but their exact location and intensity is not always well simulated. The meteotsunami hazards (which can be defined both as the maximum coastal sea elevation – meteotsunami surge – and/ or meteotsunami wave height) can thus be numerically quantified for the known hotspot locations. Nevertheless, even for a 3-day forecast, running sub-kilometre scale models has proven to be numerically expensive and, for the Adriatic Sea, the operational forecasting service was discontinued. Finally, deterministic forecasts often fail to predict the meteotsunami surges at hotspot locations due to the difficulty to properly simulate the exact location, speed, period, amplitude, etc., of the atmospheric disturbances driving such events. Consequently, meteotsunami hazards can only be

properly quantified via ensemble or stochastic approaches. In the Balearic Islands, following Mourre et al. (2021), using multiple atmospheric model configurations improved the forecast of meteotsunami events. However, ensembles of kilometre-scale (or km-scale) atmospheric models have an enormous computational cost which can be prohibitive for their operational implementation. Stochastic methods (Geist et al., 2014) and surrogate models or ocean emulators (Denamiel et al., 2019b; Denamiel et al., 2020a; Denamiel et al., 2021a) are thus promising avenues to account for the uncertainty on simulating meteotsunami events with deterministic models. For example, such a meteotsunami surrogate model has been successfully implemented in the Adriatic Sea where it can run operationally at nearly no numerical cost (i.e., stochastic results based on 20000 samples produced in a few minutes on a laptop) despite being trained on more than 4000 simulations (i.e., running in parallel on High Performance Computers) and, hence, being numerically expensive to design (Tojčić et al., 2021).

Following these major advances, climate projection of meteotsunami hazards is the next big challenge faced by the meteotsunami community. Generally speaking, in this era of anthropogenically-induced climate changes, the climate research community needs to provide more accurate climate projections of the entire Earth system to the decision makers (Smith et al., 2014), in order to better adapt to the societal impact of future extreme events (e.g., droughts, storms, sea-level rise, etc.). Further, a great number of extreme events are localized, thus leading to an improper quantification of the hazards by state-of-the-art global and regional circulation models. This is very well illustrated in the Venice Lagoon, where underestimations of just 40 cm in storm surge height by operational forecasts (Ferrarin et al., 2021) can change the flooded area of the city of Venice from ca. 25% to 80% (Cavaleri et al., 2020), resulting in much larger flood risks and damages (estimated to up to 1.1 billion of euros just in Venice). This is also the case for meteotsunami events, which are driven by atmospheric conditions highly influenced by the on-going global warming. For example, the positive trends of temperature and maximum wind speed over the Adriatic Sea during the 1987-2017 period (Tojčić et al., 2023) might already impact the meteotsunamigenic conditions at the synoptic scale in this region. Globally, mid-troposphere jet stream intensity, meandering and latitudinal range present the highest correlations with meteotsunami occurrences (Vilibić and Šepić, 2017; Zemunik et al., 2022) and are undoubtedly affected by the ongoing climate change (Hallam et al., 2022; Moon et al., 2023). Till now, little is known about meteotsunami hazard assessments under climate change as only two studies have tried to quantify the impact of global warming on meteotsunamis. One used the synoptic index-based approach in the Balearic Islands (Vilibić et al., 2018) and found that the number of days with synoptic conditions prone to the generation of meteotsunamis could increase by one third under extreme warming conditions (Representative Concentration Pathway RCP 8.5 scenario). The other used the pseudo-global warming (PGW) downscaling approach (Schär et al., 1996; Denamiel et al., 2020b) for half a dozen meteotsunami events in the Adriatic Sea (Denamiel et al., 2022) and found a strong impact of climate warming on the spatial variability of the meteotsunami intensity under RCP 8.5 scenario. It should also be

noted that both studies were carried out with a single Regional Climate Model (RCM) and for a single climate scenario, and thus do not account for the climate uncertainty.

To bridge the gap between climate modelling and accurate meteotsunami hazard assessments, this article presents a new methodology that could be used to lower the computational costs of sub-kilometre-scale meteotsunami climate modelling while keeping a fair description of the climate projection uncertainties.

2 Research hypotheses

We postulate that targeted downscaling of short-term meteotsunami events from global climate models (GCMs) to sub-kilometre-scale resolutions is key to assess meteotsunami hazards (i.e., maximum coastal sea levels or meteotsunami surges, and maximum meteotsunami wave heights) in future climates at a reasonable numerical cost. Hereafter, the four presented hypotheses on which our methodology is based address three scientific challenges previously highlighted by Sillmann et al. (2017): (1) What are the relevant sources of predictability of meteotsunami events that can support their attribution, prediction and projection? (2) What is the relevant definition of a meteotsunami event, as a short-term extreme? (3) What are the necessary model output requirements to analyse meteotsunami events?

2.1 Hypothesis 1: conditions for local meteotsunami events can be seen and automatically extracted at the synoptic level

This hypothesis partially addresses question 1 of Sillmann et al. (2017), and follows the early findings of Lorenz (1956; 1969), who argues that two relatively similar synoptic situations are likely to produce similar local effects. This finding has been successfully automatized and implemented for precipitation climate studies (e.g., Radanovics et al., 2013; Dayon et al., 2015; Chardon et al., 2018). For meteotsunami events, the global research is ongoing and has shown promising results along the worldwide coastlines. However, as stated in Šepić et al. (2016), the detection of real meteotsunami events with synoptic indices only works in 20% of the cases which means that 80% of false positives (i.e., flagging of non-extreme events) can be expected when using this approach. Further, Zemunik et al. (2022) show that similar synoptic patterns are common to all meteotsunami events but that the efficiency of the synoptic indices (i.e., their capability to accurately detect meteotsunami events) might strongly vary depending on the studied geographical location, as seen in Figure 2 (Hypothesis 1).

We thus propose (1) to create synoptic meteotsunami indices for specific locations where the indices are found to be efficient, and (2) to apply the indices to GCM ensembles in order to automatically pinpoint similar synoptic conditions and extract ensembles of meteotsunami events.

2.2 Hypothesis 2: uncertainty in climate projections can be captured by sub-sampling meteotsunami events only

Although GCM ensembles do not necessarily represent the full uncertainty in climate projections (Knutti, 2010), they allow investigating uncertainty in future projections and particularly examining the maximum–minimum climate change scenarios. Due to limitations in computational resources, RCM ensembles only downscale subsets of the GCM ensembles (Ito et al., 2020). To avoid erroneous interpretations of the obtained climate impact assessments, several strategies have been derived to select subsets of GCMs (e.g., smaller biases in the historical climate simulations, coverage of the widest possible uncertainty range of future projections; Reichler and Kim, 2008; Cannon, 2015; Mendlik and Gobiet, 2016). Therefore, to fully address question 1 of Sillmann et al. (2017) and to obtain meteotsunami hazard estimates as robust as possible, we propose to downscale all events from all appropriate GCMs. Consequently, the subsampling procedure will not anymore be applied to select CGMs but to detect meteotsunami events.

Provided that the synoptic index is efficient (i.e., that enough meteotsunami events are extracted despite the known false alarm rate), the range of the climate uncertainty derived with the proposed approach will thus be similar to the one derived with the GCM ensembles as illustrated in Figure 2 (Hypothesis 2).

2.3 Hypothesis 3: short-term simulations are suitable for the kilometre-scale reproduction of meteotsunami events

This hypothesis addresses question 2 of Sillmann et al. (2017) and is based on the fact that simulations of meteotsunami events mostly rely on favourable initial states and the presence of large-scale drivers, which are both seen at the synoptic scale by GCMs, as well as positive feedbacks and mesoscale processes which are well-reproduced by kilometre-scale short-term simulations. Short-term forecasts of meteotsunami events (e.g., Renault et al., 2011; Denamiel et al., 2019a; Denamiel et al., 2019b; Mourre et al., 2021; Kim et al., 2022) have demonstrated that kilometre-scale coupled atmosphere-ocean models used in 3 day-long simulations forced by global or regional model outputs realistically represent processes which are too small to be reproduced by coarser long-term simulations and are capable to simulate meteotsunami hazards (i.e., maximum coastal sea levels or meteotsunami surges, and maximum meteotsunami wave heights).

For event-based meteotsunami downscaling, we thus propose to use specialized kilometre-scale modelling suites that have already been successfully tested in operational mode but that have also been demonstrated to often fail to simulate the proper location, speed, period, amplitude, etc., of the atmospheric disturbances, as shown in Figure 2 (Hypothesis 3 & 4) for Adriatic Sea meteotsunami events. Consequently, we also recommend the use of surrogate models to account for these uncertainties.
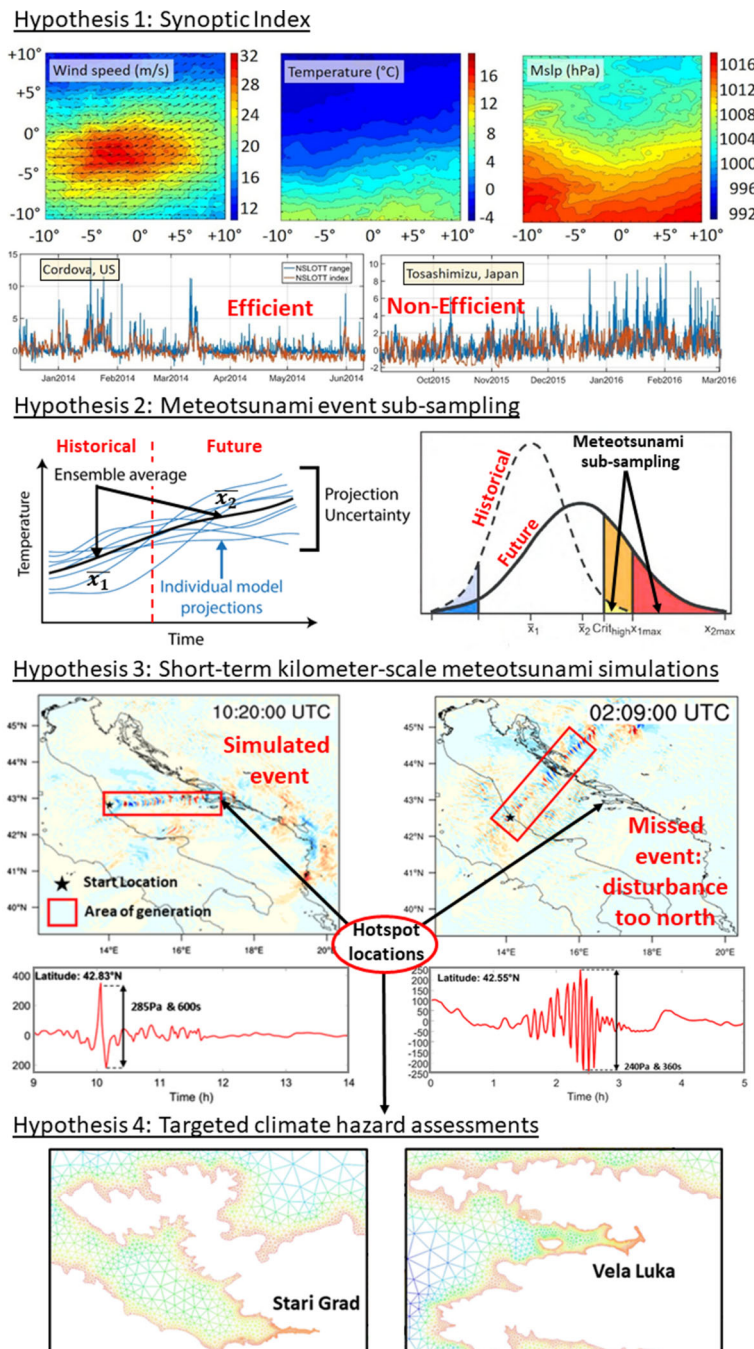
FIGURE 2

Illustration of the research hypotheses. Hypothesis 1: Average of the synoptic conditions (wind speed at 850 hPa, temperature at 550 hPa and mean sea level pressure or mslp) for meteotsunami events at northern hemisphere stations and time series of non-seismic sea level oscillations at tsunami timescales (NSLOTT) and synoptic index ranges (after Zemunik et al., 2022). Hypothesis 2: Selection of meteotsunami events from ensemble global climate models to account for the projection uncertainty (after Jentsch et al., 2007). Hypothesis 3: atmospheric disturbances (i.e., high-pass filtered mean sea level pressure) in the Adriatic Sea extracted from 1.5-day long AdriSC model kilometre-scale simulations (after Denamiel et al., 2019a). Hypothesis 4: Adriatic meteotsunami hotspot locations (Vela Luka and Stari Grad, Croatia) represented with a 10 m resolution in the ocean mesh for precise meteotsunami hazards (i.e., maximum coastal sea levels or meteotsunami surges, and maximum meteotsunami wave heights) assessments (after Denamiel et al., 2018).

2.4 Hypothesis 4: targeted climate hazard assessments are crucial for extreme event adaptation

As demonstrated by Schewe et al. (2019), state-of-the-art economic assessments of climate change impacts presently rely on global models which underestimate extreme events and associated societal risks. Additionally, in the Earth system modelling community, the accuracy of the models and thus of the climate projections during extreme events has been undeniably linked to the increase in spatial resolution of these models (Prein et al., 2015; Lucas-Picher et al., 2021). Consequently, we propose to downscale

meteotsunami events to sub-kilometre-scale in order to precisely derive the impact of climate change on the meteotsunami hazards. This is particularly important for hotspot areas where the proper representation of the geomorphology but also of the human made infrastructures is strongly affecting the assessments of the climate hazards leading to the adaptation strategies – as illustrated in Figure 2 (Hypothesis 4) for the Vela Luka and Stari Grad harbours in the Adriatic Sea.

This hypothesis thus addresses question 3 of Sillmann et al. (2017) by defining the output of method and, hence, the meteotsunami hazards as distributions of maximum coastal sea levels (or meteotsunami surges) and maximum meteotsunami wave heights at precise hotspot locations depending on both the climate uncertainty (Hypothesis 2) and the atmospheric disturbance simulation uncertainty (Hypothesis 3).

3 Methods

The conceptual design of the methodology using synoptic indices to derive targeted meteotsunami hazards from GCM simulations is presented in Figure 3. It is based on three different modules. First, the synoptic index module will automatically extract meteotsunami events for specific regions from the available GCM ensembles (i.e., different models and climate projections). The chosen synoptic indices will optimize the extraction of true meteotsunami events from the GCMs and minimize the flagging of non-extreme events (i.e., false positive). Then, the kilometre downscaling module will consist of 3 day-long kilometre-scale simulations of all the meteotsunami events extracted from the GCMs, thus necessarily including false positives. This module will rely on a cascade of nested grids from 15-km to 1-km resolution to properly downscale the GCM results. Finally, the targeted meteotsunami hazard module, the product-oriented part of the methodology, will downscale the kilometre-scale simulations with meteotsunami event realizations (i.e., excluding false positives) to sub-kilometre-scale 1 day-long simulations and will provide targeted hazard assessments for future projections from this specific ensemble of simulations. The detailed description of the three modules is as follows.

3.1 Synoptic index module

Establishes a connection between synoptic patterns and observations at a given location. It thus requires two different datasets: (1) a meteorological dataset describing the state of the atmosphere at a synoptic scale, such as a reanalysis dataset or a GCM, at different hours of the day, and (2) a dataset of quality-checked observations including high-frequency sea level data, preferably with a resolution of a minute, collected over a prolonged period (i.e., several years to decades). This module will aim to achieve the best efficiency for synoptic indices providing multivariate predictions that are (1) physically consistent (Raynaud et al., 2016), (2) spatially transferable (Radanovics et al., 2013; Chardon et al., 2018), and (3) temporally extendable to past and future climates (Dayon et al., 2015; Vilibić et al., 2018). For meteotsunami synoptic indices, points 1 and 2 have already been proven to be true as demonstrated by Zemunik et al. (2022) with averaging the synoptic conditions during meteotsunami events over the northern hemisphere stations and obtaining distinguishable characteristics (Figure 2, Hypothesis 1). The third point can only be reasonably proven by applying the presented methodology in known meteotsunami hotspot locations (e.g., Vela Luka, Croatia; Ciutadella, Spain). In practice, meteotsunami indices can be built by using either a multi-regression analysis (Šepić et al., 2016; Zemunik et al., 2022) or pattern recognition and machine learning algorithms (Cheng et al., 2014; Leuenberger and Kanevski, 2015).

3.2 Kilometre-downscaling module

Is state-of-the-art in the limited-area modelling community. It telescopically nests domains at a decreasing horizontal grid spacing with boundary conditions provided by GCMs or reanalyses, until kilometre-scales are reached (Prein et al., 2015). For meteotsunami events, we propose to downscale the atmosphere-ocean conditions to 1-km resolution from ensembles of climate projections such as CMIP6 (Coupled Model Intercomparison Project Phase 6, Eyring et al., 2016). Kilometre-scale models, such as the Weather Research and Forecasting (WRF; Skamarock et al., 2005) model in the atmosphere and the Regional Ocean Modelling System (ROMS, Shchepetkin and McWilliams, 2005; Shchepetkin and McWilliams, 2009) in the ocean, that have been successfully applied in the reproduction of meteotsunami events (Renault et al., 2011; Denamiel et al., 2019a; Mourre et al., 2021; Kim et al., 2022), can be used in this module.

3.3 Targeted meteotsunami hazard module

Aims to further downscale the kilometre-scale meteotsunami simulations, excluding the false positive events. We propose to use sub-kilometre-scale unstructured models properly representing the geomorphology of the selected regions of interest – e.g., the ADCIRC-SWAN model (Dietrich et al., 2012) which was previously successfully applied to reproduce meteotsunami waves (Denamiel et al., 2019a). Further, when the deterministic downscaling of the atmospheric conditions will lead to the reproduction of meteotsunamigenic disturbances, but not of meteotsunami surges at hotspot locations (similarly to the operational meteotsunami forecasts), we also propose to use an ocean emulator or surrogate model approach to define the meteotsunami hazards (e.g., Denamiel et al., 2019b; Denamiel et al., 2020a; Denamiel et al., 2021a). Finally, the output of the method consists in robust statistics of targeted climate projections of meteotsunami hazards (i.e., maximum coastal sea levels or meteotsunami surges), derived from ensembles of deterministic sub-kilometre-scale simulations and stochastic surrogate models/ ocean emulators for the selected regions of interest where the adaptation strategies of the coastal communities can be updated with this new information.
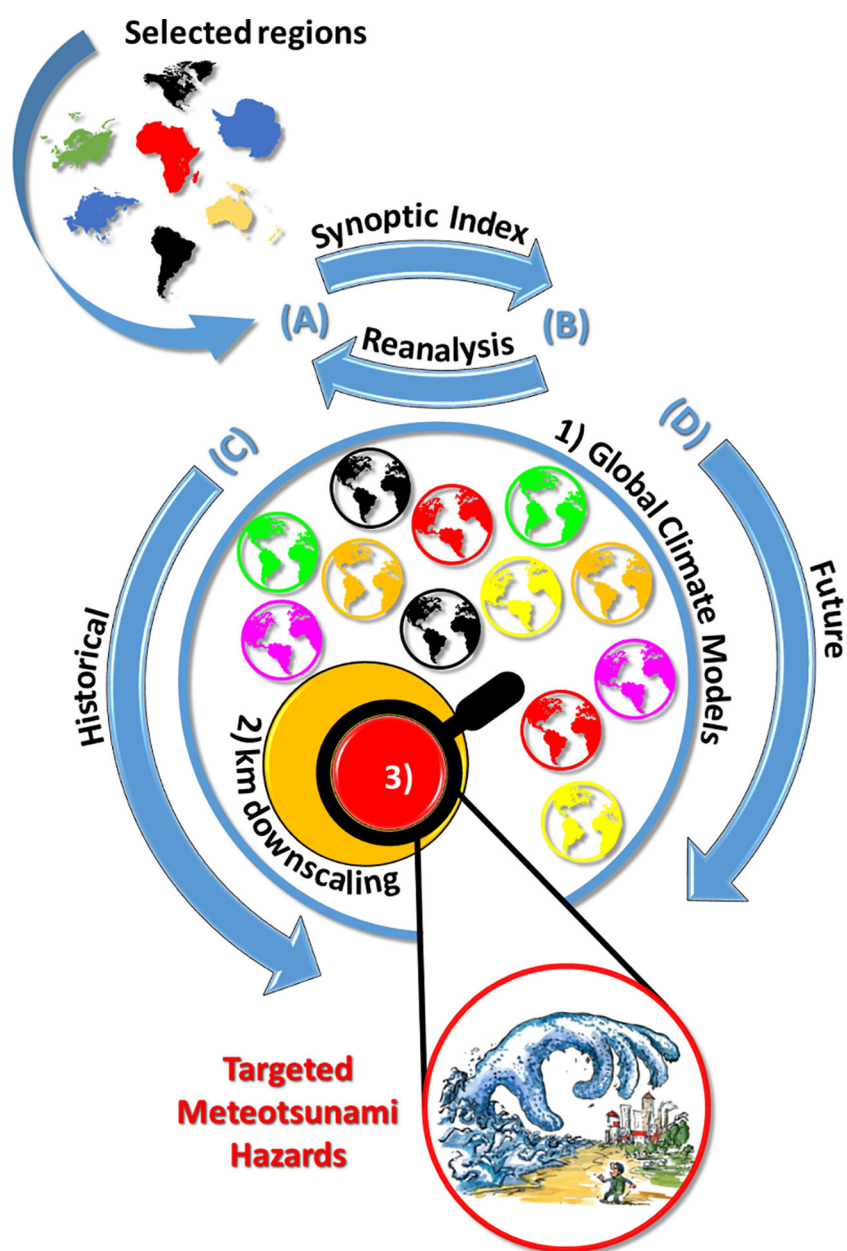
FIGURE 3
Outline of the methodology using **(A)** synoptic indices designed with **(B)** global reanalysis products to derive targeted meteotsunami hazards by downscaling **(C)** historical and **(D)** future GCM simulations. For a selected region: (1) the synoptic index is used to automatically extract extreme events from GCM ensembles (blue circle), (2) the GCM results are downscaled to kilometre-scale for all chosen events (orange circle) and (3) the kilometre-scale simulations with extreme event realizations (red circle) are further downscaled to sub-kilometre-scale and targeted hazard assessment projections are derived. Artwork from Frits Ahlefeldt: https://fritsahlefeldt.com.

4 Anticipated results

A practical implementation of the methodology could follow the seven steps of the workflow presented below and in Figure 4:

4.1 ERA5 design step

In practice, meteotsunami synoptic indices are used to reconstruct the high-frequency sea level time variations at a given coastal station depending only on a combination of several wisely chosen atmospheric variables extracted from numerical models. For a selected region of interest, ERA5 atmospheric reanalysis fields (Hersbach et al., 2020) and available multi-year observations of high-frequency sea levels are used to build the synoptic index (e.g., during the 2012-2018 period) which can then be applied for any time period and any model at this station (e.g., using CMIP6 during the 2070-2100 period). To evaluate the design of the synoptic index and the capacity of the models to simulate meteotsunamis, the events extracted from ERA5 reanalysis with the synoptic index are then downscaled to sub-kilometre-scale and the

FIGURE 4
Workflow of the methodology for projecting meteotsunami hazards
using synoptic indices designed with global reanalysis products
(ERA5 Design) and GCM historical simulations (CMIP6 Design) to
derive targeted meteotsunami hazards including the climate
uncertainty (Clim. UQ) by downscaling (Km-scale Downscaling and
Sub-km Down.) historical (CMIP6 Eval.) and future (CMIP6 Scen.)
GCM simulations and using ocean emulators (Ocean Emul.).

surrogate model/ocean emulator is used to account for the
atmospheric disturbance simulation uncertainties. The obtained
results are compared with the sea level observations and the
expected efficiency of the synoptic index is derived.

4.2 CMIP6 evaluation step

First, the synoptic index is calculated from the historical CMIP6
simulations for the region of interest chosen in step 1. Second, the

synoptic index distributions derived from ERA5 and CMIP6 are
compared. Then, if the comparison is successful – e.g., if the
synoptic index distributions are significantly similar following
statistical tests such as the Z-test – the extracted meteotsunami
events from ERA5 reanalysis and CMIP6 historical simulations are
downscaled to the kilometre-scale. Finally, the atmospheric and sea
level distributions obtained at hotspot locations by downscaling
ERA5 reanalysis and CMIP6 historical simulations are compared.

4.3 CMIP6 Design Step

If the CMIP6 Evaluation Step fails (e.g., distributions
significantly different following the Z-test), the synoptic index is
redesigned by considering both the CMIP6 historical simulations
and the ERA5 reanalysis until success of the CMIP6 Evaluation Step.

4.4 CMIP6 Scenario Step

Kilometre-scale downscaling of the CMIP6 future climate scenario
ensembles for the meteotsunami events extracted with the synoptic
index. It is important to highlight that despite the optimization of the
synoptic index presented in steps 1 to 3, many meteotsunami events
might still be missed by the methodology (i.e., false negatives).
Consequently, to properly account for the climate uncertainty, robust
meteotsunami synoptic indices must be built to minimize the number
of missed events (false negatives) and not the number of false positives.

4.5 Sub-kilometre-scale downscaling step

First, false positive events are excluded from the ensemble of
kilometre-scale simulations for both historical and future
simulations. The selection of the events is based on the automatic
detection of meteotsunamigenic disturbances from the 1 km
resolution atmospheric results – e.g., as presented in Denamiel
et al. (2019a) for the Adriatic Sea. Second, the historical and future
ensembles of positive events are further downscaled in the ocean to
sub-kilometre resolutions (up to 10 m).

4.6 Ocean Emulator Step

Based on the experience built with operational meteotsunami
forecasts, simulated meteotsunamigenic disturbances often fail to
generate meteotsunami waves at hotspot locations due to a shift in
space, speed, period, etc. In this case, mathematical emulators or
surrogate models can be used to assess the meteotsunami hazards
linked to the failed event.

4.7 Climate Uncertainty Quantification Step

The targeted meteotsunami hazards and their associated
climate uncertainty are quantified for both historical and
future simulations.

The anticipated results from such a procedure are the generation of datasets of historical and scenario based sub-kilometre-scale meteotsunami simulations providing targeted hazard assessments and their associated uncertainties linked to both atmospheric disturbance simulations (following the results provided by the surrogate models/ocean emulators) and climate warming (following the main trends of the CMIP6 simulations). These datasets are of critical importance for the design of climate adaption strategies at hotspot locations (e.g., Great Lakes, USA; Vela Luka, Croatia; Ciutadella, Spain; Nagasaki Bay, Japan; Freemantle, Australia) where meteotsunami events pose a threat to the population.

5 Discussion

In contrast with the other tsunami sources (e.g. earthquakes, volcanoes, landslides), meteotsunami events are thought to be influenced by the on-going climate warning. Consequently, classical tsunami methods (e.g., Poisson rate of occurrence) cannot be applied to quantify the long-term frequency and intensity of these events, and, hence, to assess meteotsunami hazards. Instead, a climate change approach trying to extract the past and future events from climate models in order to derive statistics on their behaviour and characteristics should be used. However, running models and model ensembles at sub-kilometre-scale resolution is known to require enormous computing resources and the efficiency (in terms of improvement of the results relative to the numerical cost) of producing such climate projections for long-term simulations can be questioned. For example, despite the modern technological advances and the numerical resources available to climate scientists, the coupled atmosphere-ocean kilometre-scale climate model implemented in the Adriatic basin with nested grids ranging from 15 to 1 km resolutions takes 18 months of continuous calculation with 260 CPUs to generate 31-year long climate simulations (Denamiel et al., 2021b; Pranić et al., 2021). In other words, to produce results for only one climate scenario (e.g., RCP 8.5) during the 1950-2100 period, this model would have to be run for more than 7 years. Further, meteotsunami events would still have to be extracted and downscaled to sub-kilometre, for the entire 1950-2100 period, in order to provide accurate hazard assessments. Consequently, this numerical cost is far too prohibitive to envision running ensembles of simulations forced by multiple GCMs under multiple warming scenarios (Semenov and Stratonovitch, 2010) and to properly assess the kilometre-scale uncertainties under climate warming.

The presented method is detouring this major obstacle by efficiently using the numerical resources – previously spent to produce long-term climate simulations – to quantify the climate change uncertainty and to properly assess the meter-scale meteotsunami hazards. However, several questions concerning the validity of the approach remain unanswered at this stage. Is the degree of connection between meteotsunami events and synoptic patterns high enough along the entire world's coastlines

for the method to be generalized worldwide (or should the method only be applied in areas like the Mediterranean basin)? Synoptic indices built with the set of synoptic variables optimized for Ciutadella (Spain) have already been demonstrated to be more efficient for Mediterranean locations than for the rest of the world (Zemunik et al., 2022). Consequently, sensitivity studies should be performed, at each station individually, to define the optimal set of synoptic variables needed to build the most efficient index at a given location. Will the extraction of the meteotsunami events with the synoptic indices lead to a large number of false positive events? Currently, meteotsunami synoptic indices, even derived for well-known Mediterranean hotspot locations (e.g., Ciutadella, Spain) have been leading to up to 80% of false positives (Šepić et al., 2016). Consequently, in order to reduce the numerical cost of the method, the general efficiency of the synoptic indices should be improved by, for example, using machine learning techniques (e.g., pattern recognition) to better identify the meteotsunamigenic synoptic conditions. Will the use of surrogate models/ocean emulators to compensate the failures of the deterministic downscaling add a bias to the climate uncertainty quantification? Meteotsunami surrogate models have only been used in the Adriatic Sea to improve the forecasts of these extreme events (Denamiel et al., 2019b; Denamiel et al., 2020a) and their impact on the final hazard assessments is, for now, difficult to quantify. Meteotsunami climate modelling is at its early stage, and we believe that many of these questions could find an answer in the decade to come when more and more scientists around the world will be able to test the presented methodology.

Finally, we argue that this targeted climate modelling strategy could be adapted to other extreme climate hazards such as convective storms, whose proper reproduction is still considered as one of the greatest challenges in the atmospheric climate community (Stephens et al., 2010; Coppola et al., 2020). Consequently, the presented methodology could lead to more accurate economic assessments of the climate change impacts on extreme events with a low carbon footprint coming out of extensive numerical computations. This could result in increasing preparation and adaptation of the worldwide communities to the upcoming local risks posed by climate warming.

Data availability statement

The original contributions presented in the study are included in the article/supplementary material. Further inquiries can be directed to the corresponding author.

Author contributions

CD and IV wrote the initial version of the manuscript. CD, IV and DB developed the conceptual design for assessing meteotsunami hazard in future climates. CD prepared the figures. All authors revised the manuscript, reviewed and approved the final manuscript.

Funding

We acknowledge the support of ChEESE-2P, a project funded by EuroHPC under the grant agreement No. 101093038.

Acknowledgments

The presented research is partially derived from the project proposal "Projecting climate hazards at sub-kilometre scales (REASSESS)", submitted to the European Research Council Advanced Research projects call of 2022. The comments raised by two reviewers greatly improved the manuscript.

Conflict of interest

The authors declare that the research was conducted in the absence of any commercial or financial relationships that could be construed as a potential conflict of interest.

Publisher's note

All claims expressed in this article are solely those of the authors and do not necessarily represent those of their affiliated organizations, or those of the publisher, the editors and the reviewers. Any product that may be evaluated in this article, or claim that may be made by its manufacturer, is not guaranteed or endorsed by the publisher.

References

Anderson, E. J., and Mann, G. E. (2021). A high-amplitude atmospheric inertia–gravity wave-induced meteotsunami in Lake Michigan. *Nat. Hazards* 106, 1489–1501. doi: 10.1007/s11069-020-04195-2

Angove, M., Kozlosky, L., Chu, P., Dusek, G., Mann, G., Anderson, E., et al. (2021). Addressing the meteotsunami risk in the United States. *Nat. Hazards* 106, 1467–1487. doi: 10.1007/s11069-020-04499-3

Belušić, D., and Strelec Mahović, N. (2009). Detecting and following atmospheric disturbances with a potential to generate meteotsunamis in the Adriatic. *Phys. Chem. Earth* 34, 918–927. doi: 10.1016/j.pce.2009.08.009

Cannon, A. J. (2015). Selecting GCM scenarios that span the range of changes in a multimodel ensemble: application to CMIP5 climate extremes indices. *J. Clim.* 28, 1260–1267. doi: 10.1175/JCLI-D-14-00636.1

Cavaleri, L., Bajo, M., Barbariol, F., Bastianini, M., Benetazzo, A., Bertotti, L., et al. (2020). The 2019 flooding of Venice and its implications for future predictions. *Oceanography* 33 (1), 42–49. doi: 10.5670/oceanog.2020.105

Chardon, J., Hingray, B., and Favre, A.-C. (2018). An adaptive two-stage analog/regression model for probabilistic prediction of small-scale precipitation in France. *Hydrol. Earth Syst. Sci.* 22, 265–286. doi: 10.5194/hess-22-265-2018

Cheng, L., AghaKouchak, A., Gilleland, E., and Katz, R. W. (2014). Non-stationary extreme value analysis in a changing climate. *Clim. Change* 127, 353–369. doi: 10.1007/s10584-014-1254-5

Coppola, E., Sobolowski, S., Pichelli, E., Raffaele, F., Ahrens, B., Anders, I., et al. (2020). A first-of-its-kind multi-model convection permitting ensemble for investigating convective phenomena over Europe and the Mediterranean. *Clim. Dyn.* 55, 3–34. doi: 10.1007/s00382-018-4521-8

Dayon, G., Boé, J., and Martin, E. (2015). Transferability in the future climate of a statistical downscaling method for precipitation in France. *J. Geophys. Res. Atmos.* 120, 1023–1043. doi: 10.1002/2014JD022236

Denamiel, C., Huan, X., Šepić, J., and Vilibić, I. (2020a). Uncertainty propagation using polynomial chaos expansions for extreme sea level hazard assessment: The case of the eastern Adriatic meteotsunamis. *J. Phys. Oceanogr.* 50 (4), 1005–1021. doi: 10.1175/JPO-D-19-0147.1D

Denamiel, C., Huan, X., and Vilibić, I. (2021a). Conceptual design of extreme sea-level early warning systems based on uncertainty quantification and engineering optimization methods. *Front. Mar. Sci.* 8. doi: 10.3389/fmars.2021.650279

Denamiel, C., Pranić, P., Ivanković, D., Tojčić, I., and Vilibić, I. (2021b). Performance of the Adriatic Sea and coast (AdriSC) climate component –A COAWST V3.3-based coupled atmosphere–ocean modelling suite: Atmospheric dataset. *Geosci. Model. Dev.* 14, 3995–4017. doi: 10.5194/gmd-14-3995-2021

Denamiel, C., Pranić, P., Quentin, F., Mihanović, H., and Vilibić, I. (2020b). Pseudo-global warming projections of extreme wave storms in complex coastal regions: The case of the Adriatic Sea. *Clim. Dyn.* 55, 2483–2509. doi: 10.1007/s00382-020-05397-x

Denamiel, C., Šepić, J., Huan, X., Bolzer, C., and Vilibić, I. (2019b). Stochastic surrogate model for meteotsunami early warning system in the eastern Adriatic Sea. *J. Geophys. Res. Oceans* 124, 8485–8499. doi: 10.1029/2019JC015574

Denamiel, C., Šepić, J., Ivanković, D., and Vilibić, I. (2019a). The Adriatic Sea and coast modelling suite: Evaluation of the meteotsunami forecast component. *Ocean Model.* 135, 71–93. doi: 10.1016/j.ocemod.2019.02.003

Denamiel, C., Šepić, J., and Vilibić, I. (2018). Impact of geomorphological changes to harbor resonance during meteotsunamis: The Vela Luka bay test case. *Pure Appl. Geophys.* 175, 3839–3859. doi: 10.1007/S00024-018-1862-5

Denamiel, C., Tojčić, I., and Vilibić, I. (2022). Meteotsunamis in orography-free, flat bathymetry and warming climate conditions. *J. Geophys. Res. Oceans* 127, e2021JC017386. doi: 10.1029/2021JC017386

Dietrich, J. C., Tanaka, S., Westerink, J. J., Dawson, C. N., Luettich, R. A.Jr., Zijlema, M., et al. (2012). Performance of the Unstructured-Mesh, SWAN+ADCIRC Model in computing hurricane waves and surge. *J. Sci. Comput.* 52, 468–497. doi: 10.1007/s10915-011-9555-6

Eyring, V., Bony, S., Meehl, G. A., Senior, C. A., Stevens, B., Stouffer, R. J., et al. (2016). Overview of the Coupled Model Intercomparison Project Phase 6 (CMIP6) experimental design and organization. *Geosci. Model. Dev.* 9, 1937–1958. doi: 10.5194/gmd-9-1937-2016

Ferrarin, C., Bajo, M., Benetazzo, A., Cavaleri, L., Chiggiato, J., Davison, S., et al. (2021). Local and large-scale controls of the exceptional Venice floods of November 2019. *Prog. Oceanogr.* 197, 102628. doi: 10.1016/j.pocean.2021.102628

Geist, E. L., ten Brink, U., and Gove, M. (2014). A framework for the probabilistic analysis of meteotsunamis. *Nat. Hazards* 74, 123–142. doi: 10.1007/S11069-014-1294-1

Greenspan, H. P. (1956). The generation of edge waves by moving pressure disturbances. *J. Fluid Mech.* 1, 574–592. doi: 10.1017/S002211205600038X

Hallam, S., Josey, S. A., McCarthy, G. D., and Hirschi, J. J. M. (2022). A regional (land-ocean) comparison of the seasonal to decadal variability of the Northern Hemisphere jet stream 1871-2011. *Clim. Dyn.* 59, 1897–1918. doi: 10.1007/s00382-022-06185-5

Hersbach, H., Bell, B., Berrisford, P., Hirahara, S., Horányi, A., Muñoz-Sabater, J., et al. (2020). The ERA5 global reanalysis. *Q. J. R. Meteorol. Soc.* 146, 1999–2049. doi: 10.1002/qj.3803

Ito, R., Shiogama, H., Nakaegawa, T., and Takayabu, I. (2020). Uncertainties in climate change projections covered by the ISIMIP and CORDEX model subsets from CMIP5. *Geosci. Model. Dev.* 13, 859–872. doi: 10.5194/gmd-13-859-2020

Jentsch, A., Kreyling, J., and Beierkuhnlein, C. (2007). A new generation of climate-change experiments: events, not trends. *Front. Ecol. Environ.* 5, 365–374. doi: 10.1890/1540-9295(2007)5[365:ANGOCE]2.0.CO;2

Kim, M.-S., Woo, S.-B., Eom, H., You, S. H., and Lee, H. M. (2022). Towards observation- and atmospheric model-based early warning systems for meteotsunami mitigation: A case study of Korea. *Weather Clim. Extrem.* 37, 100463. doi: 10.1016/j.wace.2022.100463

Knutti, R. (2010). The end of model democracy? *Clim. Change* 102, 395–404. doi: 10.1007/s10584-010-9800-2

Leuenberger, M., and Kanevski, M. (2015). Extreme Learning Machines for spatial environmental data. *Comput. Geosci.* 85, 64–73. doi: 10.1016/j.cageo.2015.06.020

Lindzen, R. S., and Tung, K.-K. (1976). Banded convective activity and ducted gravity waves. *Mon. Wea. Rev.* 104, 1602–1617. doi: 10.1175/1520-0493(1976)104<1602:BCAADG>2.0.CO;2

Lorenz, E. (1956). *Empirical orthogonal functions and statistical weather prediction, Tech. rep* (Cambridge: Massachusetts Institute of Technology, Department of Meteorology, Massachusetts Institute of Technology, Dept. of Meteorology). Available at: https://eapsweb.mit.edu/sites/default/files/Empirical_Orthogonal_Functions_1956.pdf.

Lorenz, E. (1969). Atmospheric predictability as revealed by naturally occurring analogues. *J. Atmos. Sci.* 26, 636–646. doi: 10.1175/1520-0469(1969)26<636:APARBN>2.0.CO;2

Lucas-Picher, P., Argueso, D., Brisson, E., Tramblay, Y., Berg, P., Lemonsu, A., et al. (2021). Convection-permitting modeling with regional climate models: Latest developments and next steps. *WIREs Clim. Change* 12, e731. doi: 10.1002/wcc.731

Mendlik, T., and Gobiet, A. (2016). Selecting climate simulations for impact studies based on multivariate patterns of climate change. *Clim. Change* 135, 381–393. doi: 10.1007/s10584-015-1582-0

Monserrat, S., and Thorpe, A. J. (1996). Use of ducting theory in an observed case of gravity waves. *J. Atmos. Sci.* 53, 1724–1736. doi: 10.1175/1520-0469(1996)053<1724:UODTIA>2.0.CO;2

Monserrat, S., Vilibić, I., and Rabinovich, A. B. (2006). Meteotsunamis: atmospherically induced destructive ocean waves in the tsunami frequency band. *Nat. Hazards Earth Syst. Sci.* 6, 1035–1051. doi: 10.5194/nhess-6-1035-2006

Moon, W., Kim, B. M., Yang, G. H., and Wettlaufer, J. S. (2023). Wavier jet streams driven by zonally asymmetric surface thermal forcing. *Proc. Natl. Acad. Sci. U.S.A.* 119, e2200890119. doi: 10.1073/pnas.2200890119

Mourre, B., Santana, A., Buils, A., Gautreau, L., Ličer, M., Jansà, A., et al. (2021). On the potential of ensemble forecasting for the prediction of meteotsunamis in the Balearic Islands: Sensitivity to atmospheric model parameterizations. *Nat. Hazards* 106, 1315–1336. doi: 10.1007/s11069-020-03908-x

Pattiaratchi, C. B., and Wijeratne, E. M. S. (2015). Are meteotsunamis an underrated hazard? *Philos. Trans. R. Soc. A* 373, 20140377. doi: 10.1098/rsta.2014.0377

Pranić, P., Denamiel, C., and Vilibić, I. (2021). Performance of the Adriatic Sea and coast (AdriSC) climate component—A COAWST V3.3-based one-way coupled atmosphere–ocean modelling suite: Ocean results. *Geosci. Model. Dev.* 14, 5927–5955. doi: 10.5194/gmd-14-5927-2021P

Prein, A. F., Langhans, W., Fosser, G., Ferrone, A., Ban, N., Goergen, K., et al. (2015). A review on regional convection-permitting climate modeling: Demonstrations, prospects and challenges. *Rev. Geophys.* 53, 323–361. doi: 10.1002/2014RG000475

Proudman, J. (1929). The effects on the sea of changes in atmospheric pressure. *Geophys. Suppl. Mon. Not. R. Astron. Soc.* 2, 197–209. doi: 10.1111/j.1365-246X.1929.tb05408.x

Rabinovich, A. B. (2020). Twenty-seven years of progress in the science of meteorological tsunamis following the 1992 Daytona Beach event. *Pure Appl. Geophys.* 177, 1193–1230. doi: 10.1007/s00024-019-02349-3

Radanovics, S., Vidal, J.-P., Sauquet, E., Ben Daoud, A., and Bontron, G. (2013). Optimising predictor domains for spatially coherent precipitation downscaling. *Hydrol. Earth Syst. Sci.* 17, 4189–4208. doi: 10.5194/hess-17-4189-2013

Rahimian, M., Beyramzadeh, M., and Siadatmousavi, S. M. (2022). The skill assessment of Weather and Research Forecasting and WAVEWATCH-III models during recent meteotsunami event in the Persian Gulf. *Front. Mar. Sci.* 9. doi: 10.3389/fmars.2022.834151

Ramis, C., and Jansà, A. (1983). Condiciones meteorológicas simultáneas a la aparición de oscilaciones del nivel del mar de amplitud extraordinaria en el Mediterráneo occidental. *Rev. Geofisica* 39, 35–42.

Raynaud, D., Hingray, B., Zin, I., Anquetin, S., Debionne, S., and Vautard, R. (2016). Atmospheric analogues for physically consistent scenarios of surface weather in Europe and Maghreb. *Int. J. Clim.* 37, 2160–2176. doi: 10.1002/joc.4844

Reichler, T., and Kim, J. (2008). How well do coupled models simulate Today's climate? *Bull. Am. Meteorol. Soc.* 89, 303–312. doi: 10.1175/BAMS-89-3-303

Renault, L., Vizoso, G., Jansà, A., Wilkin, J., and Tintoré, J. (2011). Toward the predictability of meteotsunamis in the Balearic Sea using regional nested atmosphere and ocean models. *Geophys. Res. Lett.* 38, L10601. doi: 10.1029/2011gl047361

Ruppert, J. H., Koch, S. E., Chen, X., Du, Y., Seimon, A., Sun, Y. Q., et al. (2022). Mesoscale gravity waves and midlatitude weather: A tribute to Fuqing Zhang. *Bull. Am. Meteorol. Soc.* 103, E129–E156. doi: 10.1175/BAMS-D-20-0005.1

Schär, C., Frei, C., Luthi, D., and Davies, H. C. (1996). Surrogate climate-change scenarios for regional climate models. *Geophys. Res. Lett.* 23, 669–672. doi: 10.1029/96GL00265

Schewe, J., Gosling, S. N., Reyer, C., Zhao, F., Ciais, P., Elliott, J., et al. (2019). State-of-the-art global models underestimate impacts from climate extremes. *Nat. Commun.* 10, 1005. doi: 10.1038/s41467-019-08745-6

Semenov, M. A., and Stratonovitch, P. (2010). Use of multi-model ensembles from global climate models for assessment of climate change impacts. *Clim. Res.* 41, 1–14. doi: 10.3354/cr00836

Šepić, J., and Rabinovich, A. B. (2014). Meteotsunami in the Great Lakes and on the Atlantic coast of the United States generated by the "derecho" of June 29–30, 2012. *Nat. Hazards* 74, 75–107. doi: 10.1007/s11069-014-1310-5

Šepić, J., Vilibić, I., and Monserrat, S. (2016). Quantifying the probability of meteotsunami occurrence from synoptic atmospheric patterns. *Geophys. Res. Lett.* 43, 10377–10384. doi: 10.1002/2016GL070754

Šepić, J., Vilibić, I., Rabinovich, A., and Monserrat, S. (2015). Widespread tsunami-like waves of 23-27 June in the Mediterranean and Black Seas generated by high-altitude atmospheric forcing. *Sci. Rep.* 5, 11682. doi: 10.1038/srep11682

Shchepetkin, A. F., and McWilliams, J. C. (2005). The regional oceanic modeling system: A split-explicit, free-surface, topography-following-coordinate. *Ocean Model.* 9, 347–404. doi: 10.1016/j.ocemod.2004.08.002

Shchepetkin, A. F., and McWilliams, J. C. (2009). Correction and commentary for "Ocean forecasting in terrain-following coordinates: Formulation and skill assessment of the regional ocean modeling system" by Haidvogel et al., J. Comput. Phys., 227, pp. 3595–3624. *J. Comp. Phys.* 228, 8985–9000. doi: 10.1016/j.jcp.2009.09.002

Sheremet, A., Gravois, U., and Shrira, V. (2016). Observations of meteotsunami on the Louisiana shelf: a lone soliton with a soliton pack. *Nat. Hazards* 84, 471–492. doi: 10.1007/s11069-016-2446-2

Shi, L., Olabarrieta, M., Nolan, D. S., and Warner, J. C. (2020). Tropical cyclone rainbands can trigger meteotsunamis. *Nat. Commun.* 11, 678. doi: 10.1038/s41467-020-14423-9

Sillmann, J., Thorarinsdottir, T., Keenlyside, N., Schaller, N., Alexander, L. V., Hegerl, G., et al. (2017). Understanding, modeling and predicting weather and climate extremes: Challenges and opportunities. *Weather Clim. Extrem.* 18, 65–74. doi: 10.1016/j.wace.2017.10.003

Skamarock, W. C., Klemp, J. P., Dudhia, J., Gill, D. O., and Barker, D. M. (2005). A description of the advanced research WRF version 2. NCAR technical note NCAR/TN-468+STR *National Center for Atmospheric Research, Boulder*, 88 pp. doi: 10.5065/D6DZ069T

Smith, M. J., Palmer, P. I., Purves, D. W., Vanderwel, M. C., Lyutsarev, V., Calderhead, B., et al. (2014). Changing how Earth system modeling is done to provide more useful information for decision making, science, and society. *Bull. Am. Meteorol. Soc.* 95, 1453–1464. doi: 10.1175/BAMS-D-13-00080.1

Stephens, G. L., L'Ecuyer, T., Forbes, R., Gettelmen, A., Golaz, J.-C., Bodas-Salcedo, A., et al. (2010). Dreary state of precipitation in global models. *J. Geophys. Res. Atmos.* 115, D24211. doi: 10.1029/2010JD014532

Sun, Q., and Niu, X. (2021). Harbor resonance triggered by atmospherically driven edge waves. *Ocean Eng.* 224, 108735. doi: 10.1016/j.oceaneng.2021.108735

Tojčić, I., Denamiel, C., and Vilibić, I. (2021). Performance of the Adriatic early warning system during the multi-meteotsunami event of 11–19 May 2020: an assessment using energy banners. *Nat. Hazards Earth Syst. Sci.* 21, 2427–2446. doi: 10.5194/nhess-21-2427-2021

Tojčić, I., Denamiel, C., and Vilibić, I. (2023). Kilometer-scale trends and variability of the Adriatic present climate, (1987–2017). *Clim. Dyn.* 61, 2521–2545. doi: 10.1007/s00382-023-06700-2

Vich, M. D. M., and Romero, R. (2021). Forecasting meteotsunamis with neural networks: the case of Ciutadella harbour (Balearic Islands). *Nat. Hazards* 106, 1299–1314. doi: 10.1007/s11069-020-04041-5

Vilibić, I. (2008). Numerical simulations of the Proudman resonance. *Cont. Shelf Res.* 28, 574–581. doi: 10.1016/j.csr.2007.11.005

Vilibić, I., Rabinovich, A. B., and Anderson, E. J. (2021). Special issue on the global perspective on meteotsunami science: editorial. *Nat. Hazards* 106, 1087–1104. doi: 10.1007/s11069-021-04679-9

Vilibić, I., and Šepić, J. (2017). Global mapping of nonseismic sea level oscillations at tsunami timescales. *Sci. Rep.* 7, 40818. doi: 10.1038/srep40818

Vilibić, I., Šepić, J., Dunić, N., Sevault, F., Monserrat, S., and Jordà, G. (2018). Proxy-based assessment of strength and frequency of meteotsunamis in future climate. *Geophys. Res. Lett.* 45, 10501–10508. doi: 10.1029/2018GL079566

Vilibić, I., Šepić, J., Rabinovich, A. B., and Monserrat, S. (2016). Modern approaches in meteotsunami research and early warning. *Front. Mar. Sci.* 3, 57. doi: 10.3389/fmars.2016.00057

Vučetić, T., and Barčot, T. (2008). *Records on 'tidal wave' that hit Vela Luka on 21 June 1978* (Vela Luka–Split: Municipality of Vela Luka and Institute of Oceanography and Fisheries), 80.

Wertman, C., Yablonsky, R., Shen, Y., Merrill, J., Kincaid, C. R., and Pockalny, R. A. (2014). Mesoscale convective system surface pressure anoMalies responsible for meteotsunamis along the U.S. East Coast on June 13th 2013. *Sci. Rep.* 4, 7143. doi: 10.1038/srep07143

Zemunik, P., Denamiel, C., Williams, J., and Vilibić, I. (2022). High-frequency sea-level analysis: global correlations to synoptic atmospheric patterns. *Weather Clim. Extrem.* 38 (7), 100516. doi: 10.1016/j.wace.2022.100516

Frontiers in
Marine Science

Explores ocean-based solutions for emerging global challenges

The third most-cited marine and freshwater biology journal, advancing our understanding of marine systems and addressing global challenges including overfishing, pollution, and climate change.

Discover the latest Research Topics

See more →

frontiers | Research Topics